PROCEEDINGS OF SCIENCE

Frank N. Bash Symposium 2011: New Horizons in Astronomy

Edited by Sarah Salviander, Joel Green, and Andreas Pawlik

University of Texas at Austin

Frank N. Bash Symposium: New Horizons In Astronomy,
October 9-11, 2011
Austin Texas

 http://pos.sissa.it/

PoS(Bash11)032


BASH '11
October 9 - 11, 2011
Austin, Texas
Frank N. Bash Symposium 2011
New Horizons In Astronomy
Meredith Hughes
- Protoplanetary Disks and Star Formation
Simon Albrecht
- Extrasolar Planets
Michel Nuevo
- Astrobiology and Solar System Chemistry
Patrick Lenz
- Stellar Pulsation
Elizabeth Jeffery
- Late-Type Compact Objects
Matt Povich
- ISM/HII Regions
Stephanie Tonnesen
- Environmentally-Driven Galaxy Evolution
Eilat Glikman
- Quasars
Kevin Schawinski
- Black Hole Galaxy Coevolution
Kristian Finlator
- Reionization
John Wise
- First Light
Annika Peter
- Dark Matter
Mustafa Amin
- Inflation and the Early Universe
Mike Kesden
- Black Hole Mergers
Sarah Tuttle
- HETDEX/GMT
Fritz Benedict
- Banquet Speaker
Organizing Committee
Joel Green (chair)
Barbara Castanheira
Julie Comerford
Emily Freeland
Andreas Pawlik
Sarah Salviander
Colette Salyk
Pearl Sandick
Navin Sivanandam
Sarah Tuttle
Mary Lindholm
Matthew McDaniel
Shelley Stone
Jim Umbarger
Debbie Winegarten
McDonald Observatory
THE UNIVERSITY OF TEXAS AT AUSTIN
The Frank N. Bash Symposium 2011 is made possible by the generous contributions of The University of Texas at Austin McDonald Observatory and Department of Astronomy Board of Visitors
http://www.as.utexas.edu/bov/bov.html
bashsymposium.org

Preface

The 4th Frank N. Bash Symposium took place on October 9-11, 2011, in the central campus of the University of the Texas at Austin. The Symposium is held biannually in honor of former McDonald Observatory Director, Frank Bash. A total of fourteen review talks were presented by a first-class group of invited postdoctoral researchers. Their topics spanned all of modern astronomy, from the local universe to the very beginnings of space and time. Highlights were local researcher Sarah Tuttle's presentation of the UT role in the Giant Magellan Telescope project, as well as the posters by graduate students and undergraduates from universities around Texas. During the speaker and poster sessions, social luncheons, dinners, and meetings, a vigorous spirit of scientific inquiry and community was fostered between the research visitors, the faculty and staff of UT, and the McDonald Observatory Board of Visitors (which provides ongoing financial support for the Symposium). The Symposium was a great success, with 120 visitors from across Texas, the United States, and Europe. We demonstrated that it is truly possible to span the Universe in fifteen well-tuned talks when using engaging speakers selected from the ranks of enthusiastic young researchers.

An event like this requires the supporting efforts of many individuals. We would like to extend our thanks to the following people for their contributions to the Symposium: Associate Chair of Astronomy Karl Gebhardt for starting off the festivities, and Astronomy Department Chair Dan Jaffe for offering much-needed support and advice; all of the staff whose assistance made the Symposium run smoothly, including Shelley Stone, Matthew McDaniel, Mary Lindholm, Jim Umbarger, Kelly Quinney, Gordon Orris, and Debbie Winegarten, who collectively manned the registration desk, organized and scheduled events, managed poster stands, and crafted and updated the Bashfest webpage; Lara Eakins for providing a seamless audio-visual experience that kept the audience engaged throughout; Jim Umbarger and others who took photographs for the webpage and these proceedings; our banquet speaker, Fritz Benedict, for an entertaining and thought-provoking talk; Judit Györgyey Ries for her inventive poster design; Sarah Tuttle and Colette Salyk for their beautiful T-shirt design; postoc Mia Bovill for her enthusiastic and efficient organization of the flash poster talks; and past Bashfest organizers, particularly Remco van den Bosch and Tom Barnes, for guidance.

The sessions were chaired by Colette Salyk, Joel Green, Julie Comerford, and Andreas Pawlik. The SOC and LOC were combined for this occasion and included: Joel Green (chair), Barbara Castanheira, Julie Comerford, Emily Freeland (Texas A&M University) Andreas Pawlik (proceedings editor), Sarah Salviander (proceedings senior editor), Colette Salyk, Pearl Sandick, Navin Sivanandam, and Sarah Tuttle (representing postdocs); additionally, Mary Lindholm, Matthew McDaniel, Shelley Stone, Jim Umbarger, Lara Eakins, Kelly Quinney, Gordon Orris, and Debbie Winegarten (representing staff). Finally, we would like to extend our heartfelt thanks to the McDonald Observatory Board of Visitors for their interest and support, both financial and moral, all of which makes this Symposium possible.

On behalf of the LOC, SOC, and Proceedings Editors,
Joel Green, Sarah Salviander & Andreas Pawlik

PoS(Bash11)032

Frank Bash

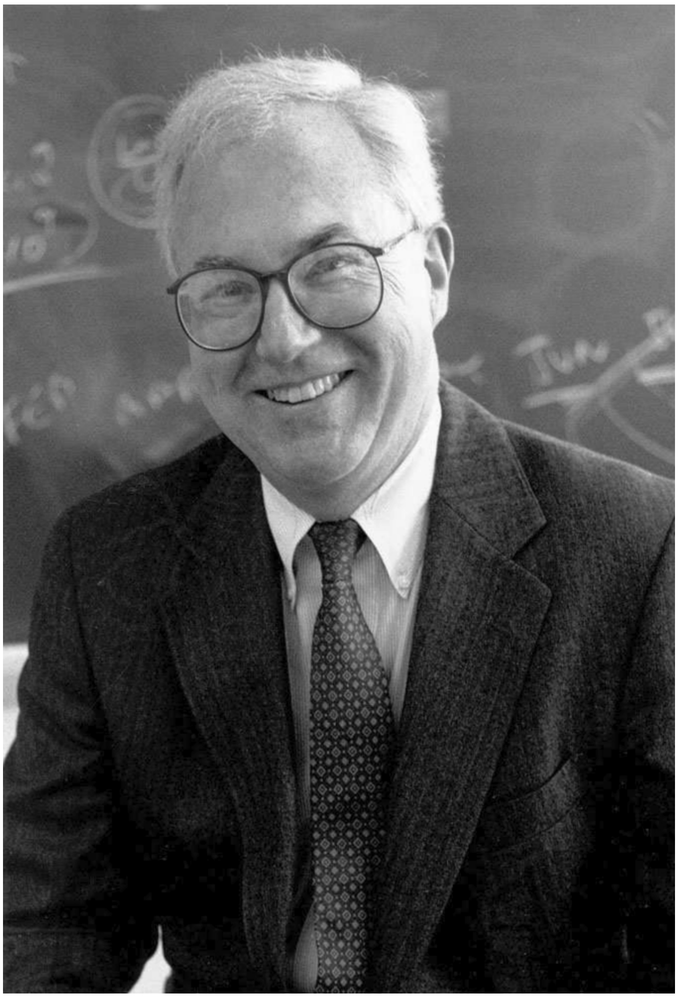

Frank N. Bash, Ph.D., served as director of McDonald Observatory from 1989-2003. A native of Medford, Oregon, Bash earned his bachelor’s degree from Willamette University in Salem, Oregon; his master’s degree in astronomy from Harvard University; and his doctorate from the University of Virginia. A well-known and widely published specialist in radio astronomy, Dr. Bash’s research interests include large-scale formation processes in spiral galaxies. Dr. Bash joined the faculty of the University of Texas at Austin in 1969. Serving as Chairman of the Astronomy Department from 1982 through 1986, in 1985 he was named the Frank N. Edmonds Regents Professor. Among numerous awards for quality teaching, he was named to the teaching excellence Hall of Fame at UT Austin in 1984. As Director of McDonald, Dr. Bash led the effort for design, funding, and construction of the Hobby-Eberly Telescope. Dr. Bash also led the effort to expand the public-outreach programs of the Observatory. These programs include the Observatory’s Visitors Center, which hosts approximately 60,000 visitors per year, and StarDate radio, which reaches millions of people each day in English, Spanish, and German.

Frank N. Bash Symposium: New Horizons In Astronomy speakers and SOC

Speakers

Simon Albrecht

Exoplanets

In this paper I will discuss the current knowledge we have on planets orbiting other stars than our sun: exoplanets. Our ability to learn about exoplanets depends on the method we choose to search for them. Therefore I will give a short overview of the different detection techniques that are used to find planets. Special emphasis is placed on two techniques, radial velocity search and transit search.

I will also focus on a long standing riddle of the field: The occurrence of gas giant planets on orbits with periods of only a few days (Hot-Jupiters). These planets are similar to Jupiter but orbit their stars much closer than even Mercury orbits our own sun. The detection of these Hot-Jupiters was a surprise, as it is thought that they cannot form so close to their stars. Recent measurements of the Rossiter-McLaughlin effect helped to shed light on the formation and evolution of these systems.

Finally I will highlight some exciting new developments and recent detections of exoplanets in extreme environments.

Patrick Lenz

Asteroseismology of Stars on the Upper Main Sequence

I review the properties of pulsators located on the upper main sequence in the HR diagram and discuss asteroseismic inferences on the internal structure of stars of spectral type A and B. Special attention is given to the problem of uncertainties in stellar opacities in modeling.

Michel Nuevo

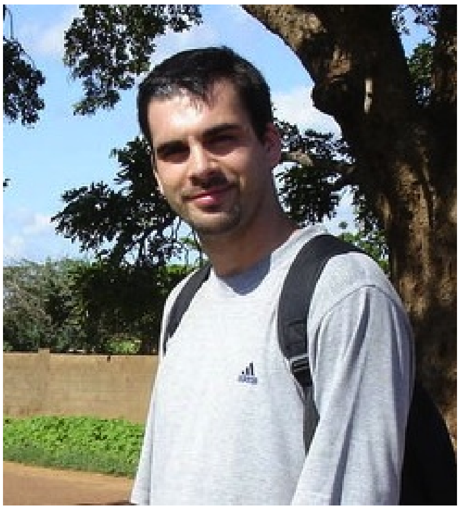

Laboratory Astrochemistry: A Powerful Tool to Understand the Origin of Organic Molecules in the Interstellar Medium, Comets, and Meteorites

During the past two decades, astrochemistry laboratory simulations have shown that complex organic molecules can be formed under simulated astrophysical conditions from the vacuum ultraviolet (UV) irradiation of ice mixtures containing simple species such as H_2O, CO, CO_2, CH_3OH, and NH_3. These organics include compounds of biological and prebiotic interests such as amino acids—the building blocks of proteins, and nucleobases—the informational subunits of DNA and RNA. Although the presence of amino acids in the interstellar medium (ISM) has not been confirmed by observations to date, they have been detected in meteorites, indicating that biomolecules and/or their precursors can be formed under extraterrestrial, non-biological conditions. Nucleobases have also been detected in meteorites, broadening the variety of complex organic molecules that can be formed in astrophysical environments. Like amino acids, nucleobases and other N-heterocycles have not been observed in the ISM. In the following, I will review some of the progress made by laboratory astrochemistry towards understanding the formation of organic species from the UV irradiation of ices at low temperature under astrophysically relevant conditions. This discussion will be focused on the formation of amino acids and other molecules of prebiotic interest such as urea and glycerol. Then, I will present recent studies on the for- mation of nucleobases and related compounds from the UV irradiation of pyrimidine in H_2O, NH_3, and CH_3OH ices, which show the formation of a large suite of photo-products including the nucleobases uracil and cytosine.

Elizabeth Jeffery

Late-type Compact Objects

The final stages of stellar evolution for a low mass star are fairly unspectacular when compared to their high mass siblings. Once the outer layers of a star are shed, the hot exposed core that’s left behind and begins to cool. As it does so, it exhibits several interesting (and useful!) character traits. In this paper I will give an overview of the discovery of white dwarf stars and what we now understand about their formation and place within the story of stellar evolution. The fate of $\sim 98\%$ of the stars in our Galaxy, white dwarfs continue to prove their usefulness and versatility as probes of understanding a number of interesting astrophysical problems. I will discuss a few of these applications, with particular emphasis on work done studying white dwarfs in star clusters.

Matt Povich

Beyond Strömgren Spheres and Wind-Blown Bubbles: An Observational Perspective on H II *Region Feedback*

Massive stars produce copious quantities of ultraviolet radiation beyond the Lyman limit, photoionizing the interstellar medium (ISM) and producing H II regions. As strong sources of recombination- and forbidden-line emission, infrared continuum, and thermal (free-free) radio continuum, H II regions serve as readily-observable beacons of massive star formation in the Milky Way and external galaxies. Along with supernovae, H II regions are dominant sources of feedback in star-forming galaxies, injecting radiative and mechanical luminosity into the ISM. H II regions may prove more important than supernovae as triggers of star formation through localized compression of cold cloud cores. In this review, I give a broad overview of the structure and time-evolution of H II regions, emphasizing complications to the theoretical picture revealed by multiwavelength observations. I discuss a recent controversy surrounding the dominant feed- back mechanism in 30 Doradus, the most luminous H II region in the Local Group. I summarize the first results from the Milky Way Project (MWP), which has produced a new catalog of several thousand candidate Galactic H II regions by enlisting $> 35,000$ "citizen scientists" to search *Spitzer Space Telescope* survey images for bubble-shaped structures. The MWP and similar large catalogs enable empirical studies of Galactic H II region evolution across the full range of luminosities and statistical studies of triggered star formation.

Michael Kesden

Black-Hole Mergers

Observations of black-hole mergers will provide unique insights into both general relativity and cosmology. The gravitational waves produced in such mergers directly probe strong-field solutions to Einstein's equations, and the rate at which mergers occur constrains the hierarchical formation of supermassive black holes and their host galaxies. The three primary theoretical tools for studying merging black holes are post-Newtonian expansions, black-hole perturbation theory, and numerical relativity. I will briefly explain how these tools complement each other in developing a general solution to the problem of black-hole mergers, highlighting some of my own research in each of these three areas.

Stephanie Tonnesen

Environmentally-Driven Galaxy Evolution

The galaxy population in clusters differs from that in the field. The cluster galaxy population (at $z \leq 0.4$) is dominated by red, early-type galaxies. Although some of this can be explained by the mass-morphology relation, in this proceedings I discuss work that has shown that, particularly in low-mass galaxies, there is environmentally-driven evolution from blue (star-forming) to red (non-star-forming). While environment can be measured in several ways, I show that local environment affects galaxies up to the scale of the halo in which they reside. Focusing on clusters, I introduce the different mechanisms that can affect galaxies: galaxy-cluster, galaxy-galaxy, and galaxy-intracluster medium interactions. I then give an overview of the evidence that the color-evolution of galaxies from blue to red is reflected in the morphological evolution of galaxies from spiral to S0, and discuss the necessary steps in the evolution of spirals into S0s. I then briefly describe some of my own research examining the role of ram pressure stripping on the morphological evolution of spiral galaxies. While ram pressure stripping can effectively remove the fuel for star formation and redden galaxies, this will form S0s that are less luminous than their spiral progenitors. Therefore, while ram pressure stripping may be an important mechanism driving the formation of S0s from spirals, it cannot be the only process driving this morphological evolution.

Eilat Glikman

The Reddest Quasars: A Transitional Phase in Quasar/Galaxy Co-Evolution

Quasars are extremely luminous sources powered by accretion of gas onto a supermassive black hole in the nucleus of some galaxies. Most of the $> 10^5$ quasars identified in the literature have been identified in optical surveys through the "ultraviolet excess" (UVX) method. However, these samples are known to be incomplete and biased because of obscuration and anisotropic radiation. To overcome some of these biases and search for candidate obscured quasars, we matched radio sources from the FIRST 1.4 GHz survey with the 2MASS near-infrared survey and selected objects with red optical-to-near-infrared colors. We followed up our candidates with optical and/or near-infrared spectroscopy and identified 119 dust-reddened quasars, defined as having at least one broad emission line in and a reddening of $E(B-V) > 0.1$. The sample spans a wide redshift range, $0.1 < z < 3$ and reaches a reddening, $E(B-V) \lesssim 1.5$. When corrected for extinction, red quasars are the most luminous objects at every redshift and the fraction of red quasars increases with luminosity. The properties of red quasars suggest that they are revealing an evolutionary phase where the heavily obscured quasar is emerging from its dusty environment prior to becoming a "normal" blue quasar. We compute the fraction of quasars that are in this red phase and determine that its duration is $\sim 20\%$ as long as the unobscured quasars phase: a few million years.

Kevin Schawinski

Black Hole Galaxy Coevolution

The growth of black holes and the formation and evolution of galaxies appear to be linked at such a fundamental level that we think of the two as 'co-evolving.' Recent observations show that this co-evolution may be complex and be the result of several different pathways. While it is clear that black hole accretion is linked to specific phases of the evolution of the host galaxy, the impact of the energy liberated by the black hole on the evolutionary trajectory of the host by feedback is less clear. In this contribution, I review the motivations for co-evolution, the current state of the observational picture, and some challenges by black hole feedback.

Sarah Tuttle

Spectroscopy and the Age of Giant Telescopes

Is your 4 meter telescope just not cutting it anymore? Embarrassed to mention the telescope time you had just the other week when talking about your newest data project? Don’t worry, the age of the giant telescope is upon us. I will review the status of the three current ELT projects, as well as spectroscopic technologies focusing on multi-object spectroscopy. HETDEX (the Hobby Eberly Dark Energy Experiment) uses a new approach to large instruments, replicating a spectrograph channel 150 times to produce 33,600 individual spectra across a 22 arcminute field. The technology being built can be easily modified and ported to other telescopes to take quick advantage of the integral field approach. I will touch on the many experiments that await first light as these instruments come to fruition. Let’s discuss why we are pouring massive resources into these telescopes and see what they can do for us.

PoS(Bash11)032

Kristian Finlator

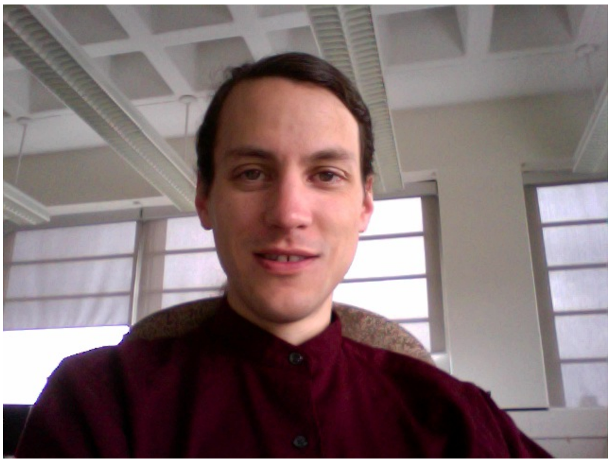

Recent Advances in Cosmological Hydrogen Reionization

I discuss recent advances in the study of hydrogen reionization, focusing on progress that was achieved during the years 2010-2011. First, I discuss recent measurements of the progress of reionization. Next, I discuss recent observational constraints on the nature and abundance of the dominant ionizing sources. Finally, I discuss recent progress in modeling reionization. This review is written for an audience of astronomers who do not specialize in the high-redshift Universe.

John Wise

First Light

The first stars in the universe are thought to be massive, forming in dark matter halos with masses around 10^6 solar masses. Recent simulations suggest that these metal-free (Population III) stars may form in binary or multiple systems. Because of their high stellar masses and small host halos, their feedback ionizes the surrounding 3 kpc of intergalactic medium and drives the majority of the gas from the potential well. The next generation of stars then must form in this gas-poor environment, creating the first galaxies that produce the majority of ionizing radiation during cosmic reionization. I will review the latest developments in the field of Population III star formation and feedback and its impact on galaxy formation prior to reionization. In particular, I will focus on the numerical simulations that have demonstrated this sequence of events, ultimately leading to cosmic reionization.

Annika Peter

Dark Matter

From astronomical observations, we know that dark matter exists, makes up 23% of the mass budget of the Universe, clusters strongly to form the load-bearing frame of structure for galaxy formation, and hardly interacts with ordinary matter except gravitationally. However, this information is not enough to identify the particle specie(s) that make up dark matter. As such, the problem of determining the identity of dark matter has largely shifted to the fields of astroparticle and particle physics. In this talk, I will review the current status of the search for the nature of dark matter. I will provide an introduction to possible particle candidates for dark matter and highlight recent experimental astroparticle- and particle-physics results that constrain the properties of those candidates. Given the absence of detections in those experiments, I will advocate a return of the problem of dark-matter identification to astronomy, and show what kinds of theoretical and observational work might be used to pin down the nature of dark matter once and for all. This talk is intended for a broad astronomy audience.

Poster Presenters

Taylor S. Chonis
Photometry of the Stellar Tidal Stream in the Halo of Messier 63

Anson D’Aloisio
The Effects of Primordial Non-Gaussianity on Giant-Arc Statistics: A Scale-Dependent Example

Amanda Heiderman
The VIRUS-P Investigation of the eXtreme Environments of Starbursts (VIXENS): Survey and First Results

Jacob A. Hummel
The Hunt for the First Supernovae: The Source Density and Observability of Pair-Instability Supernovae from the First Stars

John R. Jardel
Integral Field Spectroscopy of the Center of the Draco Dwarf Spheroidal

Myoungwon Jeon
The First Galaxies: Assembly with Black Hole Feedback

Hyo Jeong Kim
Evidence of Episodic Accretion in Spitzer IRS Spectra of Low-Luminosity Embedded Protostars

Hyunbae Park
Revisiting the Post-reionization Kinetic Sunyaev-Zel’dovich Effect on the Cosmic Microwave Background Fluctuations

Chalence Safranek-Shrader
Primordial Star Formation in the First Galaxies

PROCEEDINGS OF SCIENCE

Exoplanets

Simon Albrecht*
Massachusetts Institute of Technology, Kavli Institute for Astrophysics and Space Research, Cambridge, MA 02139, USA
E-mail: albrecht@space.mit.edu

In this paper I will discuss the current knowledge we have on planets orbiting other stars than our sun: exoplanets. Our ability to learn about exoplanets depends on the method we choose to search for them. Therefore I will give a short overview of the different detection techniques that are used to find planets. Special emphasis is placed on two techniques, radial velocity search and transit search.
I will also focus on a long standing riddle of the field: The occurrence of gas giant planets on orbits with periods of only a few days (Hot-Jupiters). These planets are similar to Jupiter but orbit their stars much closer than even Mercury orbits our own sun. The detection of these Hot-Jupiters was a surprise, as it is thought that they cannot form so close to their stars. Recent measurements of the Rossiter-McLaughlin effect helped to shed light on the formation and evolution of these systems.

Finally I will highlight some exciting new developments and recent detections of exoplanets in extreme environments.

Frank N. Bash Symposium New Horizons In Astronomy,
October 9-11, 2011
Austin Texas

*Speaker.

PoS(Bash11)002

1. Introduction

Until the first exoplanet was detected around a sunlike star in 1995, only one planetary system had been available for study: our own. The theories that explained how planets formed out of a disk with smaller rocky planets closer in and gas giants further out could not be tested on new data. There was no way to know how common our type of system was or even if planets were common at all. By the close of 2011, about 600 exoplanets had been discovered, and even though there are biases as to what kinds of planets we can detect, interesting patterns have emerged, that shed new light on the main questions in the field.

We are on our way to finding out which other stars have planets and to what extent the architecture of these systems is similar to the solar system. We are constantly improving our understanding of planet formation, and are getting the first information on planetary atmospheres. There is an ongoing search for planets that are very similar to Earth and may be able to support life.

Our ability to learn about exoplanets depends on the method we choose to search for them. Therefore this paper will begin with an overview of the different detection techniques that are used to find planets. Special emphasis is placed on two techniques, radial velocity search and transit search.

In section 3 we will highlight one of the challenges to our current understanding of (exo)planet formation: the occurrence of Hot-Jupiters, gas giants on orbits around main sequence stars with orbital periods of only a few days. We will look into the progress which has been made in explaining these. We focus on evidence which comes from an until recently seldomly measured observable in astronomy: the angle between the orbital and rotational angular momentum of the stellar body. The Kepler observatory delivered some very exciting new results over the last months and we will highlight a few of these in section 4 before closing with an outlook in section 5.

This short review cannot possibly cover all the knowledge which has been accumulated over the last few years in the field of exoplanets. Good sources of information are the textbooks edited by Seager[42] and written by Perryman [33].

2. Detection techniques for extra solar planets

2.1 Radial velocity

Due to the gravitational pull of a planet on its host star, the orbit of the planet is mirrored in a much smaller movement in the star. The star makes a tiny orbit around the common center of mass of the star–planet system, which can be located inside the star. The component of this stellar wobble along the line of sight manifests itself in the form of a blueshift of the stellar absorption lines when the star is moving towards us and a redshift when it is moving away from us. The amount of displacement of the stellar absorption lines, measured with a spectrograph, lets us compute the radial velocity (RV) of the star. The amplitude (K) of these RV changes depends on the orbital period (P), and the eccentricity (e) of the orbit. It increases with the mass of the unseen planet (M_p), and decreases with the mass of the star ($M_\star$) (e.g [13]);

$$K = \left(\frac{2\pi G}{P}\right)^{1/3} \frac{M_\mathrm{p} \sin i_\mathrm{o}}{M_\star + M_\mathrm{p}} \frac{1}{(1-e^2)^{1/2}}. \tag{2.1}$$

Here i_o indicates the inclination of the orbit, where an inclination of 90° indicates an edge-on orbit with the observer located within the orbital plane of the planet. Equation 2.1 shows that to obtain the mass of an exoplanet, the mass of the host star needs to be estimated from stellar modeling. For non transiting planets the orbital plane is not known; only the minimum mass of the planet can be estimated. This is similar to the situation one encounters for single lined binary systems, where only the radial velocity of one star can be measured. If radial velocities of both stars can be measured, a double lined binary, and the system shows eclipses then the mass of both components can be measured independently of any model assumptions. These measurements are important to calibrate models of stellar structure and evolution [48]. In rare cases the radial velocity of an exoplanet can also be obtained directly, leading to a model-independent measurement of the masses in that system [44].

Due to the great difference between planetary and stellar mass, the amplitudes of the RV changes are small in exoplanet systems. For Jupiter the maximum amplitude of the RV signal would be 12.5 m s^{-1} and it would be as small as 0.09 m s^{-1} for the Earth. With

$$\frac{V_r}{v} = \frac{\Delta\lambda}{\lambda} \quad \text{for} \quad V_r << c, \tag{2.2}$$

where c indicates the speed of light, V_r the radial velocity of the star, λ the measurement wavelength, and $\Delta\lambda$ the shift in wavelength; this translates into small shifts in positions of stellar absorption lines. Techniques to measure these small shifts therefore measure not only the position of a single stellar absorption line but all the absorption lines in a large spectral window. Commonly a window between $\sim$ 400 nm and $\sim$ 700 nm is used depending on the particular technique applied. One technique uses a mask, nowadays a software mask, for cross-correlation with the stellar absorption line spectrum [18, 4, 35]. A single very high SNR line of which the shift can be measured with high accuracy is obtained. In another approach the light of the star passes through a gas absorption cell just before entering the slit of the spectrograph, imprinting the absorption of this particular gas on the stellar spectrum. In effect this multiplies the stellar spectrum by the gas spectrum. These observations are then compared to a combination of 1) a stellar spectrum observed without the gas cell and 2) a spectrum only containing absorption lines of the gas. The radial velocity of the star at a given observation is found by combining the gas cell spectrum with the clean stellar spectrum and applying a RV shift between the two. The RV which give the best fit represents the measured RV [7, 27].

The first exoplanet orbiting a sunlike star, 51 Pegasi, was detected via radial velocity measurements [29]. 51 Peg b orbits its host star in only 4.2 days and creates periodical radial velocity changes in its host star with an amplitude of 59 m s^{-1}. The current limit on the precision of radial velocity is about ~ 0.5 m s^{-1} and programs are under way to further improve this accuracy [26].

2.2 Photometry

Occasionally we are able to observe a solar eclipse, when the moon moves between the sun and the observer. If a celestial body occults only a smaller part of the sun, like Venus will do June 5/6, 2012, only small parts of the solar surface will be blocked from view, leading to a small reduction of overall flux from the sun during the time Venus transits in front of the sun (Figure 2.2).

When the line of sight towards a star hosting a planet coincides with the orbital plane of the planet, then every time the planet travels in front of its host star a small part of the disk would

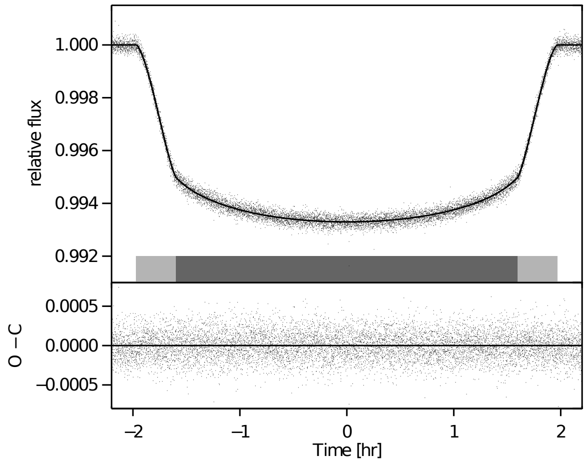

Figure 1: Transit Photometry *Left:* Transit of Venus 2004. Picture obtained from: `http://en.wikipedia.org/wiki/Transit_of_Venus` *Right:* Light observed from the HAT-P-7 system before, during, and after HAT-P-7b transits in front of its host star. The data was obtained by the Kepler spacecraft during Q6. The upper panel shows the phase folded light curve of a few transits and the best fitting model. The gray bars indicate the times of first, second, third, and forth contact. At times of first and forth contact the two disks touch. Between second and third contact the planetary disk is completely in fornt of the stellar disk. The depth of a Venus transit would be much smaller than the HAT-P-7b transit, as Venus occults only about 0.1% of the sun.

be obscured from the view. By monitoring stars for periodical brightness changes exoplanets can be discovered. If a Jupiter sized planet would transit a solar type star, a reduction of about 1% in total light would be observed, while an earth sized planet transiting the same star would only lead to a reduction of about 10^{-4} in flux. The first exoplanet which was found to transit its host star is HD 209458b [20, 8]. This star was first found via a radial velocity search. Since then HATnet [3], OGLE [49], WASP [34], and XO [30] and other ground based surveys (see [33] for a more complete listing) have discovered over 100 planets.

Most of these planets transit their stars on short orbits of only a few days. This is a selection effect, the wider the planet orbits the lower the probability to see it transit. The probability that a planet with $R_{\rm p} \ll R_{\star}$, on a circular orbit ($e \equiv 0$) is seen in transit ($P_{\rm tra}$) or occultation ($P_{\rm occ}$) is

$$P_{\rm tra} = P_{\rm occ} = R_{\star}/a \approx 0.005 \frac{R_{\star}}{R_{\odot}} \left(\frac{\rm a}{\rm AU}\right)^{-1}, \tag{2.3}$$

for a circular orbit (equ. 11, [50]). Here $R_{\star}$ indicated the stellar radius, $R_{\odot}$ the radius of the sun and a the semi major axis and AU one astronomical unit. An observer at a random position outside the solar system would be able to see a transit of Earth in front of the sun with a probability of 0.5%. To actually observe a transit, the observations would have to take place around the 13 hours which the earth needs to cross the solar disk once a year. Therefore a ground based transit search, interrupted by daylight will only effectively find planets on orbits of a few days and will not be able find long period systems.

Surveying smaller and cooler M dwarfs for transits has the advantage that for the same planetary radii the depth of the transit is deeper, leading to the discovery of smaller planets with the same measurement precision. In addition, planets with relatively short periods will be located nearer the habitable zone of that star, defined by the distance from the host star where water is liquid. However, late type stars are intrinsically faint, leading to a low density of suitable search targets on the plane of the sky and the need to be targeted separately. The MEarth survey detected the 6.5 M_{Earth} planet GJ 1214b with this approach [9].

Continuous observations from a space-based observatory would increase the sensitivity towards smaller transit depths as variations in the earth's atmosphere do not corrupt the measurements. In addition the sensitivity towards planets with longer orbital periods would be increased as near continuous observations are possible. Recent results from the Kepler satellite are discussed in section 4.

2.3 Other techniques to search for exoplanets

There are a variety of other techniques to search for planets outside our own solar system. Each of these has particular advantages and disadvantages. We refer the reader to [42] and [33] for a more detailed overview and discuss them here only briefly:

- **Direct Imaging:** Obtaining photons from an exoplanet directly would enable the study of their atmospheres, important if we want to learn about the planets ability to host life. As the contrast ratios between planets and host stars are steep and the separations are small, this is at the same time also a very challenging method. If we were to observe the solar system from a distance of 10 pc, we would observe Jupiter at an angular distance of only 0.5 arcsec and with a contrast ratio of 10^{-9} in the visible. Therefore direct imaging surveys work in the near infrared where contrast ratios between the cold body, the planet, and the hot body, the star, are reduced. Surveys also often target young systems, where planets still emit gravitational energy from their formation. This way a few systems have been detected via direct imaging (e.g. [28]). With a new generation of dedicated instruments which are currently installed at different observatories, direct imaging might soon contribute to many new discoveries in exoplanet science. As direct imaging is sensitive to planets on wide orbits, a different planet population is probed than with previous methods.

- **Astrometry:** While with the radial velocity method we can measure velocity change along the line-of-sight, with astrometry measurements of stellar positions and their changes, projected on the sky, are measured. An unseen companion can cause both, changes in radial velocity and the projected position changes. While the radial velocity signal decreases with separation between the star and the planet the astrometric signal is proportional to the separation. This increased sensitivity towards companions on wider orbits, and the different sets of orbital parameters that are measured make astrometric observations complementary to the RV method. Using the fine guidance sensors on board *Hubble*, the astrometric signature of a few already known planets has been detected, and the masses of these non transiting planets have been determined. Benedict et al. 2006 [5] detected the astrometric signature of the planet orbiting ε Eridani. Using *Hipparcos* data, Reffert & Quirrenbach 2011 [37] have set upper mass limits on additional planets also found via the RV method. With the space-based GAIA mission [24] and the ESPRI planet search using the VLT Interferometer

[22], this method will likely deliver new planet detection around relatively nearby stars and will remove the ambiguity in the planetary mass of a number of already detected systems.

- **Microlensing:** If a star passes near the line of sight between the observer and a more distant background star, then multiple images of the background star are created. These images can not be separated and the light from the background star simply appears magnified. If the foreground star harbors a planet then additional substructure can be seen on the light curve of these microlensing events, enabling the detection of these lensing planets. This detection technique has some unique advantages and disadvantages and we refer the interested reader to [16] for a thorough review. One recent interesting result of microlensing surveys was the realization that our galaxy harbors many free floating planets [46].

- **Timing:** The first discovery of an exoplanet was achieved by timing the pulsar PSR B1257+12 [53]. The planets founds around this neutron star have masses of only a few earth masses. By carefully modeling the planetary orbits and their evolution the presence of a third planet, with a mass of 0.02 M_{Earth} was inferred. While planets around supernova remnants remain rare, the existence of only a few of these planets poses some interesting questions about planet formation and evolution. As we will see in section 4, the timing of eclipses and transits can also lead to the discovery of planetary companions.

3. Hot-Jupiters

3.1 Star and planet formation in a nutshell

Star formation occurs in cold dense clouds of gas and dust. While the cloud is supported by magnetic fields and turbulence, the densest regions can collapse under the influence of gravity. At the center of these dense cores, a star begins to form. During this process it is thought that a circumstellar disk is formed by infalling material due to its non-zero angular momentum. Accretion from the disk onto the star is believed to drive bipolar outflows that help to transport the excess angular momentum away. When the reservoir of cloud material that feeds the disk is exhausted, the accretion rate from the disk onto the star drops. While the star contracts, its temperature increases and the developing stellar winds clear away the remaining material from the cloud. In the disk, planetesimals and finally planets are thought to be able to form. The star, which thus far has generated most of its energy from contraction, is now mainly powered by hydrogen fusion and does not contract anymore. It has reached the main sequence. The surrounding disk is dissipated and the leftover material comprises a debris-disk, possibly with planets.

The properties of the planetary systems discovered over the last years often have surprised us and challenged our paradigmata of planet formation and evolution. One of these surprises was the discovery of gas giant planets, like Jupiter, but on very close orbits leading to orbital periods of only a few days. The discovery of these Hot-Jupiters was a surprise, as it is believed that gas giants can form only at distances of a few AU behind the *snow line*. It is thought that only there enough solid material is present to rapidly form a solid proto-planet which acts as a seed for the gas giant.

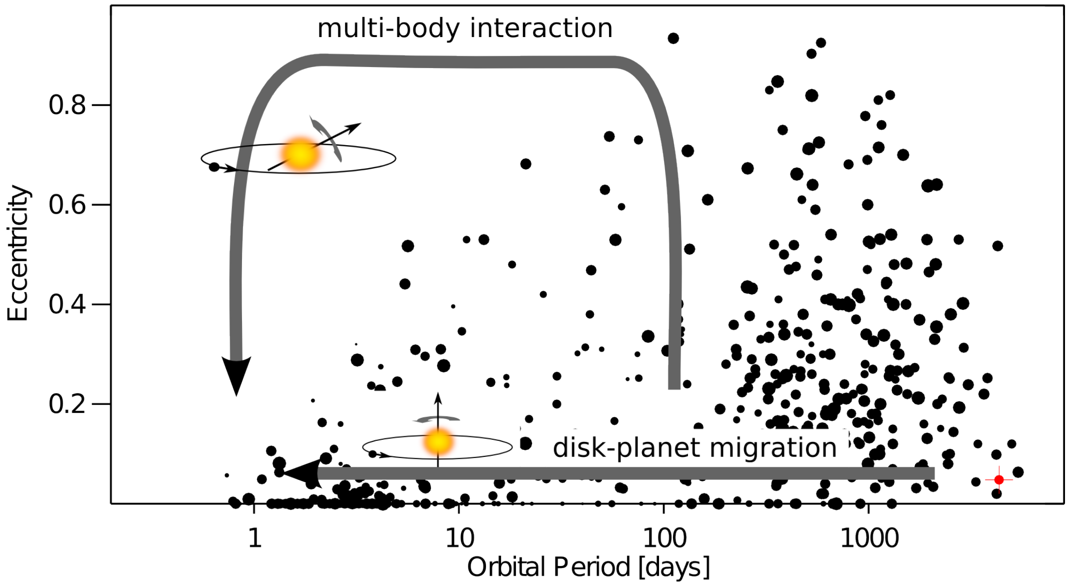

Figure 2: Migration of giant planets. Orbital period and eccentricity of 600 exoplanets. The size of the dots indicates the mass of the planets. The gas giant in the solar system with the shortest orbital period, Jupiter, is indicated by the red circle with a cross. Migration of the planet via an interaction with the disk would effect the orbital period but would not significantly change the orbital, eccentricity and inclination. A migration also involving multi body interaction, like planet-planet scattering or Kozai migration, would increase the orbital eccentricity and inclination. Orbital eccentricities eventually decrease for close systems. For star-planet systems the damping of obliquities might take much longer. This makes the stellar obliquity a good tracer of the migration history in these systems.

3.2 Migration of giant planets

Different classes of processes have been proposed which might transport giant planets from their presumed birthplaces at distances of many astronomical units from their host stars, inward to a fraction of an astronomical unit, where we find them. Some of these processes are expected to change the relative orientation between the stellar and orbital spin (e.g. [32, 15, 10]). These processes involve planet-planet scattering or Kozai migration. Migration via an interaction between the young planet and the disk out of which it formed would not change the orbital plane of the planet. Therefore, if good alignment between disk and stellar equator is assumed, then this migration would lead to a good alignment between the orbital and stellar angular momenta (e.g. [23]), or even reduce a misalignment between them [12]. Measuring stellar obliquities, the angle between the stellar rotation axis and orbital angular momentum, might therefore help to distinguish between different migration theories and improve our understanding of the formation and evolution of these systems (Figure 2).

3.3 Measuring stellar obliquities through the RM effect

The sun is the only star for which we can obtain detailed information on spacial scales much smaller than its diameter. For most stars, we are not able to resolve their surfaces. These stars are essentially point sources, even for the biggest telescopes.

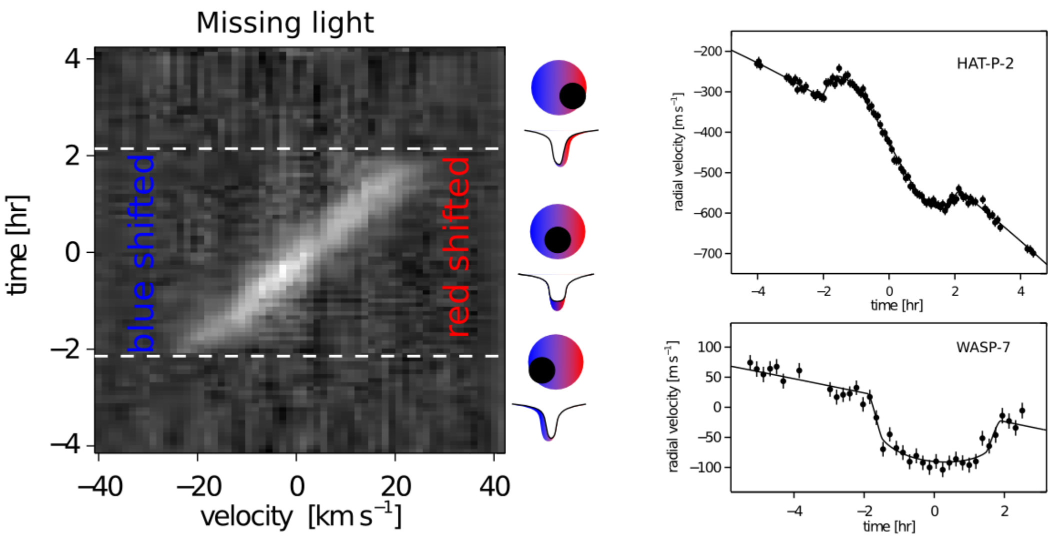

Figure 3: The Rossiter-McLaughlin effect. During the transit of a planet in front of its star different parts of the stellar absorption lines are hidden from view. The left panel shows this missing component during a transit in the HAT-P-2 system. At the beginning of the transit, parts of the approaching stellar surface area are hidden from you, blueshifted light is missing. At the end, red shifted light is missing. The RVs measured during this transit are shown in the upper left panel, where one can see the change in RV due to the orbital velocity and the RM effect. The lower left panel shows the RM effect in the WASP-7 system, where the stellar rotation is by $\sim 90^\circ$ titled agains the orbital angular momentum [2].

A transit of an exoplanet over the disk of its host star can provide us with an opportunity to obtain high spatial resolution. During transits, telescopes integrate not over the complete stellar disk, as parts are hidden from view. Already Holt 1893 [21] realized that, for the case of eclipsing double stars, this is an opportunity to measure the projected stellar rotation speed ($v \sin i_\star$) independently from a measurement of the width of the absorption lines. Stellar lines are broadened by the Doppler shift due to rotation. Light emitted from approaching stellar surface areas is blue shifted and light emitted from receding stellar surface areas is red shifted. During eclipse parts of the rotating stellar surface is hidden, causing a weakening of the corresponding velocity component of the stellar absorption lines. Modeling of this spectral distortion reveals $v \sin i_\star$ and the angle between the stellar and orbital spins projected on the plane of the sky: the projected obliquity (see Figure 3).

A claim of the detection of the rotation anomaly was made by Schlesinger 1910 [41], but more definitive measurements were achieved by Rossiter 1924 [38] and McLaughlin1924 [31] for the β Lyrae and Algol systems, respectively. These researchers reported the change of the first moment of the absorption lines, sometimes called center of gravity, derived form the shape of the absorption line. Struve 1931[45] reported the shape and its change during eclipse in the Algol system. The phenomenon is now known as the Rossiter-McLaughlin (RM) effect.

3.4 Results for obliquities in extrasolar planetary systems

The first measurement of a projected obliquity in an extrasolar system was made by Queloz et al. 2000 [36]. They found that HD 209458 has a low obliquity. Over the following years the angle between the stellar and orbital spins have been measured in about 30 systems. It was found that for some of these systems the orbits are inclined or even retrograde with respect to the rotational spins of their host stars [19, 51, 43, 1].

Winn et al. 2010 [52] found that close-in giant planets tend to have orbits aligned with the stellar spin if the effective temperature ($T_{\rm eff}$) of their host star is $\lesssim 6250$ K and misaligned otherwise. Schlaufman 2010[40] obtained similar results measuring the inclination of spin axes along the line of sight. Winn et al. 2010 [52] further speculated that this might indicate that *all* giant planets are transported inward by processes which randomize the obliquity. In this picture tidal waves raised on the star by the close-in planet realign the two angular momentum vectors. The realignment time scale would be short for planets around stars with convective envelopes ($T_{\rm eff} \lesssim 6250$ K), but long, compared to the lifetime of the system, if the star does not have a convective envelope ($T_{\rm eff} \gtrsim 6250$ K).

Over the last $1\frac{1}{2}$ years the number of systems with measured projected obliquities nearly doubled and the predictions made by Winn et al. 2010 [52] have been confirmed for these systems (see Figure 4) lending support to the idea that systems with close giant planets generally started out with a very broad range of obliquities, and that the observed low obliquities of many systems are a consequence of tidal dissipation. Assuming that the protoplanetary disks are aligned with the stellar equator, this points to a migration path which involves, next to disk-planet interactions, also scattering processes or Kozai migration, changing the orbital plane of the planet.

It would be educational to measure obliquities also in systems with smaller planets, planets on wider orbits, and systems with multiple planets. The *Kepler* satellite provides us with these kind of systems, and measurements of obliquities in these systems are underway.

4. Kepler

The *Kepler* observatory was launched March 6, 2009 into an earth trailing orbit. It has a modified Schmidt telescope with 0.95 m of effective aperture. The light from 115 square degree on the sky is focused on an array of 42 CCDs [6], enabling the near continuous monitoring of the light of $\sim 150\,000$ stars in the constellation of Cygnus over mission time of Kepler.

The main goal of Kepler is to determine the frequency of Earth sized planets in the habitable zones of Sun-like stars (η-Earth). In its now nearly three years in space it has discovered a number of new types of planetary systems and lead to some interesting results in astronomy which would not have been possible otherwise. I list here a short and subjective selection.

- Kepler has found hundreds of systems with multiple transiting planets. The current record holder is the Kepler-11 system which harbors 6 transiting planets [25]. These planets have mutual inclinations of less then 0.6° and all orbit their sun-like host star on orbits with smaller semi-major axes than Venus the sun.

- In systems with multiple planets, the planets do not only move in the gravitational field of their host star, but their orbits are also influenced by the gravitation of the other planets. This

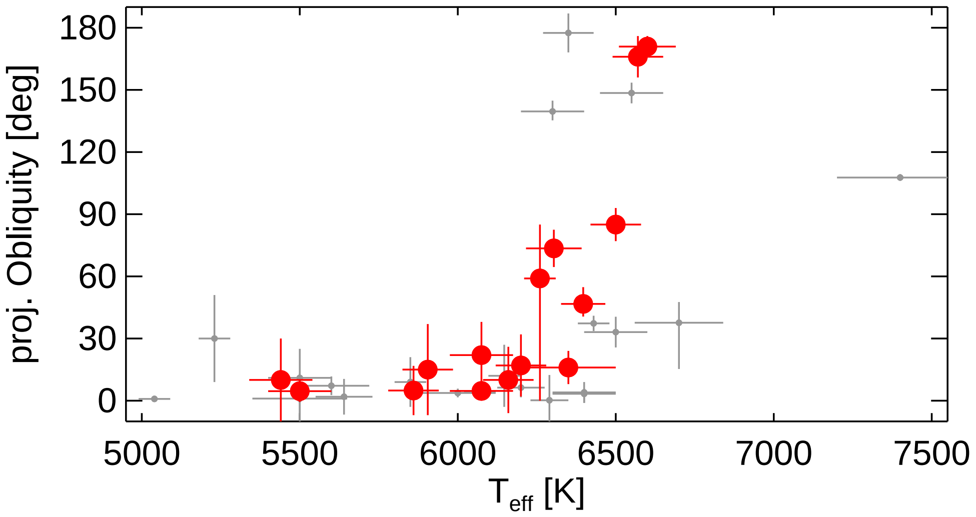

Figure 4: Hotter stars have oblique rotation. The projected obliquity of Hot Jupiter ($M_{planet} > 0.2\ M_{\mathrm{Jupiter}}$; Period $<$ 6 days) systems is plotted as function of the effective temperature of the host star. Using measurements available at that time, [52] noticed that systems with cool stars are aligned, while the obliquities of hot stars tends to be higher (gray small circles). Since then 16 new RM measurements have been reported (red large circles.

modulation of the orbits is most readily seen as variations in the times the planets transit in front of their host stars. These transit timing variations (TTV) provide us with an elegant way to derive the masses of the perturbing planets (e.g. [11]).

- While many planets have been detected around single stars or orbiting a single members of wide ($>$ 20 AU) double star systems, planets orbiting two stars have until recently been elusive. Doyle et al. 2011 [14] announced that the two stars in the Kepler-16 system, which orbit each other every 41 days, have a Saturn like companion in a 229 day orbit around both stars.

- Kepler also opens the opportunity to measure stellar obliquities without the need of dedicated spectroscopic observations. For slowly rotating stars the crossing of star-spots can be used as a tracer of stellar obliquity (e.g. [39]). For rapidly rotating stars which exhibit gravity darkening, the projected obliquity can be estimated from high quality photometry [47].

- Modeling stellar interiors and characteristics via asteroseismology also benefits from the long duration, high precision light curves obtained by Kepler [17]. The results obtained this way are not only very interesting by themselves, they will also lead to better constrains on planetary parameters. The later often depend on stellar parameters. for example the measured value for the absolute radius of the planet depends on the measurement of the stellar radius, which in turn can be obtained via asteroseismology.

5. Outlook

Unearthing the treasure trove of Kepler data has just begun and more discoveries are probably to come. In addition new photometric missions are in the planning stage (e.g. TESS). Improvements of techniques like direct imaging and RV should lead in the near future to discoveries of more alien worlds different from (exo)planets we know so far.

Acknowledgements I am grateful to the scientific and local organizing committees for organizing a very enjoyable and stimulating meeting. I am thankful to Hilke Reckman for help with the preparation of the manuscript and to Josh Winn for comments on the manuscript.

References

[1] Albrecht, S., Winn, J. N., Johnson, J. A., Butler, R. P., Crane, J. D., Shectman, S. A., Thompson, I. B., Narita, N., Sato, B., Hirano, T., Enya, K., & Fischer, D. (2011). *Two Upper Limits on the Rossiter-Mclaughlin Effect, with Differing Implications: WASP-1 has a High Obliquity and WASP-2 is Indeterminate*. ApJ, **738**, 50.

[2] Albrecht, S., Winn, J. N., Butler, R. P., Crane, J. D., Shectman, S. A., Thompson, I. B., Hirano, T., & Wittenmyer, R. A. (2012). *A High Stellar Obliquity in the WASP-7 Exoplanetary System*. ApJ, **744**, 189.

[3] Bakos, G. Á., Lázár, J., Papp, I., Sári, P., & Green, E. M. (2002). *System Description and First Light Curves of the Hungarian Automated Telescope, an Autonomous Observatory for Variability Search*. PASP, **114**, 974.

[4] Baranne, A., Mayor, M., & Poncet, J. L. (1979). *CORAVEL - A new tool for radial velocity measurements*. Vistas in Astronomy, **23**, 279.

[5] Benedict, G. F., McArthur, B. E., Gatewood, G., Nelan, E., Cochran, W. D., Hatzes, A., Endl, M., Wittenmyer, R., Baliunas, S. L., Walker, G. A. H., Yang, S., Kürster, M., Els, S., & Paulson, D. B. (2006). *The Extrasolar Planet ε Eridani b: Orbit and Mass*. AJ, **132**, 2206.

[6] Borucki, W. J., Koch, D., Basri, G., Batalha, N., Brown, T., Caldwell, D., Caldwell, J., Christensen-Dalsgaard, J., Cochran, W. D., DeVore, E., Dunham, E. W., Dupree, A. K., Gautier, T. N., Geary, J. C., Gilliland, R., Gould, A., Howell, S. B., Jenkins, J. M., Kondo, Y., Latham, D. W., Marcy, G. W., Meibom, S., Kjeldsen, H., Lissauer, J. J., Monet, D. G., Morrison, D., Sasselov, D., Tarter, J., Boss, A., Brownlee, D., Owen, T., Buzasi, D., Charbonneau, D., Doyle, L., Fortney, J., Ford, E. B., Holman, M. J., Seager, S., Steffen, J. H., Welsh, W. F., Rowe, J., Anderson, H., Buchhave, L., Ciardi, D., Walkowicz, L., Sherry, W., Horch, E., Isaacson, H., Everett, M. E., Fischer, D., Torres, G., Johnson, J. A., Endl, M., MacQueen, P., Bryson, S. T., Dotson, J., Haas, M., Kolodziejczak, J., Van Cleve, J., Chandrasekaran, H., Twicken, J. D., Quintana, E. V., Clarke, B. D., Allen, C., Li, J., Wu, H., Tenenbaum, P., Verner, E., Bruhweiler, F., Barnes, J., & Prsa, A. (2010). *Kepler Planet-Detection Mission: Introduction and First Results*. Science, **327**, 977.

[7] Campbell, B. & Walker, G. A. H. (1979). *Precision radial velocities with an absorption cell*. PASP, **91**, 540.

[8] Charbonneau, D., Brown, T. M., Latham, D. W., & Mayor, M. (2000). *Detection of Planetary Transits Across a Sun-like Star*. ApJ, **529**, L45.

[9] Charbonneau, D., Berta, Z. K., Irwin, J., Burke, C. J., Nutzman, P., Buchhave, L. A., Lovis, C., Bonfils, X., Latham, D. W., Udry, S., Murray-Clay, R. A., Holman, M. J., Falco, E. E., Winn, J. N., Queloz, D., Pepe, F., Mayor, M., Delfosse, X., & Forveille, T. (2009). *A super-Earth transiting a nearby low-mass star*. Nature, **462**, 891.

[10] Chatterjee, S., Ford, E. B., Matsumura, S., & Rasio, F. A. (2008). *Dynamical Outcomes of Planet-Planet Scattering*. ApJ, **686**, 580.

[11] Cochran, W. D., Fabrycky, D. C., Torres, G., Fressin, F., Désert, J.-M., Ragozzine, D., Sasselov, D., Fortney, J. J., Rowe, J. F., Brugamyer, E. J., Bryson, S. T., Carter, J. A., Ciardi, D. R., Howell, S. B., Steffen, J. H., Borucki, W. J., Koch, D. G., Winn, J. N., Welsh, W. F., Uddin, K., Tenenbaum, P., Still, M., Seager, S., Quinn, S. N., Mullally, F., Miller, N., Marcy, G. W., MacQueen, P. J., Lucas, P., Lissauer, J. J., Latham, D. W., Knutson, H., Kinemuchi, K., Johnson, J. A., Jenkins, J. M., Isaacson, H., Howard, A., Horch, E., Holman, M. J., Henze, C. E., Haas, M. R., Gilliland, R. L., Gautier, III, T. N., Ford, E. B., Fischer, D. A., Everett, M., Endl, M., Demory, B.-O., Deming, D., Charbonneau, D., Caldwell, D., Buchhave, L., Brown, T. M., & Batalha, N. (2011). *Kepler-18b, c, and d: A System of Three Planets Confirmed by Transit Timing Variations, Light Curve Validation, Warm-Spitzer Photometry, and Radial Velocity Measurements*. ApJS, **197**, 7.

[12] Cresswell, P., Dirksen, G., Kley, W., & Nelson, R. P. (2007). *On the evolution of eccentric and inclined protoplanets embedded in protoplanetary disks*. A&A, **473**, 329.

[13] Cumming, A., Marcy, G. W., & Butler, R. P. (1999). *The Lick Planet Search: Detectability and Mass Thresholds*. ApJ, **526**, 890.

[14] Doyle, L. R., Carter, J. A., Fabrycky, D. C., Slawson, R. W., Howell, S. B., Winn, J. N., Orosz, J. A., Prcaronsa, A., Welsh, W. F., Quinn, S. N., Latham, D., Torres, G., Buchhave, L. A., Marcy, G. W., Fortney, J. J., Shporer, A., Ford, E. B., Lissauer, J. J., Ragozzine, D., Rucker, M., Batalha, N., Jenkins, J. M., Borucki, W. J., Koch, D., Middour, C. K., Hall, J. R., McCauliff, S., Fanelli, M. N., Quintana, E. V., Holman, M. J., Caldwell, D. A., Still, M., Stefanik, R. P., Brown, W. R., Esquerdo, G. A., Tang, S., Furesz, G., Geary, J. C., Berlind, P., Calkins, M. L., Short, D. R., Steffen, J. H., Sasselov, D., Dunham, E. W., Cochran, W. D., Boss, A., Haas, M. R., Buzasi, D., & Fischer, D. (2011). *Kepler-16: A Transiting Circumbinary Planet*. Science, **333**, 1602.

[15] Fabrycky, D. & Tremaine, S. (2007). *Shrinking Binary and Planetary Orbits by Kozai Cycles with Tidal Friction*. ApJ, **669**, 1298.

[16] Gaudi, B. S. (2010). *Exoplanetary Microlensing*. ArXiv e-prints.

[17] Gilliland, R. L., Brown, T. M., Christensen-Dalsgaard, J., Kjeldsen, H., Aerts, C., Appourchaux, T., Basu, S., Bedding, T. R., Chaplin, W. J., Cunha, M. S., De Cat, P., De Ridder, J., Guzik, J. A., Handler, G., Kawaler, S., Kiss, L., Kolenberg, K., Kurtz, D. W., Metcalfe, T. S., Monteiro, M. J. P. F. G., Szabó, R., Arentoft, T., Balona, L., Debosscher, J., Elsworth, Y. P., Quirion, P.-O., Stello, D., Suárez, J. C., Borucki, W. J., Jenkins, J. M., Koch, D., Kondo, Y., Latham, D. W., Rowe, J. F., & Steffen, J. H. (2010). *Kepler Asteroseismology Program: Introduction and First Results*. PASP, **122**, 131.

[18] Griffin, R. F. (1967). *A Photoelectric Radial-Velocity Spectrometer*. ApJ, **148**, 465.

[19] Hébrard, G., Bouchy, F., Pont, F., Loeillet, B., Rabus, M., Bonfils, X., Moutou, C., Boisse, I., Delfosse, X., Desort, M., Eggenberger, A., Ehrenreich, D., Forveille, T., Lagrange, A., Lovis, C., Mayor, M., Pepe, F., Perrier, C., Queloz, D., Santos, N. C., Ségransan, D., Udry, S., & Vidal-Madjar, A. (2008). *Misaligned spin-orbit in the XO-3 planetary system?* A&A, **488**, 763.

[20] Henry, G. W., Marcy, G., Butler, R. P., & Vogt, S. S. (1999). *HD 209458*. IAU Circ., **7307**, 1.

[21] Holt, J. R. (1893). *Spectroscopic Determination of Stellar Rotation*. A&A, **12**, 646.

[22] Launhardt, R. (2009). *Exoplanet search with astrometry*. New A Rev., **53**, 294.

[23] Lin, D. N. C., Bodenheimer, P., & Richardson, D. C. (1996). *Orbital migration of the planetary companion of 51 Pegasi to its present location*. Nature, **380**, 606.

[24] Lindegren, L., Babusiaux, C., Bailer-Jones, C., Bastian, U., Brown, A. G. A., Cropper, M., Høg, E., Jordi, C., Katz, D., van Leeuwen, F., Luri, X., Mignard, F., de Bruijne, J. H. J., & Prusti, T. (2008). *The Gaia mission: science, organization and present status*. In W. J. Jin, I. Platais, & M. A. C. Perryman, editor, IAU Symposium, volume 248 , 217.

[25] Lissauer, J. J., Fabrycky, D. C., Ford, E. B., Borucki, W. J., Fressin, F., Marcy, G. W., Orosz, J. A., Rowe, J. F., Torres, G., Welsh, W. F., Batalha, N. M., Bryson, S. T., Buchhave, L. A., Caldwell, D. A., Carter, J. A., Charbonneau, D., Christiansen, J. L., Cochran, W. D., Desert, J.-M., Dunham, E. W., Fanelli, M. N., Fortney, J. J., Gautier, III, T. N., Geary, J. C., Gilliland, R. L., Haas, M. R., Hall, J. R., Holman, M. J., Koch, D. G., Latham, D. W., Lopez, E., McCauliff, S., Miller, N., Morehead, R. C., Quintana, E. V., Ragozzine, D., Sasselov, D., Short, D. R., & Steffen, J. H. (2011). *A closely packed system of low-mass, low-density planets transiting Kepler-11*. Nature, **470**, 53.

[26] Lovis, C. & Fischer, D. (2010). *Radial Velocity Techniques for Exoplanets*, 27.

[27] Marcy, G. W. & Butler, R. P. (1992). *Precision radial velocities with an iodine absorption cell*. PASP, **104**, 270.

[28] Marois, C., Macintosh, B., Barman, T., Zuckerman, B., Song, I., Patience, J., Lafrenière, D., & Doyon, R. (2008). *Direct Imaging of Multiple Planets Orbiting the Star HR 8799*. Science, **322**, 1348.

[29] Mayor, M. & Queloz, D. (1995). *A Jupiter-mass companion to a solar-type star*. Nature, **378**, 355.

[30] McCullough, P. R., Stys, J. E., Valenti, J. A., Fleming, S. W., Janes, K. A., & Heasley, J. N. (2005). *The XO Project: Searching for Transiting Extrasolar Planet Candidates*. PASP, **117**, 783.

[31] McLaughlin, D. B. (1924). *Some Results of a Spectrographic Study of the Algol System.* ApJ, **60**, 22.

[32] Nagasawa, M., Ida, S., & Bessho, T. (2008). *Formation of Hot Planets by a Combination of Planet Scattering, Tidal Circularization, and the Kozai Mechanism*. ApJ, **678**, 498.

[33] Perryman, M. (2011). *The Exoplanet Handbook*.

[34] Pollacco, D. L., Skillen, I., Collier Cameron, A., Christian, D. J., Hellier, C., Irwin, J., Lister, T. A., Street, R. A., West, R. G., Anderson, D., Clarkson, W. I., Deeg, H., Enoch, B., Evans, A., Fitzsimmons, A., Haswell, C. A., Hodgkin, S., Horne, K., Kane, S. R., Keenan, F. P., Maxted, P. F. L., Norton, A. J., Osborne, J., Parley, N. R., Ryans, R. S. I., Smalley, B., Wheatley, P. J., & Wilson, D. M. (2006). *The WASP Project and the SuperWASP Cameras*. PASP, **118**, 1407.

[35] Queloz, D. (1995). *Echelle Spectroscopy with a CCD at Low Signal-To-Noise Ratio*. In A. G. D. Philip, K. Janes, & A. R. Upgren, editor, New Developments in Array Technology and Applications, volume 167 of IAU Symposium, 221.

[36] Queloz, D., Eggenberger, A., Mayor, M., Perrier, C., Beuzit, J. L., Naef, D., Sivan, J. P., & Udry, S. (2000). *Detection of a spectroscopic transit by the planet orbiting the star HD209458*. A&A, **359**, L13.

[37] Reffert, S. & Quirrenbach, A. (2011). *Mass constraints on substellar companion candidates from the re-reduced Hipparcos intermediate astrometric data: nine confirmed planets and two confirmed brown dwarfs*. A&A, **527**, A140.

[38] Rossiter, R. A. (1924). *On the Detection of an Effect of Rotation During Eclipse in the Velocity of the Brigher Component of Beta Lyrae, and on the Constancy of Velocity of this System.* ApJ, **60**, 15.

[39] Sanchis-Ojeda, R. & Winn, J. N. (2011). *Starspots, spin-orbit misalignment, and active latitudes in the HAT-P-11 exoplanetary system*. ArXiv: 1107.2920.

[40] Schlaufman, K. C. (2010). *Evidence of Possible Spin-orbit Misalignment Along the Line of Sight in Transiting Exoplanet Systems*. ApJ, **719**, 602

[41] Schlesinger, F. (1910). *The Algol-variable delta Librae*. *Publications of the Allegheny Observatory of the University of Pittsburgh*, **1**, 123.

[42] Seager, S. (2011). *Exoplanets*.

[43] Simpson, E. K., Pollacco, D., Cameron, A. C., Hébrard, G., Anderson, D. R., Barros, S. C. C., Boisse, I., Bouchy, F., Faedi, F., Gillon, M., Hebb, L., Keenan, F. P., Miller, G. R. M., Moutou, C., Queloz, D., Skillen, I., Sorensen, P., Stempels, H. C., Triaud, A., Watson, C. A., & Wilson, P. A. (2011). *The spin-orbit angles of the transiting exoplanets WASP-1b, WASP-24b, WASP-38b and HAT-P-8b from Rossiter-McLaughlin observations*. MNRAS, **414**, 3023.

[44] Snellen, I. A. G., de Kok, R. J., de Mooij, E. J. W., & Albrecht, S. (2010). *The orbital motion, absolute mass and high-altitude winds of exoplanet HD209458b*. Nature, **465**, 1049.

[45] Struve, O. & Elvey, C. T. (1931). *Algol and stellar rotation*. MNRAS, **91**, 663.

[46] Sumi, T., Kamiya, K., Bennett, D. P., Bond, I. A., Abe, F., Botzler, C. S., Fukui, A., Furusawa, K., Hearnshaw, J. B., Itow, Y., Kilmartin, P. M., Korpela, A., Lin, W., Ling, C. H., Masuda, K., Matsubara, Y., Miyake, N., Motomura, M., Muraki, Y., Nagaya, M., Nakamura, S., Ohnishi, K., Okumura, T., Perrott, Y. C., Rattenbury, N., Saito, T., Sako, T., Sullivan, D. J., Sweatman, W. L., Tristram, P. J., Udalski, A., Szymański, M. K., Kubiak, M., Pietrzyński, G., Poleski, R., Soszyński, I., Wyrzykowski, Ł., Ulaczyk, K., & Microlensing Observations in Astrophysics (MOA) Collaboration (2011). *Unbound or distant planetary mass population detected by gravitational microlensing*. Nature, **473**, 349.

[47] Szabó, G. M., Szabó, R., Benkő, J. M., Lehmann, H., Mező, G., Simon, A. E., Kővári, Z., Hodosán, G., Regály, Z., & Kiss, L. L. (2011). *Asymmetric Transit Curves as Indication of Orbital Obliquity: Clues from the Late-type Dwarf Companion in KOI-13*. ApJ, **736**, L4.

[48] Torres, G., Andersen, J., & Giménez, A. (2010). *Accurate masses and radii of normal stars: modern results and applications*. A&A Rev., **18**, 67.

[49] Udalski, A., Paczynski, B., Zebrun, K., Szymanski, M., Kubiak, M., Soszynski, I., Szewczyk, O., Wyrzykowski, L., & Pietrzynski, G. (2002). *The Optical Gravitational Lensing Experiment. Search for Planetary and Low-Luminosity Object Transits in the Galactic Disk. Results of 2001 Campaign*. Acta Astron., **52**, 1.

[50] Winn, J. N. (2010). *Transits and Occultations*. ArXiv: 1001.2010.

[51] Winn, J. N., Johnson, J. A., Albrecht, S., Howard, A. W., Marcy, G. W., Crossfield, I. J., & Holman, M. J. (2009). *HAT-P-7: A Retrograde or Polar Orbit, and a Third Body*. ApJ, **703**, L99.

[52] Winn, J. N., Fabrycky, D., Albrecht, S., & Johnson, J. A. (2010). *Hot Stars with Hot Jupiters Have High Obliquities*. ApJ, **718**, L145.

[53] Wolszczan, A. & Frail, D. A. (1992). *A planetary system around the millisecond pulsar PSR1257 + 12*. Nature, **355**, 145.

PROCEEDINGS OF SCIENCE

Asteroseismology of stars on the upper main sequence

Patrick Lenz[*] [†]
Copernicus Astronomical Center, Polish Academy of Sciences, ul. Bartycka 18, 00-716 Warsaw, Poland
E-mail: `lenz@camk.edu.pl`

I review the properties of pulsators located on the upper main sequence in the HR diagram and discuss asteroseismic inferences on the internal structure of stars of spectral type A and B. Special attention is given to the problem of uncertainties in stellar opacities in modelling.

Frank N. Bash Symposium New Horizons In Astronomy,
October 9-11, 2011
Austin Texas

[*]Speaker.
[†]The author is partially supported by the Polish MNiSW grant No. N N203 379636.

PoS(Bash11)003

Pulsating stars on the upper main sequence in the HR diagram commonly exhibit a convective core (which appears if M > 1.2 $M_\odot$) and a radiative envelope with thin convection zones close to the surface. The evolutionary status of pulsators located in this region in the HR diagram can be manifold, however: beside common main sequence pulsators (in which hydrogen core burning takes place) we also have pre-main sequence stars (no efficient nuclear reactions) and post-main sequence stars (hydrogen shell burning). We distinguish different types of pulsators along the main sequence band: among B and late type O stars we have the so-called β Cephei pulsators with periods of hours and masses of 8–20 $M_\odot$ and the long-period SPB oscillators (slowly pulsating B stars) with periods of days and masses of 3–12 $M_\odot$. Moving towards lower masses, there are the δ Scuti pulsators (M = 1.5–2.5 $M_\odot$), which are dwarfs or giants of spectral type A2–F5 located in the extension of the Cepheid instability strip with periods of 0.02–0.3d. Pulsating magnetic stars among A stars are known as roAp pulsators with periods of 5–15 minutes. Among F-type stars there are the γ Dor pulsators with masses of 1.4–1.6 $M_\odot$ and periods of 0.3–3 d. Recent observational reviews on these pulsators based on satellite photometry can be found in [1 – 3] for A and F pulsators and for B stars in [4, 5]. Prior to the discussion of recent asteroseismic results on the physics in these stars I will review some basics of stellar pulsation.

1. Stellar oscillations

Stellar pulsation occurs if a star undergoes free or forced oscillations. In the limit of slow rotation, the star is spherically symmetric in its equilibrium. In this case the geometrical perturbation of the equilibrium through a pulsation mode can be characterized by a spherical harmonic $Y_\ell^m(\theta,\phi)$, where θ is the colatitude, ϕ the azimuthal angle, ℓ the degree (i.e. the number of nodal lines on the surface) and m the number of nodal lines crossing the equator. If $\ell = 0$ we have radial pulsation (i.e. a spherically symmetric oscillation) and if $\ell > 0$ we have nonradial oscillations. For a spherical degree, ℓ, the eigenfunctions are degenerate by (2ℓ+1)-folds in m. Rotation lifts this degeneracy and leads to mode frequencies depending on m. Finally, a pulsation mode is also characterized by the number of nodes, n, in the radial component of the displacement between the center and the surface. The radial fundamental mode has no node, i.e. n=0, the first overtone n=1, and so forth.

The symmetry axis of pulsation is commonly aligned to the dominant symmetry axis in the star. It is often the rotation axis; however, in case of the presence of a strong magnetic field it is the magnetic axis, or in a close binary system the tidal axis. If no symmetry axis clearly dominates, the pulsation symmetry axis may lie in between two symmetry axes, e.g., in between the rotation axis and the magnetic field axis [6]. Such an example has already been found in a magnetic A-type star observed by the *Kepler* satellite [7].

1.1 Propagation of waves inside a star

As for every oscillating body its structure and composition determines its frequencies. The solution of the oscillation equations for a star reveals two characteristic (critical) frequencies: (i) the Lamb frequency, $L_\ell = \sqrt{\ell(\ell+1)}\frac{c_s}{r}$, where c_s is the local speed of sound, and (ii) the Brunt-Väisälä frequency, N, defined as $N^2 = g\left(\frac{1}{\Gamma_1}\frac{d\ln p_0}{dr} - \frac{d\ln\rho_0}{dr}\right)$, where the subscript 0 denotes equilibrium values. The Lamb frequency corresponds to the inverse travel time of a sound wave, i.e. a wave front propagates the distance $2\pi r/\ell$ horizontally within the period $2\pi/L_\ell$. The Brunt-Väisälä frequency

PoS(Bash11)003

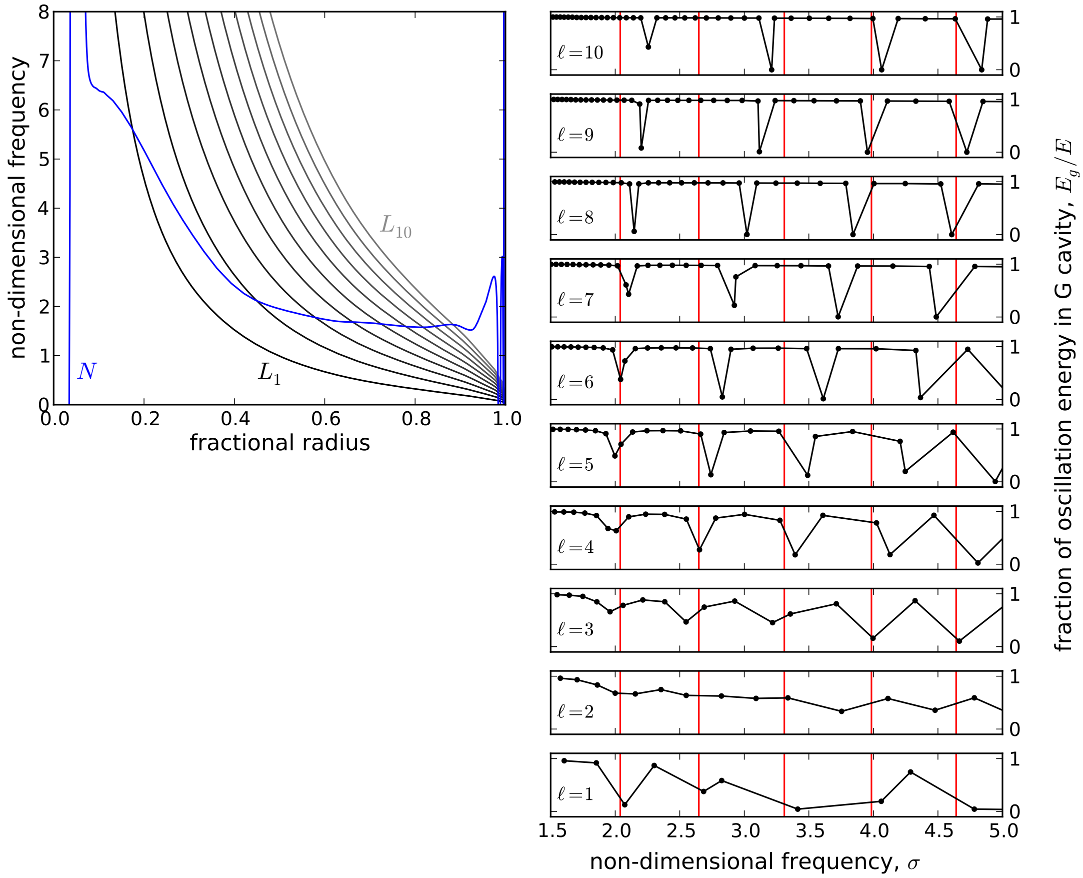

Figure 1: Left panel: propagation diagram for modes up to ℓ=10 in a model of the δ Scuti star 44 Tau. Right panel: fraction of oscillation mode energy confined in the g mode propagation zone for modes of different ℓ. Modes with $E_g/E \approx 1$ are effectively trapped in the g-mode cavity, while modes with $E_g/E \approx 0$ are trapped in the envelope. The location of the radial modes is indicated by red vertical lines.

describes the frequency of the adiabatic oscillation of a bubble of gas in vertical direction under the influence of buoyancy. Both critical frequencies depend on the local physical conditions inside the star and they determine the cavities in which oscillation may take place. The propagation zone for acoustic waves (p modes) is defined by $\sigma > L_\ell$ and $\sigma > N$, where σ is the oscillation frequency, and the gravity wave (g mode) propagation zone resides in regions where $\sigma < L_\ell$ and $\sigma < N$. In between these two cavities the amplitude of an oscillation mode decreases exponentially with distance, this region is therefore called evanescent zone. Additionally, at high frequencies the acoustic cavity is limited by the acoustic cut-off frequency, above which the oscillation is no longer reflected at the outer boundary but propagates outwards in the atmosphere.

A typical example of propagation zones in a pulsating star of $\approx 1.9\ \mathrm{M}_\odot$ at the end of hydrogen core burning is given in the left panel of Fig. 1. The high values of N close to the center are due to the strong gradient in mean molecular weight which grows during main sequence evolution because of the receding convective core. This development allows g modes to move to higher frequencies. In the outer envelope two convection zones ($N < 0$) corresponding to partial ionization of He II and

HeI/H are located. A significant part of the energy in these zones is still transported by radiation, but the efficiency of convection increases with decreasing effective temperatures of the star. If the two wave propagation zones are separated only by a small evanescent zone a "tunnel effect" may occur. If the evanescent zone is large enough, however, the propagation zones can be treated as independent and oscillation energy is effectively trapped in a given propagation zone. If this is the case we speak of *trapped modes*. It can be seen in Fig. 1 that while we expect oscillation modes of higher ℓ to be effectively trapped in the envelope or in the interior; for low degree modes only partial trapping occurs. In fact partial trapping is least effective for $\ell = 2$ modes in main sequence stars because for these modes the evanescent zone is thinnest in the range of typically excited modes and therefore these modes are strongly coupled to the interior. Consequently, they have both g mode and p mode properties and are therefore called *mixed modes*. This effect is also illustrated in the right panel of Fig. 1 which shows the fraction of oscillation energy of a mode confined in the gravity wave propagation zone, E_g/E. Modes trapped in the envelope, i.e. modes with low E_g/E, are essentially decoupled from the interior and have the highest probability to be observed. The agglomeration of modes trapped in the envelope close to the frequency of the fundamental radial mode is due to the fact that the modes of all ℓ values are limited by the Brunt-Väisälä frequency which itself is ℓ-independent (see left panel in Fig. 1). Although modes with high spherical degrees suffer from stronger cancellation effects compared to ℓ=1,2 modes [8] they are now also detectable with present day high-precision satellite photometry.

2. Excitation and damping of oscillation modes

What causes an oscillation mode to grow in amplitude? We distinguish between free and forced oscillations. In the latter case a linearly damped oscillation is excited by a periodic external force, e.g., due to a periodic tidal distortion, or generally, due to resonance. In case of free oscillations the oscillations are excited by an internal driving mechanism. Such an excitation mechanism should be located in a region that lies within a propagation zone and the propagation zones should exclude the common damping regions in a star. Moreover, the oscillation mode should not exhibit a node in the driving region. The most relevant mode driving mechanism for self-excited oscillation are outlined in the following paragraphs.

2.1 κ-mechanism

Opacity (κ), i.e. the quantity which describes the transport of radiation through matter, is temperature-dependent and can act as a valve under certain circumstances. Depending on the layer inside the star, κ increases or decreases with increasing temperature which is reflected in the behaviour of the temperature derivative of opacity, κ_T (see Fig. 2). One condition for the κ-mechanism to work in a certain region in a star is that this opacity derivative increases in the outward direction. Consequently during a compression phase radiative flux is blocked and performs work as can be seen from the differential work diagram in Fig. 2.

The conditions for pulsational instability of a mode (i.e. for its amplitude to grow with time) was reviewed, e.g., by [9] and only the main points will be repeated here: (i) the amplitude of the pressure eigenfunction has to be large and vary slowly within the driving zone, (ii) the pulsation has to occur faster than the redistribution of thermal energy, i.e. the thermal timescale in the

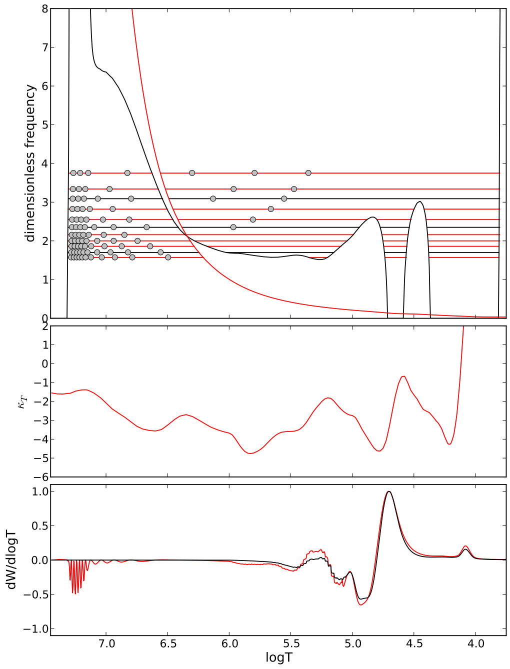

Figure 2: Propagation diagram, temperature derivative of opacity, κ_T, and differential work integral for two $\ell = 2$ modes (p mode in black, g mode in red) as a function of $\log T$ in a 44 Tau model.

driving region has to be comparable or longer than the period of the mode. The second condition determines the depth of the driving zone in a star. The given conditions can be met by two frequency ranges in the same star, as for example in hybrid B pulsators: low-order low-degree acoustic or mixed modes with periods of 3–6 hours (β Cep-type pulsation) and high-order low-degree gravity modes with periods of 1.5–3 days (SPB-type pulsation). Condition (ii) implies that these longer period modes are driven in slightly deeper layers than the β Cep-type modes.

There are also important damping effects such as radiative dissipation in the gravity mode cavity. The strength of this effect depends on the efficiency of mode trapping in this cavity and it is therefore strong for g modes (see lower panel of Fig. 2). The dissipation increases with the degree of central condensation, which generally increases with age. E.g., Cepheids have a very high central concentration and the strong radiative dissipation in the core region damps g modes before they are reflected at the center. Hence in these stars only acoustic modes trapped in the envelope are observed. In δ Scuti stars radiative dissipation of modes provides strong damping for g modes of higher ℓ. At $\ell > 12$ only acoustic modes trapped in the envelope remain unstable [8].

2.2 Convective driving and convective blocking

Efficient convection may also cause self-excited oscillations. For example in ZZ Ceti stars the convective energy flux in the H-ionization zone is much larger than radiative flux. Since convection occurs on a much shorter timescale compared to g mode oscillations, the instantaneous adjustment of convection to pulsation leads to thermal energy being stored in the convection zone during the compression phase of pulsation (i.e. the convection zone stores heat) thus providing efficient driving [10].

However, excitation of g mode pulsation is also possible if the convective time scale is very long against the pulsation period, such as in F stars in case of γ Dor pulsation. The radiative flux may be effectively blocked by convection at the base of the convection zone, which also leads to heating upon compression [11]. For this mechanism to work, the base of the convection zone should match the region where the thermal relaxation time is similar to the pulsation periods of the modes [3].

2.3 Stochastic driving

Forced excitation of modes within a certain frequency band due to acoustic noise in an efficient convective envelope is another possible driving mechanism. This excitation mechanism drives the 5-min oscillations in the Sun. Although envelope convection in upper main sequence stars is less efficient than in the Sun, evidence for stochastically excited oscillations has been found in a few stars, partly additional to common opacity mechanism driving. There are examples among A/F stars [12] and O/B stars [13, 14]. However, in one of these cases the stochastic nature of the modes could not be confirmed, since non-linear resonant mode excitation by the large-amplitude radial mode provides similar observational features [15].

2.4 Modification of mode excitation through a magnetic field

The presence of a magnetic field modifies driving by the κ-mechanism in two ways: (i) convection is inhibited in the polar regions of the magnetic field, where inward propagating magnetic slow waves carry away pulsational energy, (ii) more effective gravitational settling leading to hydrogen-enriched surface layers. In fact, a nonadiabatic analysis [16] for A-type stars showed that a dipole magnetic field stabilizes low-order acoustic modes at 1 kG, while high-order modes of $\ell = 1,2$ (roAp-type pulsation) become pulsationally unstable due to driving in the H-ionization zone.

3. Asteroseismic inferences from upper main sequence stars

3.1 Probing stellar opacities

Opacities are a fundamental ingredient in the calculation of stellar structure and evolution and, therefore, asteroseismic models are very sensitive to them. The opacity coefficients $\kappa(T,\rho,X_i)$ define the interacting cross sections of radiation with matter and determine the efficiency of radiative energy transport in a star. Naturally, these opacity coefficients are high for elements with many electrons. In most of the interior of a main sequence star hydrogen and helium are completely ionized except for the outer envelope. Consequently in the deeper interior heavy elements have a high contribution to the opacity coefficients. Therefore, despite their small mass fractions, heavy elements play an important role in stellar physics.

For practical reasons we commonly use tabulated Rosseland-mean opacities, κ_R, in stellar models. Two sets of opacity tables are currently widely used, the Lawrence Livermore National Laboratory opacity table computed with the OPAL code [17] and the tables of the international Opacity Project collaboration (commonly referred to as OP opacities) [18].

PoS(Bash11)003

In their most recent incarnations the OPAL calculations are based on the 21 most abundant elements in a star while OP considers 17 species (i.e. the same elements as OPAL with exception of P, Cl, K and Ti, which have the lowest abundances in the given mixture). There are also differences in the computational approach, e.g., in the equation of state (EOS) which determines ionization equilibria and level populations required for opacity calculation. The EOS used by OP calculations [19] is based on the 'chemical picture', while the OPAL EOS [20] considers a 'physical picture'. A detailed comparison of both EOS is given in [21].

Seaton et al. [22] compared the Rosseland mean opacities for six elements (H, He, C, O, S, Fe) and generally found good agreement between OPAL and OP. If one compares the OPAL and OP opacities for the full set of species, the differences are more significant, however. The third panel from the top in Fig. 3 shows $\kappa_{\rm OPAL}/\kappa_{\rm OP}$ evaluated for the most recent solar element mixture [23] as a function of temperature and density. The most striking difference is the well known fact that the metal opacity bump is shifted to higher temperatures in the OP data. Another feature is that the OPAL table exhibits higher opacities compared to OP at log T = 6 and log(ρ/T_6^3) = -3 where $T_6 \equiv T/10^6$. The figure illustrates the stellar profile of different pulsators such as a δ Scuti star (1.9 $M_\odot$), a SPB pulsator (4 $M_\odot$) and a β Cephei star (12 $M_\odot$) in the temperature-density plane of the opacity table. As can be seen, different regions in the opacity tables are probed by pulsators on the upper main sequence and the differences between OP and OPAL influence the pulsation models for these stars.

As discussed in the previous section a positive temperature derivative of opacity, κ_T, in outward direction is one important condition for driving pulsations. This condition is fulfilled at the hotter wings of bumps in opacity. We will now discuss the different opacity bumps as shown in the top panel of Fig. 3 and relate them to their corresponding types of pulsators:

The **He II bump** at log T $\approx$ 4.65 is due to the second ionization of helium. It is responsible for pulsation in the classical instability strip in the HR diagram, e.g., δ Scuti pulsators, RR Lyrae stars and Cepheids.

The **Z bump** is formed due to a large number of intra-M shell transitions in highly excited ions of iron-group elements which take place at approximately log T $\approx$ 5.3. Iron has the strongest contribution, but also Nickel is a significant contributor of opacity, despite its lower abundance [24]. The temperature of the Nickel opacity bump is significantly higher in the OP data compared to OPAL which poses an interesting problem. The Z bump is responsible for pulsational driving in massive main sequence B stars (β Cep and SPB type), but also in evolved stars such as hot subdwarf B and O stars (sdB, sdO) on the extreme horizontal branch. The Z bump instability strip for radial modes connecting main sequence pulsators of β Cep and SPB type with low mass sdO and sdB pulsators is shown, e.g., in Fig. 1 in [25].

The **deep opacity bump (DOB)** occurs from the partial ionization of L-shell electrons of Iron at log T $\approx$ 6.3 and of K-shell electrons of C, O, Ne at log T $\approx$ 6.2. This bump may excite pulsation in hydrogen-rich Wolf-Rayet stars [26] and GW Vir stars [27].

Asteroseismology probes the stellar opacities through different observables for each oscillation mode:
(i) its pulsational instability (in opacity-driven pulsators): as instability critically depends on the opacity profile in the vicinity of the bump responsible for driving (see Fig. 2) [28]
(ii) its frequency: because the oscillation frequencies depend on the radiative properties of the stel-

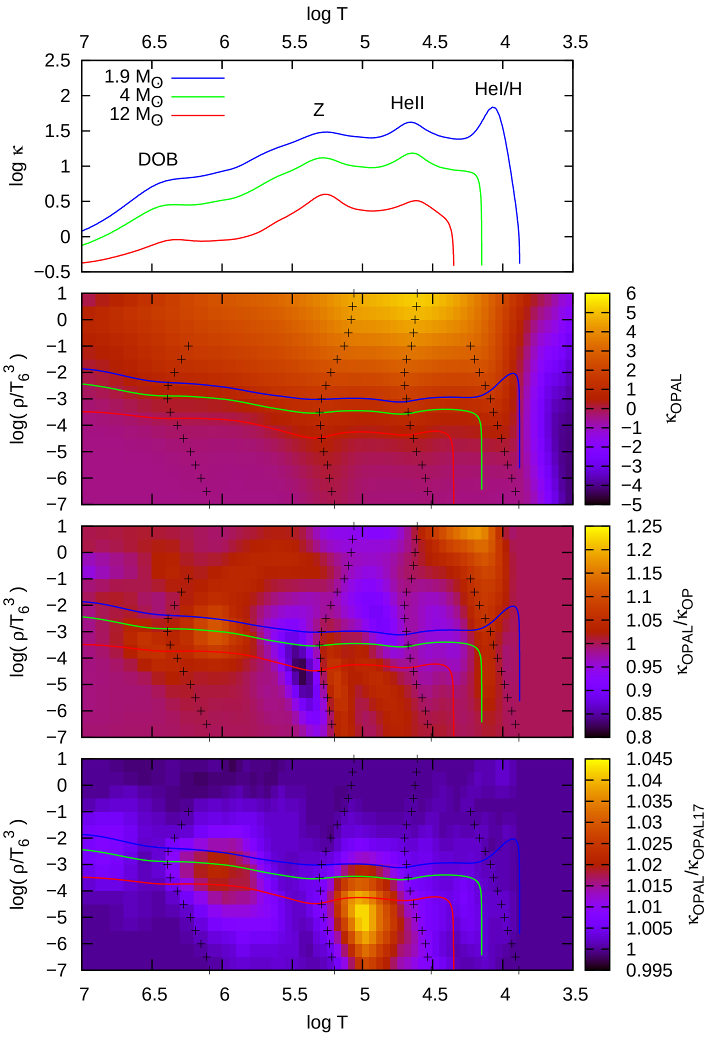

Figure 3: Probing differences in opacity tables by means of main sequence pulsators. The uppermost panel shows Rosseland mean opacity in the envelope of a δ Scuti model (1.9 $M_{\odot}$), a SPB-type model (4 $M_{\odot}$) and a β Cephei model (12 $M_{\odot}$). The adjacent panel shows the profile of these models in the temperature-density plane of the OPAL opacity table for X=0.74, Z=0.0134. Around logT=3.95 the transition to the low-temperature opacities by [29] occurs. For clarity crosses roughly mark the location of the different opacity bumps. The third panel shows $\kappa_{\rm OPAL}/\kappa_{\rm OP}$ in the same plane and the lowermost panel shows the effect of the four elements (P,Cl,K,Ti) which are included in OPAL but not in OP.

lar medium in the propagation zone(s) of the mode.
(iii) its nonadiabatic f parameter (i.e. the ratio of bolometric flux perturbation to the radial displacement at photosphere level): because the complex quantity f probes the nonadiabatic regions and, therefore, is sensitive to the conditions in regions with temperatures below the temperature of the driving opacity bump. Seismic analyses involving the f parameter are commonly termed complex asteroseismology [30, 31].

History has taught us that updates in theoretical opacity calculations (due to improved physics and consideration of additional elements) generally lead to an increase in opacity and an improvement of our understanding of the excitation of pulsation in stars. For example, based on observational evidence for higher opacity, Simon pleaded for a reinvestigation of heavy element opacities in 1982 [34]. In 1992 the OPAL team published new tables which included new spin-orbit interactions causing an increase of opacity at the Z bump. This led to the successful explanation of the driving of the observed pulsation in B stars [35, 36]. Consequently, asteroseismology can serve as a tool to help us to identify flaws in certain parts of the opacity tables. Today there is again observational evidence that present day mean opacities underestimate real opacity.

Opacities have been tested by conducting instability surveys (i.e. calculation of instability strips and comparing them to observed positions of pulsators in the HRD) for different types of pulsators. Various effects on the location of the instability strips of upper main sequence pulsators are discussed in [9] and the effect of the latest update of OP opacities and solar element abundances in [37, 38]. Generally, the last update of OP data in 2005 resulted in larger instability domains for both β Cephei and SPB pulsators in the HR diagram, and the domains shifted to hotter temperatures. The overlap region that hosts β Cephei and SPB hybrid stars is very sensitive to these changes and consequently a good observational probe. For this reason many of these hybrid pulsators were observed in detail during the recent years. Particularly well-studied cases are 12 Lac (M $\approx$ 11.5 $M_\odot$, [39 – 41]), ν Eri (M $\approx$ 9.5 $M_\odot$, [42 – 46, 40]) and γ Peg (M $\approx$ 8.5 $M_\odot$, [47 – 51]). It is striking that in asteroseismic models of these stars certain common problems occur. With OPAL the predicted frequency range of unstable β Cephei modes is too narrow. The use of OP data improves the predicted mode instability for β Cephei modes in comparison with OPAL but additional instability is needed. With OPAL it is often not possible to excite low-frequency SPB modes at all, while with OP we do obtain unstable high-order g-modes but matching them with observed frequencies is difficult [40]. For example in γ Peg $\ell = 2$ SPB modes are predicted to be excited with OP opacities but observations indicate $\ell = 1$ [50].

The underestimation of driving for β Cep modes can be rectified by increasing the opacity bump responsible for driving, since driving is more effective if the bump is more prominent in comparison with its surrounding. An increase in OP opacity by about 50% at the Z bump at log T≈5.3-5.5 and an increase of a few % up to 20% at the deep opacity bump at log T≈6.3 improves the agreement in terms of excitation and frequency fits for β Cephei pulsation [52, 50]. Additional evidence comes from pulsating B stars found in the low-metal environment SMC for which opacity enhancement is needed at the Z bump to excite the observed modes [53].

Unfortunately there are not many successfully modelled A-F stars. However, there is one star which is well understood and provided some hints on opacities: the δ Scuti pulsator 44 Tau (M $\approx$ 1.9 $M_\odot$, [54, 55]). For this star the fact that OP opacities are lower than OPAL by 10% at log T=6.05 caused serious problems in modelling, in particular when fitting the period ratio [56, 28]. This temperature is close to the deep opacity bump and the problem of OP opacities can be solved by an increase of opacity at log T=6.05 [55] which is close to the temperature region where an opacity increase is also required in B stars.

Studies focussing on the nonadiabatic f parameter, which is sensitive to opacities in the outer envelope, reveal an ambivalent picture. For the β Cep star θ Ophiuchi (M $\approx$ 8.2 $M_\odot$, [57 – 60]) as well as for ν Eri [62] the comparison between emprically determined f and theoretically computed values show preference for OPAL opacities [61, 62]. In γ Peg, however, models based on both OP and OPAL fail to reproduce the nonadiabatic properties of observed SPB-type modes [63].

Consequently, [40] pointed out the requirement of enhancement of opacity in the driving region in order to explain the instability of SPB-type frequencies in these hybrid pulsators. In B stars opacity enhancement tests have the following effect: increasing opacity at the driving bump (e.g., the Z bump in B stars) affects mode instability for SPB and β Cep pulsation but does not change the frequencies significantly because the opacity was changed at low densities. Since the DOB is located in denser layers it influences the mode frequencies strongly and hence, if we fit theoretical frequencies to observed counterparts, the position in the HR diagram changes. Additional evidence for more opacity also comes from recent observations hardening the claim of β Cep-type pulsations in O stars, e.g., the O9V star HD 46202 [64], or the O9.5V star ζ Oph [72]. These observations could be explained by widening the β Cep instability strip by means of additional opacity at the Z bump. In the Sun an opacity enhancement of 30 % at the base of the convective zone (which approximately corresponds to the deep opacity bump) and a few percent in the solar core has also been suggested to solve the discrepancy between the solar model and helioseismology based on the current version of solar abundances [65].

A possible explanation for underestimated opacity, apart from uncertainties in the calculations (especially concerning the peak temperature of the Nickel bump), is the possible opacity contribution from elements with low abundances which currently are not included in opacity calculations. In the OPAL calculations four species (P, Cl, K, Ti) are considered which are not included in the OP computations. Using the OPAL web interface[1] we retrieved a table which adopts the element abundances from the most recent solar mixture [23] but setting the number fraction of these four elements to zero. Since this table is then based only on 17 elements we denote this table as OPAL17 hereafter. Due to the renormalization of the number fractions, we have a minor abundance increase in all metal elements. The lowest panel in Fig. 3 shows the ratio $\kappa_{\mathrm{OPAL}}/\kappa_{\mathrm{OPAL17}}$ for the solar chemical composition illustrating where these four elements contribute opacity. They augment up to a few % of opacity for upper main-sequence stars at the hot wing of the Z bump around log T$\approx$5 and close to the DOB at log T$\approx$6.0. Consequently one may conclude that the inclusion of more species may partly solve the problems in asteroseismic modelling of star on the upper main sequence. We also note that for denser stars with masses comparable to the Sun the contribution is negligible which confirms the findings of [66].

The differences between OP and OPAL concerning the opacity peak temperature of Nickel showed that there are interesting things to be learned from the opacity calculations. The need for a reinvestigation was also realized by atomic physicists. Therefore, new activities in the determination of opacity for astrophysical purposes on both the theoretical and experimental side have started [67]. The theoretical activities include for example the comparison of spectral opacities for certain elements between different theoretical groups. It is important to validate the theoretical results with experimentally determined spectral opacities using modern high-energy laser facilities. These tests are important to check whether the calculations use proper physics. While the stellar densities are too low to be reproduced in the laboratory, it is possible to draw conclusions by studying equivalent plasma conditions that have similar mean ionization states. New calculations concentrate on the conditions at the base of the solar convection zone and in the driving zone in B stars. Preliminary results of a comparison of calculated spectral opacities (with 8 codes participating) and experiments

[1] http://opalopacity.llnl.gov/new.html

done at the LULI 2000 facility in France are given in [67 – 69]. These experiments/calculations are not only important to determine accurate mean opacities; in fact accurate spectral opacities are very important to determine reliable opacity coefficients for radiative accelerations.

3.2 Chemical evolution

Stellar opacities depend on the chemical composition. For example there is observational evidence that the photospheric abundances of certain metal species of B stars may be lower than solar [32] and it was shown [33] that this chemical composition leads to a higher opacity peak at log T=5.3 and produces a wider instability strip. In computations one often assumes the chemical abundances to be homogeneous in the whole envelope. However, atomic diffusion, unless hampered by mixing effects, rearranges elements.

Atomic diffusion, see e.g. [70], is a slow process that modifies the local element abundances due to the counterplay between radiative acceleration vs. gravitional settling which is different for ions of different species. Regrettably, there are currently large uncertainties in the determination of radiative accelerations since they depend on spectral opacities. In main sequence stars atomic diffusion is responsible for shaping the superficial abundance pattern of Ap and Cp stars. Diffusion may also be partly responsible for the enhancement of opacity around the Z bump in B stars, because elements accumulate due to diffusion where their specific opacity is large. The effect of diffusion is however swept out if mixing processes are effective.

Element mixing in main sequence stars occurs due to different processes such as convection, convective core overshooting and rotationally induced element mixing like meridional circulation. These processes smooth the stratification of elements and our knowledge about their efficiency is still subject to uncertainties.

Among these processes, the extent of overshooting above the convective core is the easiest one to be measured observationally. Common values for slowly rotating β Cep stars are an overshooting layer with an extent of 0.1–0.4 pressure scale heights [73]. To disentangle the effect of overshooting from rotationally induced mixing, studies of more rapid rotators are needed [40]. Asteroseismic analyses of rapid rotators, however, require 2D models which are currently in development [74]. Nonetheless, the derived overshooting parameter also depends on the chemical stratification and the corresponding opacities.

4. Outlook on the near future

Solving the remaining problems related to mean opacities is important to obtain accurate asteroseismic models. Precisely determined stellar masses and other fundamental parameters are also important in studies on exoplanets [75]. Satellite missions devoted to the detection of earth-like planets such as *Kepler* and CoRoT are currently continuing their observations and provide excellent data for asteroseismic studies. The Canadian mission MOST is also still delivering data despite exceding its projected mission lifetime.

New projects are on the horizon:

BRITE constellation[2] is an Austrian-Polish-Canadian mission consisting of a set of 6 nanosatellites to observe luminosity variations of bright stars. The unique feature of this mission is that

[2] http://www.brite-constellation.at

the satellites are equipped with a filter in a red or blue passband respectively. The amplitude and phase difference between the two wavelength bands allows for the photometric determination of the surface geometry of pulsation modes at an unprecedent accuracy for bright stars. The launch of the first pair of satellites is scheduled for spring 2012.

The SONG project (short for: Stellar Observations Network Group) consists of a network of 1-meter robotic telescopes devoted to observing bright stars to do asteroseismology and follow-up observations of exoplanet hosts. Each node of this network is equipped with a high-resolution echelle spectrograph. The prototype node in Tenerife is expected to deliver first light by the end of 2011 [71].

Along with additional observations theoretical models and asteroseismic tools are being improved. One example is the open access evolutionary code within the MESA package [76] which is rapidly developed and currently adapted to asteroseismic use.

Consequently the future of asteroseismology is bright.

References

[1] Uytterhoeven, K., Moya, A., Grigahcéne, A., et al., *The Kepler characterization of the variability among A- and F-type stars*, 2011, *A&A*, 534, A125

[2] Balona, L. A., & Dziembowski, W. A., *Kepler observations of δ Scuti stars*, 2011, *MNRAS*, 417, 591

[3] Balona, L. A., Guzik, J. A., Uytterhoeven, K., et al., *The Kepler view of γ Doradus stars*, 2011, *MNRAS*, 415, 3531

[4] Balona, L. A., Pigulski, A., De Cat, P., et al., *Kepler observations of the variability in B-type stars*, 2011, *MNRAS*, 413, 2403

[5] Degroote, P., Aerts, C., & Ollivier, M., *CoRoT's view of newly discovered B-star pulsators: results for 358 candidate B pulsators from the initial run's exoplanet field data*, 2009, *A&A*, 506, 471

[6] Bigot, L., & Dziembowski, W. A., *The oblique pulsator model revisited*, 2002, *A&A*, 391, 235

[7] Kurtz, D. W., Cunha, M. S., Saio, H., et al., *The first evidence for multiple pulsation axes: a new rapidly oscillating Ap star in the Kepler field, KIC 10195926*, 2011, *MNRAS*, 414, 2550

[8] Balona, L. A. & Dziembowski, W. A., *Excitation and visibility of high-degree modes in stars*, 1999, *MNRAS*, 309, 221

[9] Pamyatnykh, A. A., *Pulsational Instability Domains in the Upper Main Sequence*, 1999, *AcA*, 49, 119

[10] Goldreich, P., & Wu, Y., *Gravity Modes in ZZ Ceti Stars. I. Quasi-adiabatic Analysis of Overstability*, 1999, *ApJ*, 511, 904

[11] Guzik, J. A., Kaye, A. B., Bradley, P. A., et al., *Driving the Gravity-Mode Pulsations in γ Doradus Variables*, 2000, *ApJ*, 542, 57

[12] Antoci, V., Handler, G., Campante, T. L., et al., *The excitation of solar-like oscillations in a δ Sct star by efficient envelope convection*, 2011, *Nature*, 477, 570

[13] Belkacem, K., Samadi, R., Goupil, M.-J., et al., *Solar-Like Oscillations in a Massive Star*, 2009, *Science*, 324, 1540

[14] Degroote, P., Briquet, M., Auvergne, M., et al., *Detection of frequency spacings in the young O-type binary HD 46149 from CoRoT photometry*, 2010, *A&A*, 519, 38

[15] Aerts, C., Briquet, M., Degroote, P., et al., *Seismic modelling of the β Cephei star HD 180642 (V1449 Aquilae)*, 2011, *A&A*, 534, 98

[16] Saio, H., *A non-adiabatic analysis for axisymmetric pulsations of magnetic stars*, 2005, *MNRAS*, 360, 1022

[17] Iglesias, C. A., & Rogers, F. J., *Updated Opal Opacities*, 1996, *AJ*, 464, 943

[18] Badnell, N. R., Bautista, M. A., Butler, K., et al., *Updated opacities from the Opacity Project*, 2005, *MNRAS*, 360, 458

[19] Hummer, D. G., & Mihalas, D., *The equation of state for stellar envelopes. I* , 1988, *ApJ*, 331, 794

[20] Rogers, F. J., & Nayfonov, A., *Updated and Expanded OPAL Equation-of-State Tables: Implications for Helioseismology*, 2002, *ApJ*, 576, 1064

[21] Trampedach, R., Däppen, W., & Baturin, V. A., *A Synoptic Comparison of the Mihalas-Hummer-Dppen and OPAL Equations of State*, 2006, *ApJ*, 646, 560

[22] Seaton, M. J., & Badnell, N. R., *A comparison of Rosseland-mean opacities from OP and OPAL*, 2004, *MNRAS*, 354, 457

[23] Asplund, M., Grevesse, N., Sauval, J. A., & Scott, P., *The Chemical Composition of the Sun*, 2009, *Annual Review of Astronomy & Astrophysics*, 47, Issue 1, 481

[24] Jeffery, C. S., & Saio, H., *Gravity-mode pulsations in subdwarf B stars: a critical test of stellar opacity*, 2006, *MNRAS*, 372, 48

[25] Jeffery, C. S., & Saio, H., *Improved Opacities and Pulsation Models for sdB and sdO Stars*, 2008, *ASPC*, 392, 245

[26] Townsend, R. H. D., & MacDonald, J., *Excitation of g modes in Wolf-Rayet stars by a deep opacity bump*, 2006, *MNRAS*, 368, 57

[27] Gautschy, A., Althaus, L. G., & Saio, H., *On the excitation of PG 1159-type pulsations*, 2005, *A&A*, 438, 1013

[28] Montalbán, J., & Miglio, A., *Input from opacity data in computation of pulsation instability*, 2008, *CoAst*, 157, 160

[29] Ferguson, J. W., Alexander, D. R., Allard, F., et al., *Low-Temperature Opacities*, 2005, *ApJ*, 623, 585

[30] Daszyńska-Daszkiewicz, J., & Walczak, P., *Complex asteroseismology of the B-type main sequence pulsators*, 2010, *Highlights of Astronomy*, 15, 364

[31] Daszyńska-Daszkiewicz, J., & Walczak, P., *Constraints on opacities from complex asteroseismology of B-type pulsators: the β Cephei star θ Ophiuchi*, 2009, *MNRAS*, 398, 1961

[32] Morel, T., *Abundances of massive stars: some recent developments*, 2009, *CoAst*, 158, 122

[33] Montalbán, J., Miglio, A., & Morel, T., *Uncertainties in the chemical composition of B-type stars: effects on the opacity and on the excitation of pulsation modes*, 2009, *CoAst*, 158, 288

[34] Simon, N. R., *A plea for reexamining heavy element opacities in stars*, 1982, *ApJ*, 260, 87

[35] Dziembowski, W. A., & Pamiatnykh, A. A., *The opacity mechanism in B-type stars. I - Unstable modes in Beta Cephei star models*, 1993, *MNRAS*, 262, 204

[36] Dziembowski, W. A., Moskalik, P., & Pamyatnykh, A. A., *The Opacity Mechanism in B-Type Stars - Part Two - Excitation of High-Order G-Modes in Main Sequence Stars*, 1993, *MNRAS*, 265, 588

[37] Miglio, A., Montalbán, J., & Dupret, M.-A., *Instability strips of slowly pulsating B stars and β Cephei stars: the effect of the updated OP opacities and of the metal mixture*, 2007, *MNRAS*, 375, 21

[38] Zdravkov, T., & Pamyatnykh, A. A., *Main-sequence instability strip for different opacities and heavy element abundances: a comparison with observations*, 2008, *Jour. of Phys.: Conf. Series*, 118, 012079

[39] Handler, G., Jerzykiewicz, M., Rodríguez, E., et al., *Asteroseismology of the β Cephei star 12 Lac: photom. observations, pulsational frequency analysis & mode identification*, 2006, *MNRAS*, 365, 327

[40] Dziembowski, W. A. and Pamyatnykh, A. A., *The two hybrid B-type pulsators: ν Eridani and 12 Lacertae*, 2008, *MNRAS*, 385, 2061

[41] Desmet, M., Briquet, M., Thoul, A., et al., *An asteroseismic study of the β Cephei star 12 Lac: multisite spectrosc. observations, mode identification & seismic modelling*, 2009, *MNRAS*, 396, 1460

[42] Handler, G., Shobbrook, R. R., Jerzykiewicz, M., et al., *Asteroseismology of the β Cephei star ν Eridani - I. Photometric observations and pulsational frequency analysis*, 2004, *MNRAS*, 347, 454

[43] Aerts, C., De Cat, P., Handler, G., et al., *Asteroseismology of the β Cephei star ν Eridani - II. Spectroscopic observations and pulsational frequency analysis*, 2004, *MNRAS*, 347, 463

[44] De Ridder, J., Telting, J. H., Balona, L. A., et al., *Asteroseismology of the β Cephei star ν Eridani - III. Extended frequency analysis and mode identification*, 2004, *MNRAS*, 351, 324

[45] Pamyatnykh, A. A., Handler, G., & Dziembowski, W. A., *Asteroseismology of the β Cephei star ν Eridani: interpretation and applications of the oscillation spectrum*, 2004, *MNRAS*, 350, 1022

[46] Jerzykiewicz, M., Handler, G., Shobbrook, R. R., et al., *Asteroseismology of the β Cephei star ν Eridani - IV. The 2003-2004 multisite photometric campaign and the combined 2002-2004 data*, 2005, *MNRAS*, 360, 619

[47] Chapellier, E., Le Contel, D., Le Contel, J. M., et al., *A hybrid β Cephei-SPB star in a binary system: γ Pegasi*, 2006, *A&A*, 448, 697

[48] Handler, G., Matthews, J. M., Eaton, J. A., et al., *Asteroseismology of Hybrid Pulsators Made Possible: Simultaneous MOST Space Photometry and Ground-Based Spectroscopy of γ Peg*, 2009, *ApJ*, 698, 56

[49] Handler, G., *Confirmation of simultaneous p and g mode excitation in HD 8801 and γ Peg from time-resolved multicolour photometry of six candidate 'hybrid' pulsators*, 2009, *MNRAS*, 398, 1339

[50] Zdravkov, T., & Pamyatnykh, A. A., *Modelling hybrid β Cephei/SPB pulsations: γ Pegasi*, 2009, *AIPC*, 1170, 388

[51] Pandey, C. P., Morel, T., Briquet, M., et al., *A spectroscopic study of the hybrid pulsator Gamma Pegasi*, 2011, *CoAst*, 162, 21

[52] Zdravkov, T., & Pamyatnykh, A. A., *Can opacity changes help to reproduce the hybrid star pulsations?*, 2008, *CoAst*, 157, 385

[53] Salmon, S., Montalbán, J., Miglio, A., et al., *Can an underestimation of opacity explain B-type pulsators in the SMC?*, 2010, arXiv:1007.3088

[54] Antoci, V., Breger, M., Rodler, F., et al., *Is 44 Tauri an exceptional case among the δ Scuti stars?*, 2007, *A&A*, 463, 225

[55] Lenz, P., Pamyatnykh, A. A., Zdravkov, T., & Breger, M., *A δ Scuti star in the post-MS contraction phase: 44 Tauri*, 2010, *A&A*, 509, 90

[56] Lenz, P., Pamyatnykh, A. A., & Breger, M., *The Effect of Different Opacity Data and Chemical Element Mixture on the Petersen Diagram*, 2007, *AIPC*, 948, 201

[57] Handler, G., Shobbrook, R. R., & Mokgwetsi, T., *An asteroseismic study of the β Cephei star θ Ophiuchi: photometric results*, 2005, *MNRAS*, 362, 612

[58] Briquet, M., Lefever, K., Uytterhoeven, K., & Aerts, C., *An asteroseismic study of the β Cephei star θ Ophiuchi: spectroscopic results*, 2005, *MNRAS*, 362, 619

[59] Briquet, M., Morel, T., Thoul, A., et al., *An asteroseismic study of the β Cephei star θ Ophiuchi: constraints on global stellar parameters and core overshooting*, 2007, *MNRAS*, 381, 1482

[60] Lovekin, C. C., Goupil, M.-J., *Rotation and convective core overshoot in θ Oph*, 2010, *A&A*, 515, 58

[61] Daszyńska-Daszkiewicz, J., & Walczak, P., *Constraints on opacities from complex asteroseismology of B-type pulsators: the β Cephei star θ Ophiuchi*, 2009, *MNRAS*, 398, 1961

[62] Daszyńska-Daszkiewicz, J., & Walczak, P., *A complex asteroseismic study of the hybrid B-type pulsator ν Eridani*, 2010, *Ap&SS*, 328, 97

[63] Walczak, P., & Daszyńska-Daszkiewicz, J., *Complex asteroseismology of the hybrid B-type pulsator γ Pegasi: A test of stellar opacities*, 2010, *AN*, 331, 1057

[64] Briquet, M., Aerts, C., Baglin, A., et al., *An asteroseismic study of the O9V star HD 46202 from CoRoT space-based photometry*, 2011, *A&A*, 527, 112

[65] Christensen-Dalsgaard, J., di Mauro, M. P., Houdek, G., & Pijpers, F., *On the opacity change required to compensate for the revised solar composition*, 2009, *A&A*, 494, 205

[66] Guzik, J. A., Keady, J. J., & Kilcrease, D. P., *Early Solar Mass Loss, Opacity Uncertainties, and the Solar Abundance Problem*, 2009, *AIPC*, 1170, 577

[67] Turck-Chièze, S., Loisel, G., Gilles, D., et al., *Theoretical and experimental activities on opacities for a good interpretation of seismic stellar probes*, 2011, *Jour. of Phys.: Conf. Series*, 271, 012035

[68] Turck-Chièze, S., Loisel, G., Gilles, D., et al., *Radiative properties of stellar plasmas and open challenges*, 2011, *Ap&SS*, 336, 103

[69] Gilles, D., Turck-Chièze, S., Loisel, G., et al., *Comparison of Fe and Ni opacity calculations for a better understanding of pulsating stellar envelopes*, 2011, *HEDP*, 7, 312

[70] Alecian, G., *Gravitational settling and radiative accelerations*, 2009, *CoAst*, 158, 34

[71] Creevey, O. L., Grundahl, F., Pallé, P. L., et al., *The Observatorio del Teide welcomes SONG:the Stellar Observations Network Group*, 2012, *Highlights of Spanish Astrophysics VI, Proceedings of the IX Scientific Meeting of the Spanish Astronomical Society (SEA)*, 686

[72] Walker, G. A. H., Kuschnig, R., Matthews, J. M., et al., *Pulsations of the Oe Star ζ Ophiuchi from MOST Satellite Photometry and Ground-based Spectroscopy*, 2005, *ApJ*, 623, 145

[73] Thoul, A., *Asteroseismology of B stars*, 2009, *CoAst*, 159, 35

[74] Reese, D. R., *Oscillations in rapidly rotating stars*, 2010, *AN*, 331, 1038

[75] Moya, A., *Pulsating stars harbouring planets*, 2012, arXiv:1111.2274

[76] Paxton, B., Bildsten, L., Dotter, A., et al., *Modules for Experiments in Stellar Astrophysics (MESA)*, 2011, *ApJS*, 192, 3

PROCEEDINGS OF SCIENCE

Laboratory Astrochemistry: A Powerful Tool to Understand the Origin of Organic Molecules in the Interstellar Medium, Comets, and Meteorites

Michel Nuevo[∗†]
NASA Ames Research Center, Moffett Field, CA, USA & SETI Institute, Mountain View, CA, USA
E-mail: michel.nuevo-1@nasa.gov

During the past two decades, astrochemistry laboratory simulations have shown that complex organic molecules can be formed under simulated astrophysical conditions from the vacuum ultraviolet (UV) irradiation of ice mixtures containing simple species such as H_2O, CO, CO_2, CH_3OH, and NH_3. These organics include compounds of biological and prebiotic interests such as amino acids—the building blocks of proteins, and nucleobases—the informational subunits of DNA and RNA. Although the presence of amino acids in the interstellar medium (ISM) has not been confirmed by observations to date, they have been detected in meteorites, indicating that biomolecules and/or their precursors can be formed under extraterrestrial, non-biological conditions. Nucleobases have also been detected in meteorites, broadening the variety of complex organic molecules that can be formed in astrophysical environments. Like amino acids, nucleobases and other *N*-heterocycles have not been observed in the ISM. In the following, I will review some of the progress made by laboratory astrochemistry towards understanding the formation of organic species from the UV irradiation of ices at low temperature under astrophysically relevant conditions. This discussion will be focused on the formation of amino acids and other molecules of prebiotic interest such as urea and glycerol. Then, I will present recent studies on the formation of nucleobases and related compounds from the UV irradiation of pyrimidine in H_2O, NH_3, and CH_3OH ices, which show the formation of a large suite of photo-products including the nucleobases uracil and cytosine.

Frank N. Bash Symposium New Horizons In Astronomy,
October 9-11, 2011
Austin Texas

∗Speaker.
†With the collaboration of, in an alphabetical order: G. Auger, D. Blanot, J.H. Bredehöft, Y.-J. Chen, G.D. Cody, E. Dartois, B.T. De Gregorio, D. Deboffle, J.P. Dworkin, J.E. Elsila, W.-H. Ip, A.L.D. Kilcoyne, L. Le Sergeant d'Hendecourt, P. de Marcellus, C.K. Materese, U.J. Meierhenrich, S.N. Milam, G.M. Muñoz Caro, L. Nahon, S.A. Sandford, W.H.-P. Thiemann, C.-Y.R. Wu, and T.-S. Yih.

PoS(Bash11)004

1. Ices and organics in the Solar System and the interstellar medium

Gas (atoms, molecules, ions) and dust grains (solid particles) in the interstellar medium (ISM) are clumped into clouds and processed by energetic particles, mainly photons (ultraviolet, X-rays, γ-rays) and cosmic rays (high energy protons and other heavier nuclei). Given sufficient mass, the gravitational collapse of these clouds will eventually lead to the formation of stars via several stages of evolution, from diffuse clouds to denser molecular clouds, and finally to protostellar objects surrounded by debris disks.

Dust grains have a typical size of $\sim$0.1 μm and are usually made of carbonaceous material [1, 2] or minerals (amorphous or crystalline) [3, 4]. In cold environments such as interstellar dense clouds and inside disks around protostars, grains are coated with a volatile mantle consisting of ices. Here the term "ice" refers to any volatile species that can condense on cold grains, mainly H_2O, CO, CO_2, CH_3OH, NH_3, and CH_4 [5 – 10], but they can also be other more complex organic molecules, including polycyclic aromatic hydrocarbons (PAHs) [11 – 13]. Icy compounds are usually bound together by Van der Waals interaction and/or hydrogen bonds, and participate actively to the chemical and thermal coupling between the grains and the surrounding gas.

Ices are ubiquitous in the ISM, and present in the (outer) Solar System (Table 1). It first appears that the composition of astrophysical ices is comparable in astrophysical objects and in comets. The most abundant component of astrophysical ices is H_2O. Small carbon- and oxygen-bearing molecules such as CO, CO_2, and CH_3OH have abundances ranging from a few percent to 30% compared with H_2O. NH_3 is not very abundant, but its photochemistry in the presence of the other ices leads to the formation of new species including OCN^-, observed in many astrophysical ices with detectable abundances [14].

The interaction of the ices with ultraviolet (UV) photons and cosmic rays modifies the chemical structure of the mantle. As more and more complex molecules are formed, an organic refractory layer starts to form on the grains. Experimental simulations have shown that such a refractory material, often called organic residue, can be formed from the irradiation of astrophysically relevant ice mixtures with UV photons or high-energy protons [15 – 17]. Stable at room temperature, residues can then be analyzed with several techniques.

These complex organic molecules are then probably incorporated into small objects during the formation of the protoplanetary disk and the stellar system, such as comets, asteroids, and interplanetary dust particles (IDPs). The bombardment of planets from comets and asteroids during the heavy bombardment period in the early stages of the formation of our Solar System may have seeded the primitive Earth, as well as other planets, with a broad range of organic molecules, including the ingredients necessary for the emergence of life as we know it [18, 19]. These ingredients are amino acids (the building blocks of proteins), nucleobases (the informational subunits of DNA and RNA), ribose (the carbonaceous backbone of DNA and RNA), as well as other sugars, and lipids (constituents of cell walls). The detection of these compounds in meteorites [20 – 22] strongly supports an extraterrestrial origin of the building blocks of life.

In the following, I will review what is known about the composition of organic residues formed from the UV irradiation of astrophysically relevant ices. I will discuss the detection and formation of amino acids and nucleobases in these residues, and compare those results with what has been observed in meteorites and collected extraterrestrial materials.

Table 1: Composition and relative abundances of ices in the interstellar medium and comparison with comets. The abundance of H_2O, most abundant ice component, has been set to 100 for all these objects.

Species	*RAFGL 7009S* [23]	*NGC 7538 IRS9* [24, 25]	*W33A* [5]	*Elias 16* [5]	*Comets* [5]
H_2O	100	100	100	100	100
CO	15	12	8	25	5–3
CO_2	21	15	13	18	3–20
CH_3OH	30	4–12	18	< 3	0.3–5
CH_4	3.6	2	0.4	–	1
NH_3	–	13	15	≤ 9	0.1–1.8
OCN^-	3.7	2	3.5	< 0.5	–

2. Laboratory simulations

Mixtures of the compounds to be studied are prepared in the gas phase in a stainless steel or glass mixing line (background pressure: $\leq 10^{-5}$ mbar). Relative abundances between components are determined by their partial pressures. Gas mixtures are transferred into bulbs, which are then connected to the deposition tube of a vacuum chamber. Vacuum chambers consist of a stainless steel cage pumped to a pressure of a few 10^{-8} mbar and cooled to temperatures as low as 10 K with a closed-cycle He cryocooler. A detailed description of typical vacuum system set-ups can be found in refs. [26 – 28].

Mixtures are then simultaneously deposited on a cold substrate (infrared-transparent KBr or MgF_2 windows, aluminum, etc.) and irradiated with UV photons or energetic protons. UV photons can be provided either by a microwave-powered H_2-discharge lamp, emitting mainly Lyman-α and a continuum centered around 160 nm [27 – 30], or by a synchrotron radiation beam (tunable light source), provided by facilities such as former LURE (Orsay, France) [31], recently open SOLEIL (Gif-sur-Yvette, France) [32], or NSRRC (Hsinchu, Taiwan) [26, 33]. UV lamp radiation is a good analog to the light emitted by young stars, whereas UV light from synchrotron can be used to study a given photochemical reaction or pathway at a specific wavelength. Ices can also be bombarded with energetic protons produced by a Van de Graaff accelerator [34]. The deposition/irradiation duration can vary from a few minutes to a few days, with typical experiments lasting 1 to 2 days. After irradiation, samples are usually warmed to room temperature, at which time they are recovered from their substrate and conserved before they are analyzed with different techniques. Some vacuum systems are also equipped with a Fourier-transform infrared (FTIR) spectrometer in order to monitor the composition of the ices during irradiation and warm-up. The infrared (IR) spectra obtained from such experiments can in some cases be directly compared with astronomical data in order to search for the presence of ice components (see, e.g., refs. [35, 36]) and/or the physical conditions in the media where those species are observed.

3. Composition of organic residues

Infrared spectroscopy is a powerful tool to monitor the evolution of the ices during irradiation at low temperature and warm-up to room temperature. UV irradiation of ices induces the breaking

PoS(Bash11)004

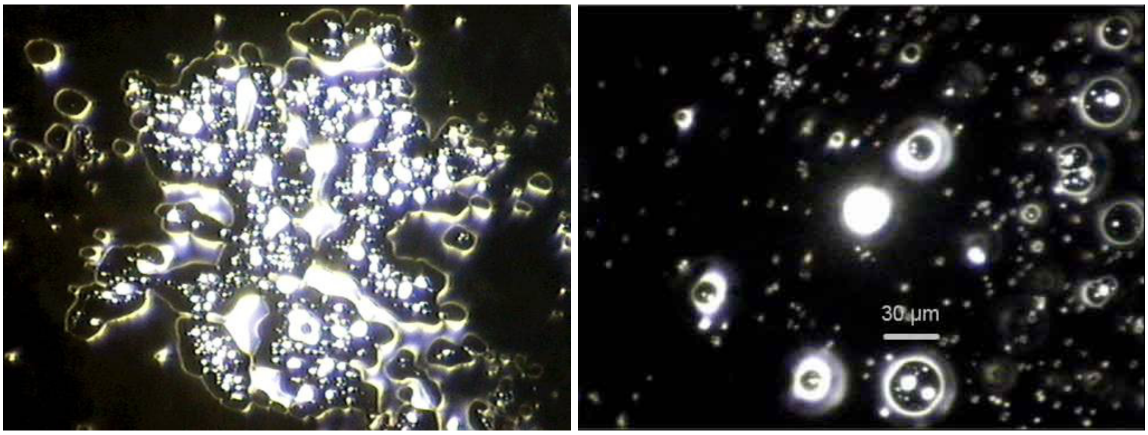

Figure 1: Infrared microscopy images of an organic residue produced from the UV irradiation of an H_2O:CH_3OH:NH_3 ice mixture. Organic molecules form vesicle-like structures that are soluble in water.

of chemical bonds and/or the ionization of some compounds, leading to the formation of reactive species such as ions and radicals. The mobility of radicals in an ice matrix is usually very limited at low temperature, and only first-opportunity reactions between nearby species can take place at this stage. After irradiation and during warm-up, photo-produced species become more mobile and react with each other to form more complex molecules. IR spectra at low temperature of photolyzed ice mixtures containing H_2O and combinations of CO, CO_2, CH_3OH, CH_4, and NH_3 indicate the presence of several families of molecules including alcohols, amines, carboxylic acids, alkanes, and alkenes, as well as species such as H_2CO (formaldehyde), NH_4^+ (ammonium ion), OCN^- (cyanate ion, observed in astrophysical objects, see Table 1), the $HCO^\bullet$ radical, HNCO (isocyanic acid), and organic molecules as complex as NH_2CHO (formamide) [26, 31, 37].

During the warm-up phase, all volatile species (both starting ices and new photo-products), sublime away from the substrate. Some of those volatile compounds can be identified by mass spectrometry, such as carbamic acid, produced from the irradiation of an H_2O:CO_2:NH_3 mixture, and observed to sublime around 250 K [26].

At room temperature, organic residues usually appear oil-like with a flavescent tinge. They are sometimes referred to as "yellow stuff", and are soluble in water [16, 38]. They usually consist of 10–50 μm droplets (Fig. 1), suggesting that a decent fraction of the formed photo-products can self-assemble into vesicle structures [39]. Laser-desorption mass spectrometry of one residue showed a very complex mass spectrum displaying a peak for almost every single mass from 40 to 400 atomic mass units (amu), indicating that this material is very complex and probably macromolecular [40].

IR spectra of organic residues show a number of characteristic bands assigned to molecular families including alcohols, amines, carboxylic acids, alkanes, alkenes, nitriles/isonitriles, ketones, esters, and amides, as well as carboxylate salts [31, 37]. Specific compounds could not be identified in residues, with the exception of hexamethylenetetramine (HMT) [17] and NH_4^+ [41].

More recently, X-ray absorption near-edge structure (XANES) spectra of similar residues have been measured in the carbon, oxygen, and nitrogen edges at the Advanced Light Source (Berkeley, USA) [42]. These measurements confirmed the presence of several families of chemical groups (aromatic and aliphatic CH_x bonds, carboxyls, amides, ketones, nitriles, etc.). This study also indicated that oxygen and nitrogen atoms are very efficiently incorporated into carbonaceous chains, resulting in a very nitrogen- and oxygen-rich material, with elemental N/C and O/C ratios of 0.1–0.3 and 0.4–0.6, respectively [42]. Compared with XANES measurements of extraterrestrial materials, the N/C and O/C ratios found in organic residues are up to 2 times higher than what was measured in cometary particles returned by Stardust [43, 44], and 2–10 times higher than for organic matter extracted from the Murchison meteorite [45, 46].

However, mass spectrometry as well as IR and X-ray absorption spectroscopies techniques are usually not sufficient to identify specific organic molecules. For this, residues need to be analyzed with chemical techniques such as liquid and gas chromatographies.

4. Amino acids in organic residues

The first organic molecules that were searched for in residues as well as in carbonaceous chondrites were amino acids. Amino acids are the building blocks of proteins for all life on Earth. There are 20 proteinic amino acids, plus 2 additional rare ones—selenocysteine and pyrrolysine— that were found in some proteins. Other non-proteinic amino acids can also be found in biological systems, such as sarcosine or β-alanine [47]. In proteins, amino acids are only present in their enantiomeric form L. This property of homochirality is chemically favored for amino acid polymerization, and gives a particular chiral 3-dimensional structure. D-Amino acids, such as D-alanine and D-aspartic acid, are also found in some biological systems such as bacteria cell membranes [47].

Organic residues produced from the UV irradiation of ice mixtures containing H_2O, CO, CO_2, CH_3OH, CH_4, and NH_3, and analyzed with high-performance liquid chromatography (HPLC) and/or gas chromatography coupled with mass spectrometry (GC-MS) showed the presence of a broad variety of amino acids [27, 29], up to 16 in one sample [30]. These amino acids are mostly detected after acid hydrolysis of the residues, as only very small quantities of free amino acids are present in non-hydrolyzed residues [27], indicating that organic residues consist of either a macromolecular material that can be easily hydrolyzed, or precursors which are more photo-stable to UV photons than the compounds detected after hydrolysis, or both.

Because they are formed from achiral starting compounds under achiral experimental conditions, amino acids detected in residues are racemic, i.e., they have equal amounts of D- and L-enantiomers [29, 30, 48]. In addition, the distribution of amino acids is different from what is observed in biological proteins, as the most abundant amino acid—glycine—is also the simplest, and the abundance of larger amino acids decreases with their molecular weight [27, 48]. Finally, the formation of amino acids from the UV irradiation of astrophysical ice analogs has proven efficient as long as the starting ices contain C, H, N, and O atoms, regardless of the starting carbon source [27]. For example, amino acids have been detected in residues formed from the UV irradiation of a fully inorganic starting mixture H_2O:CO_2:NH_3 [33], as well as from the UV/EUV irradiation of naphthalene ($C_{10}H_8$), the smallest PAH, in an H_2O:NH_3 ice mixture [49]. These characteristics are consistent with non-biological formation pathways, and indicate that the amino acids detected in residues are not due to biological contamination.

Amino acids have been extensively searched for in the ISM in the gas phase (radio astronomy) [50], but none of them have been detected, though the possible detection of glycine is still under debate [51, 52]. In contrast, up to 70 amino acids have been found in carbonaceous chondrites such as the Murchison and Murray meteorites [20, 53, 54]. These meteoritic amino acids, of which only a small fraction are found in proteins, have isotopic ratios consistent with an extraterrestrial origin [55] and a non-racemic distribution, with enantiomeric excesses of a few percent for proteinic-like α-hydrogenated amino acids [21, 56, 57], and up to 18% for isovaline, a non-proteinic α-methylated amino acid [58, 59].

The origin of this asymmetry in the chiral distribution of amino acids is still a mystery, and a number of theoretical and experimental studies have attempted to reproduce such a result by adding asymmetry to the formation of organic residues from the UV irradiation of ices [31]. Recently, the irradiation of H_2O:CH_3OH:NH_3 (achiral) ice mixtures with circularly polarized light (CPL) in the UV range has shown that alanine, the smallest chiral proteinic amino acid, was formed with enantiomeric excesses of opposite signs when left or right polarizations of the light were used [32]. Moreover, enantiomeric excesses seem to be directly proportional to the number of polarized photons irradiating the ices. Astronomical observations showed that CPL could be present in the ISM and affect the stereochemistry of carbonaceous molecules formed in astrophysical environments [60, 61].

5. Other molecules of prebiotic interest in organic residues

Although present in all organic residues formed from the UV irradiation of simple astrophysical ice analogs (H_2O, CO, CO_2, CH_3OH, CH_4, NH_3, etc.), amino acids only represent a small fraction of the residue material, with a quantum yield estimated to be of the order of 10^{-4} for the total amount of amino acids [30]. Other molecules of prebiotic interest, in particular DNA- and RNA-like nucleobases, have been searched for in organic residues, with no success.

Nonetheless, molecules such as urea, glycerol, and a number of its derivatives including glyceric amide, glycolic acid, and glycerolic acid [62] have been detected in residues. These compounds are known to perform different functions in biological systems, and some of them have been detected in meteorites [22, 63, 64]. The presence of these compounds in residues has been confirmed in other experiments, which also showed the presence of hydantoin [65]. This compound, also detected in meteorites [64, 66], is particularly interesting because its hydrolysis leads to the formation of carbamoyl amino acids (CAAs), which can also be formed from the addition of isocyanic acid (HNCO) to α-amino acids. CAAs are the precursors of *N*-carboxyanhydride amino acids, which can polymerize into poly- and oligopeptides, that is, primitive proteins [67, 68].

Finally, amphiphilic molecules, consisting of a hydrophilic head and a hydrophobic tail, are also present in organic residues (see Fig. 1 and ref. [39]). These compounds have the ability of self-assembling into vesicles. The delivery of amphiphiles via meteorites and comets to the primitive Earth may have led to the formation of the first cell membranes, within which chemical reactions are protected from the outside environment [69].

Future analysis of organic residues will focus on the search for sugar compounds, which are assumed to be present, but whose presence in residues has never been demonstrated, though they have been detected in the Murchison meteorite [22].

6. Formation of nucleobases from pyrimidine in astrophysical ices

Nucleobases, the informational subunits of DNA and RNA, are compounds based on the backbones of two *N*-heterocyclic compounds, namely, pyrimidine and purine. Biological pyrimidine-based nucleobases are uracil (RNA), thymine (DNA), and cytosine (DNA/RNA), whereas biological purine-based nucleobases are adenine and guanine, both found in DNA and RNA. There are also other pyrimidine- and purine-based compounds in the nature including barbituric acid, its derivatives, and caffein.

Nucleobases have been extensively searched for in the ISM in the gas phase [70 – 72], but never been detected. Only an upper limit for the column density of pyrimidine of 1.7–3.4 $\times 10^{14}$ cm^{-2} could be derived from these observations [71]. More generally, no *N*-heterocyclic molecules have been unequivocally detected so far in the ISM [72], although there are observational indications that they may be present [73]. However, purines have been found in a large number of carbonaceous chondrites including Murchison, Murray, and Orgueil [74 – 77]. Meteoritic pyrimidines are usually detected with smaller abundances than purines because they are more subject to chemical and photochemical processes. Nonetheless, uracil was found in water extracts of Murchison, Murray, and Orgueil [78]. Finally, the extraterrestrial origin of nucleobases in Murchison has been confirmed by isotopic measurements [79].

Therefore, pyrimidines and purines must be present in astrophysical environments. Since they are not observed in the gas phase, they may be condensed on the surface of cold grains, mixed with ices, together with other aromatic molecules [11, 12]. Moreover, some theoretical studies suggest that pyrimidine and other aromatic compounds could be formed via polymerization of smaller molecules [80]. For this reason, experiments in which pyrimidine is mixed with ices of astrophysical interest and irradiated with UV photons has been and are currently being performed [28, 81].

The UV irradiation of pyrimidine mixed with pure H_2O ice leads to the formation of an organic residue in which several pyrimidine derivatives have been detected, including the nucleobase uracil and its precursor 4(3*H*)-pyrimidone [28]. Theoretical calculations simulating such reactions are in agreement with experimental results, and showed that 4(3*H*)-pyrimidone and uracil are the most stable singly and doubly oxidized derivatives formed, respectively [82]. These calculations also showed that H_2O plays an essential as an ice matrix to stabilize the formation of these photo-products.

The photochemistry of pyrimidine mixed other pure ices such as NH_3 (ammonia), CH_3OH (methanol), or CH_4 (methane) is not as efficient, although a few singly substituted pyrimidine derivatives do form, such as 4-aminopyrimidine in NH_3+pyrimidine mixtures [81], or 4-pyrimidinemethanol in CH_3OH+pyrimidine mixtures (unpublished results). The addition of H_2O in those mixtures not only diversifies the chemistry by oxidizing pyrimidine and its amino derivatives, but it also increases the efficiency of addition of NH_2, CH_2OH, and CH_3 groups to pyrimidine, probably via the same matrix effect as observed for H_2O+pyrimidine mixtures [82]. In H_2O-rich mixtures, identified photo-products include the nucleobases uracil and cytosine, as well as small quantities of non-aromatic species such as glycine, urea, and small amino acids [81]. However, the addition of CH_3 groups to pyrimidine appears to be an inefficient process. Consequently, thymine, the third pyrimidine-based nucleobase, can only form when the number of UV photons per deposited molecule is significantly higher (unpublished results).

Future experiments will focus on the study of the irradiation of pyrimidine in a realistic mixture of astrophysical ice analogs, in order to assess the role of each ice component in the formation of pyrimidine derivatives, including nucleobases and their isomers.

7. Laboratory astrochemistry, extraterrestrial materials, and space missions

IR studies of ice mixture irradiations can be directly compared with IR astronomical observations of a broad range of astrophysical objects from ISO (European Space Agency, ESA) and Spitzer (NASA). For instance, laboratory experiments helped identifying the interstellar bands of OCN^- [83, 84] and NH_3 [35, 36]. On the other hand, techniques used to analyzed organic residues produced in the laboratory are usually applicable to the analysis of extraterrestrial materials such as meteorites, IDPs, and samples returned by space missions, for a direct comparison.

For example, cometary grains collected by Stardust from comet Wild 2 and returned to Earth have been analyzed with IR and XANES spectroscopies, as well as liquid and gas chromatographies. Results show that the composition of these grains varies significantly from one to another, displaying a broad range of organic compounds [43, 44, 85]. These measurements can be directly compared with what is observed for IDPs [86] and laboratory organic residues [42], and constrain the conditions in which those materials form in astrophysical environments [87]. NASA is already planning a future sample-return mission (OSIRIS-REx) currently scheduled for launch in 2016 for an encounter with asteroid 1999 RQ36 in 2023.

Similar analyses for the search of organics will probably be performed on the grains returned by Hayabusa from asteroid Itokawa, although mineralogical analysis showed that this S-type asteroid has the same IR characteristic features as LL ordinary chondrites [88], known to be poor in carbonaceous matter. The Japanese space agency (JAXA) is currently working on Hayabusa 2.

Analysis of the fragments of the Almahata Sitta meteorite, collected in Sudan after asteroid 2008 TC_3 entered the Earth's atmosphere [89], showed that this unique ureilite contains organic compounds including amino acids [90, 91]. Almahata Sitta was also found to contain adenine, one of the purine nucleobases [77]. Further analysis of these meteoritic fragments may be conducted in order to identify other organic compounds of prebiotic interest.

Finally, the Rosetta mission (ESA), launched in 2004 [92], will encounter comet Churyumov–Gerasimenko and land the Philae probe on its nucleus in 2014, where several in-situ analytical techniques will be performed. Instruments onboard Philae include a GC-MS instrument which can automatically prepare and run samples [93]. These data will be directly comparable with laboratory measurements of organic residues, meteoritic samples, IDPs, and Stardust grains.

8. Conclusion

Laboratory astrochemistry is a rich, powerful research field in constant evolution. Laboratory experiments can constrain physical and chemical parameters in observed astrophysical environments, while astronomical observations can test laboratory predictions. In addition, analytical techniques used to analyze samples produced in the laboratory are in most cases applicable to the study of extraterrestrial materials such as meteorites, IDPs, and samples returned from Solar

System objects such as comets and asteroids. Direct comparison between these data is a powerful tool to assess the composition, the origin, and the evolution of extraterrestrial matter, as well as the link between astronomical observations and extraterrestrial material collected on Earth. In particular, one of the goals of astrochemistry is to study the evolution and origin of molecules of biological interest, from the astrophysical environments where they form, to their incorporation into Solar System bodies and their delivery to telluric planets such as the primitive Earth.

References

[1] A. Blanco, S. Fonti, & V. Orofino, *On the interstellar extinction hump and laboratory carbonaceous grains*, *Astrophys. J.* **462** (1996) 1020.

[2] E. Dartois, *Interstellar dust grains: the hydrogenated amorphous carbon contribution*, proceedings of *Molecules in Space and Laboratory*, Paris, France, 14–18 May 2007, J.L. Lemaire & F. Combes, Eds. (2007) p. 54.

[3] D.M. Watson, J.M. Leisenring, E. Furlan, et al., *Crystalline silicates and dust processing in the protoplanetary disks of the Taurus young cluster*, *Astrophys. J. Supp.* **180** (2009) 84.

[4] I. Oliveira, J. Olofsson, K.M. Pontoppidan, et al., *On the evolution of dust mineralogy, from protoplanetary disks to planetary systems*, *Astrophys. J.* **734** (2011) 51.

[5] E.L. Gibb, D.C.B. Whittet, W.A. Schutte, et al., *An inventory of interstellar ices toward the embedded protostar W33A*, *Astrophys. J.* **536** (2000) 347.

[6] E. Dartois, *The ice survey opportunity of ISO*, *Space Sci. Rev.* **119** (2005) 293.

[7] A.C.A. Boogert, K.M. Pontoppidan, C. Knez, C., et al., *The c2d Spitzer spectroscopic survey of ices around low-mass young stellar objects. I. H_2O and the 5–8 μm bands*, *Astrophys. J.* **678** (2008) 985.

[8] K.M. Pontoppidan, A.C.A. Boogert, H.J. Fraser, et al., *The c2d Spitzer spectroscopic survey of ices around low-mass young stellar objects. II. CO_2*, *Astrophys. J.* **678** (2008) 1005.

[9] K.I. Öberg, A.C.A. Boogert, K.M. Pontoppidan, et al., *The c2d Spitzer spectroscopic survey of ices around low-mass young stellar objects. III. CH_4*, *Astrophys. J.* **678** (2008) 1032.

[10] S. Bottinelli, A.C.A. Boogert, J. Bouwman, et al., *The c2d Spitzer spectroscopic survey of ices around low-mass young stellar objects. IV. NH_3 and CH_3OH*, *Astrophys. J.* **718** (2010) 1100.

[11] S.A. Sandford, M.P. Bernstein, & L.J. Allamandola, *The mid-infrared laboratory spectra of naphthalene ($C_{10}H_8$) in solid H_2O*, *Astrophys. J.* **607** (2004) 346.

[12] M.P. Bernstein, S.A. Sandford, & L.J. Allamandola, *The mid-infrared absorption spectra of neutral polycyclic aromatic hydrocarbons in conditions relevant to dense interstellar clouds*, *Astrophys. J. Suppl. Ser.* **161** (2005) 53.

[13] V.C. Geers, E.F. van Dishoeck, R. Visser, R., et al., *Spatially extended polycyclic aromatic hydrocarbons in circumstellar disks around T Tauri and Herbig Ae stars*, *Astron. Astrophys.* **476** (2007) 279.

[14] R.J.A. Grim & J.M. Greenberg, *Ions in grain mantles – The 4.62 micron absorption by OCN^- in W33A*, *Astrophys. J.* **321** (1987) L91.

[15] W. Hagen, L.J. Allamandola, & J.M. Greenberg, *Interstellar molecule formation in grain mantles – The laboratory analog experiments, results and implications*, *Astrophys. Space Sci.* **65** (1979) 215.

[16] V.K. Agarwal, W. Schutte, W., J.M. Greenberg, et al., *Photochemical reactions in interstellar grains – Photolysis of CO/NH_3 and H_2O*, *Orig. Life* **16** (1985) 21.

[17] M.P. Bernstein, S.A. Sandford, L.J. Allamandola, & S. Chang, *Organic compounds produced by photolysis of realistic interstellar and cometary ice analogs containing methanol*, *Astrophys. J.* **454** (1995) 327.

[18] J. Oró, *Comets and the formation of biochemical compounds on the primitive Earth*, *Nature* **190** (1961) 389.

[19] C.F. Chyba & C. Sagan, *Endogenous production, exogenous delivery and impact-shock synthesis of organic molecules: an inventory for the origins of life*, *Nature* **335** (1992) 125.

[20] K.A. Kvenvolden, J.G. Lawless, & C. Ponnamperuna, *Nonprotein amino acids in the Murchison meteorite*, *Proc. Natl. Acad. Sci.* **68** (1971) 486.

[21] J.R. Cronin & S. Pizzarello, *Amino acid enantiomer excesses in meteorites: origin and significance*, *Adv. Space Res.* **23** (1999) 293.

[22] G. Cooper, N. Kimmich, W. Belisle, et al., *Carbonaceous meteorites as a source of sugar-related organic compounds for the early Earth*, *Nature* **414** (2001) 879.

[23] L. d'Hendecourt, M. Jourdain de Muizon, E. Dartois, et al., *ISO-SWS observations of solid state features towards RAFGL 7009S*, *Astron. Astrophys.* **315** (1996) L365.

[24] D.C.B. Whittet, W.A. Schutte, A.G.G.M. Tielens, et al., *An ISO SWS view of interstellar ices: First results*, *Astron. Astrophys.* **315** (1996) L357.

[25] J.H. Lacy, H. Faraji, S.A. Sandford, & L.J. Allamandola, *Unraveling the 10 micron "silicate" feature of protostars: The detection of frozen interstellar ammonia*, *Astrophys. J. Lett.* **501** (1998) L105.

[26] Y.-J. Chen, M. Nuevo, J.-M. Hsieh, et al., *Carbamic acid produced by the UV/EUV irradiation of interstellar ice analogs*, *Astron. Astrophys.* **464** (2007) 253.

[27] M. Nuevo, G. Auger, D. Blanot, & L. d'Hendecourt, *A detailed study of the amino acids produced from the vacuum UV irradiation of interstellar ice analogs*, *Orig. Life Evol. Biosph.* **38** (2008) 37.

[28] M. Nuevo, S.N. Milam, S.A. Sandford, et al., *Formation of uracil from the ultraviolet photo-irradiation of pyrimidine in pure H_2O ices*, *Astrobiology* **9** (2009) 683.

[29] M.P. Bernstein, J.P. Dworkin, S.A. Sandford, et al., *Racemic amino acids from the ultraviolet photolysis of interstellar ice analogues*, *Nature* **416** (2002) 401.

[30] G.M. Muñoz Caro, U.J. Meierhenrich, W.A. Schutte, et al., *Amino acids from ultraviolet irradiation of interstellar ice analogues*, *Nature* **416** (2002) 403.

[31] M. Nuevo, U.J. Meierhenrich, G.M. Muñoz Caro, et al., *The effects of circularly polarized light on amino acid enantiomers produced by the UV irradiation of interstellar ice analogs*, *Astron. Astrophys.* **457** (2006) 741.

[32] P. de Marcellus, C. Meinert, M. Nuevo, et al., *Non-racemic amino acid production by ultraviolet irradiation of achiral interstellar ice analogs with circularly polarized light*, *Astrophys. J. Lett.* **727** (2011a) L27.

[33] M. Nuevo, Y.-J. Chen, T.-S. Yih, et al., *Amino acids formed from the UV/EUV irradiation of inorganic ices of astrophysical interest*, *Adv. Space Res.* **40** (2007a) 1628.

[34] P.A. Gerakines, M.H. Moore, & R. Hudson, *Energetic processing of laboratory ice analogs: UV photolysis versus ion bombardment*, *J. Geophys. Res.* **106** (2001) 33381.

[35] E. Dartois, L. d'Hendecourt, W. Thi, et al., *Combined VLT ISAAC/ISO SWS spectroscopy of two protostellar sources. The importance of minor solid state features*, *Astron. Astrophys.* **394** (2002) 1057.

[36] E. Dartois, G.M. Muñoz Caro, D. Deboffle, & L. d'Hendecourt, *Diffuse interstellar medium organic polymers. Photoproduction of the 3.4, 6.85 and 7.25 μm features*, *Astron. Astrophys.* **423** (2004) L33.

[37] G.M. Muñoz Caro & W.A. Schutte, *UV-photoprocessing of interstellar ice analogs: New infrared spectroscopic results*, *Astron. Astrophys.* **412** (2003) 121.

[38] J.M. Greenberg, *Chemical evolution in space – A source of prebiotic molecules*, *Adv. Space Res.* **3** (1983) 19.

[39] J.P. Dworkin, D.W. Deamer, S.A. Sandford, & L.J. Allamandola, *Self-assembling amphiphilic molecules: Synthesis in simulated interstellar/precometary ices*, *Proc. Natl. Acad. Sci.* **98** (2001) 815.

[40] J.P. Dworkin, J.S. Gillette, M.P. Bernstein, et al., *An evolutionary connection between interstellar ices and IDPs? Clues from mass spectroscopy measurements of laboratory simulations*, *Adv. Space Res.* **33** (2004) 67.

[41] E.L. Wagner & D.F. Hornig, *The vibrational spectra of molecules and complex ions in crystals III. Ammonium chloride and deutero-ammonium chloride J. Chem. Phys.* **18** (1950) 296.

[42] M. Nuevo, S.N. Milam, S.A. Sandford, et al., *XANES analysis of organic residues produced from the UV irradiation of astrophysical ice analogs*, *Adv. Space Res.* **48** (2011) 1126.

[43] S.A. Sandford, J. Aléon, C.M.O'D. Alexander, et al., *Organics captured from comet 81P/Wild 2 by the Stardust spacecraft*, *Science* **314** (2006) 1720.

[44] G.D. Cody, H. Ade, C.M.O'D. Alexander, et al., *Quantitative organic and light-element analysis of comet 81P/Wild 2 particles using C-, N-, and O-μ-XANES*, *Meteorit. Planet. Sci.* **43** (2008) 353.

[45] C.M.O'D. Alexander, M. Fogel, H. Yabuta, & G.D. Cody, *The origin and evolution of chondrites recorded in the elemental and isotopic compositions of their macromolecular organic matter*, *Geochim. Cosmochim. Acta* **71** (2007) 4380.

[46] G.D. Cody, C.M.O'D. Alexander, H. Yabuta, et al., *Organic thermometry for chondritic parent bodies*, *Earth Planet. Sci. Lett.* **272** (2008) 446.

[47] J.P. Greenstein & M. Winitz, *Chemistry of the amino acids*, John Wiley & Sons Inc., New York, U.S.A. (1961) pp. 3–45.

[48] M. Nuevo, U.J. Meierhenrich, L. d'Hendecourt, et al., *Enantiomeric separation of complex organic molecules produced from irradiation of interstellar/circumstellar ice analogs*, *Adv. Space Res.* **39** (2007b) 400.

[49] Y.-J. Chen, M. Nuevo, T.-S. Yih, et al., *Amino acids produced from the ultraviolet/extreme-ultraviolet irradiation of naphthalene in a H_2O+NH_3 ice mixture*, *Month. Not. R. Astron. Soc.* **384** (2008) 605.

[50] F. Combes, F., Nguyen-Q-Rieu, & G. Wlodarczak, *Search for interstellar glycine*, *Astron. Astrophys.* **308** (1996) 618.

[51] Y.-J. Kuan, S.B. Charnley, H.-C. Huang, et al., *Interstellar glycine*, *Astrophys. J.* **593** (2003a) 848.

[52] L.E. Snyder, F.J. Lovas, J.M. Hollis, et al., *A rigorous attempt to verify interstellar glycine*, *Astrophys. J.* **619** (2005) 914.

[53] E.L. Shock & M.D. Schulte, *Summary and implications of reported amino acid concentrations in the Murchison meteorite*, *Geochim. Cosmochim. Acta* **54** (1990) 3159.

[54] M.A. Sephton, I.P. Wright, I. Gilmour, et al., *High molecular weight organic matter in martian meteorites*, *Planet. Space Sci.* **50** (2002) 711.

[55] Z. Martins, C.M.O'D. Alexander, G.E. Orzechowska, et al., *Amino acid composition of primitive CR2 chondrites*, *Meteor. Planet. Sci. Suppl.* **43** (2008a) 5195.

[56] M.H. Engel & S.A. Macko, *Isotopic evidence for extraterrestrial non- racemic amino acids in the Murchison meteorite*, *Nature* **389** (1997) 265.

[57] J.R. Cronin & S. Pizzarello, *Enantiomeric excesses in meteoritic amino acids*, *Science* **275** (1997) 951.

[58] S. Pizzarello, M. Zolensky, & K.A. Turk, *Nonracemic isovaline in the Murchison meteorite: Chiral distribution and mineral association*, *Geochim. Cosmochim. Acta* **67** (2003) 1589.

[59] D.P. Glavin & J.P. Dworkin, *Enrichment in L-isovaline by aqueous alteration on CI and CM meteorite parent bodies*, *Proc. Natl. Acad. Sci.* **106** (2009) 5487.

[60] J. Bailey, A. Chrysostomou, J.H. Hough, et al., *Circular polarization in star-formation regions: Implications for biomolecular homochirality*, *Science* **281** (1998) 672.

[61] T. Fukue, M. Tamura, R. Kandori, et al., *Extended high circular polarization in the orion massive star forming region: Implications for the origin of homochirality in the Solar System*, *Orig. Life Evol. Biosph.* arXiv reference: 1001.2608 (2010).

[62] M. Nuevo, J.H. Bredehöft, U.J. Meierhenrich, et al., *Urea, glycolic acid, and glycerol in an organic residue produced by ultraviolet irradiation of interstellar/pre-cometary ice analogs*, *Astrobiology* **10** (2010) 245.

[63] J.R. Cronin & S. Chang, *Chemistry of life's origins*, J.M. Greenberg, V. Pirronello, & C. Mendoza-Gómez, Eds., Kluwer, Dordrecht, the Netherlands (1993) pp. 209–258.

[64] G.W. Cooper & J.R. Cronin, *Linear and cyclic aliphatic carboxamides of the Murchison meteorite: Hydrolyzable derivatives of amino acids and other carboxylic acids*, *Geochim. Cosmochim. Acta* **59** (1995) 1003.

[65] P. de Marcellus, M. Bertrand, M. Nuevo, et al., *Prebiotic significance of extraterrestrial ice photochemistry: Detection of hydantoin in organic residues*, *Astrobiology* **11** (2011b) 847.

[66] A. Shimoyama & R. Ogasawara, *Dipeptides and diketopiperazines in the Yamato-791198 and Murchison carbonaceous chondrites*, *Orig. Life Evol. Biosph.* **32** (2002) 165.

[67] A. Commeyras, J. Taillades, H. Collet, et al., *Dynamic co-evolution of peptides and chemical energetics, a gateway to the emergence of homochirality and the catalytic activity of peptides*, *Orig. Life Evol. Biosph.* **34** (2004) 35.

[68] G. Danger, L. Boiteau, H. Cottet, & R. Pascal, *The peptide formation mediated by cyanate revisited. N-carboxyanhydrides as accessible intermediates in the decomposition of N-carbamoylamino acids*, *J. Am. Chem. Soc.* **128** (2006) 7412.

[69] D. Deamer, J.P. Dworkin, S.A. Sandford, et al., *The first cell membranes*, *Astrobiology* **2** (2002) 371.

[70] M.N. Simon & M. Simon, *Search for interstellar acrylonitrile, pyrimidine, and pyridine*, *Astrophys. J.* **184** (1973) 757.

[71] Y.-J. Kuan, C.-H. Yan, S.B. Charnley, et al., *A search for interstellar pyrimidine*, *Monthly Not. R. Astron. Soc.* **345** (2003b) 650.

[72] S.B. Charnley, Y.-J. Kuan, H.-C. Huang, et al., *Astronomical searches for nitrogen heterocycles*, *Adv. Space Res.* **36** (2005) 137.

[73] E. Peeters, A.L. Mattioda, D.M. Hudgins, & L.J. Allamandola, *Polycyclic aromatic hydrocarbon emission in the 15–21 micron region*, *Astrophys. J.* **617** (2004) L65.

[74] C.E. Folsome, J. Lawless, M. Romiez, & C. Ponnamperuma, *Heterocyclic compounds indigenous to the Murchison meteorite*, *Nature* **232** (1971) 108.

[75] R. Hayatsu, E. Anders, M.H. Studier, & L.P. Moore, *Purines and triazines in the Murchison meteorite*, *Geochim. Cosmochim. Acta* **39** (1975) 471.

[76] W. van der Velden & A. Schwartz, *Search for purines and pyrimidines in the Murchison meteorite*, *Geochim. Cosmochim. Acta* **41** (1977) 961.

[77] M.P. Callahan, K.E. Smith, H.J. Cleaves II, et al., *Carbonaceous meteorites contain a wide range of extraterrestrial nucleobases*, *Proc. Natl. Acad. Sci.* **108** (2011) 13995.

[78] P. Stoks & A. Schwartz, *Uracil in carbonaceous meteorites*, *Nature* **282** (1979) 709.

[79] Z. Martins, O. Botta, M.L. Fogel, et al., *Extraterrestrial nucleobases in the Murchison meteorite*, *Earth Plan. Sci. Lett.* **270** (2008b) 130.

[80] A. Ricca, C.W. Bauschlicher, & E.L.O. Bakes, *A computational study of the mechanisms for the incorporation of a nitrogen atom into polycyclic aromatic hydrocarbons in the Titan haze*, *Icarus* **154** (2001) 516.

[81] M. Nuevo, S.N. Milam, & S.A. Sandford, *Nucleobases and prebiotic molecules in organic residues produced from the ultraviolet photo-irradiation of pyrimidine in NH_3 and H_2O+NH_3 ices*, *Astrobiology* **12** (2012) in press.

[82] P.P. Bera, M. Nuevo, S.N. Milam, et al., *Mechanism for the abiotic synthesis of uracil via UV-induced oxidation of pyrimidine in pure H_2O ices under astrophysical conditions*, *J. Chem. Phys.* **133** (2010) 104303.

[83] J.H. Lacy, F. Baas, L.J. Allamandola, et al., *4.6 micron absorption features due to solid phase CO and cyano group molecules toward compact infrared sources*, *Astrophys. J.* **276** (1984) 533.

[84] K. Demyk, E. Dartois, L. d'Hendecourt, et al., *Laboratory identification of the 4.62 μm solid state absorption band in the ISO-SWS spectrum of RAFGL 7009S*, *Astron. Astrophys.* **339** (1998) 553.

[85] L.P. Keller, S. Bajt, G.A. Baratta, et al. *Infrared spectroscopy of Comet 81P/Wild 2 samples returned by Stardust*, *Science* **314** (2006) 1728.

[86] G.J. Flynn, L.P. Keller, M. Feser, et al., *The origin of organic matter in the solar system: evidence from the interplanetary dust particles*, *Geochim. Cosmochim. Acta* **67** (2003) 4791.

[87] S. Wirick, G.J. Flynn, L.P. Keller, et al. *Organic matter from comet 81P/Wild 2, IDPs, and carbonaceous meteorites; similarities and differences*, *Meteor. Planet. Sci.* **44** (2009) 1611.

[88] M. Abe, Y. Takagi, K. Kitazato, et al., *Near-Infrared Spectral Results of Asteroid Itokawa from the Hayabusa Spacecraft*, *Science* **312** (2006) 1334.

[89] P. Jenniskens, M.H. Shaddad, D. Numan, et al., *The impact and recovery of asteroid 2008 TC_3*, *Nature* **458** (2009) 485.

[90] D.P. Glavin, A.D. Aubrey, M.P. Callahan, et al., *Extraterrestrial amino acids in the Almahata Sitta meteorite*, *Meteor. Planet. Sci.* **45** (2010) 1695.

[91] A.S. Burton, D.P. Glavin, M.P. Callahan, et al., *Heterogeneous distributions of amino acids provide evidence of multiple sources within the Almahata Sitta parent body, asteroid 2008 TC_3*, *Meteor. Planet. Sci.* **46** (2011) 1703.

[92] W.H.-P. Thiemann & U. Meierhenrich, *ESA mission ROSETTA will probe for chirality of cometary amino acids*, *Orig. Life Evol. Biosph.* **31** (2001) 199.

[93] F. Goesmann, H. Rosenbauer, R. Roll, et al., *COSAC, the cometary sampling and composition experiment on Philae*, *Space Sci. Rev.* **128** (2007) 257.

PROCEEDINGS OF SCIENCE

Late-Type Compact Objects

Elizabeth J. Jeffery*
James Madison University
901 Carrier Dr., MSC 4502
Harrisonburg, VA 22801, USA
E-mail: jeffe2ej@jmu.edu

The final stages of stellar evolution for a low mass star are fairly unspectacular when compared to their high mass siblings. Once the outer layers of a star are shed, the hot exposed core that's left behind and begins to cool. As it does so, it exhibits several interesting (and useful!) character traits. In this paper I will give an overview of the discovery of white dwarf stars and what we now understand about their formation and place within the story of stellar evolution. The fate of 98% of the stars in our Galaxy, white dwarfs continue to prove their usefulness and versatility as probes of understanding a number of interesting astrophysical problems. I will discuss a few of these applications, with particular emphasis on work done studying white dwarfs in star clusters.

Frank N. Bash Symposium New Horizons In Astronomy,
October 9-11, 2011
Austin Texas

*Speaker.

PoS(Bash11)005

1. Introduction

A white dwarf star, as we now know today, is the end point of a low mass star's life. Although only about the size of the Earth, their average mass is about $0.6M_{\odot}$, making them extremely dense. They are typically composed of mostly carbon and oxygen, with a thin layer of helium and maybe hydrogen surrounding the C/O core. Nuclear fusion is no longer powering this type of star; the core is supported against further gravitational collapse by the electron degeneracy pressure.

While interesting in their own right, white dwarfs also serve astronomers in a variety of ways, as a probe to many different astrophysically interesting problems. In this paper I will discuss a variety of science questions that are and can be addressed with white dwarf stars. The range of their applications is a testament to their versatility as astrophysical probes.

This paper is arranged as follows: In Section 2 I briefly review the evolution of a low mass star to its ultimate fate as a white dwarf. In Section 3 I then discuss the different applications of white dwarfs, arranged roughly in order of temperature: interesting problems relating to hot, "warm," and cool white dwarfs. I particularly emphasize the use of WDs in star clusters, an area that has become more observationally feasible over the last 20 (or so) years with the use of large ground-based telescopes, as well as space-based telescopes, such as the *Hubble Space Telescope*. I summarize the discussion in Section 4.

2. A White Dwarf's Place in Stellar Evolution

The first white dwarf (WD) stars that were discovered were found as companions to brighter stars. They revealed themselves by the gravitational tugs they exerted on their companion stars. By measuring the periodic wobble of the brighter star, the smaller WD's mass can be measured. We now understand that WDs are the end point of a low mass star's evolution.

2.1 The H-R Diagram and the Evolution of Low Mass Stars

Ejnar Hertzsprung and Henry Norris Russell independently discovered relationships between a star's intrinsic brightness and its temperature. These patterns are most easily seen on what later became known as the Hertzsprung-Russell (H-R) Diagram, named in honor of its co-founders. The first H-R Diagram included a WD star (the companion star to 40 Eridani), although Russell dismissed it as a most likely an anomaly. (See Figure 1, taken from [26].) Of this "outlier" he said: "It is immediately conspicuous that one corner of the diagram is vacant (except for one star whose spectrum is very doubtful)." [25] More modern H-R Diagrams show that the lower left corner of the diagram, once thought to be vacant, is actually populated by the WDs.

All stars begin life when a cloud of gas and dust collapses to the point that temperatures and pressures in the core are hot and high enough to ignite hydrogen fusion. A star spends most of its life on the main sequence (MS), and will stay in this stage until it has exhausted its core hydrogen supply. When this occurs, the star's core (made now mostly of helium, the by-

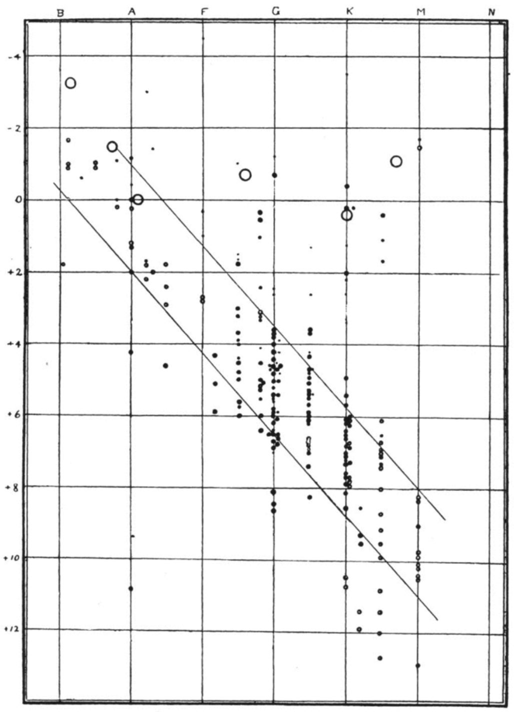

FIGURE 1. An early H-R Diagram taken from [26]. The only star in the bottom left corner is the WD 40 Eridani, although it was not known to be a WD at the time.

product of hydrogen fusion) begins to collapse while its outer layers swell in size, becoming a red giant star. Eventually the core becomes hot enough to begin fusing helium to heavier elements, including carbon and oxygen. While interesting in its own right, for our present purposes, we will skip over the details of this stage of a star's evolution.

Eventually the outer layers of the star are shed, as a planetary nebula, and the hot core is left exposed. This leftover core is a WD star. As I mentioned previously, it is composed mostly of carbon and oxygen, the result of the helium fusion stage. This is where we begin our investigation of the applications of these simple and versatile stars.

2.2 White Dwarf Cooling

Because there is no internal fusion occurring, a WD star shines because it is so hot, with its initial temperature often exceeding 100,000 K. With no internal heat sources, over time the WD will begin to cool and, after some time, begin to crystallize. Eventually it will reach the temperature of its surroundings, fading completely out of our sight. The evolutionary path a star takes on the H-R Diagram from the MS to a cooling WD is indicated by the gray line in Figure 2 (taken from [33]). (The regions labeled as "DOV," "DBV," and "DAV" are the various instability strips a WD will pass through as it cools. I will discuss these more later.)

Mestel [18] was the first to describe and quantify how the rate of cooling of a WD relates to its luminosity, using standard cooling physics. Since then, it has been realized that there are

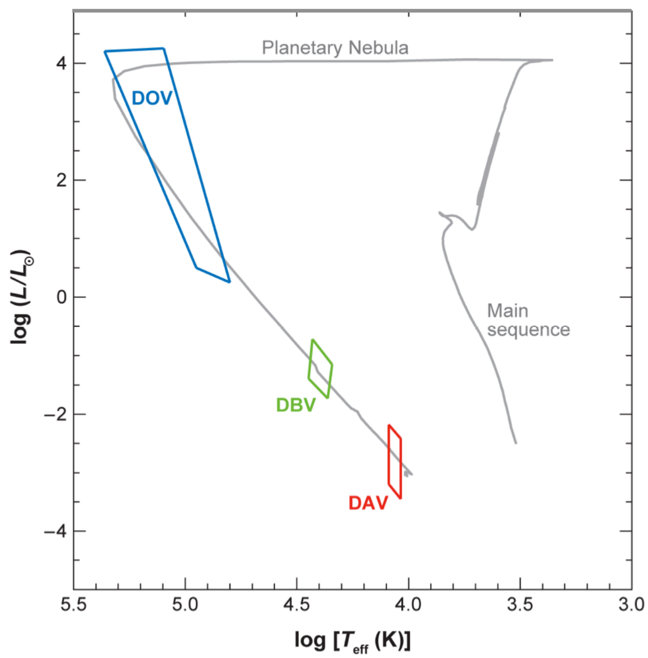

FIGURE 2. A schematic of the evolutionary track of a typical WD on the H-R Diagram, taken from [33]. The regions marked "DOV," "DBV," and "DAV" are the various instability strips a WD passes through in its evolution.

five physical effects during a WD's cooling that can provide a deviation from this classical theory. These effects, as described by [15], are as follows: (1) initial neutrino loss; (2) possible residual nuclear burning in the outer hydrogen layer; (3) gravitational contraction; (4) surface convection; and (5) crystallization.

For simplicity in our current discussion, I will classify WD cooling into three main stages: "hot," "warm," and "cool." While "hot" and "cool" are used commonly throughout the WD community, describing a WD as "warm" is somewhat unconventional; but I have chosen it here to clarify the discussion of those WDs that are neither classified as "hot" nor "cool," but rather have temperatures somewhere in between these two.

3. Applications of White Dwarf Science

Several of the properties of WDs also make them very useful as probes to address several astrophysically interesting problems. As the eventual fate of 98% of the stars in our Galaxy, they contain an archeological history of our own Milky Way. The conditions of high density and temperatures on a WD make them extreme physics laboratories, allowing us to test the behavior of material in an environment that cannot be replicated in the laboratory on Earth. When compared to their MS counterparts, WD stars are relatively simple and therefore easier to model and understand.

Some of the applications of WD science that I will discuss below include probing questions related to particle physics (specifically neutrinos); asteroseismology; searching for planets, dust and debris disks of remnant solar systems; understanding the origins of Type Ia supernovae; and measuring the ages of stellar populations, including star clusters (both open and globular clusters) and constituents of our Milky Way Galaxy. The study of WDs in clusters is especially interesting for a wide variety of topics; finding WDs in clusters allows us to fit WDs into the whole picture of stellar evolution and address many outstanding issues.

3.1 Hot White Dwarfs

The hottest WDs mark the transition between the planetary nebula phase and the WD phase. A study of the very hottest WDs is important for understanding this important transition in stellar evolution. When these WDs have cooled to roughly 18,000 – 28,000 K they will begin to pulsate (classified as DBVs). (The "DB" classification indicates the WD stars with observed helium in their atmospheres; the "V" classification indicates it is a variable WD.) Like all WD pulsators, they are non-radial pulsators. Unlike radial pulsating stars that change brightness because of actual changes in the size and effective temperature of the star, non-radial pulsators vary in brightness because of temperature fluctuations over their surface. Typically, they are multi-periodic and can show more complicated light curves than radial pulsators. This is illustrated in Figure 3, taken from [33], which shows the modeled surface brightness (on the right) along with the corresponding observed light output (i.e., photon flux, shown on the left) at various times for a given star.

A WD, like any hot object, initially cools very quickly. With time that cooling rate begins to slow. A WD's thermal energy is being carried away by photons, but also by other particles, including neutrinos and axions. In the early hot stages of a WD's cooling, the neutrino flux can actually be greater than the photon flux. As I mentioned above, it has been noted that the rate at which a WD actually cools is affected by the initial neutrino losses. For the hottest WDs in the DBV instability strip, the WD is still hot enough that its cooling is still dominated by neutrino losses. This effect is illustrated in Figure 4 (taken from [14]). Observations of the rate of change of the period of DBV stars allow us to measure their cooling rate. By comparing the expected cooling rate from photons alone to the observed cooling rate, we are able to probe the properties of these exotic particles that are being emitted from the WD star. (See [1] for more details on this application of WD studies.)

3.2 Warm White Dwarfs

Some of the earliest uses of WDs to probe various astrophysical questions came from studying the warm WDs. For example, the largest class of pulsating WD stars actually belong to the DAV class. (The "DA" classification indicates the WD stars with observed hydrogen in their atmospheres; the "V" classification indicates it is a variable WD.) These are WDs with hydrogen-rich atmospheres that are roughly 12,000 K. Also known as the ZZ Ceti stars, this class of WD pulsators was first discovered by Landolt (1968), and there are about 143 known members today ([9]; [2]). (Compare this to the DBVs, with roughly 18 members, [22]; [23]).

PoS(Bash11)005

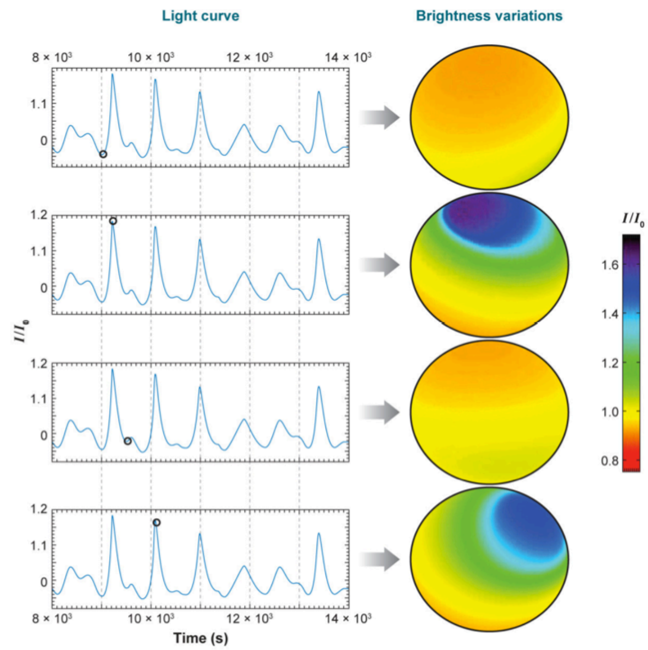

FIGURE 3. Surface brightness changes for a non-radial pulsating WD star. The left side shows the observed brightness (photon flux) corresponding to surface brightness changes modeled on the right. (Taken from [33].)

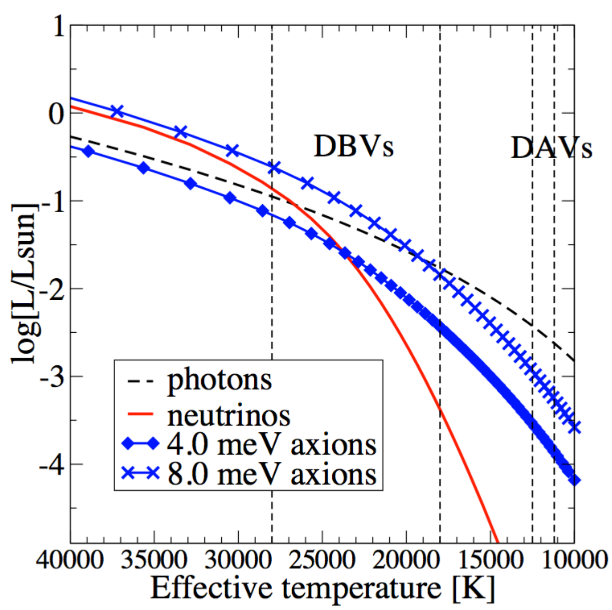

FIGURE 4. Expected flux from photons, neutrinos, and axions as a WD initially cools. Note that initially the flux from the neutrinos and 8.0 meV axions are greater than the photon flux. This trend continues into the DBV instability strip. Measuring the cooling rate for hot DBVs and comparing to the expected cooling rate from photons alone can give insight to the nature and amount of other particles carrying away thermal energy from the WD. (Plot taken from [14].)

DAV stars have been used in many applications. Astereoseismology of these stars can be used to probe their interiors. For example, this allows for a more thorough study of crystallization as the WD cools (e.g., [20]). Studies of the pulsations can also be used to measure the mass of the star and the mass of its layers ([33]), as well as to study the processes of convection ([19]).

More recently DAVs have been used to search for planets. Finding planets around WD stars is an exciting prospect because these WDs could give insight into the eventual fate of our own Solar System. (Particularly because our Sun will one day become a WD star.) Because the pulsation periods of some DAV stars are extremely stable, any periodic change in the pulse arrival time may indicate the wobble of a star due to an unseen companion as the two stars orbit their common center of mass. Such work has been started by [21] and built upon by [8]. Figure 5, taken from [8] shows a plot of observed minus calculated (O – C) values of pulse arrival times for the star GD66. The blue sinusoid corresponds to the effect on a DAV caused by a $2.7M_J \sin i$ planet at 4.9 AU with a 14.3 year orbit.

Related to the search for planets around other stars is the work looking for debris or dust disks around WD stars. For example, infrared observations of some WD stars indicate excess flux that is indicative of a debris disk around the star (see, e.g., [13]). Also, [27] have studied the presence of calcium across the surface of G29-38 using time-series spectroscopy (see Figure 6, taken from this study). Because the metals would settle on short time scales, the continual presence of calcium in the spectrum indicates that it is being replenished, likely from the debris disk that surrounds it.

3.3 Binary White Dwarfs

WD stars are candidate progenitors for Type Ia supernovae (SNIa). One hypothesis is that when a WD is in a binary system with a less evolved star, and that star expands to fill its Roche Lobe, the WD begins accreting material onto its surface. As it gains more and more mass it soon reaches the Chandrasekhar limit. When this happens, the WD explodes. Because the Chandrasekhar limit is universally the same, all SNIa have the same brightness and can be used as standard candles to measure distances to the furthest galaxies. SNIa were used to discover the acceleration of the Universe and continue to be an important cosmological tool.

However, saying that every SNIa has exactly the same luminosity is oversimplifying the problem. Effects such as crystallization, phase separation, dynamical and pulsational modes of energy transport, the dependence of mass loss on metallicity, and other aspects of WD physics must be understood. These factors may affect our interpretation of variations in the brightness of SNIa with redshift, and subsequently affect our interpretation of cosmological observations and implications.

3.4 Cool White Dwarfs

Early observations of the WD luminosity functions (LFs) of the Galactic disk (e.g., [17]) showed a steep drop off at the faint end. Theoretical calculations of the WDLF by [34] showed that the observed turndown of the WDLF was indeed a measure of the age of the Galactic disk. I display the early WDLF fit with theoretical models in the left panel of Figure 7, taken from

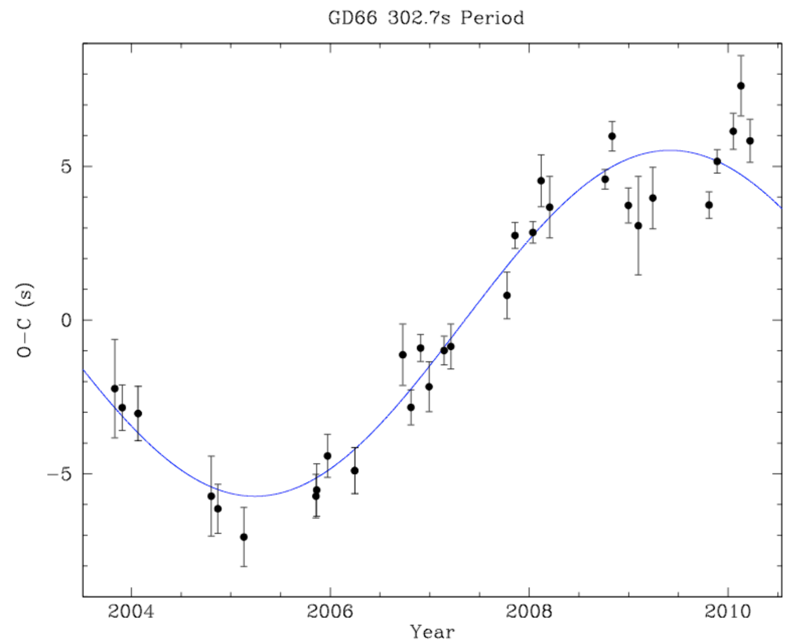

FIGURE 5. Taken from [8], the O – C diagram for the 302.7 s period mode of GD 66. The observed changes in pulse arrival time are too great to be explained by the cooling of the star and are likely indicative of a companion planet.

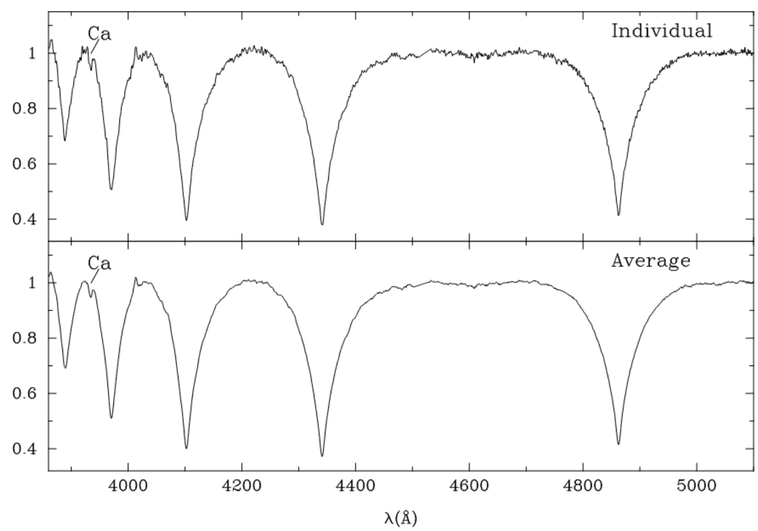

FIGURE 6. Spectra of GD29-38, taken from [27]. Note the presence of a calcium feature. Because metals would settle out of the atmosphere on extremely short timescales, the continual presence of calcium indicates that it must be replenished by some external source (e.g., dust disk, small planetary bodies, etc.).

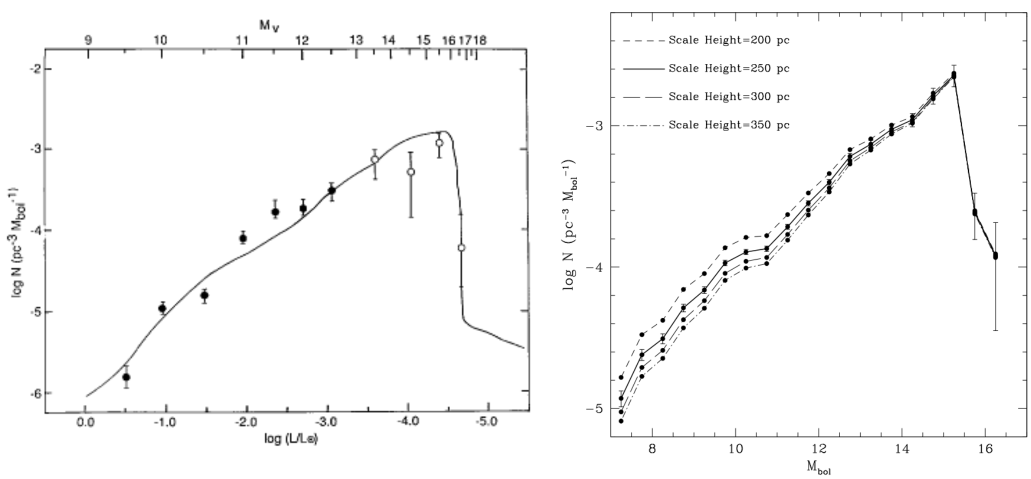

FIGURE 7. WDLF for the Galactic disk. It was first theoretically calculated by [34], left panel) that the WDLF could be used to determine the age of the disk. Over time, more WDs have been added to the WDLF and calculations and models continue to progress (left panel, taken from [7]).

[34]. The reason for this turndown is that the finite age of the disk does not allow the WD stars to cool beyond a certain luminosity. Because the luminosity of a WD star is related to its cooling time ([18]) and hence WD age, the turndown luminosity of a population's WDLF was therefore related to the age of the population. This work also demonstrated the feasibility of using the WDLF to constrain aspects of the star formation history of the Galactic disk.

In the roughly two decades that have passed between these initial studies, sample sizes have increased (e.g., [7]) to allow for us to disentangle effects from such things as WD mass distributions (e.g., [4]), as well as to extend the use of WDs as chronometers to various scale heights of the Galaxy. Work has been done to further improve both the observations and theoretical calculations of the WDLF. An example of this is the recent sample of [7], reproduced in the right panel of Figure 7.

3.5 White Dwarfs in Star Clusters

Star clusters are Nature's stellar laboratory. By removing uncertainties in the star-to-star differences in distance, age, reddening, and metallicity that plague field-star work, we are able to study the evolution of stars in an essentially pure environment. Observations of WDs in open and globular clusters have reached an exciting development in the last decade or two, thanks to the advancement of large ground-based and space telescopes. In this section I will briefly discuss some of the exciting questions that can now more fully be addressed by studying WDs in the controlled environment of a star cluster.

3.5.1 Maximum Mass for a White Dwarf Progenitor

Not all stars will become WDs. The stars that are massive enough will reach the endpoint of their evolution as either a neutron star or a black hole. But the key question is: how massive is “massive enough” to be considered high mass? Which stars will become WDs and which stars won’t? Star clusters can be used to answer this question, by connecting the mass of stars at a cluster’s main sequence turn off (MSTO) to the presence (or lack) of WDs. The current best estimate for this value is $8M_{\odot}$ [32].

3.5.2 Initial-Final Mass Relation

The mass distribution for WD stars in the field shows a fairly sharp peak at approximately $0.6M_{\odot}$. However, the mass of the WD progenitors shows a much broader range. Our understanding of the processes involved in mass loss from when a star leaves the MS to when in becomes a WD is poor, at best. There is much we do not understand. Star clusters can aid us in this process as well. Studying the initial-final mass relation (IFMR) – that is, the relationship between a star’s initial MS mass and its final WD mass – can only be done reliably in star clusters. Studying the IFMR in many clusters can shed light on the processes of mass loss, as well as give indications of metallicity dependence on mass loss.

3.5.3 Observations of White Dwarfs in Globular Clusters

An important and exciting advancement in the study of WDs in clusters is the observation of the terminus of the WD cooling track in three globular clusters. These clusters are M4, NGC 6397, and 47 Tuc. These observations provide information about cluster ages, crystallization (see Section 3.5.4), and collisionally-induced absorption opacities in these extremely old WDs. These studies are being aided by the superb datasets made available from the *Hubble Space Telescope*, especially in proper-motion cleaned color-magnitude diagrams. In Figure 8, I display the color-magnitude diagram for NGC 6397 with pre- and post-proper motion cleaning. (These figures were taken from [24].)

3.5.4 Crystallization of White Dwarfs

Observations of the terminus of WDs in globular clusters have created a rich dataset for a variety of studies. One of these applications is the ability to study the crystallization of the oldest cluster WDs as they cool. Winget et al. [35] fit models to observations of the WDs in NGC 6397 to demonstrate the effects of crystallization on the cooling of the WDs. (See Figure 9, taken from their paper.)

3.5.5 Star Cluster Ages

As discussed in Section 3.4, WDs can be used to determine the age of a stellar population. The same methods discussed there of finding the coolest WDs in the population can be applied to star clusters. The earliest attempts to do this were done by [3] and [30]. In Figure 10 I show a plot of the current agreement between open clusters from [11], an updated version of the same plot from [29].

An important motivation of these studies is to calibrate ages determined from the MSTO and those measured from the WDs. These two age methods are used to measure the ages of

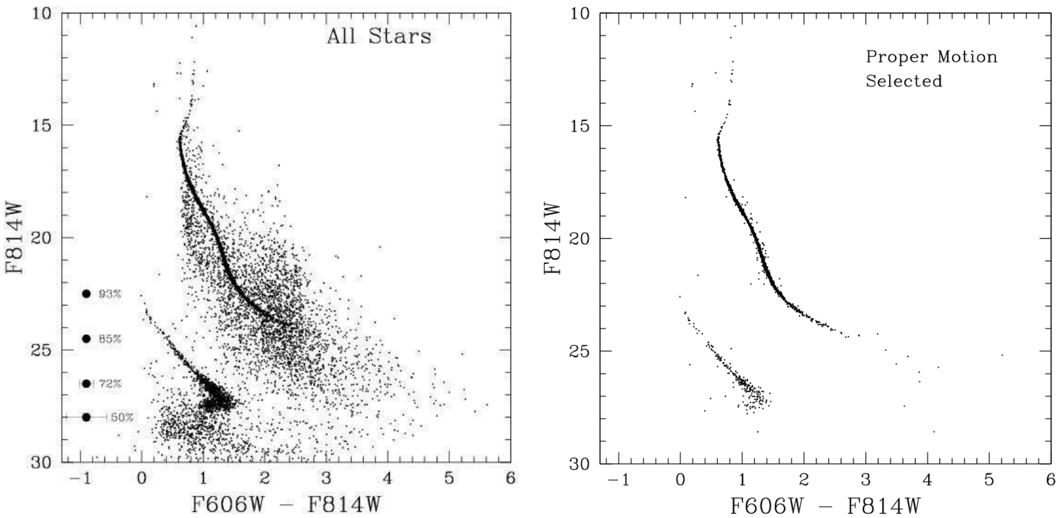

FIGURE 8. Color-magnitude diagram for NGC 6397 [24]. Data are taken with the *Hubble Space Telescope*; the panel on the left is the entire field, while the right panel is the proper motion cleaned, showing only those stars that are most likely to be cluster members

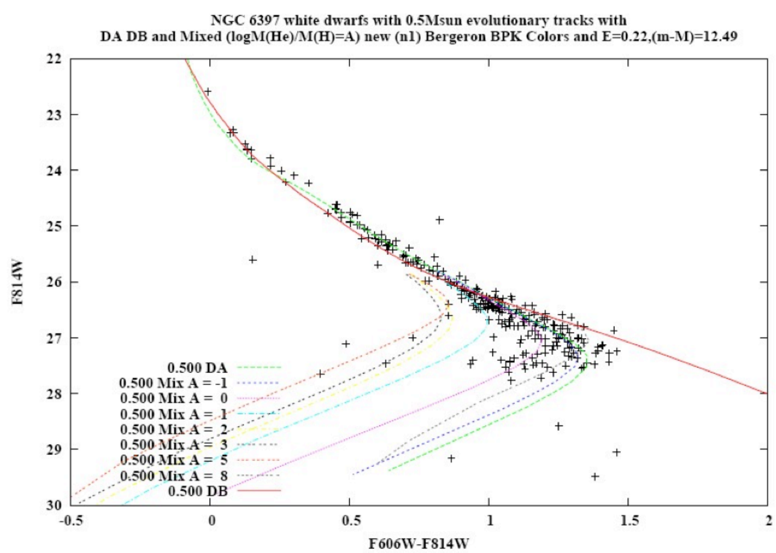

FIGURE 9. The WD cooling sequence of NGC 6397 with various models to investigate the effects of crystallization on the observed WDs. (Taken from [35].)

different parts of the Galaxy: the best age of the halo from the MSTO of globular clusters and the best age of the disk from the WDLF (Section 3.4). Uncertainty exist in the models used for both methods. MSTO model uncertainties includes nuclear reaction rates, uncertainties in the population's metallicity, the equation of state, as well as second-order effects including diffusion, rotation, and turbulence. Uncertainties in WD ages can arise from the mass

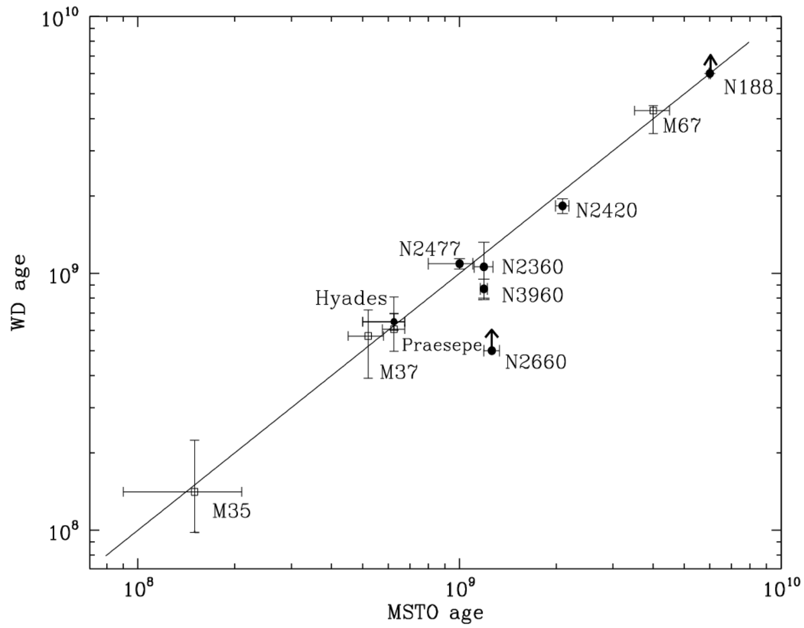

FIGURE 10. The current agreement of WD age vs. MSTO age for open clusters, taken from [11], an updated version of the original plot from [29].

distribution, the onset of core crystallization, molecular hydrogen opacities, and unknown DA/DB ratios. Because each model relies on different physics with different limitations, measuring the ages of clusters with each method allows us to more directly determine and isolate problems in the models, based on any disagreement that may arise between the ages calculated for a single population.

Over time our ability to obtain data of higher and higher precision has increased. However, in the coming years, the greatest improvements in age determinations of clusters will likely come in improvements in modeling. One such improvement is being developed by von Hippel and collaborators, using an algorithm that utilizes Bayesian statistics to objectively and simultaneously fit cluster-wide parameters such as age, metallicity, distance, and reddening to input models. (For more information, see [31], [12], [28], and [5].) Part of the power of the technique lies in being able to compare the posterior distribution for each of these parameters among a variety of model sets.

For example, in Figure 11 (taken from [11]), comparisons are made of the best age, metallicity, distance, and reddening determined from the best fit of three different MS model sets for the WD age of the open cluster NGC 2477. (In this case the different MS models were: [6]; [36]; and [10]. Other model ingredients were unchanged, but can – and will – eventually be varied for comparison. See [11] for further discussion on the exact model ingredients used.) The statistics that can be calculated from this method can now include internal errors (error within a particular model, i.e., the width of the distributions) and the external errors (errors

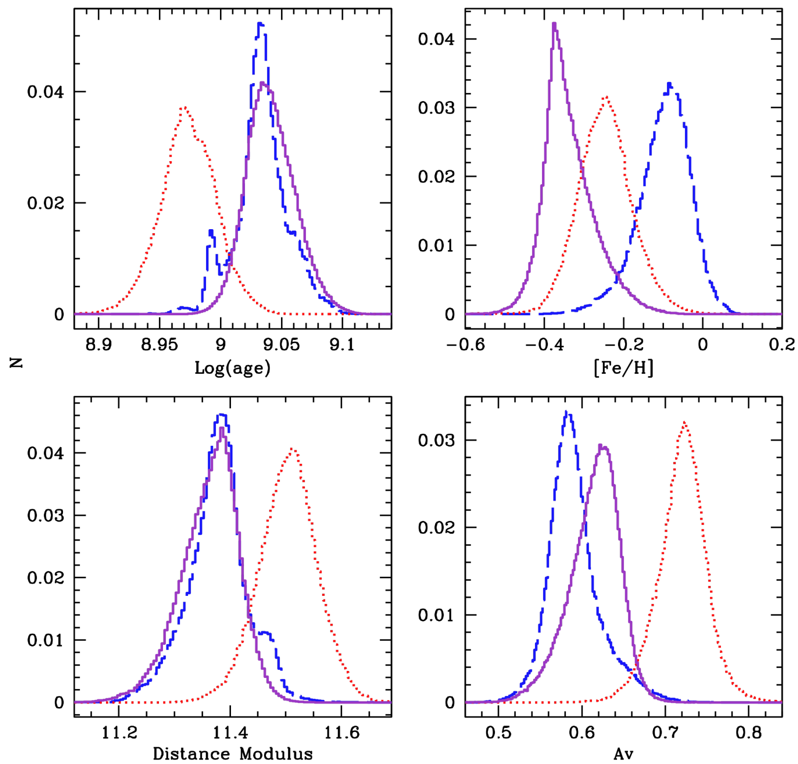

FIGURE 11. Posterior distributions for cluster-wide parameters of NGC 2477 (WD age) for three different MS models. The dashed lines are using the models of [6]; the dotted lines are using [36]; the solid lines are using [10]. The power of the Bayesian technique comes from being able to compare entire distributions, rather a single number.

among the models, i.e., taking into account the differences in the different distributions).

4. Summary

WDs, the endpoint of the evolution of 98% of stars, are simple stars, but have far-reaching applications to many fields of astrophysics. From hot WDs to cool WDs, some applications include particle and extreme physics, asteroseismology, the study of planets, understanding the expansion of the Universe (through Type Ia supernovae), measuring the ages of stars, and understanding important aspects of stellar evolution with the study of WDs in star clusters. In this paper I have reviewed a few of the applications of these interesting stars.

With the improvement of datasets and modeling techniques, we will be able to continue to push the boundaries of WD physics. There are still many puzzles in WD physics to study and explore. Doing so will improve the usability of these interesting objects and increase our understanding of many aspects of the Universe around us.

References

[1] Bischoff-Kim, A. et al., 2008, *ApJ*, 675, 1505

[2] Castanheira, B.G., et al. 2007, *A&A*, 462, 989

[3] Claver, C.F. 1995, PhD Thesis, The University of Texas at Austin

[4] DeGennaro, S. et al. 2007, *AJ*, 135, 1

[5] DeGennaro, S. et al. 2009, *ApJ*, 696, 12

[6] Dotter, A. et al. 2008, *ApJS*, 178, 89

[7] Harris, H.C., et al. 2006, *AJ*, 131, 571

[8] Heremes, J.J., et al. 2010, Proceedings of the 17th European White Dwarf Workshop, *AIP Conference Proceedings*, 1273, 446

[9] Gianninas, A., et al. 2006, *AJ*, 132, 831

[10] Girardi, L. et al. 2000, *A&AS*, 141, 371

[11] Jeffery, E.J. 2009, PhD Thesis, The University of Texas at Austin

[12] Jeffery, E.J. et al. 2006, *ApJ*, 658, 391

[13] Jura, M. et al., 2009, *AJ*, 137, 3191

[14] Kim, A. 2007, PhD Thesis, The University of Texas at Austin

[15] Lamb & Van Horn, 1975, *ApJ*, 200, 306

[16] Landolt, A.U. 1968, *ApJ*, 200, 306

[17] Liebert, J. et al. 1988, *ApJ*, 332, 891

[18] Mestel, L. 1952, *MNRAS*, 112, 583

[19] Montgomery, M.H., et al. 2005, *ApJ*, 633, 1142

[20] Montgomery, M.H. & Winget, D.E. 1999, *ApJ*, 526, 976

[21] Mullally, F. et al. 2008, *ApJ*, 676, 966

[22] Nitta, A., et al. 2007, *Commun. Asteroseismol.*, 150, 249

[23] Nitta, A., et al. 2009, *ApJ*, 690, 560

[24] Richer, H.B. et al. 2008, *AJ*, 135, 2141

[25] Russell, H.N. 1913, *The Observatory*, 36, 324

[26] Russell, H.N. 1914, *Nature*, 93, 52

[27] Thompson, S.E. et al. 2010, *ApJ*, 714, 296

[28] van Dyk, D.A., et al. 2009, The Annals of Applied Statistics, 3, 117

[29] von Hippel, T. 2005, *ApJ*, 622, 565

[30] von Hippel, T., et al. 1995, MNRAS, 273, L39

[31] von Hippel, T. et al. 2006, *ApJ*, 645, 1436

[32] Weidemann, V. & Koester, D. 1983, *A&A*, 121, 77

[33] Winget, D.E. & Kepler, S.O. 2008, *ARA&A,* 46, 157

[34] Winget D.E., et al. 1987, *ApJ*, 315, L77

[35] Winget, D.E., et al. 2009, *ApJ*, 693, L6

[36] Yi, S., et al. 2001, *ApJS*, 136, 417

PROCEEDINGS OF SCIENCE

Beyond Strömgren Spheres and Wind-Blown Bubbles: An Observational Perspective on H II Region Feedback

Matthew S. Povich[*][†]
Penn State
E-mail: povich@astro.psu.edu

Massive stars produce copious quantities of ultraviolet radiation beyond the Lyman limit, photoionizing the interstellar medium (ISM) and producing H II regions. As strong sources of recombination- and forbidden-line emission, infrared continuum, and thermal (free-free) radio continuum, H II regions serve as readily-observable beacons of massive star formation in the Milky Way and external galaxies. Along with supernovae, H II regions are dominant sources of feedback in star-forming galaxies, injecting radiative and mechanical luminosity into the ISM. H II regions may prove more important than supernovae as triggers of star formation through localized compression of cold cloud cores. In this review, I give a broad overview of the structure and time-evolution of H II regions, emphasizing complications to the theoretical picture revealed by multiwavelength observations. I discuss a recent controversy surrounding the dominant feedback mechanism in 30 Doradus, the most luminous H II region in the Local Group. I summarize the first results from the Milky Way Project (MWP), which has produced a new catalog of several thousand candidate Galactic H II regions by enlisting >35,000 "citizen scientists" to search *Spitzer Space Telescope* survey images for bubble-shaped structures. The MWP and similar large catalogs enable empirical studies of Galactic H II region evolution across the full range of luminosities and statistical studies of triggered star formation.

Frank N. Bash Symposium 2011: New Horizons in Astronomy
October 9-11, 2011
Austin, Texas, USA

[*]Speaker.
[†]NSF Astronomy and Astrophysics Postdoctoral Fellow.

 http://pos.sissa.it/

PoS(Bash11)006

1. Introduction: The Interstellar Medium Out of Balance

Most students of astronomy will encounter a course on the physics of the interstellar medium (ISM; the gas and dust occupying the space between the stars) at some point in their undergraduate or post-graduate studies. Hence the concept that the ISM exists in several distinct "phases," in rough pressure equilibrium with each other, may be familiar to most readers. Physical quantities characterizing the major phases of ISM gas in the Milky Way are summarized in Table 1, compiled from the textbooks by Tielens [1] and Draine [2]. The coexistence of gas at such dramatically different densities, temperatures, and ionization fractions in the same galaxy is explained by the different filling factors of each phase. While the precise values for the filling factors remain poorly-measured and controversial, the basic picture that the colder, denser phases of the ISM exists as smaller clouds within the more diffuse, warm/hot phases, is well established. H II regions, localized regions of photo-ionized gas produced by hot, massive, OB-type stars, occupy a negligible fraction of the ISM volume, hence perhaps H II regions ought not to be regarded as a proper ISM phase at all. However, massive stars form in the densest regions of cold, molecular clouds, and as their far-ultraviolet (UV) radiation first photo-dissociates molecules and then photo-ionizes atoms, the multi-phase physics of the ISM can be studied within a single, small volume.

Phase	Density (cm^{-3})	T (K)	Total Mass (10^9 $M_\odot$)	Scaleheight (pc)	Filling factor
Hot ionized medium	$\sim$0.004	$\sim 10^6$	—	3000	$\sim$0.5
Warm neutral medium	0.5–0.6	8000	2.8	$\sim$300	$\sim$0.4
Warm ionized medium	0.1–0.3	$\sim$5000	1.0	900	$\sim$0.1
Cold neutral medium	30–50	80–100	2.2	100	$\sim$0.01
Molecular Clouds	10^2–10^6	10–50	1.3	75	$\sim 10^{-4}$
H II Regions	1–10^4	10^4	0.05	70	—

Table 1: Phases of ISM Gas in the Milky Way

In one of the immortalized insights of early modern astrophysics, Strömgren [3] realized that the mean free path in neutral hydrogen of UV photons beyond the Lyman limit ($\lambda < 912$ Å) is negligibly small compared to the size of the ionized hydrogen region produced by a hot star. H II regions therefore have sharp boundaries, or I-fronts, where the recombination rate balances the ionization rate. For a single star in an ambient medium of constant density, this boundary is defined as the Strömgren radius,

$$R_{S0} = \left(\frac{3Q_0}{4\pi n_H^2 a_B} \right)^{1/3}, \tag{1.1}$$

where Q_0 is the ionizing photon rate (which depends on the star or stars responsible for the H II region), n_H is the hydrogen gas density, and a_B is the Case B recombination coefficient [4]. Generally speaking, main-sequence or giant stars earlier than B3 emit sufficient Q_0 to produce observable Galactic H II regions.

Because the ionizing stars provide an internal source of radiative and mechanical luminosity, H II regions rapidly become overpressured compared to the ambient ISM and expand. If the dominant source of pressure is collisional heating of gas by free electrons, then the time-evolution of the expansion follows the simple analytic relation from Lyman Spitzer's classic ISM text [4]:

$$R_S(t) = \left(1 + \frac{7}{4}\frac{c_{s2}t}{R_{S0}}\right)^{4/7}, \tag{1.2}$$

where $c_{s2} \sim 10$ km s^{-1} is the sound speed in the ionized gas. The expansion velocity obtained by differentiating this relation can exceed the (significantly lower) sound speed in the ambient medium, hence expanding I-fronts often become shock waves. If the ambient medium is molecular, UV photons emerging from the H II region destroy the molecules, creating a photodissociation region (PDR) around the H II region.

Early O stars and OB giants drive powerful winds that fundamentally alter the structure of more luminous H II regions. Castor et al. [5] and Weaver et al. [6] provided analytical models for wind-blown bubbles produced by isolated, hot stars, and numerous authors have subsequently refined these models using a variety of semi-analytical and numerical techniques [7 – 11]. The basic, "onion-layer" structure of a wind-blown bubble is illustrated in Figure 1. The highly supersonic (1000–2000 km s^{-1}) stellar wind flows freely outward for a short distance R_W from the star before it is shocked, producing a bubble of very hot, ionized gas. The "classical" H II region collapses into a photoionized shell of gas, (imperfectly) separated from the hot gas zone by a contact discontinuity at R_C. The I-front at R_{IF} still represents the outer boundary of the H II region.

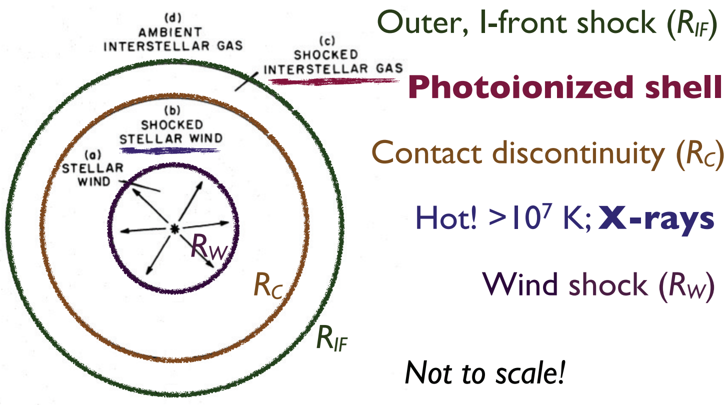

Figure 1: Anatomy of a wind-blown bubble, adapted from Weaver et al. [6]

Many complications separate the ideal models of Strömgren spheres and wind-blown bubbles from reality. The ISM is clumpy, hence the ambient medium surrounding an H II region is never uniform. Massive stars tend to form in clusters, hence multiple stars often contribute to the ionization of a single H II region. The ambient ISM is generally in motion with respect to the ionizing star(s), and stellar winds need not be spherically symmetric. Dust mixed with gas in H II regions enables dramatic, radiative cooling [12], and magnetic fields threading through the clouds contribute anisotropic pressure support [13]. Turbulence provides additional pressure and facilitates mixing at the interfaces between gas layers. Early models neglected completely the contribution of radiation pressure [14, 15].

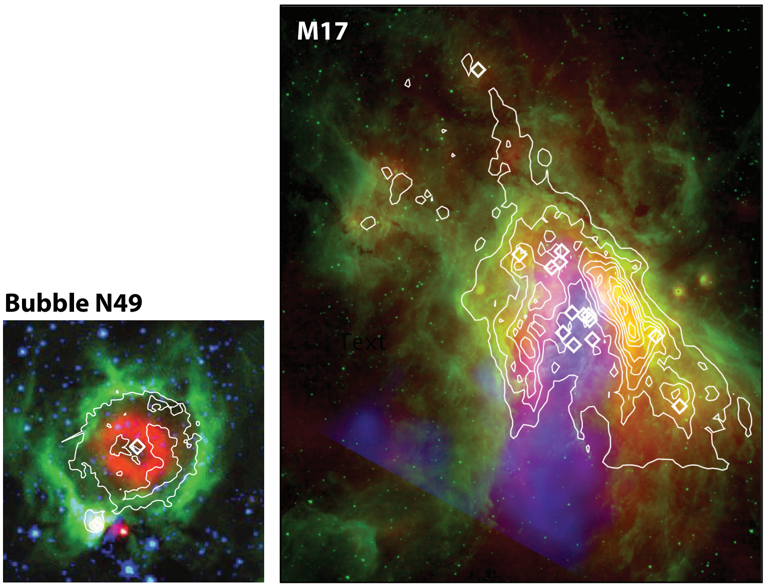

Figure 2: Multiwavelength images of the wind-blown bubble N49 [17] and the giant H II region M17 [18], displayed at approximately the same physical scale. N49 image: red = *Spitzer*/MIPS 24 μm, green/blue = *Spitzer*/IRAC 8.0/4.5 μm. M17 image: red = *MSX* 21.3 μm, green = IRAC 5.8 μm, blue = *Chandra* soft (0.5–2 keV), diffuse X-rays. In both images, diamonds denote known O and early B stars and contours show 20 cm thermal radio continuum.

2. Multiwavelength Observations of H II Regions

In spite of the messy complexity governing the structure of real H II regions, the basic structures predicted by the wind-blown bubble models are identifiable in modern, multiwavelength images. In Figure 2, a prototypical wind-blown bubble ionized by a single O6.5 V star ($Q_0 = 8.5 \times 10^{48}$ s^{-1}) [16, 17] is compared to the giant H II region M17, ionized by a dozen O stars, including several O4 V stars ($Q_0 = 3 \times 10^{50}$ s^{-1}) [18]. In N49, the I-front at R_{IF} is defined by the sharp inner rim of 8.0 μm (green) polycyclic aromatic hydrocarbon (PAH) emission from the PDR, neatly encapsulating the photoionized gas shell (contours). Dust mixed with the photoionized gas and heated by radiation from the central star forms a torus of 24 μm emission. Everett & Churchwell [12] found that the lifetime of dust grains within the harsh environment of this H II region is extremely short, and suggested that dust must be continuously replenished from evaporating dense clumps to produce the observed 24 μm emission. Draine [15] demonstrated that radiation pressure can produce evacuated cavities in the centers of H II regions, but noted that the central hole in N49 is too large to be explained by radiation pressure alone and suggested that the stellar wind also contributes. An interface analogous to the contact discontinuity R_C in Figure 1 is likely located within the radio shell/24 μm torus in N49, hence $R_C/R_{IF} < 1/2$.

Unlike N49, M17 is far from round, yet similar morphological features can be discerned, with one important addition (Figure 2). A spectacular plume of hot, X-ray-emitting plasma (blue) occupies the central cavity of M17 [19]. This X-ray emission provides *direct* evidence for stellar wind shocks. At an absorption-corrected X-ray luminosity $L_X = 7 \times 10^{34}$ erg s^{-1}, this plasma is unusually bright in comparison to other H II regions, but *it is fainter than the predictions of wind-blown-bubble theory by more than an order of magnitude* [20]. This discrepancy may be explained by collisional interactions with dust grains providing a mechanism for cooling the hot plasma, and/or depressurization of the wind-blown bubble where the plasma is not completely confined by the nebula. Either interpretation implies that the contact discontinuity in Figure 1 does not effectively separate the photoionzed gas/dusty shell from the hot gas bubble in M17. Again assuming R_C falls at the inner edge of the photoionized shell and heated dust emission, $R_C/R_{IF} \approx 1/2$ in M17. The inner cavity in M17 is clearly larger (both in absolute volume and as a fraction of the H II region volume) in comparison to that of N49. The photoionized shell in M17 is supported by a combination of radiation pressure and hot gas pressure [13].

Although N49 and M17 are representative of a range of Galactic H II regions where stellar winds play an important role, on the Galactic scale feedback is dominated by the most luminous, starburst regions. In Figure 3, a Galactic starburst region, W43, is compared to 30 Doradus in the Large Magellanic Cloud (LMC), the most luminous H II region in the Local Group ($Q_0 = 4.2 \times 10^{51}$ s^{-1}; [21]). Mid-infrared (IR) images of the starburst H II regions reveal layered bubble morphologies that are remarkably similar between the two regions. The large bubble lobes shown in each panel of Figure 3 are part of larger H II region complexes, with the ionizing clusters partially (in 30 Dor) or completely (W43) obscured by dense, foreground filaments of bright, mid-IR emission. In the 30 Dor image, the PDRs appear pink and the photo-ionized shells green, while the W43 image matches the color-code of Figure 2, in which the PDRs appear yellow-green and dust mixed within photoionized shell appears red. Here it is most appropriate to describe the photoionized gas struc-

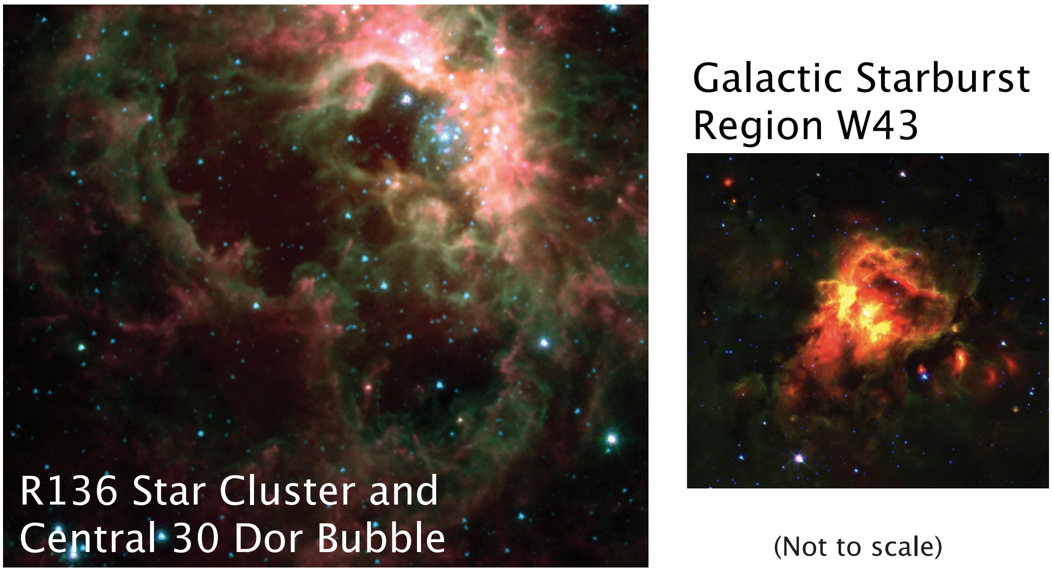

Figure 3: *Spitzer* mid-IR images of two starburst H II regions. Left: Image of 30 Dor in the Large Magellanic Cloud, red = 8.0 μm, green = 4.5 μm, blue = 3.6 μm. Right: Image of W43, red = 24 μm, green = 8.0 μm, blue = 4.5 μm.

tures as shells, occupying thin layers just interior to the PDRs, with $R_C \approx R_{IF}$. Indeed, the bubbles in 30 Dor are known to be filled with hot, X-ray-emitting plasma [22], and similar plasma would likely be found in W43 if comparable *Chandra X-ray Observatory* observations were obtained.

Comparing Figures 2 and 3, a trend becomes apparent: as the luminosity of the ionizing cluster increases, so does R_C/R_{IF}, the size of the central cavity relative to the overall size of the H II region. We may extend this trend down to low-luminosity H II regions ionized by late O or early B stars, for which the central cavity disappears entirely ($R_C = 0$). It will be useful to bear this trend in mind when considering the controversial issue of precisely which feedback mechanism, hot gas pressure or direct radiation pressure, dominates H II region structure at the high-luminosity extreme.

3. A Rumble in the Tarantula: What is the Dominant Feedback Mechanism in 30 Doradus?

Thanks to its status as the most luminous H II region in the Local Group and its location in the low-metallicity environment of the LMC, 30 Dor (popularly known as the Tarantula Nebula) has long received intense observational scrutiny. At $d = 50$ kpc, 30 Dor is the best nearby laboratory for studying the physical conditions that prevailed in the unresolvable, high-redshift star-forming regions that dominated the major cosmological epoch of galaxy-building [21]. Recently, Lopez et al. [23, hereafter L11] and Pellegrini et al. [21, hereafter P11] carried out independent, parallel studies of the feedback processes shaping 30 Dor. Using fundamentally different approaches to interpreting multiwavelength datasets, these authors reached diametrically opposed conclusions; L11 reported that direct stellar radiation pressure dominates the interior of the H II region, while P11 argued that the pressure of the hot, X-ray-emitting plasma shapes the large-scale structure and dynamics. This disagreement is rooted in the different definitions of radiation pressure and the different assumed nebular geometries used in the two studies.

L11 used the simplest definition of direct radiation pressure,

$$P_{\rm dir} = \sum \frac{L_{\rm bol}}{4\pi r^2 c} \tag{3.1}$$

(their equation 1), where $L_{\rm bol}$ is the bolometric luminosity of each star and r is the distance traveled by the starlight to reach a given point in the nebula, deprojected assuming a spherical geometry. $P_{\rm dir}$ declines sharply with distance from the central star cluster, R136 (note that this expression diverges for $r = 0$).

By contrast, P11 constructed a non-symmetric, cavity model (based on the central region of 30 Dor shown in Figure 3) for the nebular geometry and used photoionization models to calculate the density of H atoms n_H and hence the ionization parameter U at each position,

$$U = \frac{Q_0}{4\pi r^2 c n_H}. \tag{3.2}$$

The divergent behavior of this expression is avoided by implementing the cavity model, in which the ionized gas is confined to shell structures near the I-fronts, and U is not calculated for the cavity interiors, where $r^2 n_H \to 0$. P11 then approximated the pressure exerted on the observed ionized gas by starlight in terms of the ionization parameter as

$$P_{\rm stars} = U n_H \langle h\nu \rangle \frac{L_{\rm bol}}{L_0}, \tag{3.3}$$

where $L_{\rm bol}$ and L_0 are the total bolometric and ionizing photon luminosity for *all* stars (assumed to be centered at R136) and $\langle h\nu \rangle \sim 20$ eV is average energy per ionizing photon (their equation 8).

Although Equations 3.3 and 3.2 can be combined and trivially reduced to Equation 3.1, doing so hides the ambiguous role of radiation pressure in regions where n_H vanishes. $P_{\rm stars}$ as definited by P11 represents the momentum imparted to the observed nebular gas. L11 acknowledge this alternative definition of radiation pressure, but claim that "it is necessary to characterize $P_{\rm dir}$ as the energy density of the radiation field, since that definition reflects the total energy and momentum budget available to drive motion." This definition implies that the luminosity emitted by the OB stars could impart momentum with 100% efficiency everywhere in the nebula at once, an ideal case that could never occur in a real H II region. The justification brings to mind the old philosophical thought experiment about whether a tree falling in a forest makes a sound if there is no one around to hear it. If one dropped a cloud of dense, neutral gas close to the R136 star cluster, it would experience an enormous radiation pressure. But there are no dense clouds of neutral gas within the radiation-pressure-dominated region identified by L11. Instead, the interior structure of 30 Dor consists of evacuated cavities filled with hot, highly ionized plasma [22], and pressure from either the hot, X-ray plasma or the warm, photoionized gas can exceed the radiation pressure on the cavity walls (L11, P11). Radiation pressure could have dominated the expansion of these large cavities in the past, when they were smaller (P11). It is difficult to answer this question definitively because the hot gas pressure in 30 Dor remains uncertain.

Both L11 and P11 reported values for the hot gas pressure in 30 Dor. The pressure of the X-ray-emitting plasma can be calculated as

$$P_X = 1.9 n_X k T_X, \tag{3.4}$$

where n_X and T_X are the density and temperature of the X-ray-emitting plasma. P11 used the results of spectral fits by Townsley et al. [22] while L11 performed their own spectral fitting to the same archival data plus a newer, 90-ks *Chandra* observation of 30 Dor [24]. It is difficult to derive n_X accurately from the emission measure returned by spectral fitting because it depends strongly on the assumed geometry of the X-ray bubbles. L11 treated 30 Dor as a "beach ball" with a global, spherical geometry, which effectively minimizes n_X. P11 treated 30 Dor as a "bunch of grapes," assuming a spherical geometry for each smaller, diffuse X-ray region identified by Townsley et al. [22], which yields higher n_X. Spectral modeling of diffuse emission structures in regions like 30 Dor is a tremendously complicated task [20], as any given sightline will contain plasma from multiple origins, including both stellar wind shocks and supernova, at a variety of temperatures, densities, and compositions. To illustrate the pitfalls of over-interpreting these data, I note that different approaches to the spectral fitting of the the global, diffuse X-ray emission of 30 Dor yield significantly different results. L11 fit a single-temperature plasma model and reported $kT_X = 0.64^{+0.03}_{-0.02}$ keV and absorption-corrected $L_X = 4.5 \times 10^{36}$ erg s^{-1}. In contrast, the most recent spectral fits by L. K. Townsley (private communication) employ 3 plasma components (plus numerous gaussian profiles to fit unidentified emission lines) ranging from 0.3–0.8 keV and yield $L_X = 1.2$–1.9×10^{37} erg s^{-1}. It is particularly difficult to discern whether regions of 30 Dor that appear X-ray dark represent the boundaries of confined, hot plasma bubbles, or whether the plasma extends behind foreground material that absorbs the soft X-rays. The existing 114 ks combined *Chandra* integration represents a very shallow observation at the distance of 30 Dor when compared to observations of Galactic H II regions.

The story of 30 Dor has a moral; given the complexity and ambiguity involved in interpreting the multiwavelength data on this *resolved* starburst region, investigators wishing to extend these results to draw conclusions about feedback mechanisms shaping *unresolved* regions at cosmological distances do so at their own risk.

4. The Milky Way Project H II Region Catalog

Strong empirical constraints on the time-evolution of feedback-driven H II regions require the comparative study of large observational samples of H II regions. The wealth of new IR imaging data provided by the *Spitzer* Galactic Legacy Infrared Mid-Plane Extraordinaire (GLIMPSE) [25] and subsequent high-resolution surveys of the Milky Way allow us to penetrate the obscuring veil of dust in the Galactic plane, revealing the structure of H II regions and PDRs in unprecedented detail. Using the GLIMPSE images, Churchwell et al. [16, 26] cataloged nearly 600 IR bubbles, ring and arc-shaped structures apparent in 8 μm PAH emission. The majority of these structures are PDRs surrounding H II regions, from energetic, wind-blown bubbles to low-luminosity nebulae surrounding B-type stars.

Over the past year, $>35,000$ internet users from around the world have been searching for bubbles in *Spitzer* survey images of the Galactic plane as part of the Milky Way Project (MWP; http://www.milkywayproject.org), a recent installment in the Zooniverse, the premier series of online "citizen science" projects (http://www.zooniverze.org). Upon creating a Zooniverse account and logging into milkywayproject.org, MWP volunteers are presented with a random image and instructed to identify and fit structures within that image that resemble bubble rims (PDRs resembling the regions in Figure 2) with elliptical annuli (or mark the locations of bubbles that are barely resolved with boxes). By carefully combining the results from many individuals for each part of the sky, the MWP simultaneously leverages the superior pattern-recognition skills of the human eye-brain system and takes advantage of the "wisdom of crowds." The MWP First Data Release presents a catalog of 5,106 H II regions, representing an order of magnitude improvement in completeness compared to previous catalogs [27].

The MWP bubbles catalog will facilitate the study of triggered star formation on the Galactic scale. The idea that feedback from expanding H II regions can exert external pressure on cold, molecular cloud cores, resulting in self-propagating, sequential massive star formation has been around for decades [28 – 31] but recently has seen a resurgence of observational and theoretical interest, motivated in large part by the identification of numerous instances of small bubbles, young stellar objects, masers, and other observational signposts of recent or ongoing star formation near the rims of GLIMPSE bubbles (N49 in Figure 2 provides an example, with two luminous young stellar objects and an ultracompact H II region visible on the lower rim of the bubble [17]). To date, most studies of triggered star formation have focused on individual, "best-case" regions, very round bubbles with prominent sub-clusters or smaller bubbles on their rims [32 – 34]. In spite of the long-standing, widely popular idea that supernovae trigger star formation, far fewer candidate triggering sites have been identified near supernova remnants than near H II regions.

To establish that triggering merits investigation as an *important* mode of star formation as opposed to an astrophysical curiosity, the prevalence of triggering sites must be established statistically, and in an unbiased fashion, among representative samples of H II regions. Both the GLIMPSE and MWP bubbles catalogs include flags for hierarchical structure, identifying smaller bubbles that could be the "daughters" of larger, "parent" bubbles. Among the MWP bubbles, 29% are members of hierarchies [27]. Triggered star formation need not produce observable daughter bubbles if the second generation of stars is too young to have produced H II regions. Thompson et al. [35] recently found a strong correlation between young stellar objects identified as luminous mid-IR point sources and the rims of bubbles from the Churchwell et al. [16] catalog. Corroboration of this correlation using the more complete sample of bubbles from the MWP would greatly strengthen the case that triggering is a prevalent mode of Galactic star formation.

5. Summary

In this review, I have given a brief update on recent, multiwavelength observations, particularly in the mid-IR and X-rays, that have revealed wind-blown and radiation-dominated H II region structures. Observations corroborate the basic predictions of H II region theory but reveal important differences, too. Theory still struggles to explain both the existence of dust within energetic H II regions and its effects on H II region structure. X-rays from hot, wind-shocked plasma are frequently observed to fill large, central cavities in giant H II regions, but the X-ray luminosity is more than an order of magnitude lower than predicted by wind-blown bubble theory.

The size of the central cavities as a fraction of H II region volume appears to increase with increasing ionizing luminosity (Figures 2 and 3). This trend puts dust at larger distances from the ionizing stars in starburst regions, which reduces the effective temperature of the dust compared to static or thermal pressure-dominated H II region models. Single-band IR diagnostics of extragalactic star formation rates (e.g. [36]) have become increasingly popular in the era of large, high-resolution surveys from *Spitzer* and *Herschel*. Because the effective dust temperature sets the shape of the IR spectral energy distribution in unresolved regions, feedback must be taken into account when calibrating the IR diagnostics.

Feedback in large, starburst regions like 30 Dor presents a particularly complicated problem. It would be premature to assume that a single source of feedback, radiation pressure (L11), dominates such regions until we achieve a better understanding of the contributions from massive star winds and supernovae.

H II regions are among the most beautiful objects appearing in astronomical images. The strong aesthetic appeal of these images helped to motivate MWP volunteers, the vast majority of whom were not professional scientists, to spend tens of thousands of person-hours finding and measuring several thousand H II regions in the form of IR bubbles. The large MWP database [27] provides an unmatched resource for statistical studies of H II region evolution and star formation triggered by massive star feedback. I expect that the MWP will spawn many follow-up investigations in the coming years, involving both professional researchers and citizen scientists.

Acknowledgments

I thank the organizers of the Frank N. Bash Symposium 2011 for their invitation to speak and to contribute to these proceedings. L. K. Townsley and E. W. Pellegrini provided helpful conversations and insights that greatly improved this contribution. I gratefully acknowledge support from a National Science Foundation Astronomy & Astrophysics Postdoctoral Fellowship under award AST-0901646.

References

[1] Tielens, A. G. G. M., *The Physics and Chemistry of the Interstellar Medium*, Cambridge University Press, 2005

[2] Draine, B. T., *Physics of the Interstellar and Intergalactic Medium*, Princeton University Press, 2011

[3] Strömgren, B., *The Physical State of Interstellar Hydrogen.*, 1939, *ApJ*, 89, 526

[4] Spitzer, L., *Physical processes in the interstellar medium*, Wiley-Interscience, New York, 1978

[5] Castor, J., R. McCray, & R. Weaver, *Interstellar bubbles*, 1975, *ApJ*, 200, L107

[6] Weaver, R., et al., *Interstellar bubbles. II - Structure and evolution*, 1977, *ApJ*, 218, 377

[7] McKee, C. F., D. van Buren, & B. Lazareff, *Photoionized stellar wind bubbles in a cloudy medium*, 1984, *ApJ*, 278, L115

[8] Koo, B.-C. & C. F. McKee, *Dynamics of wind bubbles and superbubbles. I - Slow winds and fast winds. II - Analytic theory*, 1992, *ApJ*, 388, 93

[9] Capriotti, E. R. & J. F. Kozminski, *Relative Effects of Ionizing Radiation and Winds from O-Type Stars on the Structure and Dynamics of H II Regions*, 2001, *PASP*, 113, 677

[10] Freyer, T., G. Hensler, & H. W. Yorke, *Massive Stars and the Energy Balance of the Interstellar Medium. I. The Impact of an Isolated 60* $M_\odot$ *Star*, 2003, *ApJ*, 594, 888

[11] Harper-Clark, E. & N. Murray, *One-Dimensional Dynamical Models of the Carina Nebula Bubble*, 2009, *ApJ*, 693, 1696

[12] Everett, J. E. & E. Churchwell, *Dusty Wind-blown Bubbles*, 2010, *ApJ*, 713, 592

[13] Pellegrini, E. W., et al., *A Magnetically Supported Photodissociation Region in M17*, 2007, *ApJ*, 658, 1119

[14] Krumholz, M. R. & C. D. Matzner, *The Dynamics of Radiation-pressure-dominated H II Regions*, 2009, *ApJ*, 703, 1352

[15] Draine, B. T., *On Radiation Pressure in Static, Dusty H II Regions*, 2011, *ApJ*, 732, 100

[16] Churchwell, E., et al., *The Bubbling Galactic Disk*, 2006, *ApJ*, 649, 759

[17] Watson, C., et al., *Infrared Dust Bubbles: Probing the Detailed Structure and Young Massive Stellar Populations of Galactic H II Regions*, 2008, *ApJ*, 681, 1341

[18] Povich, M. S., et al., *A Multiwavelength Study of M17: The Spectral Energy Distribution and PAH Emission Morphology of a Massive Star Formation Region*, 2007, *ApJ*, 660, 346

[19] Townsley, L. K., et al., *10 MK Gas in M17 and the Rosette Nebula: X-Ray Flows in Galactic H II Regions*, 2003, *ApJ*, 593, 874

[20] Townsley, L. K., et al., *The Integrated Diffuse X-ray Emission of the Carina Nebula Compared to Other Massive Star-forming Regions*, 2011, *ApJS*, 194, 16

[21] Pellegrini, E. W., J. A. Baldwin, & G. J. Ferland, *Structure and Feedback in 30 Doradus. II. Structure and Chemical Abundances*, 2011, *ApJ*, 738, 34

[22] Townsley, L. K., et al., *A Chandra ACIS Study of 30 Doradus. I. Superbubbles and Supernova Remnants*, 2006, *AJ*, 131, 2140

[23] Lopez, L. A., et al., *What Drives the Expansion of Giant H II Regions?: A Study of Stellar Feedback in 30 Doradus*, 2011, *ApJ*, 731, 91

[24] Townsley, L. K., *Diffuse X-ray Structures in Massive Star-forming Regions*, 2009, *AIPC*, 1156, 225

[25] Churchwell, E., et al., *The Spitzer/GLIMPSE Surveys: A New View of the Milky Way*, 2009, *PASP*, 121, 213

[26] Churchwell, E., et al., *The Bubbling Galactic Disk. II. The Inner* 20°, 2007, *ApJ*, 670, 428

[27] Simpson, R. J., et al., *The Milky Way Project First Data Release: A Bubblier Galactic Disk*, 2012, *MNRAS*, in press [arXiv:1201.6357]

[28] Elmegreen, B. G. & C. J. Lada, *Sequential formation of subgroups in OB associations*, 1977, *ApJ*, 214, 725

[29] Sandford, M. T., II, R. W. Whitaker, & R. I. Klein, *Radiation-driven implosions in molecular clouds*, 1982, *ApJ*, 260, 183

[30] Bertoldi, F., *The photoevaporation of interstellar clouds. I - Radiation-driven implosion*, 1989, *ApJ*, 346, 735

[31] Whitworth, A. P., et al., *The Preferential Formation of High-Mass Stars in Shocked Interstellar Gas Layers*, 1994, *MNRAS*, 268, 291

[32] Deharveng, L., A. Zavagno, & J. Caplan, *Triggered massive-star formation on the borders of Galactic H II regions. I. A search for "collect and collapse" candidates*, 2005, *A&A*, 433, 565

[33] Zavagno, A., et al., *Triggered massive-star formation on the borders of Galactic H II regions. II. Evidence for the collect and collapse process around RCW 79*, 2006, *A&A*, 446, 171

[34] Zavagno, A., et al., *Star formation triggered by the Galactic H II region RCW 120. First results from the Herschel Space Observatory*, 2010, *A&A*, 518, L81

[35] Thompson, M. A., et al., *The statistics of triggered star formation: an overdensity of massive YSOs around Spitzer bubbles*, 2011, *MNRAS*, in press [arXiv:1111.0972]

[36] Calzetti, D., et al., *The Calibration of Mid-Infrared Star Formation Rate Indicators*, 2007, *ApJ*, 666, 870

PoS(Bash11)006

PROCEEDINGS OF SCIENCE

Black-Hole Mergers

Michael Kesden*
Center for Cosmology and Particle Physics, New York University
4 Washington Pl., New York, NY 10003, USA
E-mail: mhk10@nyu.edu

Observations of black-hole mergers will provide unique insights into both general relativity and cosmology. The gravitational waves produced in such mergers directly probe strong-field solutions to Einstein's equations, and the rate at which mergers occur constrains the hierarchical formation of supermassive black holes and their host galaxies. The three primary theoretical tools for studying merging black holes are post-Newtonian expansions, black-hole perturbation theory, and numerical relativity. I will briefly explain how these tools complement each other in developing a general solution to the problem of black-hole mergers, highlighting some of my own research in each of these three areas.

Frank N. Bash Symposium New Horizons In Astronomy,
October 9-11, 2011
Austin Texas

*Speaker.

PoS(Bash11)007

1. Black holes

In 1915, Albert Einstein presented his famous field equation of general relativity

$$G_{\mu\nu} = 8\pi G T_{\mu\nu} \tag{1.1}$$

which relates the curvature of spacetime (described by the Einstein tensor $G_{\mu\nu}$) to the energy content of the universe (given by the stress-energy tensor $T_{\mu\nu}$). Roy Kerr discovered the unique *stationary, axisymmetric, vacuum* solution to this equation

$$ds^2 = -\left(1 - \frac{2Mr}{\Sigma}\right)dt^2 - \frac{4Mar\sin^2\theta}{\Sigma}dtd\phi + \frac{\Sigma}{\Delta}dr^2 + \Sigma d\theta^2 + \left(r^2 + a^2 + \frac{2Ma^2r\sin^2\theta}{\Sigma}\right)\sin^2\theta d\phi^2 \tag{1.2}$$

where $\Sigma \equiv r^2 + a^2\cos^2\theta$ and $\Delta \equiv r^2 - 2Mr + a^2$ [1]. Classical black holes described by this Kerr metric are the simplest objects in the universe, fully described by their mass M and spin angular momentum $J = aM$ in relativist's units where $G = c = 1$.

Several of the distinguishing features of black holes are their event horizons, ergospheres, and innermost stable circular orbits [2]. The *event horizon* is the boundary of the region of spacetime that is causally disconnected from future null infinity. Even light rays cannot escape from inside the event horizon, hence the term "black holes." Spinning black holes have an *ergosphere* exterior to their event horizons within which all stationary observers must orbit the black hole with positive angular velocity. Negative-energy orbits also exist within the ergosphere, allowing rotational energy to be extracted from the black hole [3]. Black holes, unlike Newtonian point masses, also have *innermost stable circular orbits* (ISCOs). Massive particles inspiraling into black holes through gravitational radiation or viscous dissipation will plunge into the event horizons after reaching the ISCO.

Astrophysical black holes are formed in two distinct channels. *Stellar-mass* black holes are formed in the gravitational collapse of stars whose cores are too massive to be supported by electron or neutron degeneracy pressure. Oppenheimer and Snyder [4] performed the first calculation of this collapse into a black hole. Stellar-mass black holes can be observed if they accrete from a stellar binary companion. The accreted material can be heated to temperatures high enough to emit copious X-rays; the nearby black-hole candidate Cygnus X-1 was discovered in a rocket-borne X-ray survey in 1964 [5]. The second kind of astrophysical black hole is the *supermassive* black holes (SBHs) that reside in the centers of most large galaxies. The Doppler broadened emission lines associated with active galactic nuclei (AGN) were discovered by Carl Seyfert in 1943 [6]. Twenty years later, theorists proposed that these AGN were powered by accretion onto compact objects of masses $10^5 - 10^8 M_\odot$ [7]. Such massive objects cannot support themselves against gravitational collapse into SBHs [8]. SBHs grow by accreting gas and merging with each other during the galaxy mergers through which large galaxies are assembled. We consider black-hole mergers in greater detail in the next section.

2. Black-hole mergers

As we learned in the last section, isolated black holes are simple objects that are fully described by their mass and spin. Widely separated binary black holes are similarly simple; they are

PoS(Bash11)007

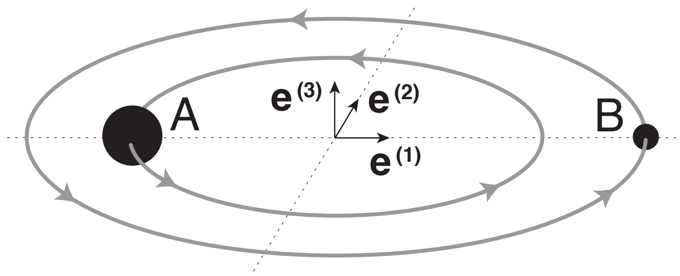

Figure 1: Binary black holes A and B on a quasi-circular orbit about their common center of mass. We define an orthonormal coordinate system such that at an initial time $\mathbf{e}^{(1)}$ points along the separation vector between the two holes, $\mathbf{e}^{(3)}$ points along the orbital angular momentum, and $\mathbf{e}^{(2)}$ completes the triad.

described by the mass and spin of the two black holes along with the orbital parameters of the binary. Any system with a time-varying mass-quadrupole moment, such as binary black holes, emits gravitational radiation that extracts energy and angular momentum from the system. This radiation circularizes the orbits of widely separated black holes [9], so for many purposes it is sufficient to restrict our attention to black holes on initially circular orbits. The reference frame we will use to describe the quasi-circular binary system is illustrated in Fig. 1. The Kerr metric given by Eq. (1.2) is scale-invariant when r and a are expressed in units of M, indicating that calculations involving the binary system can be rescaled to any desired value of the total mass. A general black-hole binary can therefore be described by 7 parameters: the binary mass ratio $q \equiv M_b/M_a \leq 1$ and the 3 components of the dimensionless spins $\mathbf{a}$ and $\mathbf{b}$ of black holes A and B.

Given this initial state, the black-hole merger proceeds in three stages. In the first stage, known as the *adiabatic inspiral*, the binary emits gravitational radiation that extracts energy and angular momentum from the orbit. The timescale $t_{\rm GW} \equiv E_{\rm orb}/\dot{E}_{\rm GW}$ for this orbital decay is much longer than the orbital time $t_{\rm orb} \simeq \Omega^{-1}$, so the binary evolves through a sequence of quasi-circular orbits of decreasing separation and increasing orbital frequency Ω. In the second stage, the *merger* itself, the individual event horizons of the binary black holes coalesce into a single perturbed horizon of the final black hole. In the final stage of the merger, the *ringdown*, the perturbed final black hole emits additional gravitational radiation until it settles down into an unperturbed Kerr black hole. This final black hole is fully characterized by its mass M_f, dimensionless spin $\mathbf{s}$, and recoil velocity $\mathbf{k}$ with respect to the center of mass of the initial binary.

We learned in the previous section that astrophysical black holes can be divided into stellar-mass black holes ($m \simeq 10M_\odot$) formed in the gravitational collapse of massive stars, and supermassive black holes ($10^6 M_\odot \lesssim m \lesssim 10^{10} M_\odot$) in galactic centers. This bimodality in the astrophysical black-hole population motivates us to distinguish between *comparable-mass* mergers for which $q \simeq 1$ and *extreme-mass-ratio inspirals* (EMRIs) for which $q \ll 1$. Comparable-mass mergers occur when both members of the binary are either stellar-mass black holes or supermassive black holes. These two different regimes of comparable-mass mergers can be analyzed with the same theoretical tools because of the scale-invariance of general relativity noted earlier. EMRIs occur when a supermassive black hole merges with a much smaller stellar-mass black hole. Different theoretical techniques must be used to study black-hole mergers in the limit $q \ll 1$ as will be discussed

PoS(Bash11)007

in later sections.

Although general-relativity calculations are independent of the total binary mass, this scale greatly affects our ability to observe the mergers themselves. Current constraints on black-hole mergers and the rates at which they occur are inferred from observations of how the black-hole population evolves with time. We have never actually observed binary stellar-mass black holes, so our predictions about their merger rates are entirely theoretical. These predictions are plagued by uncertainties about how many main-sequence stars collapse into black holes, how these stars evolve in binaries, and how many new binaries can form in dense stellar environments. Predicted rates for stellar-mass black-hole mergers vary from 10^{-4} to 0.3 Mpc^{-3} Myr^{-1} [10]. The rate at which supermassive black holes merge is also uncertain. SBH masses are tightly correlated with the luminosity [11], mass [12], and velocity dispersion [13] of the spheroidal component of their host galaxies. If we assume that SBHs merge promptly following the mergers of their host galaxies, we can use observational and theoretical predictions of galaxy-merger rates to infer SBH merger rates. Unfortunately, this assumption may not be valid as neither dynamical friction nor gravitational radiation can cause SBHs separated by ~ 1 pc to merge within a Hubble time (the so-called "final parsec problem") [14]. Though there are several proposed solutions to the final parsec problem, the effectiveness of these solutions in a cosmological context has not been established. EMRI rates are also uncertain for several reasons. Mass segregation should cause stellar-mass black holes, heavier than average stars, to settle to the center of nuclear star clusters where they are susceptible to being scattered into "loss-cone" orbits on which they can merge with SBHs. Unfortunately, the time scale for this mass segregation depends sensitively on stellar densities at the center of nuclear star clusters. Recent observations suggest that the nuclear star cluster of our own Galaxy has a core with radius $r_0 \simeq 0.5$ pc [15], and that this core may inhibit the diffusion of $10M_\odot$ black holes onto loss-cone orbits [16]. Previously unappreciated relativistic dynamics may also reduce predicted EMRI rates by factors of $\sim 10-100$ below previous predictions [17].

The cleanest probe of black-hole mergers is the gravitational waves (GWs) produced during the inspiral, merger, and ringdown described above. GWs with frequencies 10 Hz $\lesssim f \lesssim 10^4$Hz can be observed by the network of GW detectors operated by the Laser Interferometer Gravitational-wave Observatory (LIGO) [18] and the European Gravitational Observatory [19]. These frequencies correspond to the merger/ringdown stage of the merger of $\sim 200M_\odot$ black holes, or the inspiral stage of smaller comparable-mass ratio mergers. When Advanced LIGO achieves design sensitivity in ~ 2016, it should be able to detect GWs from the inspiral of $1.4M_\odot$ neutron stars out to distances of ~ 300 Mpc. The proposed Laser Interferometer Space Antenna (LISA) [20] would have observed GWs with frequencies 10^{-4}Hz $\lesssim f \lesssim 10^{-1}$Hz with enough sensitivity to detect the mergers of SBHs with $10^5 M_\odot \lesssim M \lesssim 10^7 M_\odot$ throughout the observable universe. LISA would also have seen thousands of EMRIs out to redshift $z \sim 1$. Although budgetary constraints have forced NASA and ESA to end the LISA collaboration, ESA is considering a European-only New Gravitational-wave Observatory (NGO) [21] as an L-class mission. NGO will have reduced S/N ratios compared to earlier LISA proposals, but should still be able to achieve many of LISA's core science goals. In the time domain, the expected GW strain from black-hole mergers is far below the design sensitivity of LIGO and NGO. GW sources can only be detected by convolving a predetermined template with the observed signal over many GW periods. Different theoretical methods are required to calculate these GW templates for the inspiral, merger, and ringdown stages in the comparable-mass and EMRI limits. These methods will be the subject of the next section.

3. Strategic triad of general relativity

The three legs of the U. S. nuclear triad are long-range strategic bombers, land-based intercontinental ballistic missiles (ICBMs), and ballistic-missile submarines. These three weapons complement each other, and ensure that the U. S. maintains a credible second-strike capability in spite of any conceivable first-strike attack by enemy forces. There are also three primary techniques for performing calculations in general relativity: *numerical relativity*, *black-hole perturbation theory*, and *post-Newtonian expansions*. Like the nuclear triad, these techniques complement each other and ensure that suitable GW waveforms can be calculated for all three stages of black-hole mergers as discussed in the previous section. In the remainder of this section we will briefly discuss these techniques and illustrate their utility by provided examples from my own research of problems that they can be used to solve.

3.1 Numerical relativity

In the late 1990s, the NSF awarded a "Grand Challenge" grant to encourage research to simulate the merger of binary black holes by directly solving Einstein's equation Eq. (1.1). Despite much hard work on this problem during that decade, the merger of equal-mass binary black holes on initially quasi-circular orbits was not successfully simulated until Frans Pretorius accomplished the feat in 2005 [22]. Several other numerical-relativity (NR) groups successfully simulated black-hole mergers shortly thereafter [23, 24], and to date hundreds of black-hole simulations with varying mass ratios and initial spins have been published. NR simulations are the most general technique for calculating the GWs from binary black-hole mergers, and are the *only* technique that can accurately determine the waveform from the merger stage of comparable-mass mergers. Although all relativity problems could be solved with NR simulations in theory, in practice they can be prohibitively expensive computationally. The simplest NR simulations require 10^4 CPU-hours of computing resources, and their cost scales as q^{-2} for unequal-mass mergers. The smallest mass-ratio simulation currently published has $q = 0.01$ [25], and it seems unlikely that much progress beyond this limit will be achieved with current NR techniques. NR simulations are thus unsuited to EMRIs where $q \lesssim 10^{-5}$. Given the extraordinary computational expense of NR simulations, cleverness is required to extract the most information from a small sample of simulations.

My collaborators and I developed a new spin expansion that exploits symmetry to determine the general spin dependence of GW observables from a finite number of NR simulations [26, 27]. All final quantities f that describe the final black hole produced in a merger can only depend on the 7 parameters $\{q, a_i, b_i\}$ that characterize the initial binary (see Fig. 1). Since the magnitudes of the dimensionless spin of Kerr black holes cannot exceed unity ($|a_i|, |b_i| \leq 1$), these final quantities can be Taylor expanded in terms of the initial spin components:

$$f = f^{m_1 m_2 m_3 | n_1 n_2 n_3}(q) a_1^{m_1} a_2^{m_2} a_3^{m_3} b_1^{n_1} b_2^{n_2} b_3^{n_3} \,, \tag{3.1}$$

where summation over the repeated indices m_i, n_i is implied. This spin expansion is itself not very predictive, as the number of terms at each order in the initial spin components increases rapidly and

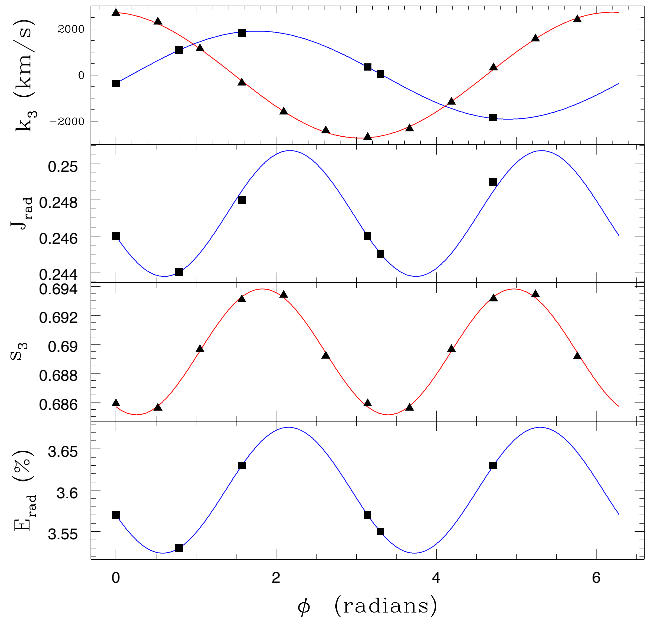

Figure 2: Kick velocity k_3, radiated angular momentum $J_{\rm rad}$, final spin s_3, and radiated energy $E_{\rm rad}$ as a function of the angle ϕ between the initial spin $\mathbf{a}$ and the coordinate vector $\mathbf{e}^{(1)}$ for equal-mass black-hole binaries with equal and opposite spins in the orbital plane. The square (triangle) data points are from [28] ([29]), while the functional form of the fitted curves are the lowest-order predictions of the spin expansion.

there is no guarantee that the series will quickly converge. However, considerable progress can be achieved by recognizing that the parameters $\{q, \mathbf{a}, \mathbf{b}\}$ that define the initial binary, the orthonormal triad $\mathbf{e}^{(i)}$, and the final quantities $\{m, \mathbf{s}, \mathbf{k}\}$ all transform in well defined way under the operations of parity P (reflection through the origin) and exchange X (exchanging the black-hole labels A and B). Because evolution according to Einstein's equation respects these symmetries, final quantities that transform in a given way under P and X can only depend on initial quantities that transform in the *same* manner. This dramatically reduces the number of terms that appear in the spin expansion of a particular quantity. We find that in practice the very lowest-order terms often provide an extremely accurate description of the desired spin dependence. This can be seen in Fig. 2, where various final quantities determined by NR simulations as a function of initial spin direction are compared to the predictions of the spin expansion. We see that final quantities $(J_{\rm rad}, s_3, E_{\rm rad})$ that are scalars (even under parity P) are determined to lowest order to scale quadratically in the initial spins and to have frequencies of 2 as predicted by our formalism. In contrast, the pseudoscalars (quantities odd under P) such as the kick velocity k_3 are permitted to have a linear spin dependence with unit frequency.

The spin expansion not only explained previously discovered spin dependence, but also uncovered new spin dependence that had been previously unappreciated. In Fig. 3 we show the residuals Δk_3 after the best lowest-order fits using the spin expansion are subtracted from the top panel of Fig. 2. As predicted by symmetry, quadratic terms in the initial spins with frequency 2 are absent, with the dominant term being cubic in the spin amplitude and having frequency 3. This example

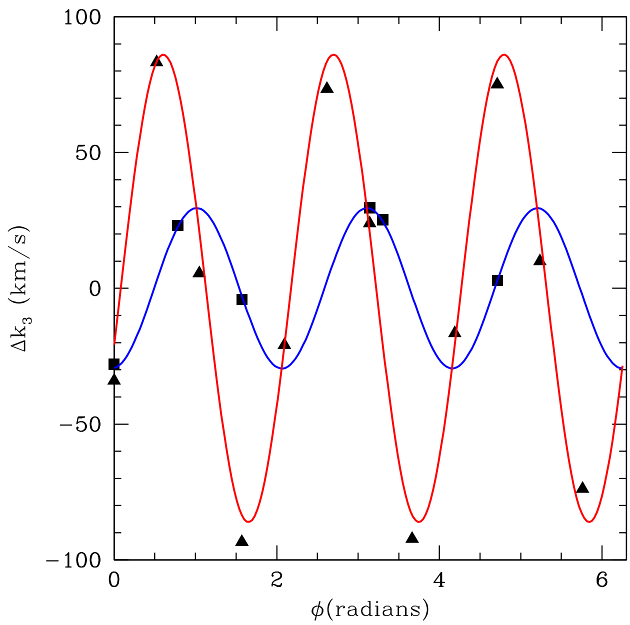

Figure 3: The residuals Δk_3 after the lowest-order spin-expansion fits are subtracted from the simulated kick velocities shown in Fig. 2. As shown by the fitted curves, these residuals are cubic in the spin magnitudes and have frequencies of 3 as predicted by our spin expansion.

illustrates both the power of NR simulations, and how this power can be best harnessed by using a small number of NR simulations to calibrate judicious fitting formulae such as our spin expansion. Our approach has been used extensively by other groups seeking to interpret their latest NR results.

3.2 Black-hole perturbation theory

Despite the extraordinary recent progress in NR, its computational expense and restriction to modest mass ratios ($q \gtrsim 0.1$) and SBH spins ($a/m \lesssim 0.9$) implies that it is not always the best technique for solving certain GR problems. EMRIs can instead be studied with *black-hole perturbation theory*, in which the smaller black hole and its accompanying gravitational radiation are treated as perturbations to the background metric of the larger black hole. Black-hole perturbation theory for the nonspinning Schwarzschild metric was introduced by Regge and Wheeler [30] and Zerilli [31] for odd- and even-parity perturbations respectively, and generalized to the spinning Kerr metric by Teukolsky [32]. Teukolsky showed that vacuum perturbations to the Kerr spacetime are fully described by the complex Weyl scalar

$$\psi_4 \equiv -C_{\alpha\beta\gamma\delta} n^\alpha \bar{m}^\beta n^\gamma \bar{m}^\delta \ , \tag{3.2}$$

where $C_{\alpha\beta\gamma\delta}$ is the Weyl curvature tensor and n^μ and $\bar{m}^\mu$ are elements of a Newman-Penrose tetrad of null 4-vectors [33]. This Weyl scalar can be decomposed into multipole moments

$$\psi_4(t,r,\theta,\phi) = \frac{1}{(r - ia\cos\theta)^4} \int_{-\infty}^{\infty} d\omega \sum_{lm} R_{lm\omega}(r) \, {}_{-2}S_{lm}^{a\omega}(\theta) e^{im\phi} e^{-i\omega t} \ , \tag{3.3}$$

where ${}_{-2}S^{a\omega}_{lm}(\theta)$ are generalizations of the Legendre functions that appear in ordinary spherical harmonics and $R_{lm\omega}(r)$ are radial functions that are solutions to the Teukolsky equation

$$\Delta^2 \frac{d}{dr}\left(\frac{1}{\Delta}\frac{dR_{lm\omega}}{dr}\right) - V(r)R_{lm\omega}(r) = \mathscr{T}_{lm\omega}(r)\ . \tag{3.4}$$

The potential $V(r)$ is a known analytic function for each harmonic, implying that the left-hand side of Eq. (3.4) depends solely on the spacetime curvature. The source term $\mathscr{T}_{lm\omega}(r)$ is an integral of the stress-energy tensor of the perturbation over the spacetime. The Teukolsky equation (3.4) is thus a linearization of Einstein's equation (1.1) in which 10 coupled, nonlinear, partial differential equations have been reduced to an infinite series of ordinary differential equations, one for each harmonic of the Weyl scalar. In practice, it is often the case that only a small number of harmonics are required to achieve the desired accuracy in a given GR calculation. Unlike NR, black-hole perturbation theory improves in accuracy as q decreases, and can be used for arbitrarily high spins. It is the technique of choice for studying EMRIs during the late inspiral, merger, and ringdown stages.

One application of black-hole perturbation theory in my own research was to calculate the maximum spin black holes can attain in binary mergers [34]. Bardeen [35] famously showed that a nonspinning black hole, accreting material from its prograde equatorial ISCO, could spin up to the Kerr limit ($a/M = 1$) after increasing its mass by a factor of $\sqrt{6}$ but could not surpass this limit. However, this analysis failed to account for what happens to the energy and angular momentum that must be lost to allow material to reach the ISCO. Thorne [36] showed that if this material is viscously transported to the ISCO through a standard thin accretion disk [37], the black hole would preferentially capture radiated photons with negative angular momentum with respect to the direction of the black hole's spin. This captured radiation would decrease the black hole's spin so that a limiting spin of only $a/m \simeq 0.998$ could be attained. Although this seems close to the Kerr limit, the gravitational binding energy at the ISCO increases sharply with black-hole spin so that the radiative efficiency of a black hole with $a/m \simeq 0.998$ is only $\eta \simeq 0.3$ compared to $\eta \simeq 0.42$ in the Kerr limit. I wondered if a similar limit might exist for black holes grown through binary mergers instead of gas accretion. During binary mergers it is gravitational radiation rather than viscous dissipation that extracts energy and angular momentum from the inspiraling material. Unlike the radiated photons studied by Thorne, whose short wavelengths imply that they travel on null geodesics of the Kerr metric, the GWs emitted during the inspiral have wavelengths comparable to the orbital radii of the inspiraling black hole and thus larger than the event horizon. This allows the GWs to be *superradiantly* scattered by the gravitational potential of the Kerr black hole, gaining amplitude before escaping to infinity. Superradiant scattering is an example of a Penrose process [3] in which rotational energy and angular momentum are extracted from a spinning black hole. Using GREMLIN (Gravitational Radiation in the Extreme Mass ratio LIMit), a black-hole perturbation theory code developed by Scott Hughes [38], I calculated the GW fluxes of energy and angular momentum both out to infinity and down to the event horizon during an EMRI. We show the effect of this superradiant scattering on the black hole's spin in Fig. 4. Highly spinning black holes rapidly spin up to the Kerr limit without accounting for superradiant scattering as shown by the dashed blue curves. Once the effects of scattering are included, only a limiting spin

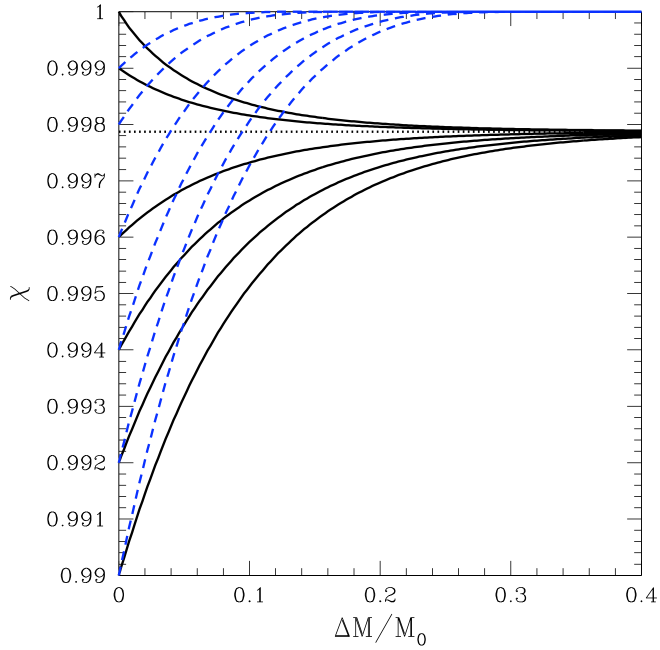

Figure 4: Dimensionless spin $\chi \equiv a/m$ of a black hole of initial mass M_0 after accreting a mass ΔM of test particles on quasi-circular prograde equatorial orbits. The different curves correspond to different values of the initial spin. The dashed blue curves show the predictions of Bardeen [35] that only include the spin dependence of the orbital energy and angular momentum at the ISCO, while the solid black curves also include the effects of the superradiant scattering of GWs as discussed in Kesden *et al.* [34].

$\chi \equiv a/m \simeq 0.998$ can be attained. The numerical value of this limit is quite close to the Thorne limit [36], although the processes setting these limits are quite different.

Predictions of the final spin resulting from EMRIs calculated using black-hole perturbation theory complement the predictions obtained from NR for comparable-mass mergers. In Fig. 5 we show the change in final spin per unit test-particle mass $\partial\chi_f/\partial q$ as a function of the initial spin χ_i. The solid black curve shows the prediction of Kesden *et al.* [34] that a black hole can only be spun up to $a/m \simeq 0.998$ by binary mergers, while the green and magenta curves, derived from extrapolations of comparable-mass NR simulations, erroneously suggest that black holes can be spun above the Kerr limit. This plot indicates that danger of relying exclusively on NR; all three techniques in the strategic triad of general relativity have their role to play in understanding black-hole mergers.

3.3 Post-Newtonian expansions

The final technique in the strategic triad of general relativity is the post-Newtonian (PN) expansion. PN expansions describing a system rapidly converge when the PN parameter $\varepsilon \approx (v/c)^2 \approx Gm/r \approx (M\omega)^{2/3} \ll 1$, where ω is the angular velocity. PN expansions are thus ideally suited to describing widely separated binary black holes, regardless of their mass ratio or the magnitude of their spins. PN expansions are the most computationally affordable of the three techniques con-

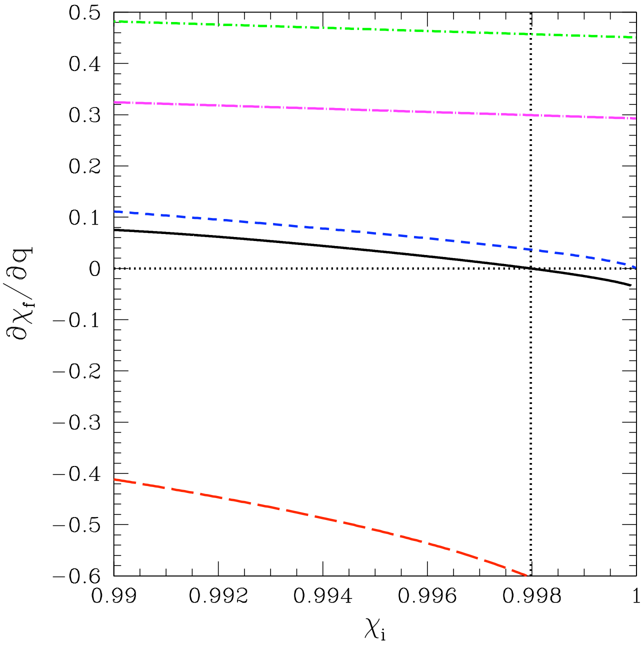

Figure 5: The change in final spin per unit test-particle mass $\partial \chi_f/\partial q$ as a function of the initial spin χ_i. The solid black curve shows the predictions of Kesden *et al.* [34], with spindown ($\partial \chi_f/\partial q \leq 0$, horizontal dotted line) possible for spins $\chi_i \geq \chi_{\rm lim}$ (vertical dotted line). The short-dashed blue curve shows how this result changes when superradiant scattering is neglected as in the models of Bardeen [35]. The long-dashed red curve gives the Buonanno *et al.* [39] prediction, while the dot-short-dashed green and dot-long-dashed magenta curves are the predictions of the NR-calibrated fitting formulae of Barausse and Rezzolla [40] and Tichy and Marronetti [41].

sidered in this section, so they should be the preferred technique during the inspiral stage of the merger. Discussion of the derivation of various PN expansions is beyond the scope of this work; I will instead focus on one particular application from my own research, the alignment of black-hole spins prior to merger.

As seen in the subsection on NR, the final spins and recoil velocities of black holes produced in mergers depend sensitively on the orientation of the initial binary black-hole spins just prior to merger. Tidal torques exerted by a circumbinary disk can extract orbital angular momentum from a black-hole binary, bringing the black holes close enough together to merge [14]. These same tidal torques can cause the black-hole spins to align with the angular momentum of the circumbinary disk [42], though it is unclear in practice how efficient this mechanism will be. At binary separations of $r_{\rm GW} \lesssim 3000M$, the torque exerted on the binary by gravitational radiation exceeds the tidal torque from the circumbinary disk. The evolution of the binary at $r \leq r_{\rm GW}$ becomes a pure general-relativity problem, one that is ideally suited to a PN analysis. Schnittman [43] discovered the existence of PN spin-orbit resonances into which black-hole binaries could become trapped, aligning their spins into special configurations. My collaborators and I [44, 45] showed that these resonances, acting on the astrophysically determined partially aligned spin configurations at $r \simeq r_{\rm GW}$, could align the spins in such a way as to profoundly influence the predicted distribu-

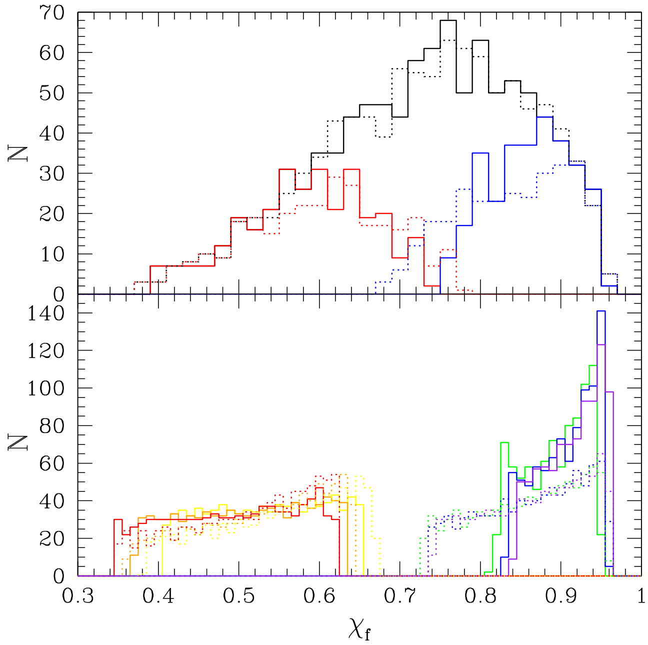

Figure 6: Histograms of the final spins predicted by the NR formula of [40] for black hole binaries with a mass ratio of $q = 9/11$ and different initial orientations of maximal spins. The dashed curves show the predictions assuming the spins remain in their initial orientations throughout the inspiral, while the solid curves include the effects of PN evolution for $r \leq 1000M$. In the top panel, the black distribution assumes isotropic initial spins for both black holes, while the blue (red) subset corresponds to the 30% of the distribution with the smallest (largest) initial angle between the spin of the more massive black hole and the orbital angular momentum. In the bottom panel, the smaller black hole has an initially isotropic spin distribution while the spin of the larger black hole is at an initial angle of 10° (purple), 20° (blue), 30° (green), 150° (yellow), 160° (orange), 170° (red) with respect to the orbital angular momentum.

tions of final spins and recoil velocities. In Fig. 6 we show how PN spin-orbit resonances affect the predicted distribution of final spins. The dominant effect is for the two initial spins to become aligned *with each other* when the larger spin is initially more closely aligned with the orbital angular momentum. This can be most clearly seen in the bottom panel, when comparing the solid and dashed distributions for the green, blue, and purple curves. Alignment of the binary spins with each other causes them to add coherently at merger, leading to a black hole with a larger final spin.

PN spin-orbit resonances have an even greater effect on the distribution of recoil velocities imparted to the final black hole. We show this effect in the histograms of Fig. 7. NR simulations show that recoil velocities are maximized when the black-hole spins are anti-aligned with each other just prior to merger [46]. Since the dominant effect of PN spin-orbit resonances is to align (anti-align) the binary spins with each other when the larger (smaller) black hole is more closely aligned with the orbital angular momentum, the recoil velocities will be suppressed (enhanced) in these cases. This is what is seen in Fig. 7; the recoil velocities are suppressed (enhanced) in the middle (bottom) panels. Most large galaxies are observed to host SBHs in their centers, which is seemingly at odds with the predictions of NR which suggest that recoils substantially exceeding

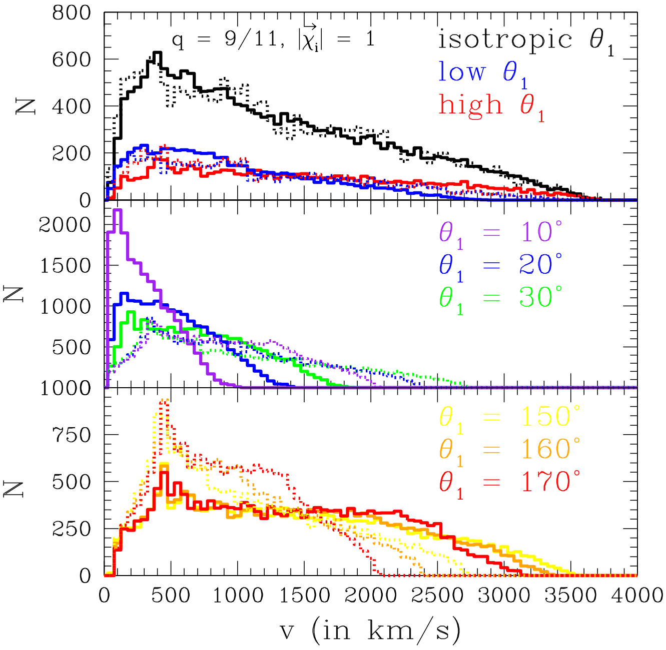

Figure 7: Histograms of the final recoils predicted by the NR formula of [46] for a mass ratio of $q = 9/11$ and different initial spin configurations. The curves in the top panel correspond to the same initial spin distributions as in the top panel of Fig. 6, while the curves in the middle and lower panels correspond to the curves in the lower panel of Fig. 6.

galactic escape velocities are generic. The effects of PN spin-orbit resonances that we discovered may help reconcile theory with observation.

4. Summary

Black-hole mergers occur throughout our universe, and provide a unique opportunity to test the predictions of Einstein's theory of general relativity. Black holes are observed to have a bimodal distribution of masses: stellar-mass black holes formed from the gravitational collapse of high-mass stars, and supermassive black holes grown through gas accretion and mergers in galactic centers. The mergers of these black holes can be distinguished into comparable-mass mergers and extreme mass-ratio inspirals (EMRIs). The mergers themselves can be separated into three stages: adiabatic inspiral, merger, and ringdown. There are three primary tools (the strategic triad of general relativity) that can be used to understand different stages of the merger. Numerical relativity is very computationally expensive but is the only tool that can be used to model the "merger" stage for comparable-mass mergers. Black-hole perturbation theory can be used for all stages of the EMRIs, where the smaller black hole and its accompanying gravitational radiation can be considered to be perturbations about the background Kerr spacetime of the larger black hole. Post-Newtonian expansions are the most computationally affordable, and can be used when velocities are not highly relativistic and the curvature is not extreme. They are ideally suited to describing the early inspiral stage of mergers. To understand black-hole mergers in full generality, we must master all these tools and use them to complement each other.

References

[1] R. P. Kerr, *Gravitational field of a spinning mass as an example of algebraically special metrics*, Phys. Rev. Lett. **11**, 237 (1963).

[2] C. W. Misner, K. S. Thorne and J. A. Wheeler, *Gravitation*, W. H. Freeman and Company, New York, (1973).

[3] R. Penrose, *Gravitational collapse: The role of general relativity*, Riv. Nuovo Cim. **1**, 252 (1969) [Gen. Rel. Grav. **34**, 1141 (2002)].

[4] J. R. Oppenheimer and H. Snyder, *On Continued gravitational contraction*, Phys. Rev. **56**, 455 (1939).

[5] S. Bowyer, E. T. Byram, T. A. Chubb and H. Friedman, *Cosmic X-ray sources*, Science **147**, 394 (1965).

[6] C. Seyfert, *Nuclear emission in spiral nebulae*, Astrophys. J. **97**, 28 (1943).

[7] F. Hoyle, W. A. Fowler, *On the nature off strong radio sources*, Mon. Not. Roy. Astron. Soc. **125**, 169 (1963).

[8] D. Lynden-Bell, *Galactic nuclei as collapsed old quasars*, Nature **223**, 690 (1969).

[9] P. C. Peters and J. Mathews, *Gravitational radiation from point masses in a Keplerian orbit*, Phys. Rev. **131**, 435 (1963).

[10] J. Abadie *et al.* [LIGO Scientific and Virgo Collaborations], *Predictions for the Rates of Compact Binary Coalescences Observable by Ground-based Gravitational-wave Detectors*, Class. Quant. Grav. **27**, 173001 (2010).

[11] J. Kormendy, D. Richstone, *Inward bound: The Search for supermassive black holes in galactic nuclei*, Ann. Rev. Astron. Astrophys. **33**, 581 (1995).

[12] J. Magorrian, S. Tremaine, D. Richstone, R. Bender, G. Bower, A. Dressler, S. M. Faber, K. Gebhardt *et al.*, *The Demography of massive dark objects in galaxy centers*, Astron. J. **115**, 2285 (1998).

[13] K. Gebhardt, R. Bender, G. Bower, A. Dressler, S. M. Faber, A. V. Filippenko, R. Green, C. Grillmair *et al.*, *A Relationship between nuclear black hole mass and galaxy velocity dispersion*, Astrophys. J. **539**, L13 (2000).

[14] M. C. Begelman, R. D. Blandford and M. J. Rees, *Massive black hole binaries in active galactic nuclei*, Nature **287**, 307 (1980).

[15] R. M. Buchholz, R. Schodel, A. Eckart, *Composition of the galactic center star cluster: Population analysis from adaptive optics narrow band spectral energy distributions*, Astron. Astrophys. **499**, 483 (2009).

[16] D. Merritt, *The Distribution of Stars and Stellar Remnants at the Galactic Center*, Astrophys. J. **718**, 739 (2010).

[17] D. Merritt, T. Alexander, S. Mikkola and C. M. Will, *Stellar Dynamics of Extreme-Mass-Ratio Inspirals*, Phys. Rev. D **84**, 044024 (2011).

[18] LIGO - Laser Interferometer Gravitational Wave Observatory, http://www.ligo.caltech.edu/.

[19] Virgo, https://wwwcascina.virgo.infn.it/.

[20] LISA - Laser Interferometer Space Antenna, http://lisa.nasa.gov/.

[21] ESA Science & Technology: Next steps for LISA, http://sci.esa.int/science-e/www/object/index.cfm?fobjectid=48728

[22] F. Pretorius, *Evolution of binary black hole spacetimes*, Phys. Rev. Lett. **95**, 121101 (2005).

[23] M. Campanelli, C. O. Lousto, P. Marronetti and Y. Zlochower, *Accurate evolutions of orbiting black-hole binaries without excision*, Phys. Rev. Lett. **96**, 111101 (2006).

[24] J. G. Baker, J. Centrella, D. -I. Choi, M. Koppitz and J. van Meter, *Gravitational wave extraction from an inspiraling configuration of merging black holes*, Phys. Rev. Lett. **96**, 111102 (2006).

[25] C. O. Lousto and Y. Zlochower, *Orbital Evolution of Extreme-Mass-Ratio Black-Hole Binaries with Numerical Relativity*, Phys. Rev. Lett. **106**, 041101 (2011).

[26] L. Boyle, M. Kesden and S. Nissanke, *Binary black hole merger: Symmetry and the spin expansion*, Phys. Rev. Lett. **100**, 151101 (2008).

[27] L. Boyle and M. Kesden, *The spin expansion for binary black hole merger: new predictions and future directions*, Phys. Rev. D **78**, 024017 (2008).

[28] M. Campanelli, C. O. Lousto, Y. Zlochower and D. Merritt, *Maximum gravitational recoil*, Phys. Rev. Lett. **98**, 231102 (2007).

[29] B. Bruegmann, J. A. Gonzalez, M. Hannam, S. Husa and U. Sperhake, *Exploring black hole superkicks*, Phys. Rev. D **77**, 124047 (2008).

[30] T. Regge and J. A. Wheeler, *Stability of a Schwarzschild singularity*, Phys. Rev. **108**, 1063 (1957).

[31] F. J. Zerilli, *Gravitational field of a particle falling in a schwarzschild geometry analyzed in tensor harmonics*, Phys. Rev. D **2**, 2141 (1970).

[32] S. A. Teukolsky, *Perturbations of a rotating black hole. 1. Fundamental equations for gravitational electromagnetic and neutrino field perturbations*, Astrophys. J. **185**, 635 (1973).

[33] E. Newman and R. Penrose, *An Approach to gravitational radiation by a method of spin coefficients*, J. Math. Phys. **3**, 566 (1962).

[34] M. Kesden, G. Lockhart and E. S. Phinney, *Maximum black-hole spin from quasi-circular binary mergers*, Phys. Rev. D **82**, 124045 (2010).

[35] J. M. Bardeen, *Kerr metric black holes*, Nature **226**, 64 (1970).

[36] K. S. Thorne, *Disk Accretion Onto A Black Hole. 2. Evolution Of The Hole*, Astrophys. J. **191**, 507 (1974).

[37] N. I. Shakura and R. A. Sunyaev, *Black holes in binary systems. Observational appearance*, Astron. Astrophys. **24**, 337 (1973).

[38] S. A. Hughes, *The evolution of circular, non-equatorial orbits of Kerr black holes due to gravitational-wave emission*, Phys. Rev. D **61**, 084004 (2000) [Erratum-ibid. D **63**, 049902 (2001 ERRAT,D65,069902.2002 ERRAT,D67,089901.2003)].

[39] A. Buonanno, L. E. Kidder and L. Lehner, *Estimating the final spin of a binary black hole coalescence*, Phys. Rev. D **77**, 026004 (2008).

[40] E. Barausse and L. Rezzolla, *Predicting the direction of the final spin from the coalescence of two black holes*, Astrophys. J. **704**, L40 (2009).

[41] W. Tichy and P. Marronetti, *The final mass and spin of black hole mergers*, Phys. Rev. D **78**, 081501 (2008).

[42] T. Bogdanovic, C. S. Reynolds and M. C. Miller, *Alignment of the spins of supermassive black holes prior to merger*, Astrophys. J. **661**, L147 (2007).

[43] J. D. Schnittman, *Spin-orbit resonance and the evolution of compact binary systems*, Phys. Rev. D **70**, 124020 (2004).

[44] M. Kesden, U. Sperhake and E. Berti, *Final spins from the merger of precessing binary black holes*, Phys. Rev. D **81**, 084054 (2010).

[45] M. Kesden, U. Sperhake and E. Berti, *Relativistic Suppression of Black Hole Recoils*, Astrophys. J. **715**, 1006 (2010).

[46] M. Campanelli, C. O. Lousto, Y. Zlochower and D. Merritt, *Large merger recoils and spin flips from generic black-hole binaries*, Astrophys. J. **659**, L5 (2007).

PROCEEDINGS OF SCIENCE

Environmentally-Driven Galaxy Evolution

Stephanie Tonnesen*
Princeton University
E-mail: stonnes@astro.princeton.edu

The galaxy population in clusters differs from that in the field. The cluster galaxy population (at $z \leq 0.4$) is dominated by red, early-type galaxies. Although some of this can be explained by the mass-morphology relation, in this proceedings I discuss work that has shown that, particularly in low-mass galaxies, there is environmentally-driven evolution from blue (star-forming) to red (non-star-forming). While environment can be measured in several ways, I show that local environment affects galaxies up to the scale of the halo in which they reside. Focusing on clusters, I introduce the different mechanisms that can affect galaxies: galaxy-cluster, galaxy-galaxy, and galaxy-intracluster medium interactions. I then give an overview of the evidence that the color-evolution of galaxies from blue to red is reflected in the morphological evolution of galaxies from spiral to S0, and discuss the necessary steps in the evolution of spirals into S0s. I then briefly describe some of my own research examining the role of ram pressure stripping on the morphological evolution of spiral galaxies. While ram pressure stripping can effectively remove the fuel for star formation and redden galaxies, this will form S0s that are less luminous than their spiral progenitors. Therefore, while ram pressure stripping may be an important mechanism driving the formation of S0s from spirals, it cannot be the only process driving this morphological evolution.

Frank N. Bash Symposium 2011: New Horizons in Astronomy
October 9-11, 2011
Austin, Texas, USA

*Speaker.

1. Introduction

In our hierarchical view of the universe, smaller halos are formed before larger ones, and large halos grow by accretion of satellites. Galaxies form, then come together to form groups and clusters. Does entering into these dense environments affect galaxy properties?

To answer this question, it is important to examine the variety of galaxies seen in our universe. The first step in this process is to categorize galaxies in ways that give us insight into their fundamental properties, and in this proceedings I will first highlight some of the methods by which galaxies have been classified (Section 2). I will then discuss whether and how galaxies evolve due to their environment (Section 3), and in Section 3.1 I will discuss the different ways in which environment can be defined. Focusing specifically on clusters (Section 4), I will introduce mechanisms that can drive the evolution of galaxies (Sections 4.1 and 4.2). Finally I will discuss the morphological evolution of spiral galaxies into S0s (Section 5), and work I have done to understand the role of ram pressure stripping in driving this evolution. I will conclude by summarizing my main points and mentioning a few avenues for future work.

2. Galaxy Types

The Hubble Sequence uses galaxy morphology to categorize galaxies [43]. Elliptical galaxies are those with ellipsoidal shapes, and spiral galaxies have flatter shapes and thus look more like disks. They also have spiral structure in their gas and stellar distribution. S0s have large bulges, like elliptical galaxies (which can be considered all bulge), and featureless disks.

It has been found that the color of galaxies is related to their Hubble type [25, 26, 80]. Elliptical galaxies tend to be redder in optical color than spiral galaxies (but see [15] for a discussion of red disk-galaxies). The bluer color of spiral galaxies is due to the younger stellar population in spirals. Galaxy color is an indicator of star formation history, or the age of the stellar population (although color is also affected by metallicity and dust, which can confuse this relation).

In addition, the most luminous galaxies tend to be red early-type galaxies (ellipticals) [12, 3]. Baldry et al. [3] find, using more than 65,000 galaxies from the Sloan Digital Sky Survey, that brighter than $M_r \sim -22$, more than 60% of galaxies are from the authors' red distribution of galaxies (and at $M_r \sim -23.5$ nearly the entire population is red).

The relationship between galaxy color (or star formation history) and luminosity (or mass) can be physically explained in a cold dark matter universe by how galaxies of different masses accrete gas. In early models of galaxy formation through spherical collapse, gas falling into a dark-matter halo is shock-heated to the virial temperature. This gas then slowly cools and falls towards the center of the halo to form the dense central luminous galaxy [70, 75, 9, 90, 30]. This leads to an upper mass threshold at which shocked gas can no longer cool within a Hubble time, and these high mass galaxies will therefore have no fuel for star formation. In lower mass halos gas does not go through an accretion shock at the virial radius, and will either never become hot or will be able to cool quickly [70, 90].

Recent numerical cosmological simulations have verified that not all gas is shock-heated to the virial temperature of the halo (e.g. [48]). Some gas penetrates the halo as unshocked cold flows, and the fraction of shock-heated gas depends on the halo mass [48, 47, 63, 13] . Kereš et

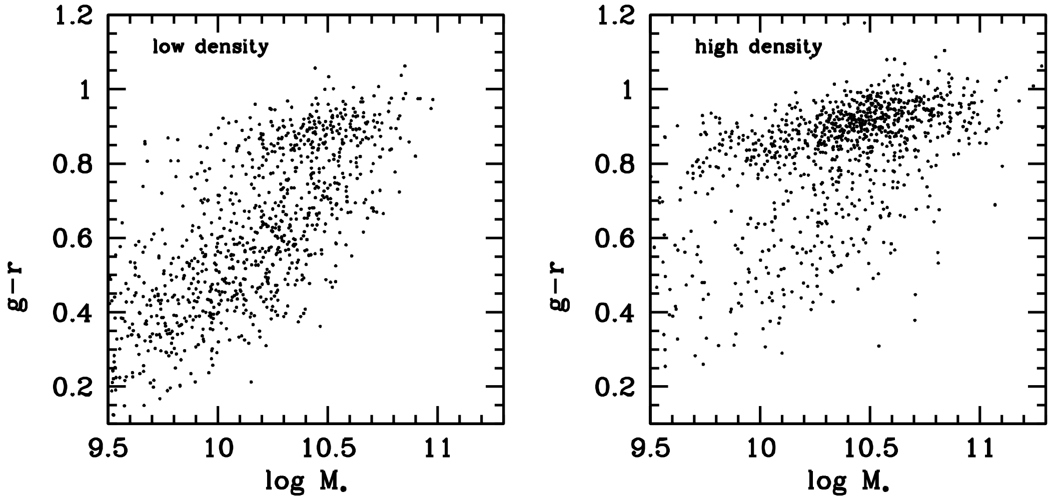

Figure 1: Figure 6 from Kauffmann et al. [46]. A plot of $g-r$ color versus stellar mass for the 1000 galaxies in the lowest density bin on the left and in the highest density bin on the right. Note the extension of the red sequence to lower mass galaxies in the right panel.

al. [48] find that cold accretion dominates in low redshift halos that have a total mass below $\sim$5 $\times$ 10^{11} $M_{\odot}$. If cold gas accretion is equated with the ability of a galaxy to form stars, then this indicates that higher mass galaxies should be redder than low mass galaxies. As discussed above, this is indeed observed in the galaxy color-magnitude diagram [12, 3]. However, as is clear from Figure 5 in Kereš et al. [48], there is still significant scatter in the fraction of gas accreted at low temperatures at a single galaxy mass. A range of galaxy colors is also seen at a single galaxy mass when examining the color-magnitude diagram (e.g. [3]).

Therefore, it is clear that while mass has an important influence on whether a galaxy can accrete cold gas and form stars, it is not the only factor to consider when understanding galaxy color (and other characteristics). While galaxy properties may be influenced by merger and mass accretion history, feedback from stellar winds, supernovae, and black holes, I will focus on the environment.

3. Galaxies and Environment

In addition to being the first to categorize galaxies, Hubble also found that galaxy morphology is correlated with environment [44]. The galaxy population in nearby clusters is dominated by red early-type galaxies, while galaxies in the field tend to be of later types [44]. The relationship between morphology and local galaxy density was quantified as the morphology-density relation [28, 64]. Galaxy color is also related to local galaxy density. Galaxy morphological type and star formation rate (SFR) has been found to smoothly change to later types with higher SFRs with increasing clustercentric distance [79, 87].

The morphology- and color-density relations can depend on galaxy mass. The stellar masses of galaxies tend to be larger in clusters [5, 12], so the relationship between galaxy mass and environmental density (and galaxy mass and color, as discussed in Section 2) can somewhat account for the color-density and morphology-density relations. However, Kauffmann et al. [46] find that star formation history depends on local galaxy density for all galaxies regardless of mass, and that in galaxies with stellar masses less than 10^{10} $M_{\odot}$ there is a relationship between galaxy morphology and local density. Further, in their Figure 6 (shown in Figure 1), the authors show color-mass diagrams for galaxies in their lowest- and highest-density regions. The red sequence for galaxies in high-density regions extends to lower galaxy masses than that for galaxies in low-density regions, indicating the importance of environment in reddening at least low-mass galaxies. Indeed, Kereš et al. [48] cite environment as an explanation for their low-mass galaxies with no cold gas accretion.

These correlations alone do not indicate whether environment affects the formation or subsequent evolution of galaxies. However, the Butcher-Oemler effect, that galaxies in clusters beyond z$\sim$0.4 tend to be bluer than galaxies in nearby clusters, is empirical evidence that spirals evolve over time after they enter the cluster environment [17]. In addition, the spiral to S0 ratio decreases with redshift [29, 31, 27]. Both the morphology-density and color-density relations have been observed at a redshift of 1, but the fractions of early-type and red galaxies continue to increase with decreasing redshift [76, 66].

3.1 Defining Galaxy Environment

When examining galaxy color or morphology relative to environment, a number of different environmental definitions can be used. Comparisons can be made between galaxies that are cluster members and those that are in the field [37, 64, 17]. Clustercentric distance can also be used as an environmental measure [52, 28, 91, 87, 77]. Local galaxy density is also frequently used as an environmental measure. This is often measured in one of two ways: 1) measuring the projected local galaxy density using the distance to the n^{th} nearest neighbor (e.g. Dressler [28]; Gomez et al. [34] used the tenth nearest neighbor; Hashimoto et al. [37] used the distance to the third nearest neighbor; Perez et al. [67] used the distance to the fifth nearest neighbor), or 2) counting the number of galaxies to a fixed absolute magnitude within a fixed volume [4, 10, 11, 12, 41, 42, 46]. Whether cluster membership or local galaxy density is the more fundamental environmental parameter is still under debate.

For example, Dressler [28] observed that morphological type was correlated with both clustercentric distance and local galaxy surface density (calculated using the 10 nearest [projected] neighbors). Illustrated in Figure 2 (Dressler [28] Figure 6), he finds that when considering six moderately irregular clusters in particular, galaxy morphological type is more cleanly related to local galaxy surface density than to clustercentric distance. However, Whitmore & Gilmore [91] reexamined his data and found that morphological fractions varied as much with clustercentric distance as with local galaxy density, and concluded that the density-morphology relation is caused by the relationship between clustercentric radius and local density.

Both cluster membership and local galaxy density have also been used to examine whether galaxy SFR is related to environment [37, 34]. Hashimoto et al. [37] compare the relationship between SFR and local galaxy density (using the third nearest neighbor) in field galaxies and in cluster galaxies. The authors find that at high levels of star formation, the SFR depends on local

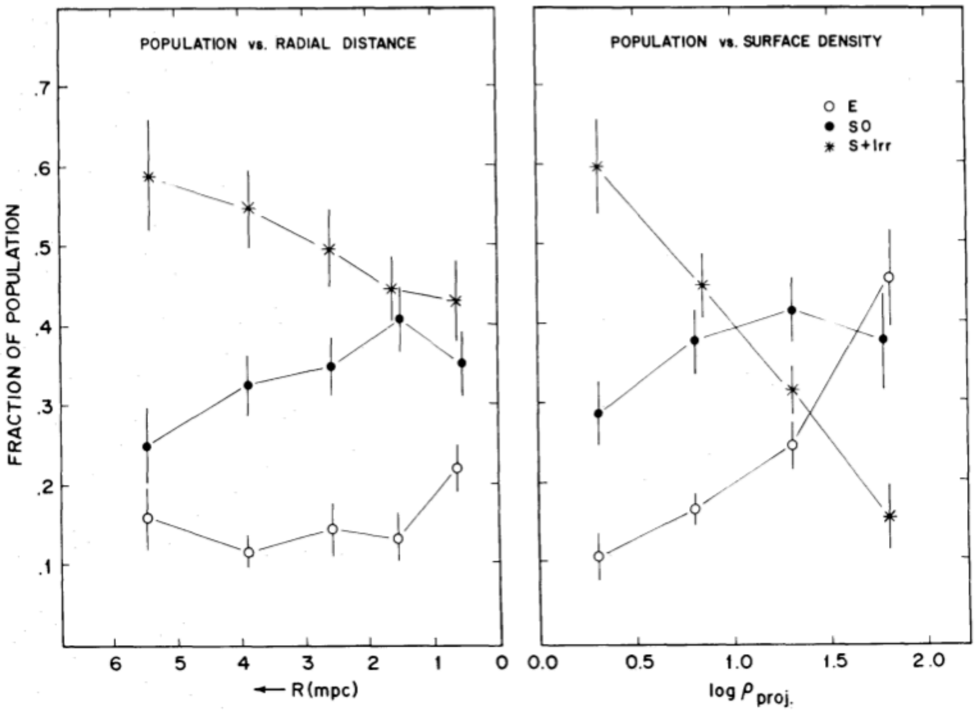

Figure 2: Figure 6 from Dressler [28]. Morphological type is correlated with both clustercentric distance and local galaxy surface density, although for the six irregular clusters used in this figure, morphological type is more cleanly related to local galaxy surface density.

galaxy density whether or not the galaxy is a cluster member, but that at low levels of star formation, the SFR varies with local density only in cluster galaxies.

Kauffmann et al. [46] use a different local density measure to examine the relationship between SFR and local density. They find that SFR is related to local density as measured by counting the number of galaxies within a projected radius of 2 Mpc and $\pm$ 500 km s^{-1}. Further, they find that the relationship between SFR and the local density within 1 Mpc is very strong, while the SFR is only weakly correlated with the local density measured within 5 Mpc. Blanton et al. [11] examined at what scale galaxy environment affects galaxy properties, using galaxy counts within several projected radii ranging from 0.2-6.0 h^{-1} Mpc. They find that the fraction of blue galaxies is affected by overdensity on all scales $\leq$1 h^{-1} Mpc, but overdensity on larger scales (6 Mpc) does not independently relate to galaxy color. They conclude that the contrasting Balogh et al. [4] result, that the fraction of star-forming galaxies depends on the galaxy density on scales of both 1.1 Mpc and 5.5 Mpc, may have been because Balogh et al. [4] introduced noise by only counting galaxies to a brighter magnitude limit. The virial radius of cluster halos is about 1-2 h^{-1} Mpc, so the Blanton et al. [11] result indicates that the halo in which a galaxy resides may be an important factor in determining galaxy color and SFR, and possibly also the smaller-scale density.

I have also considered the question of whether local density or cluster membership is important at low redshift (z $\leq$ 0.2) using cosmological simulations discussed in Cen [20]. These are performed using the adaptive mesh refinement (AMR) Eulerian hydrodynamical code *Enzo* [14, 62, 45]. Cen [20] first ran a low resolution simulation with a periodic box of 120 h^{-1} Mpc on a

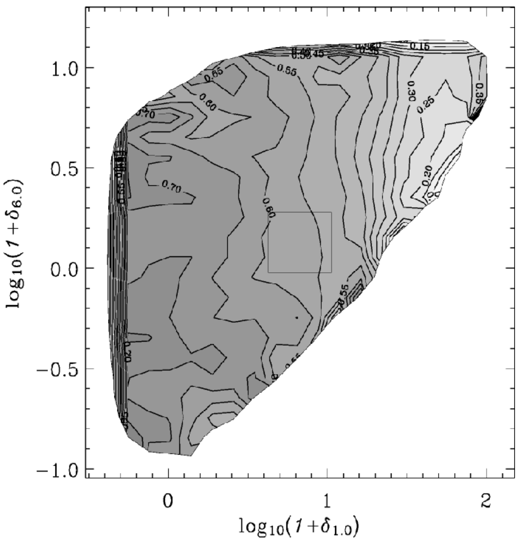

Figure 3: Figure 10 from Blanton et al. [11]. Contours and gray scale show the blue galaxy fraction as a function of local density on 1 and 6 h^{-1} Mpc scales. The vertical contours show that only the local density on the smaller scale is important.

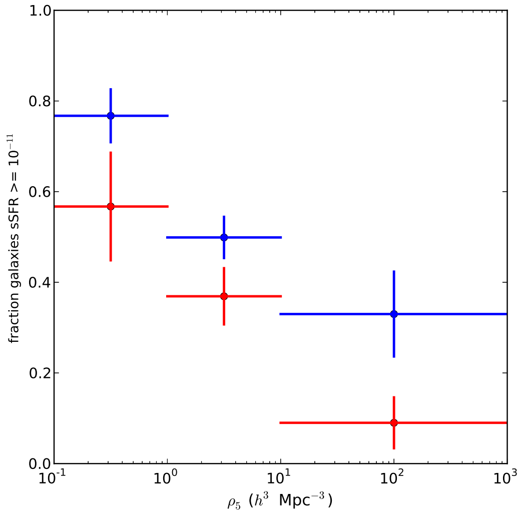

Figure 4: Fraction of star-forming galaxies as a function of local density (ρ_5), for galaxies in a cluster (red) and outside a cluster (blue). Star-forming fraction is a function of local density for galaxies both inside and outside of clusters, but at a single local density galaxies in a cluster are less likely to be star-forming.

side, and then resimulated a region around a cluster with high resolution (0.46 h^{-1} kpc), but embedded within the outer 120 h^{-1} Mpc box. The cluster refined region is 21 $\times$ 24 $\times$ 20 h^{-3} Mpc^3. The central cluster is $\sim$2 $\times$ 10^{14} M$_\odot$ with a virial radius (r$_{200}$) of 1.3 h^{-1} Mpc. This high-resolution box is much larger than the cluster at its center, so there are galaxies at a range of local densities. For details on this simulation, see Tonnesen & Cen [86].

I identify the center of the large cluster in this simulation as the position of the cD galaxy, and use a simple distance criterion to determine if a galaxy may be affected by the cluster–2 Abell radii (3 h^{-1} Mpc), which is slightly larger than 2 r$_{vir}$. The other galaxies in this box may be isolated or associated with smaller groups. I also determine the local galaxy density using the 3-dimensional distance to the fifth nearest neighbor,

$$\rho_5 = \frac{5}{\frac{4}{3}\,\pi\, d_5^3} \tag{3.1}$$

where d_5 is the distance to the fifth nearest neighbor.

I plot the fraction of star-forming galaxies, as defined by galaxies with a specific SFR (sSFR, SFR/M$_*$) greater than or equal to 10^{-11} yr^{-1} [39], as a function of ρ_5 for galaxies both inside and outside of the cluster (split at 2 r$_{Abell}$). The horizontal lines show the width of the ρ_5 bins, and the vertical lines denote the 95% confidence limits. In order to make as fair a comparison as possible, within each ρ_5 bin I match the distributions of the galaxy masses and local densities in both samples. In a KS test, this results in P values for the mass and local density distributions of 0.9 and 0.77, 0.85 and 0.96, and 0.99 and 0.99 respectively within each bin in order of increasing local density. Also, within each sample (inside and outside the cluster), the KS test P value of the mass distributions was at or above 0.68 when comparing the three density bins.

Figure 4 shows that both inside and outside of the cluster, the star-forming fraction decreases with increasing local density. However, at the same local density galaxies in clusters are less likely to be star-forming than galaxies that do not reside in such a massive halo. This supports the Blanton et al. [11] conclusion that the mass of the halo in which a galaxy resides is important, and specifically indicates that smaller-scale density is also important. Considering a galaxy's environment both in terms of cluster membership and local galaxy density is important to understanding how environment affects galaxy sSFR (and therefore color).

4. Focusing on Interactions in Galaxy Clusters

Despite the fact that clusters contain only ∼5% of galaxies [2], they are useful environments to examine carefully for several reasons. For example, focusing on clusters allows observers to examine more galaxies in a single field of view. Also, as I discussed above, clusters have a wide range of local environments. In addition, galaxies are moving quickly relative to each other and to the intracluster medium (ICM), so there are many interactions with shorter interaction timescales than in the field. Finally, clusters contain both the most massive and the least massive galaxies.

The smooth change in the galaxy population from the center of clusters to the field indicates that any processes transforming galaxy color and/or morphology act across a range of environmental densities (or across a range of cluster radii). As I discuss the different types of interactions that can affect galaxies within the cluster environment, I will comment on where in a cluster they are the most effective drivers of galaxy evolution. Evolutionary mechanisms can be split into two broad types: 1) gravitational interactions that affect both gas and stars, and 2) galaxy-ICM interactions that only affect the gas in a galaxy.

4.1 Gravitational Interactions

Gravitational interactions can occur between a galaxy and the cluster potential or between galaxies. The interaction between a galaxy and the cluster potential can strip mass from the galaxy down to the tidal truncation radius [53, 35]. The truncation radius can be expressed as:

$$r_t \sim \frac{\sigma_g}{\sigma_c} r_p \tag{4.1}$$

where r_t is the tidal radius, and r_p is the pericenter of the galaxy's orbit [35]. A simple examination of this equation shows that tidal truncation due to the cluster potential will only occur in the central regions of a cluster–at 250 kpc from the cluster center a galaxy with a velocity dispersion of 200 km s^{-1} will only be truncated to about 50 kpc. Byrd & Valtonen [18] found that the cluster potential can also perturb a galaxy, tidally-triggering SF out to about three times the core radius of a cluster.

Galaxy-galaxy interactions can occur at all cluster radii. One type of galaxy-galaxy interaction is mergers between galaxies with low relative velocities [6]. Generally, merging is unlikely due to the high velocity dispersion in clusters (see discussion in Oemler, Dressler & Butcher [65]). Galaxy harassment is a process in which the fast relative velocities between cluster galaxies result in a

PoS(Bash11)008

number of fly-bys which can disturb or strip mass from a galaxy [54]. Moore et al. [54, 56] found that harassment does not affect a system as dense as a giant elliptical or spiral bulge, so claimed that this transformation process will most strongly affect pure disk galaxies. Galaxy-galaxy interactions can affect both the gas and stellar mass of a galaxy, and can also drive a burst of star formation that may consume any gas remaining in the galaxy [7, 32, 56].

4.2 Galaxy-Intracluster Medium Interactions

Galaxy-ICM interactions are ones in which the gas in a galaxy interacts with the ambient intracluster hot gas. Therefore, these interactions most strongly affect galaxies near the center of clusters, where the ICM is the most dense. Most of these interactions also depend on the velocity difference between the galaxy and the ICM–which also increases as galaxies near the cluster center.

One such process is ram pressure stripping (RPS), which removes the interstellar medium (ISM) of a galaxy as it moves through the ICM by momentum transfer [36]. Ram pressure strength depends on both the ICM density and the relative velocity between the galaxy and the ICM.

$$P_{ram} = \rho_{ICM} v_{diff}^2 \tag{4.2}$$

In order for ram pressure to remove gas from the disk, it must overcome the gravitational force binding gas to the galaxy, calculated as the restoring force per unit area of the disk:

$$F_{grav} = 2\pi G \Sigma_{star} \Sigma_{gas} \tag{4.3}$$

Ram pressure could also compress the gas within a galaxy to increase the SFR in gas that has not been stripped [33].

A galaxy can also be continuously stripped of gas; by, for example, thermal evaporation, Kelvin-Helmholtz instabilties, or turbulent viscous stripping [24, 21, 61]. Any of these continuous stripping processes can act independently from RPS. Cowie & Songaila [24] found that galactic gas can be evaporated at either the unsaturated (in a high density or cool ICM) or saturated (in a low density or hot ICM) rates calculated by Cowie & McKee [23]. The Kelvin-Helmholtz instability occurs when velocity shear is present at the interface of two fluids [21, 1]. The timescale for cloud (or galaxy) destruction is the timescale for the growth of the unstable mode that is the size of the cloud. Finally, Nulsen [61] calculated the maximal mass-loss rate for any cloud using a momentum conservation argument, and called the process turbulent viscous stripping. Any of these processes are unlikely to entirely strip a galaxy of gas–at least not quickly. However, these processes can also aid in mixing gas that has been stripped from the galaxy by ram pressure into the ICM.

Although I have discussed galaxy-ICM interactions in terms of stripping gas from a galactic disk, they can also remove gas from the larger gas halo surrounding the galaxy. Starvation, the removal of the outer gas envelope by the ICM, can result in normal star formation slowly exhausting the gas reservoir in the galaxy disk [51].

5. Morphological Evolution from Spiral to S0

Thus far, I have focused on the color or SFR of galaxies; for example, the scatter in the galaxy color-magnitude diagram and the Butcher-Oemler effect. However, there is a large amount of evidence that the reddening of galaxies in clusters and dense environments reflects the morphological

PoS(Bash11)008

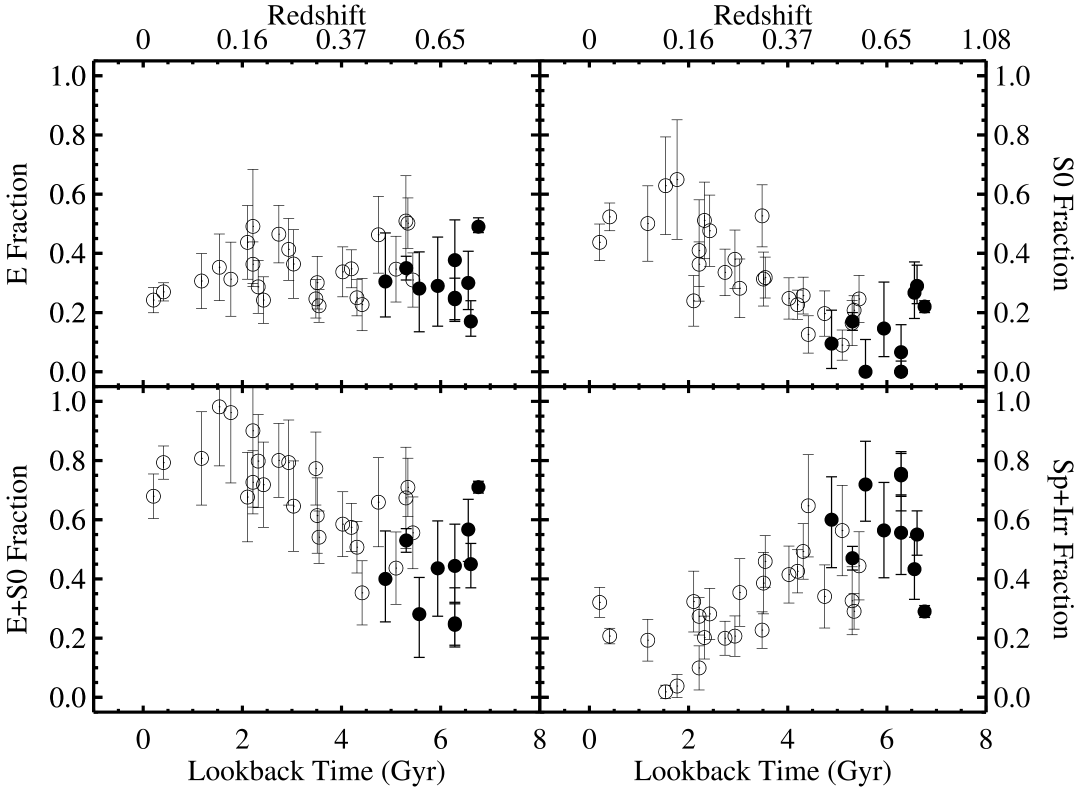

Figure 5: Figure 3 from Desai et al. [27]. As the Sp+Irr fraction of cluster galaxies (within a radius of 600 kpc using the classic cosmology) decreases, the S0 fraction increases and the E fraction remains constant at these redshifts.

evolution of spiral galaxies into S0s. The spiral to S0 ratio decreases with redshift [29, 31, 69, 27]. Desai et al. [27] consider the E, S0, and spiral fraction in clusters out to $z > 1$ (shown in Figure 5), and find that as the spiral fraction decreases, the S0 fraction increases while the elliptical fraction in clusters remains constant. They find that this evolution in morphological fraction begins at $z \sim 0.4$.

In order for a spiral to evolve into an S0, both spectroscopic and morphological changes must take place: the galaxy must become red, it must lose spiral structure in its disk, and the bulge-to-disk ratio must increase.

A simple way for a galaxy to become red is for it to lose its fuel for star formation, and there is strong evidence of pure gas removal in cluster galaxies. In fact, van den Bergh [88] proposed a new galaxy classification system that included “anemic" spirals, gas-poor spirals with low SFRs, and found that these anemic spirals were more frequently found in clusters (also called passive spirals in, e.g. [58, 68]). Poggianti et al. [68] found that at high redshifts the majority of poststarburst galaxies are morphologically identified as spirals, and concluded that the mechanism transforming galaxy color affects only the gas in the galaxies. Solanes et al. [77] studied HI deficiency in 18 clusters and found that HI deficiency–defined by Haynes & Giovanelli [38] as $log_{10}(M_{HI}\ observed/M_{HI}\ expected)$, where $M_{HI}\ expected$ is based on a sample of isolated spirals of the same morphology and optical radius–decreases smoothly out to large projected distances from cluster centers. The nearby Virgo cluster has been studied in much detail, and the spirals in the center of that cluster have smaller HI disks than stellar disks [19, 89]. Koopmann & Kenney [50] find that the reduced massive SFR in Virgo galaxies is linked the the truncation of their star-forming disks.

A galaxy-ICM interaction is the likely mechanism forming passive (or anemic) spirals, because they have had their gas removed but are morphologically spirals (so their stellar disks are relatively undisturbed). If passive spirals are precursors to S0s, then a galaxy-ICM interaction is at least part of the process driving the evolution of normal spirals into S0s. Moran et al. [57] used a simple argument to show that if the passive spiral fraction in Cl 0024+17 was universal at z=0.4, assuming all passive spirals become S0s is consistent with the S0 fraction at z=0.

In a detailed study of the passive spirals and S0s in two intermediate redshift clusters, Moran et al. [58] found that passive spirals were well-fit by stellar population models that input either the gradual cessation of star formation (by, for example, starvation), or a rapid truncation of star formation (by, for example, RPS of the disk gas). The S0s in the clusters also fit these star formation histories, indicating the populations were related. Further, the galaxies undergoing starvation tended to be infalling in groups and the galaxies with truncated star formation were near the centers of the clusters, so the transformation scenario was related to the surrounding ICM. This strongly indicated that passive spirals turn into S0s, and that galaxy-ICM interactions play a large role in that transformation.

The second component in the transformation of a spiral into an S0 is the loss of spiral structure. This can also be a result of gas loss alone. Bekki et al. [8] used simulations to show that if gas is no longer accreted by a galaxy, it will lose its spiral arms in about 3.5 Gyr. This is in good agreement with observational and model estimates for how long morphological transformation may take (e.g [49, 68]). However, as discussed above, Moran et al. [58] found similar stellar populations in passive spirals and S0s, indicating that a faster mechanism was driving morphological evolution.

Finally, I consider the necessary increase in the bulge-to-disk (B/D) ratio. This step can be the result of: 1) growing the bulge, or 2) fading the disk. It seems likely that interactions between galaxies are necessary to grow the bulge of a spiral galaxy, while only gas removal or exhaustion is necessary to fade the disk. Observations have shown that there are S0s in clusters that were likely created by each of these processes [22, 57].

Fading the disk of a galaxy with a B/D = 0.2 will result in a galaxy with a B/D = 0.5, so pure gas removal can turn an Sb galaxy into an S0 galaxy [33, 78]. Solanes et al. [78] find that the bulge luminosities of Sa galaxies are similar to those of S0s, and all types have a range of luminosities, so it is not universally necessary to increase the bulge luminosity to transform a spiral to an S0. However, if the slow fading of the disk was the mechanism at work, the total luminosity of S0s should be less than that of spirals, which is not generally the case [28, 16]. The models of Kodama & Smail [49] indicate that if the evolution of spirals is responsible for the increase in the S0 fraction, all spirals would have to become S0s, even Sc-Sd galaxies with small bulges. For most of these disk-dominated galaxies to become S0s there would have to be bulge growth.

What can grow the bulge of a spiral galaxy? Galaxy harassment can drive instabilities that will heat the disk and result in gas flowing to the galaxy center, which can grow the bulge of a galaxy [55, 56, 32]. Moran et al. [58] find that S0s in Cl 0024+17, a cluster with a recent assembly history, show more kinematic disturbance, indicating that galaxy harassment is one of the mechanisms transforming spirals into S0s. Unequal-mass mergers can also grow the bulge of a spiral galaxy without completely destroying the disk [7]. Fujita & Nagashima [33] find that ram pressure can increase the SFR of a galaxy, and while strong ram pressure will lower the SFR in the disk by removing HI, it will not strip gas from the galaxy center, so star formation will continue. If, as in Schulz & Struck [74] and Tonnesen & Bryan [84], dense gas in the disk that is not immediately stripped will spiral towards the center, the bulge may grow slightly more than just from star formation of the gas that originated in the galaxy center while the disk fades. However, RPS would grow the bulge the least of any of these processes.

5.1 Star Formation in the Disk of a Ram Pressure Stripped Galaxy

While many interactions occur in clusters (galaxy-galaxy, galaxy-cluster, and galaxy-ICM interactions), it is worthwhile to study individual types of interactions in isolation in order to constrain the effects of a single type of interaction. In Tonnesen & Bryan [82], we use the AMR code *Enzo* [14, 60, 62] to run a set of high resolution simulations (38 pc resolution, which is small enough to marginally resolve giant molecular clouds). Here I will discuss our goal to understand whether ram pressure can induce star formation in a galactic disk, producing starburst galaxies or increasing the mass of the bulge.

As discussed in detail in Tonnesen & Bryan [82, 83, 84], the simulation includes radiative cooling using the Sarazin & White [73] cooling curve extended to low temperatures ($T_{\rm min} = 300$ K) as described in Tasker & Bryan [81]. This allows cool, dense gas to form in the galaxy and generates a clumpy, multiphase ISM [81, 84].

In Tonnesen & Bryan [82], star formation occurred when two criteria were met: 1) the gas density in a cell exceeded a critical overdensity (3.85×10^{-25} g cm^{-3}), and 2) the gas temperature was below 1.1×10^4 K. The implementation of star formation and feedback is explained in detail in Tasker & Bryan [81] and in Tonnesen & Bryan [82].

We model a massive spiral galaxy with a flat rotation curve of 200 km s^{-1}. It consists of a gas disk that is followed using the AMR algorithm (including self-gravity of the gas and any newly formed stars), as well as the static potentials of the (pre-existing) stellar disk, stellar bulge, and dark matter halo [72, 82, 83, 84, 85].

In Tonnesen & Bryan [82] we compare the star formation in the disks of two simulations. They both begin with the same galaxy density profiles evolving in a static ICM. SFNW (Star Formation No Wind) evolves in a static ICM, while SFW (Stfar Formation Wind) initially evolves in a static ICM and is later (t$\sim$210 Myr) stripped by a higher-density ICM wind.

We define the disk to extend 2 kpc from the the central disk plane, which includes all of the star formation in the SFNW run. First, in the top panel of Figure 6 (Figure 1 of Tonnesen & Bryan [82]) we plot the SFR as a function of time for the SFNW and SFW runs. For the first 220 Myr the SFRs are nearly identical. Shortly after the ICM wind hits the SFW galaxy disk, its SFR drops precipitously. RPS quickly lowers the SFR and does not induce even a short-lived burst of star formation (at least at the level of ram pressure modeled here).

In the bottom panel of Figure 6 we plot the radius including 95% of the new stars formed in the disk against time. As in the panel above, we find that the two cases are nearly identical for the first 200 Myr. However, it takes until $\sim$290 Myr for the star-formation radii to diverge. This is

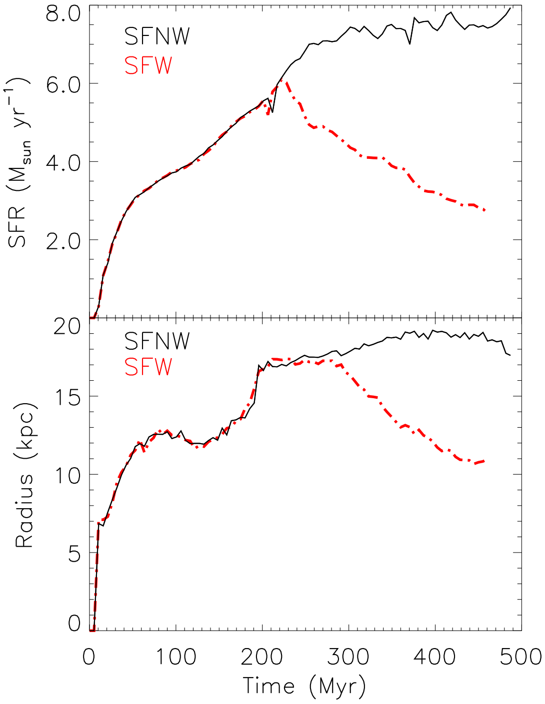

Figure 6: Top panel: SFR as a function of time in the run with no wind (SFNW, black line) and with an ICM wind after ∼210 Myr (SFW, red line). ∼10 Myr after the wind hits the disk, the SFR of SFW begins decreasing, and continues to decrease as gas is stripped. Bottom panel: the disk radius that includes 95% of the new stars formed as a function of time. The star forming radius of SFW decreases later than the SFR, probably because some dense clouds in the disk cannot be stripped by the wind, so form stars.

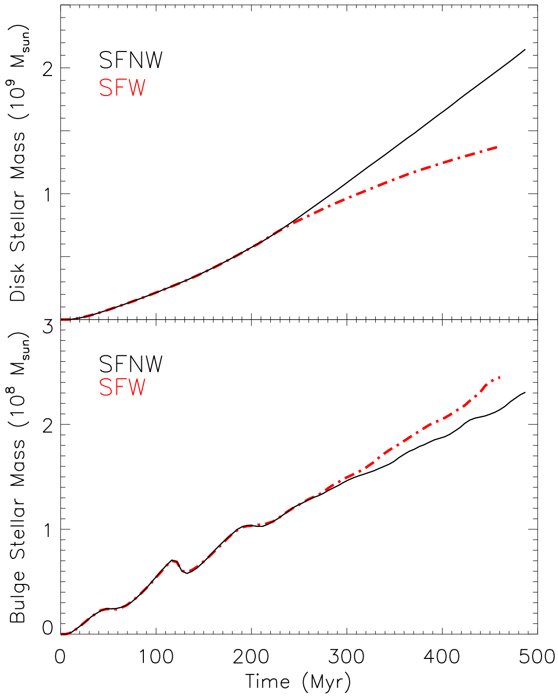

Figure 7: Top panel: Total amount of stellar mass formed in the disk (i.e. within 2 kpc of the disk plane), as a function of time. Shortly after the wind hits SFW, the SFR decreases. Bottom panel: the mass of newly formed bulge stars as a function of time. Ram pressure does lead to more stars in the bulge (all stars within 3.4 kpc of the galaxy center). However, the difference does not significantly change the B/T ratio, which begins at 0.1 with M_{Bulge} = 10^{10} $M_\odot$ and M_{Disk} = 10^{11} $M_\odot$.

likely because dense clouds have formed up to 17 kpc from the disk center that cannot be instantly stripped by the ICM wind. It is only after these clouds have formed stars or been destroyed or stripped by the ICM wind that the star-formation radius drops. Ram pressure is affecting the outer disk, resulting in a dimmer, less massive disk.

We also consider the total amount of newly formed stellar mass in the disk and in the bulge of the galaxy. As shown in the top panel of Figure 7 (Figure 4 in Tonnesen & Bryan [82]), the total stellar mass formed in the disk, since the beginning of the simulation, is nearly identical in SFNW and SFW for the first 200 Myr, but once the wind hits the disk, the two lines begin to diverge.

If we focus only on the bulge stars formed since the simulation began in a sphere with a 3.4 kpc radius from the galaxy center (this includes 80% of the mass in the spherical Hernquist bulge we initially used to determine our galaxy potential [40]), we find that including the wind leads to more stars in the galactic bulge, as shown in the bottom panel of Figure 7. As discussed in Tonnesen & Bryan [84], gas clouds that are not stripped are able to spiral towards the center of the disk due to a loss of angular momentum by drag from the ICM (initially seen by Schulz & Struck [74]). It is this inflow of gas within the disk that adds most of the stars to the bulge (rather than stellar fallback).

The bulge-to-total ratio of new stars is 0.1 in the SFNW galaxy and 0.2 in the SFW galaxy. However, the galaxy initially had a stellar disk mass of 10^{11} $M_\odot$ and a stellar bulge mass of 10^{10} $M_\odot$, so the new stars change the bulge-to-total ratio of stellar mass by at most a few percent. As expected, ram pressure is more effective at fading the galaxy disk than at growing the bulge. However, this conclusion may depend somewhat on our disk model. First, if our galaxy was much less massive, then we might expect the disk to be even more quickly stripped and to dim faster, while the bulge growth may remain very similar. This could affect the bulge-to-disk ratio. Later-type galaxies do tend to be less massive and are the very galaxies for which it is most important that the bulge mass grows in order to produce an S0 [78]. At this ram pressure strength, the galaxy would have to have 2 orders of magnitude less stellar mass for the difference in star formation to have a significant effect on the bulge-to-total mass ratio.

In summary, based on both the observations and simulations discussed in this section, it is likely that RPS alone can slowly transform spirals into S0s that are less luminous than their spiral parents. Gravitational mechanisms can also cause galaxies to lose or consume their gas, and may be more effective at growing the bulge. However, a galaxy disk will certainly survive a galaxy-ICM interaction, which is a necessary constraint on the mechanism driving this morphological evolution.

6. Summary and Future Prospects

In this proceedings, I have discussed the evidence that environment affects galaxy properties, and looked in detail at the scales at which the environment affects galaxies. I have outlined the different environmental mechanisms that can act on cluster galaxies and then focused on the morphological evolution of spirals into S0s. Finally, I focused on work by Tonnesen & Bryan [82] that examined how RPS can affect star formation in galactic disks and bulges. I summarize the main points below:

1) Galaxies in dense environments are more likely to be red. Low-mass galaxies are likely red due to environmental affects (Section 3 and Figure 1).

2) The local environment of galaxies is correlated with galaxy properties such as color, up to the scale of the halo in which a galaxy resides (Section 3.1 and Figures 3 & 4).

3) The color evolution of galaxies from blue to red is likely closely tied to the morphological evolution of galaxies from spirals to S0s (Section 5 and Figure 5).

4) While gas loss alone can drive the evolution of a spiral into an S0 (Section 5), RPS seems unable to grow the bulge enough transform most of the higher redshift cluster spiral population into the local S0 population (Section 5.1 and Figures 6 & 7). It is much more effective at fading the disk than at growing the bulge.

In Section 5 I summarized some of the work examining the mechanisms that can transform spirals into S0s, with a definite focus on the role of gas loss or ram pressure stripping. However, it is worth reiterating that there are many interactions that occur in clusters and groups that could drive the evolution of spirals into S0s. For example, while RPS is a straightforward way to create anemic, or passive, spirals, it may not be the only mechanism that can remove gas without entirely destroying spiral structure in the disk. Detailed observations of the kinematics of the disks of passive spirals in a range of environments–e.g. the centers and outskirts of low- and high-mass clusters–may be used to determine the impact, and likelihood, of gravitational interactions (similar to the work of Moran et al. [58, 59]). In addition, more work can be done to compare the stellar populations of spirals, passive spirals, and S0s to resolve the conflicting timelines of the transformations in Poggianti et al. [68] and Moran et al. [58]. Further, examinations of the kinematics of S0 bulges in a range of environments may be used to distinguish between growth through unequal-mass mergers, which may grow more classical bulges, and growth through gas inflow or excess star formation from harassment or RPS, which may be more likely to grow a psuedobulge.

There is certainly much more work that can be done to examine galaxy evolution in dense environments, and as hydrodynamical cosmological simulations continue to increase their resolution they can also be used to look in detail at both the color and morphological evolution of cluster galaxies.

References

[1] Agertz, O., Moore, B., Stadel, J., Potter, D., Miniati, F., Read, J., Mayer, L., Gawryszczak, A., Kravtsov, A., Nordlund, Å., Pearce, F., Quilis, V., Rudd, D., Springel, V., Stone, J., Tasker, E., Teyssier, R., Wadsley, J., and Walder, R.: 2007, *Monthly Notices of the Royal Astronomical Society* **380**, 963.

[2] Bahcall, N.A.: 1996, *ArXiv Astrophysics e-prints*, arXiv:astro-ph/9611148.

[3] Baldry, I.K., Glazebrook, K., Brinkmann, J., Ivezić, Ž., Lupton, R.H., Nichol, R.C., and Szalay, A.S.: 2004, *Astrophys. J.* **600**, 681.

[4] Balogh, M., Eke, V., Miller, C., Lewis, I., Bower, R., Couch, W., Nichol, R., Bland-Hawthorn, J., Baldry, I.K., Baugh, C., Bridges, T., Cannon, R., Cole, S., Colless, M., Collins, C., Cross, N., Dalton, G., de Propris, R., Driver, S.P., Efstathiou, G., Ellis, R.S., Frenk, C.S., Glazebrook, K., Gomez, P., Gray, A., Hawkins, E., Jackson, C., Lahav, O., Lumsden, S., Maddox, S., Madgwick, D., Norberg, P., Peacock, J.A., Percival, W., Peterson, B.A., Sutherland, W., and Taylor, K.: 2004, *Monthly Notices of the Royal Astronomical Society* **348**, 1355.

[5] Balogh, M.L., Pearce, F.R., Bower, R.G., and Kay, S.T.: 2001, *Monthly Notices of the Royal Astronomical Society* **326**, 1228.

[6] Barnes, J.E. and Hernquist, L.E.: 1991, *Astrophys. J.* **370**, L65.

[7] Bekki, K.: 1998, *Astrophys. J.* **502**, L133.

[8] Bekki, K., Couch, W.J., and Shioya, Y.: 2002, *Astrophys. J.* **577**, 651.

[9] Binney, J.: 1977, *Astrophys. J.* **215**, 492.

[10] Blanton, M.R., Eisenstein, D., Hogg, D.W., Schlegel, D.J., and Brinkmann, J.: 2005, *Astrophys. J.* **629**, 143.

[11] Blanton, M.R., Eisenstein, D., Hogg, D.W., and Zehavi, I.: 2006, *Astrophys. J.* **645**, 977.

[12] Blanton, M.R., Hogg, D.W., Bahcall, N.A., Baldry, I.K., Brinkmann, J., Csabai, I., Eisenstein, D., Fukugita, M., Gunn, J.E., Ivezić, Ž., Lamb, D.Q., Lupton, R.H., Loveday, J., Munn, J.A., Nichol, R.C., Okamura, S., Schlegel, D.J., Shimasaku, K., Strauss, M.A., Vogeley, M.S., and Weinberg, D.H.: 2003, *Astrophys. J.* **594**, 186.

[13] Brooks, A.M., Governato, F., Quinn, T., Brook, C.B., and Wadsley, J.: 2009, *Astrophys. J.* **694**, 396.

[14] Bryan, G.L.: 1999, *Comput. Sci. Eng., Vol. 1, No. 2, p. 46 - 53* **1**, 46.

[15] Bundy, K., Scarlata, C., Carollo, C.M., Ellis, R.S., Drory, N., Hopkins, P., Salvato, M., Leauthaud, A., Koekemoer, A.M., Murray, N., Ilbert, O., Oesch, P., Ma, C.-P., Capak, P., Pozzetti, L., and Scoville, N.: 2010, *Astrophys. J.* **719**, 1969.

[16] Burstein, D., Ho, L.C., Huchra, J.P., and Macri, L.M.: 2005, *Astrophys. J.* **621**, 246.

[17] Butcher, H. and Oemler, A., Jr.: 1978, *Astrophys. J.* **226**, 559.

[18] Byrd, G. and Valtonen, M.: 1990, *Astrophys. J.* **350**, 89.

[19] Cayatte, V., van Gorkom, J.H., Balkowski, C., and Kotanyi, C.: 1990, *The Astronomical Journal* **100**, 604.

[20] Cen, R.: 2010, *ArXiv e-prints*, arXiv:1010.5014.

[21] Chandrasekhar, S.: 1961, *International Series of Monographs on Physics, Oxford: Clarendon, 1961*.

[22] Christlein, D. and Zabludoff, A.I.: 2004, *Astrophys. J.* **616**, 192.

[23] Cowie, L.L. and McKee, C.F.: 1977, *Astrophys. J.* **211**, 135.

[24] Cowie, L.L. and Songaila, A.: 1977, *Nature* **266**, 501.

[25] de Vaucouleurs, G.: 1962, *Problems of Extra-Galactic Research* **15**, 3.

[26] de Vaucouleurs, G.: 1960, *The Astronomical Journal* **65**, 51.

[27] Desai, V., Dalcanton, J.J., Aragón-Salamanca, A., Jablonka, P., Poggianti, B., Gogarten, S.M., Simard, L., Milvang-Jensen, B., Rudnick, G., Zaritsky, D., Clowe, D., Halliday, C., Pelló, R., Saglia, R., and White, S.: 2007, *Astrophys. J.* **660**, 1151.

[28] Dressler, A.: 1980, *Astrophys. J.* **236**, 351.

[29] Dressler, A., Oemler, A., Jr., Couch, W.J., Smail, I., Ellis, R.S., Barger, A., Butcher, H., Poggianti, B.M., and Sharples, R.M.: 1997, *Astrophys. J.* **490**, 577.

[30] Fall, S.M. and Efstathiou, G.: 1980, *Monthly Notices of the Royal Astronomical Society* **193**, 189.

[31] Fasano, G., Poggianti, B.M., Couch, W.J., Bettoni, D., Kjærgaard, P., and Moles, M.: 2000, *Astrophys. J.* **542**, 673.

[32] Fujita, Y.: 1998, *Astrophys. J.* **509**, 587.

[33] Fujita, Y. and Nagashima, M.: 1999, *Astrophys. J.* **516**, 619.

[34] Gómez, P.L., Nichol, R.C., Miller, C.J., Balogh, M.L., Goto, T., Zabludoff, A.I., Romer, A.K., Bernardi, M., Sheth, R., Hopkins, A.M., Castander, F.J., Connolly, A.J., Schneider, D.P., Brinkmann, J., Lamb, D.Q., SubbaRao, M., and York, D.G.: 2003, *Astrophys. J.* **584**, 210.

[35] Gnedin, O.Y.: 2003, *Astrophys. J.* **589**, 752.

[36] Gunn, J.E. and Gott, J.R., III: 1972, *Astrophys. J.* **176**, 1.

[37] Hashimoto, Y., Oemler, A., Jr., Lin, H., and Tucker, D.L.: 1998, *Astrophys. J.* **499**, 589.

[38] Haynes, M.P. and Giovanelli, R.: 1984, *The Astronomical Journal* **89**, 758.

[39] Heinis, S., Budavári, T., Szalay, A.S., Arnouts, S., Aragón-Calvo, M.A., Wyder, T.K., Barlow, T.A., Foster, K., Peter, F.G., Martin, D.C., Morrissey, P., Neff, S.G., Schiminovich, D., Seibert, M., Bianchi, L., Donas, J., Heckman, T.M., Lee, Y.-W., Madore, B.F., Milliard, B., Rich, R.M., and Yi, S.K.: 2009, *Astrophys. J.* **698**, 1838.

[40] Hernquist, L.: 1993, *The Astrophysical Journal Supplement Series* **86**, 389.

[41] Hogg, D.W., Blanton, M.R., Brinchmann, J., Eisenstein, D.J., Schlegel, D.J., Gunn, J.E., McKay, T.A., Rix, H.-W., Bahcall, N.A., Brinkmann, J., and Meiksin, A.: 2004, *Astrophys. J.* **601**, L29.

[42] Hogg, D.W., Blanton, M.R., Eisenstein, D.J., Gunn, J.E., Schlegel, D.J., Zehavi, I., Bahcall, N.A., Brinkmann, J., Csabai, I., Schneider, D.P., Weinberg, D.H., and York, D.G.: 2003, *Astrophys. J.* **585**, L5.

[43] Hubble, E.P.: 1926, *Astrophys. J.* **64**, 321.

[44] Hubble, E. and Humason, M.L.: 1931, *Astrophys. J.* **74**, 43.

[45] Joung, M.R., Cen, R., and Bryan, G.L.: 2009, *Astrophys. J.* **692**, L1.

[46] Kauffmann, G., White, S.D.M., Heckman, T.M., Ménard, B., Brinchmann, J., Charlot, S., Tremonti, C., and Brinkmann, J.: 2004, *Monthly Notices of the Royal Astronomical Society* **353**, 713.

[47] Kereš, D., Katz, N., Fardal, M., Davé, R., and Weinberg, D.H.: 2009, *Monthly Notices of the Royal Astronomical Society* **395**, 160.

[48] Kereš, D., Katz, N., Weinberg, D.H., and Davé, R.: 2005, *Monthly Notices of the Royal Astronomical Society* **363**, 2.

[49] Kodama, T. and Smail, I.: 2001, *Monthly Notices of the Royal Astronomical Society* **326**, 637.

[50] Koopmann, R.A. and Kenney, J.D.P.: 2004, *Astrophys. J.* **613**, 866.

[51] Larson, R.B., Tinsley, B.M., and Caldwell, C.N.: 1980, *Astrophys. J.* **237**, 692.

[52] Melnick, J. and Sargent, W.L.W.: 1977, *Astrophys. J.* **215**, 401.

[53] Merritt, D.: 1984, *Astrophys. J.* **276**, 26.

[54] Moore, B., Katz, N., Lake, G., Dressler, A., and Oemler, A.: 1996, *Nature* **379**, 613.

[55] Moore, B., Lake, G., and Katz, N.: 1998, *Astrophys. J.* **495**, 139.

[56] Moore, B., Lake, G., Quinn, T., and Stadel, J.: 1999, *Monthly Notices of the Royal Astronomical Society* **304**, 465.

[57] Moran, S.M., Ellis, R.S., Treu, T., Salim, S., Rich, R.M., Smith, G.P., and Kneib, J.-P.: 2006, *Astrophys. J.* **641**, L97.

[58] Moran, S.M., Ellis, R.S., Treu, T., Smith, G.P., Rich, R.M., and Smail, I.: 2007, *Astrophys. J.* **671**, 1503.

[59] Moran, S.M., Miller, N., Treu, T., Ellis, R.S., and Smith, G.P.: 2007, *Astrophys. J.* **659**, 1138.

[60] Norman, M.L. and Bryan, G.L.: 1999, *Numerical Astrophysics* **240**, 19.

[61] Nulsen, P.E.J.: 1982, *Monthly Notices of the Royal Astronomical Society* **198**, 1007.

[62] O'Shea, B.W., Bryan, G., Bordner, J., Norman, M.L., Abel, T., Harkness, R., and Kritsuk, A.: 2004, *ArXiv Astrophysics e-prints*, arXiv:astro-ph/0403044.

[63] Ocvirk, P., Pichon, C., and Teyssier, R.: 2008, *Monthly Notices of the Royal Astronomical Society* **390**, 1326.

[64] Oemler, A., Jr.: 1974, *Astrophys. J.* **194**, 1.

[65] Oemler, A., Jr., Dressler, A., and Butcher, H.R.: 1997, *Astrophys. J.* **474**, 561.

PoS(Bash11)008

[66] Pannella, M., Gabasch, A., Goranova, Y., Drory, N., Hopp, U., Noll, S., Saglia, R.P., Strazzullo, V., and Bender, R.: 2009, *Astrophys. J.* **701**, 787.

[67] Perez, J., Tissera, P., Padilla, N., Alonso, M.S., and Lambas, D.G.: 2009, *Monthly Notices of the Royal Astronomical Society* **399**, 1157.

[68] Poggianti, B.M., Smail, I., Dressler, A., Couch, W.J., Barger, A.J., Butcher, H., Ellis, R.S., and Oemler, A., Jr.: 1999, *Astrophys. J.* **518**, 576.

[69] Postman, M., Franx, M., Cross, N.J.G., Holden, B., Ford, H.C., Illingworth, G.D., Goto, T., Demarco, R., Rosati, P., Blakeslee, J.P., Tran, K.-V., Benítez, N., Clampin, M., Hartig, G.F., Homeier, N., Ardila, D.R., Bartko, F., Bouwens, R.J., Bradley, L.D., Broadhurst, T.J., Brown, R.A., Burrows, C.J., Cheng, E.S., Feldman, P.D., Golimowski, D.A., Gronwall, C., Infante, L., Kimble, R.A., Krist, J.E., Lesser, M.P., Martel, A.R., Mei, S., Menanteau, F., Meurer, G.R., Miley, G.K., Motta, V., Sirianni, M., Sparks, W.B., Tran, H.D., Tsvetanov, Z.I., White, R.L., and Zheng, W.: 2005, *Astrophys. J.* **623**, 721.

[70] Rees, M.J. and Ostriker, J.P.: 1977, *Monthly Notices of the Royal Astronomical Society* **179**, 541.

[71] Robertson, B., Yoshida, N., Springel, V., and Hernquist, L.: 2004, *Astrophys. J.* **606**, 32.

[72] Roediger, E. and Brüggen, M.: 2006, *Monthly Notices of the Royal Astronomical Society* **369**, 567.

[73] Sarazin, C.L. and White, R.E., III: 1987, *Astrophys. J.* **320**, 32.

[74] Schulz, S. and Struck, C.: 2001, *Monthly Notices of the Royal Astronomical Society* **328**, 185.

[75] Silk, J.: 1977, *Astrophys. J.* **211**, 638.

[76] Smith, G.P., Treu, T., Ellis, R.S., Moran, S.M., and Dressler, A.: 2005, *Astrophys. J.* **620**, 78.

[77] Solanes, J.M., Manrique, A., García-Gómez, C., González-Casado, G., Giovanelli, R., and Haynes, M.P.: 2001, *Astrophys. J.* **548**, 97.

[78] Solanes, J.M., Salvador-Sole, E., and Sanroma, M.: 1989, *The Astronomical Journal* **98**, 798.

[79] Sorrentino, G., Antonuccio-Delogu, V., and Rifatto, A.: 2006, *Astron. Astroph.* **460**, 673.

[80] Strateva, I., Ivezić, Ž., Knapp, G.R., Narayanan, V.K., Strauss, M.A., Gunn, J.E., Lupton, R.H., Schlegel, D., Bahcall, N.A., Brinkmann, J., Brunner, R.J., Budavári, T., Csabai, I., Castander, F.J., Doi, M., Fukugita, M., Győry, Z., Hamabe, M., Hennessy, G., Ichikawa, T., Kunszt, P.Z., Lamb, D.Q., McKay, T.A., Okamura, S., Racusin, J., Sekiguchi, M., Schneider, D.P., Shimasaku, K., and York, D.: 2001, *The Astronomical Journal* **122**, 1861.

[81] Tasker, E.J. and Bryan, G.L.: 2006, *Astrophys. J.* **641**, 878.

[82] Tonnesen, S. and Bryan, G.L.: 2011, *submitted to Monthly Notices of the Royal Astronomical Society*

[83] Tonnesen, S. and Bryan, G.L.: 2010, *Astrophys. J.* **709**, 1203.

[84] Tonnesen, S. and Bryan, G.L.: 2009, *Astrophys. J.* **694**, 789.

[85] Tonnesen, S., Bryan, G.L., and Chen, R.: 2011, *Astrophys. J.* **731**, 98.

[86] Tonnesen, S. and Cen, R.: 2011, *ArXiv e-prints*, arXiv:1111.0636.

[87] Treu, T., Ellis, R.S., Kneib, J.-P., Dressler, A., Smail, I., Czoske, O., Oemler, A., and Natarajan, P.: 2003, *Astrophys. J.* **591**, 53.

[88] van den Bergh, S.: 1976, *Astrophys. J.* **206**, 883.

[89] Warmels, R.H.: 1988, *Astronomy and Astrophysics Supplement Series* **72**, 427.

[90] White, S.D.M. and Rees, M.J.: 1978, *Monthly Notices of the Royal Astronomical Society* **183**, 341.

[91] Whitmore, B.C. and Gilmore, D.M.: 1991, *Astrophys. J.* **367**, 64.

PROCEEDINGS OF SCIENCE

The Reddest Quasars: A Transitional Phase in Quasar/Galaxy Co-Evolution

Eilat Glikman*
Yale
E-mail: eilat.glikman@yale.edu

Quasars are extremely luminous sources powered by accretion of gas onto a supermassive black hole in the nucleus of some galaxies. Most of the $> 10^5$ quasars identified in the literature have been identified in optical surveys through the "ultraviolet excess" (UVX) method. However, these samples are known to be incomplete and biased because of obscuration and anisotropic radiation. To overcome some of these biases and search for candidate obscured quasars, we matched radio sources from the FIRST 1.4 GHz survey with the 2MASS near-infrared survey and selected objects with red optical-to-near-infrared colours. We followed up our candidates with optical and/or near-infrared spectroscopy and identified 119 dust-reddened quasars, defined as having at least one broad emission line in and a reddening of $E(B-V) > 0.1$. The sample spans a wide redshift range, $0.1 < z < 3$ and reaches a reddening, $E(B-V) \lesssim 1.5$. When corrected for extinction, red quasars are the most luminous objects at every redshift and the fraction of red quasars increases with luminosity. The properties of red quasars suggest that they are revealing an evolutionary phase where the heavily obscured quasar is emerging from its dusty environment prior to becoming a "normal" blue quasar. We compute the fraction of quasars that are in this red phase and determine that its duration is $\sim 20\%$ as long as the unobscured quasars phase: a few million years.

Frank N. Bash Symposium New Horizons In Astronomy,
October 9-11, 2011
Austin Texas

*Speaker.

PoS(Bash11)009

1. Introduction

A fundamental goal of observational cosmology is to answer the question of how galaxies evolved throughout cosmic time. Several pieces of observational evidence suggest that the growth of supermassive black holes (SMBHs) may play a key role in answering this question. Locally, SMBHs are a ubiquitous feature in massive galaxies [1] and their masses appear to correlate with the global properties of their host galaxies, such as the stellar velocity dispersion (the $M_{\rm BH} - \sigma$ relation [2, 3]) and the luminosity of the stellar bulge [4]. A recent compilation of the $M_{\rm BH} - \sigma$ relation is shown in Figure 1, left [5].

These observations are remarkable: stars in the bulge, located kiloparsecs away from their galactic centers, are not influenced by the gravitational potential of the SMBH, whose sphere of influence is a few parsecs. Since the stars cannot "know" about the SMBH, perhaps they arrived on this relation in tandem with the BH.

A third piece of evidence that supports the assertion that SMBHs and their host galaxies "co-evolved" is seen by examining the cosmological evolution of BH growth and star-formation rate. We see in Figure 1, right, that the quasar luminosity density (a proxy for the growth of SMBHs via accretion) rises sharply with redshift and peaks at $z \sim 2$ declining thereafter to $z \sim 6$. This behavior is mirrored in the evolution of the star formation rate density, suggesting that SMBHs and galaxies have built up symbiotically [6, 7, 8].

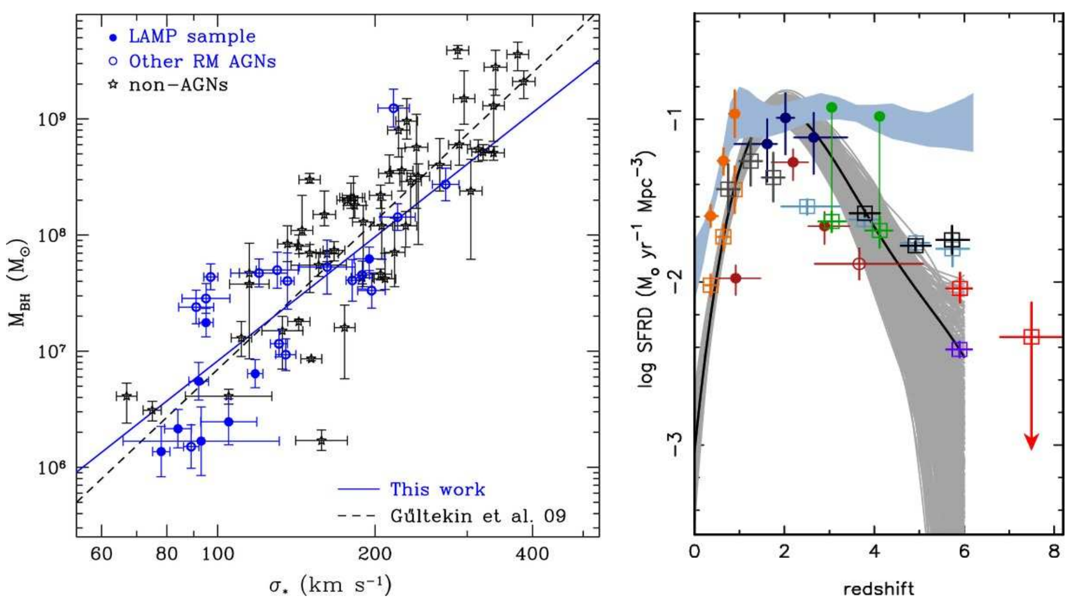

Figure 1: *Left* – The $M_{\rm BH} - \sigma$ relation from [5] showing the tight correlation between the mass of the SMBH of a galaxy and the stellar velocity dispersion, spanning ~ 4 orders of magnitude in BH mass. *Right* – The redshift evolution of QSO luminosity density is plotted in the shaded region over-plotted by measurements of the star formation rate [8].

Galaxy mergers appear to be very important in explaining the co-evolution of galaxies and SMBHs. Gas rich mergers produce bursts of star formation and provide fuel to feed the SMBH and power a quasar. The energy released by the quasar expels enough gas to quench both star formation and further black hole growth (i.e., feedback). Theoretical models of merging galaxies appear to require a SMBH in order to match observations. In particular, the absence of SMBHs, and the feedback that they generate, would produce far too much star formation than is observed [9, 11, 10].

This merger-driven model for SMBH/galaxy co-evolution links different observed types of galaxies as stages of evolution. Sanders et al. (1988) presented a picture that "... ultraluminous infrared galaxies (ULIRGs) represent the initial, dust-enshrouded stages of quasars. Once these nuclei shed their obscuring dust, allowing the AGN to visually dominate the decaying starburst, they become optically selected quasars" [9]. Local ULIRGs are predominantly seen in merging systems. Quasars live in bulge-dominated, massive ellipticals [12, 13, 14]. If the evolutionary scenario is correct, then there is a missing stage of evolution where the buried, growing BH emerges from the ULIRG as it evolves into a luminous quasar.

1.1 What is a Quasar?

Quasars are extremely luminous sources, powered by accretion of gas onto a supermassive black hole in the nucleus of a galaxy. They were originally discovered as optical counterparts to bright radio sources. The first quasar, 3C273, was cataloged as a bright radio source in the Third Cambridge (3C) radio catalog in 1963. It was coincident with an abnormally blue star with unidentifiable emission features. It was soon realized that these unusual lines were redshifted Balmer emission lines, placing this object at $z = 0.158$, the highest redshift known at the time [15]. Another bright radio source, also with a blue stellar optical counterpart, 3C48, was then interpreted as having an even higher redshift of $z = 0.367$ [16].

In the $H_0 = 100$ cosmology of 1963, the high redshift of 3C273 implied that it was at a distance of 500 Mpc. This distance, combined with its bright optical magnitude ($V = 13$) further implied that it was hundreds of times the luminosity of a typical galaxy concentrated in a region smaller than 1000 pc in diameter. Spectroscopic follow-up of dozens of optical counterparts to point-like, bright radio sources from the 3C and 4C radio catalogs led to discoveries of more such objects with the same characteristics, named Quasi-Stellar Radio Souces (Quasars):

- Broad emission lines in their optical spectra.
- Narrow forbidden emission lines of high ionization atomic species.
- Large ultraviolet flux of radiation.
- Extremely large luminosities emanating from very compact regions.
- High redshifts.
- Flux variability in many cases.

Using the fact that quasars had blue $U - B$ colors and stellar appearances on optical photographic plates, a population of objects with optical properties identical to quasars was discovered, but without the radio emission ("radio quiet quasars") [17]. With improved color selection and high-quality, wide-field, optical surveys, there are now over 10^5 known quasars and only $\sim 10\%$ are radio-loud. Figure 2 shows a quasar composite spectrum spanning the optical through near-infrared [18].

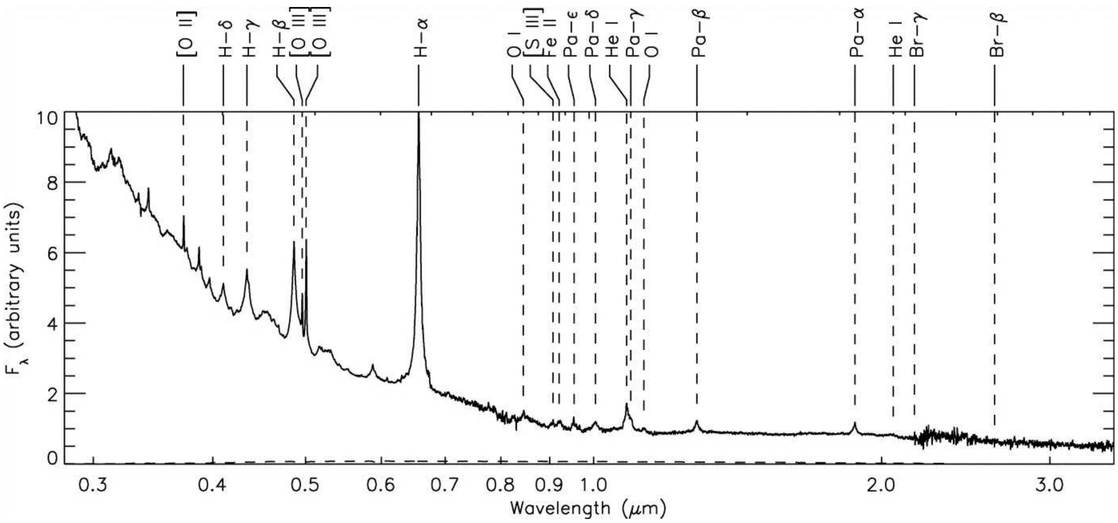

Figure 2: Optical through near-infrared composite spectrum from [18], demonstrating the strong blue optical and ultraviolet shape of the spectral energy distribution as well as the broad emission lines.

We now have a clearer picture of the physics of accretion onto nuclear SMBHs depicted by Active Galactic Nuclei (AGN), of which quasars are the most luminous type. These classifications are different manifestations of the same physical phenomena giving rise to a continuum in luminosity. Quasars outshine their host galaxies, appearing stellar in images, and can be seen to cosmological distances. They are rare, with a low volume density. On the other hand, AGN are lower luminosity. They are more numerous than quasars and are found at low redshifts in the nuclei of resolved galaxies.

1.2 Obscuration and Redding in Quasars

The properties of local AGN support an axisymmetric, orientation-based model for their structure. This model, shown in Figure 3, can explain many of their observed properties. In particular, the presence of absorption from dusty clouds, often modeled as a torus, outside the broad line region results in a spectrum showing only narrow emission lines (referred to as "Type II" sources). This model is also successful at unifying the observed properties of radio galaxies [19].

At low redshift, low-luminosity AGN fit the orientation-based picture very well. The Type I AGN are those objects observed from the pole direction. Type II AGN are those sources whose inner parts can only be seen through reflected radiation, from their polarized light. At high redshifts, Type II (obscured) quasars had been elusive. Large samples have been recovered in the Sloan Digital Sky Survey [37, SDSS] and subsequently in deep X-ray surveys [20, 21, 22, 23, 24] .

An important corollary to the orientation-based explanation is that the covering fraction of the obscuring clouds decreases with increasing luminosity; this is known as the receding torus model [25]. An increase in the ratio of obscured/unobscured AGN with decreasing luminosity has been seen in samples of X-ray selected AGN samples that show, in support of this model[26, 27, Figure 3, right].

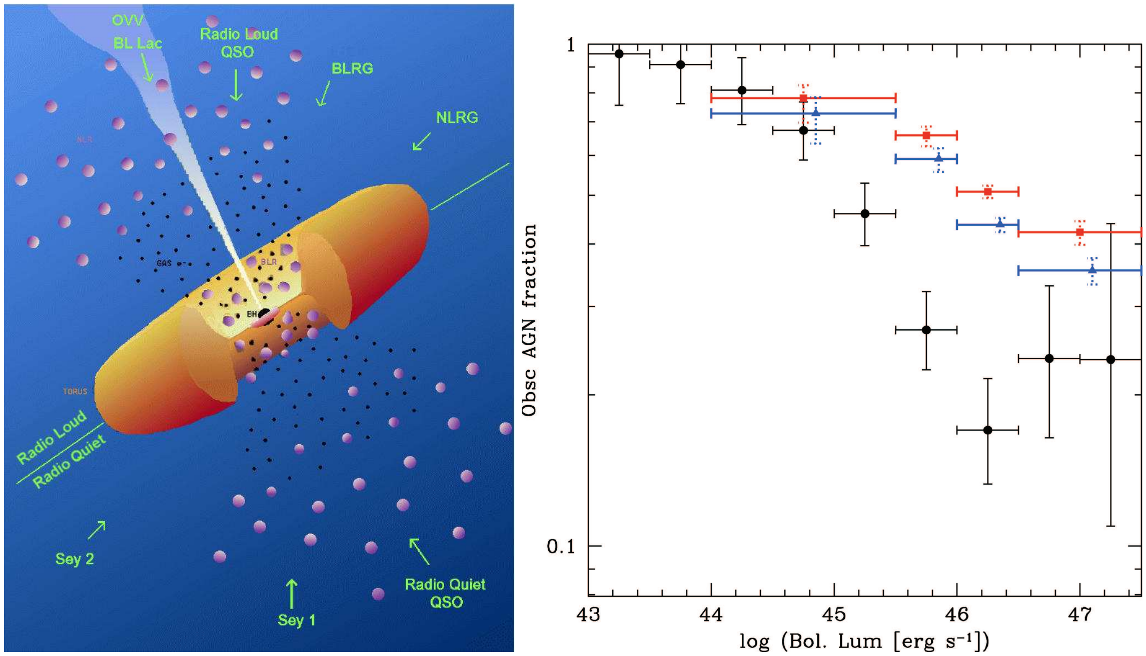

Figure 3: *Left* – Schematic unification model for AGN demonstrating the dependence of the observed radiation on the viewing angle [19]. Right – Fraction of obscured AGN as a function of AGN bolometric luminosity [27]. The fraction of obscured AGN increases strongly with decreasing luminosity, consistent with the receding torus model and AGN unificaiton.

2. Finding Red Quasars: The FIRST-2MASS Survey

The AGN obscuration described above is the result of orientation and is not part of the evolutionary picture outlined in the Introduction. To identify the missing link in the path from ULIRG to quasar, we must search for a new and different class of obscured quasars: red quasars. The rest of this paper concerns these objects, how they are different from other quasars, and why it matters.

There are $> 10^5$ quasars identified in the literature. Most are found in the optical, in searches for blue, ultraviolet excess (UVX) objects. However, the presence of dust along the line of sight to a quasar will both redden and dim the light from the quasar. As a consequence, flux-limited optically-selected quasar samples are biased against dust-obscured objects. A few magnitudes of extinction will remove faint objects and leave only the most luminous sources in a flux-limited sample [28, Figure 4]. Quasars will also be missed because their colors no longer obey the UVX color cuts. In fact, reddening can cause quasars' colors to shift into the stellar locus in their optical colors making them nearly impossible to find in optical surveys.

To address this, we conducted a deliberate search for red quasars utilizing three criteria in three wavelength regimes. We matched the FIRST[1] radio catalog [29], which mapped a quarter of the sky at 1.4 GHz to a sensitivity of 1 mJy, to the near-infrared 2MASS survey[2] (referred to as the F2M survey, hereafter) and selected objects that were *not* detected in the Automated Plate Machine (APM) scans of the first generation Palomar Sky Survey (POSS-I). This effectively imposed optical

[1]Faint Images of the Radio Sky at Twenty Centimeters, `http://sundog.stsci.edu`

[2]Two-Micron All Sky Survey, `http://www.ipac.caltech.edu/2mass/`

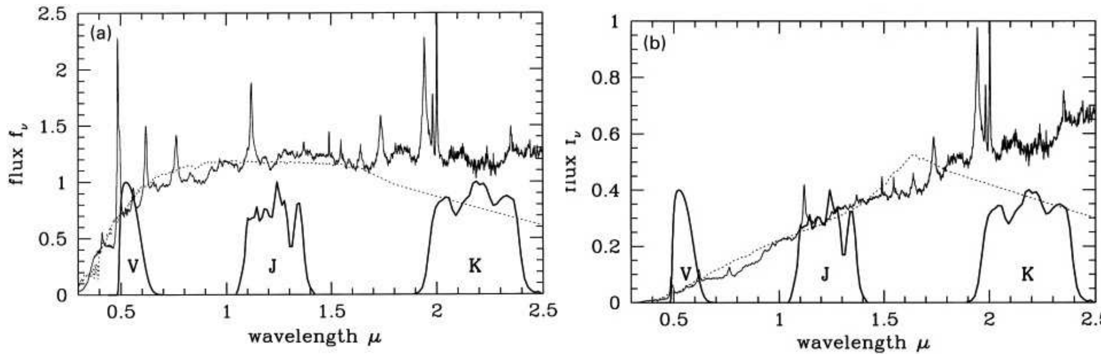

Figure 4: Optical through near-infrared spectral energy distribution for quasars (solid line) and stars (dotted line), showing typical optical and near-infrared bandpasses V, $J<$ and K. *Left* – An unreddened quasar at $z = 3$ with a K star. *Right* – Reddened quasar with E(B-V)=0.3 at z=2.5 and an early M star. While optical light is lost due to extinction, near-infrared light suffers little extinction and is a better wavelength for selecting reddened quasars [28].

flux limits of $R \gtrsim 20$ and $B \gtrsim 21.5$. We chose to include the radio criterion in order to avoid strong contamination from low mass stars (e.g., M dwarfs) which are abundant in the near infrared, but do not emit strongly in the radio. This pilot project resulted in 69 candidates over 2716 deg^2. Spectroscopic identification of 54 of these resulted in a sample of 17 heavily reddened quasars [30]. Figure 5 shows the optical-to-near-infrared colors for this sample. We identified a set of color cuts, $R-K > 4$ and $J-K > 1.7$ which maximize our efficiency of finding red quasars while avoiding stars (yellow circles) and galaxies (green circles).

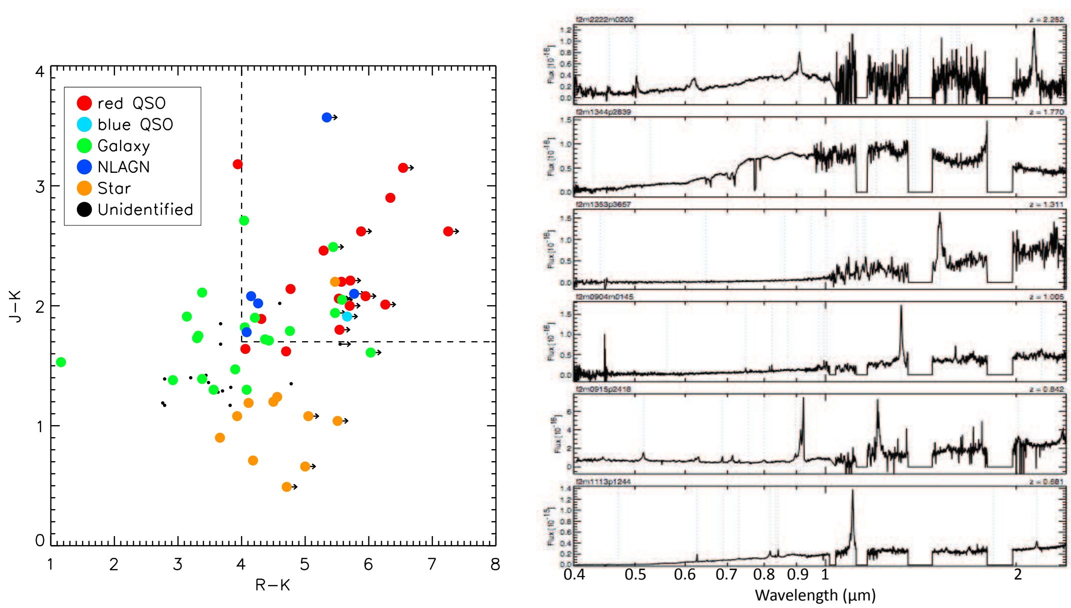

Figure 5: *Left* – $J-K$ vs. $R-K$ colors of optical drop outs in the FIRST-2MASS pilot study [30]. Spectroscopically identified objects are colored and labeled in the legend. The dashed lines define color cuts that maximize red quasar selection. *Right* – Example spectra from the F2M red quasar survey covering optical-to-near-infrared wavelengths ($0.4-2.4\mu$m).

Having identified an efficient color selection method for finding red quasars, we expanded the survey to include objects *with* optical detections, requiring only that they obey the aforementioned color cuts [31, 32] and searched the full area of the FIRST survey [33]. This effort produced a catalog of 394 candidates over 9033 deg^2. We performed a spectroscopic followup campaign in the optical and near-infrared and produced 316 spectroscopic identifications (80% completeness). Among these spectra, 119 are red quasars – *by far* the largest sample of dust reddened quasars, whose selection is uniform and well-understood, to date. A set of sample spectra from the F2M red quasar survey are shown in Figure 5, right.

3. Properties of Red Quasars

To determine the amount of dust along the line-of-sight to each quasar, we fit a reddened quasar template to our red quasar spectra applying an exponential reddening law to the composite.

$$F = F_0 \exp^{-k(\lambda)E(B-V)/1.086} \tag{3.1}$$

Where $k(\lambda)$ is the Small Magellenic Cloud (SMC) reddening law [34]. Example fits are shown in Figure 6, left.

We de-redden the F2M red quasar spectra to study their intrinsic properties. With the intrinsic brightness of the F2M red quasars in hand we can compare their number counts to the number counts of blue, optically-selected quasars to determine the fraction of quasars that are missed in optical flux-limited surveys that rely on UVX (or other blue color) optical selection. In Figure 6, right, we show the surface density of F2M red quasars before (red filled squares) and after (purple open squares) de-reddening. We compare their number counts per square degree with those of quasars from the FIRST Bright Quasar Survey ([35, 36] FBQS; crosses and x symbols). FBQS quasars were selected by matching the FIRST survey with the APM catalog and selecting objects with blue colors. We then match this sample to 2MASS to produce a quasar catalog that reaches the same flux depth as F2M in the radio and near-infrared, which makes it a natural blue-equivalent survey to F2M. We also constructed a radio- and infrared-detected catalog from the SDSS by matching the fifth quasar catalog from SDSS [38] to FIRST and 2MASS (triangles).

Comparing the space densities of red and blue quasars, we find that the observed fraction of F2M quasars make up $10 \pm 1\%$ in flux limited samples. In other words, 10% more quasars are recovered when changing to a near-infrared flux-limited survey from an optical survey such as POSS-I or SDSS. Once we correct the red quasars for extinction we see that intrinsically, F2M quasars make up $19.2 \pm 2.6\%$ of radio-selected quasars with $K \leq 14.5$ magnitudes.

Figure 7 shows the de-reddened absolute K-band magnitude for the F2M red quasars colored by the amount of reddening that we computed for each source (yellow circles are mildly reddened, while redder circles are more heavily reddenend). We plot for comparison the FBQS quasars with small black points, for which we assume no extinction correction is necessary. This figure reveals a remarkable trend: at all redshifts, red quasars are the most luminous objects. This trend showing an increase of red quasar fraction with *increasing* luminosity goes in the opposite direction as the trend for Type I/II quasars, i.e., the receding torus model. We conclude that the F2M quasars are not reddened by nuclear obscuration but are rather an evolutionary phase.

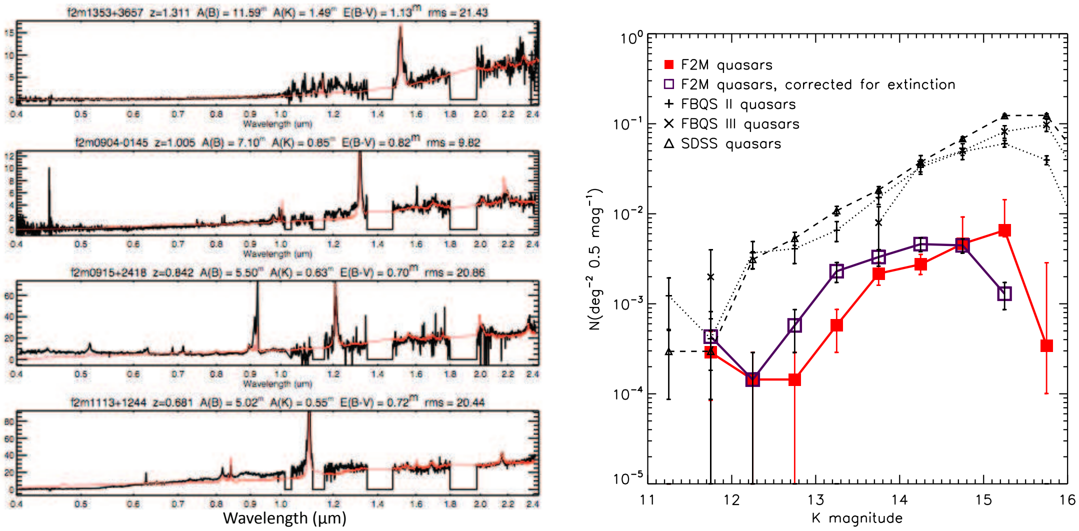

Figure 6: *Left* – Examples of fits of a reddened quasar template to F2M red quasars to determine $E(B-V)$, for each quasar which enables de-reddening. The quasar spectra are plotted with a black line and the reddend template fit is overplotted with a red line. *Right* – Number counts per square degree for F2M red quasars before and after de-reddening (filled red and open violet squares, respectively) compared with the same for FBQS (crosses and x's) and SDSS quasars matched to FIRST and 2MASS (triangles).

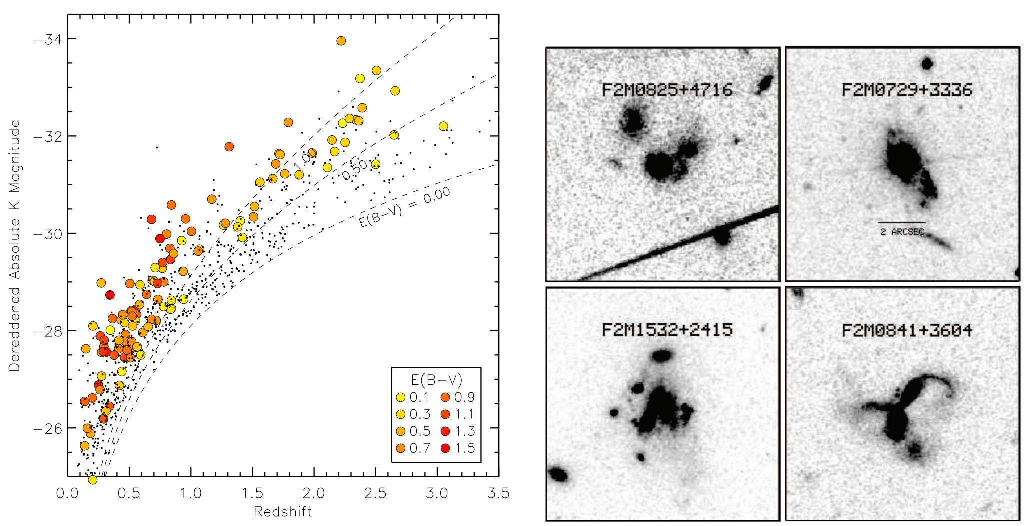

Figure 7: *Left* – De-reddened absolute $K-$band magnitude of red quasars (circles) colored by the amount of reddening that they experience, defined in the legend, compared with the same for FBQS quasars, which we assume are not obscured. At every redshift, red quasars are the most luminous objects. *Right* – Hubble Space Telescope images of four objects from our F2M sample showing intense merging and interaction in these reddened quasars.

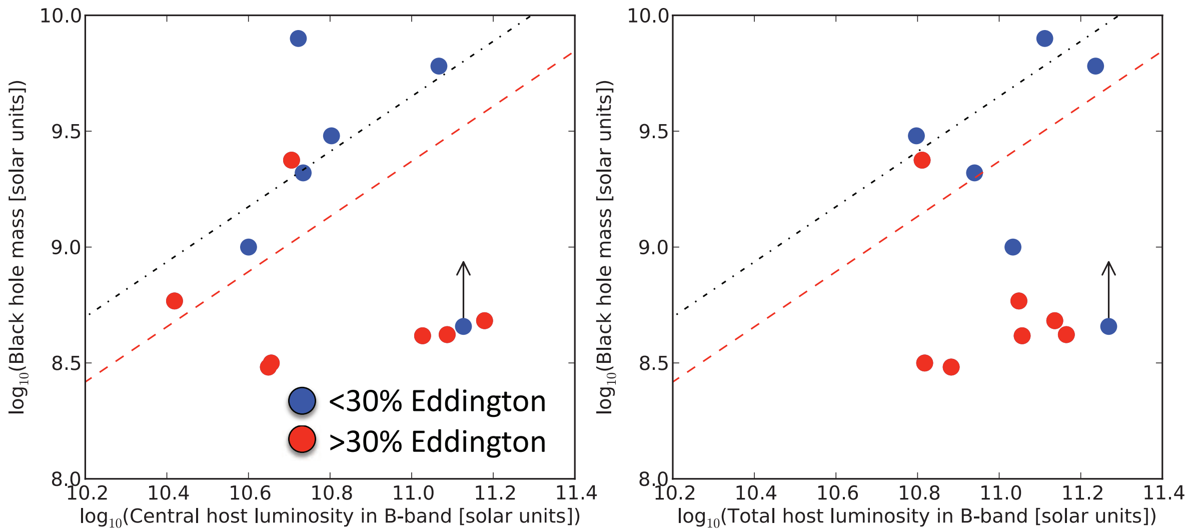

Figure 8: Black hole mass vs. host luminosity for the F2M red quasars [40]. Red circles are quasars with accretion rates higher than 30% of the Eddington rate. The objects with the highest accretion rates fall *below* the relation, suggesting that they are still growing their black holes while the stellar mass has already assembled.

4. Red Quasars are a Phase in Quasar/Galaxy Co-Evolution

We describe here the full body of evidence in support of red quasars being a phase in quasar/galaxy co-evolution rather than an orientation-based phenomenon. Thirteen red quasar hosts were imaged with the Advanced Camera for Surveys (ACS) on the *Hubble Space Telescope* (*HST*) during Cycle 13. All the images reveal a nearby companion and eleven show interacting or disrupted morphologies, as shown in Figure 7, right [39]. These images suggest that the F2M red quasars are a consequence of merger activity, as predicted by the merger driven quasar/galaxy co-evolution model.

We have also obtained *Spitzer* infrared IRS spectroscopy (covering $5-38\mu$m) and MIPS photometry (24, 70, and 160 μm) of the same thirteen red quasars that had *HST* images. This long wavelength sampling of the quasars' spectral energy distribution (SED) allowed us to determine their bolometric luminosities. Incorporating this with a black hole mass estimate based on the width of the broad lines in the red quasar spectra, we compute their accretion rates and Eddington ratios. Figure 8 shows the BH mass vs. host luminosity relation for the F2M red quasars. We see a large fraction of objects with high black hole accretion rates (red circles have $L_{\rm EDD} > 30\%$), consistent with the idea that quasar accretion rates are high in this early phase of growth. Furthermore, the red quasars with the highest Eddington rates lie below the $M_{\rm BH} - L_{\rm Bulge}$ relation. This offset from the local relation is consistent with a picture in which some of the black holes are yet to grow to their equilibrium size following a major merger [40].

The existence of a population of red quasars is consistent with a merger-driven picture of SMBH/galaxy co-evolution in which gas rich galaxies, each hosting a BH, merge and, in the process, induce both a starburst and fuel the growth of the nuclear SMBH. Figure 9 shows the predicted lightcurves from such a model [42]. On the left the full merger is shown over a 2 Gyr period. The light curves for the quasar phase, highlighted by a red oval in the lower left hand panel, is expanded on the right where the column density (i.e., obscuration) as a function of time is shown in the top panel, followed by the bolometric luminosity in the middle panel and the observed *B*-band luminosity in the bottom. In this model, the growing BH spends most of its time in a deeply buried, heavily obscured phase, followed by a clearing of the obscuring material via AGN feedback, revealing a blue, unobscured quasar as the final phase.

The characteristics of the F2M red quasars fit very well into this picture, not as the deeply obscured, earliest, growth phase (as has been seen in in ULIRGs [9]), but rather as a transitional phase from completely obscured to blue quasar. This transition is indicated by the vertical colored line in Figure 9, right. The fraction of red quasars therefore represents the duration of the phase, $\sim$ 20% of a typical quasar lifetime, which has been estimated to be a few $\times 10^7$ years [41], suggesting that the emergence phase lasts a few million years.

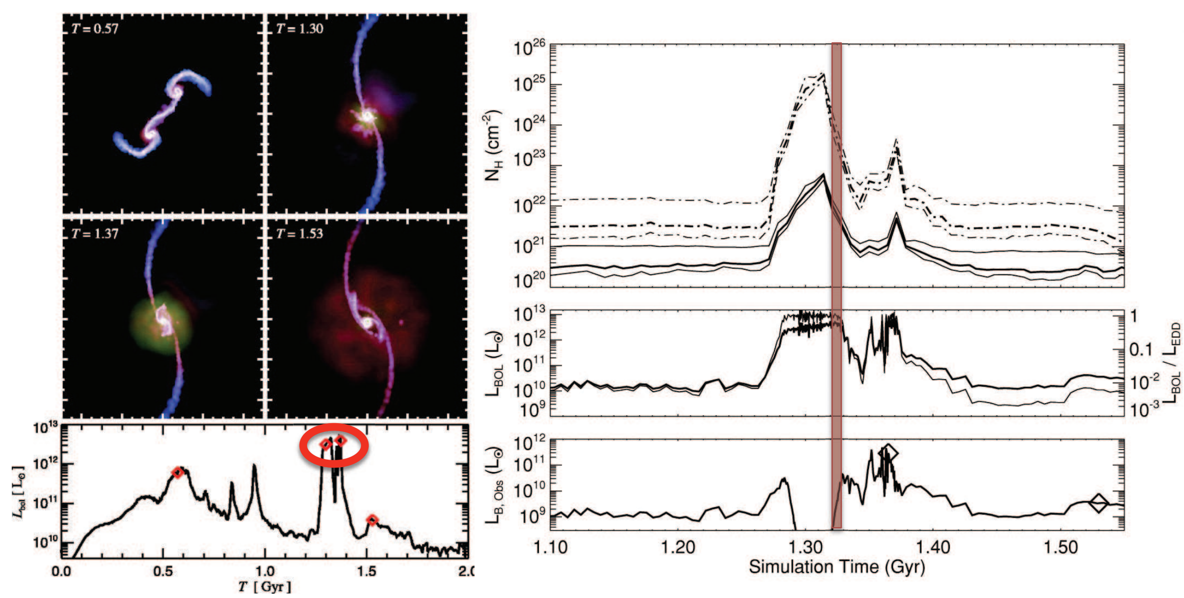

Figure 9: Quasar lightcurve during a major merger from [42]. *Left* – The full evolution of the bolometric luminosity over a 2 Gyr timespan. The quasar phase is highlighted with a red oval and zoomed in on the right-hand panel. *Right* – The evolution of the quasar phase of a major merger is shown for three observables. The the column density as a function of time is shown in the top panel, followed by the bolometric luminosity in the middle, and the observed *B*-band luminosity in the bottom panel. While the bolometric luminosity peaks twice, the first peak is obscured, hiding much of the BH growth which is invisible in the optical. The quasar emerges from the obscuration, during a reddened phase (highlighted by the shaded stripe), eventually revealing the unobscured BH growth.

5. Conclusions

We have identified a population of dust-obscured red quasars selected using a method that identified red-colored objects with detections in the radio and near-infrared. Based on their number counts compared to a well matched blue quasar comparison sample, we find that their fraction is $\sim$ 20% of the total quasar population, down to $K \leq 14.5$ magnitudes. Once we correct their observed brightness for extinction, we find that they are *the most luminous sources at every redshift*. High resolution imaging of a subsample of red quasar hosts reveals that they reside in highly disturbed, interacting galaxies. Many are accreting at or above the Eddington limit, and lie below the $M_{\rm BH} - L_{\rm Bulge}$ relation, suggesting that the black holes are rapidly growing to catch up to the relation for inactive galaxies. Our interpretation is that reddened quasars are revealing an *emergent phase* where the heavily obscured quasar is shedding its cocoon of dust prior to becoming a "normal" blue quasar. Based on the fraction of objects in this phase, the duration of this cycle is $\sim$ 20% as long as the unobscured quasar phase: a few million years.

References

[1] Kormendy, J. 2004, Coevolution of Black Holes and Galaxies, 1

[2] Ferrarese, L., & Merritt, D. 2000, ApJ, 539, L9

[3] Gebhardt, K., Bender, R., Bower, G., et al. 2000, ApJ, 539, L13

[4] Marconi, A., & Hunt, L. K. 2003, ApJ, 589, L21

[5] Woo, J.-H., Treu, T., Barth, A. J., et al. 2010, ApJ, 716, 269

[6] Shaver, P. A., Wall, J. V., Kellermann, K. I., Jackson, C. A., & Hawkins, M. R. S. 1996, Nature, 384, 439

[7] Boyle, B. J., & Terlevich, R. J. 1998, MNRAS, 293, L49

[8] Wall, J. V., Jackson, C. A., Shaver, P. A., Hook, I. M., & Kellermann, K. I. 2005, A&A, 434, 133

[9] Sanders, D. B., Soifer, B. T., Elias, J. H., et al. 1988, ApJ, 325, 74

[10] Hopkins, P. F., Hernquist, L., Cox, T. J., et al. 2006, ApJS, 163, 1

[11] Di Matteo, T., Springel, V., & Hernquist, L. 2005, Nature, 433, 604

[12] Dunlop, J. S., McLure, R. J., Kukula, M. J., et al. 2003, MNRAS, 340, 1095

[13] Floyd, D. J. E., Kukula, M. J., Dunlop, J. S., et al. 2004, MNRAS, 355, 196

[14] Floyd, D. J. E., Axon, D., Baum, S., et al. 2010, ApJ, 713, 66

[15] Schmidt, M. 1963, Nature, 197, 1040

[16] Greenstein, J. L. 1963, Nature, 197, 1041

[17] Sandage, A. 1965, ApJ, 141, 1560

[18] Glikman, E., Helfand, D. J., & White, R. L. 2006, ApJ, 640, 579

[19] Urry, C. M., & Padovani, P. 1995, PASP, 107, 803

[20] Zakamska, N. L., Strauss, M. A., Krolik, J. H., et al. 2003, AJ, 126, 2125

[21] Zakamska, N. L., Strauss, M. A., Heckman, T. M., Ivezić, Ž., & Krolik, J. H. 2004, AJ, 128, 1002

[22] Zakamska, N. L., Schmidt, G. D., Smith, P. S., et al. 2005, AJ, 129, 1212

[23] Zakamska, N. L., Strauss, M. A., Krolik, J. H., et al. 2006, AJ, 132, 1496

[24] Reyes, R., Zakamska, N. L., Strauss, M. A., et al. 2008, AJ, 136, 2373

[25] Lawrence, A. 1991, MNRAS, 252, 586

[26] Treister, E., Virani, S., Gawiser, E., et al. 2009, ApJ, 693, 1713

[27] Treister, E., Krolik, J. H., & Dullemond, C. 2008, ApJ, 679, 140

[28] Warren, S. J., Hewett, P. C., & Foltz, C. B. 2000, MNRAS, 312, 827

[29] Becker, R. H., White, R. L., & Helfand, D. J. 1995, ApJ, 450, 559

[30] Glikman, E., Gregg, M. D., Lacy, M., et al. 2004, ApJ, 607, 60

[31] Glikman, E., Helfand, D. J., White, R. L., et al. 2007, ApJ, 667, 673

[32] Urrutia, T., Becker, R. H., White, R. L., et al. 2009, ApJ, 698, 1095

[33] Glikman, E., Urrutia, T., Lacy, M., et al. 2012, Submitted to ApJ

[34] Gordon, K. D., & Clayton, G. C. 1998, ApJ, 500, 816

[35] White, R. L., Becker, R. H., Gregg, M. D., et al. 2000, ApJS, 126, 133

[36] Becker, R. H., White, R. L., Gregg, M. D., et al. 2001, ApJS, 135, 227

[37] York, D. G., Adelman, J., Anderson, J. E., Jr., et al. 2000, AJ, 120, 1579

[38] Schneider, D. P., Richards, G. T., Hall, P. B., et al. 2010, AJ, 139, 2360

[39] Urrutia, T., Lacy, M., & Becker, R. H. 2008, ApJ, 674, 80

[40] UrrutiaT., Lacy, M., Spoon, H., Glikman, E., et al. 2012, Submitted to ApJ

[41] Porciani, C., Magliocchetti, M., & Norberg, P. 2004, MNRAS, 355, 1010

[42] Hopkins, P. F., Hernquist, L., Martini, P., et al. 2005, ApJ, 625, L71

PoS(Bash11)009

PROCEEDINGS OF SCIENCE

Black Hole – Galaxy Co-evolution

Kevin Schawinski*
Einstein Fellow
Department of Physics, Yale University, New Haven, CT 06511, U.S.A.
Yale Center for Astronomy and Astrophysics, Yale University, P.O. Box 208121, New Haven, CT 06520, U.S.A.
E-mail: kevin.schawinski@yale.edu

The growth of black holes and the formation and evolution of galaxies appear to be linked at such a fundamental level that we think of the two as 'co-evolving.' Recent observations show that this co-evolution may be complex and the result of several different pathways. While it is clear that black hole accretion is linked to specific phases of the evolution of the host galaxy, the impact of the energy liberated by the black hole on the evolutionary trajectory of the host by feedback is less clear. In this contribution, I review the motivations for co-evolution, the current state of the observational picture, and some challenges by black hole feedback.

Frank N. Bash Symposium New Horizons In Astronomy,
October 9-11, 2011
Austin Texas

*Speaker.

PoS(Bash11)010

1. Why Co-evolution?

The impact that accreting black holes can have on their surrounding galaxies is profound yet still poorly understood. A full description of why, how, and when black holes alter the evolutionary pathways of their host galaxies remains one of the major outstanding questions in astrophysics.

Semi-analytic models of the formation and evolution of galaxies from cosmological initial conditions cannot produce observed galaxy population properties without the additional injection of energy. This energy is required to prevent gas cooling and therefore the runaway formation of stars [1; 3; 5; 47]. As highly efficient sources of energy, accreting black holes at the centers of galaxies are now routinely invoked as the source of this energy and thus as a fundamental component in galaxy formation theory [58] .

This process, called 'feedback,' thus casts the black hole into the role of a thermostat for the gas in galaxies. By heating and expelling gas that would otherwise cool and condense into stars, black hole feedback is capable of fundamentally changing and controlling the evolutionary trajectory of their host galaxies and in turn the further growth of the black hole as it starves itself of fuel. This close relationship between galaxies and their central black holes can thus be described as 'co-evolution,' potentially beginning with the birth of both in the early Universe.

2. Evidence for Co-evolution

The accretion of mass onto supermassive black holes and the conversion of baryons from gas into stars (observed as galaxy stellar mass growth – star formation) follow similar general trends: the cosmic star formation history and the black hole accretion history track each other preserving roughly a ratio of 1000:1, which notably corresponds to the mass ratio between galaxy bulges and black holes observed in the local $M_{\rm BH} - \sigma$ relation [9; 14; 16], whose existence is also often invoked as evidence for co-evolution. Both star formation and black hole accretion history peak around $z \sim 1-2$ and then decline rapidly towards the present day.

The two growth histories also share further similarities: the most massive galaxies form in intense starbursts at high redshift while less massive galaxies have more extended star formation histories that peak later with decreasing mass [2; 61; 62; 37]. This 'anti-hierarchical' nature is mirrored in black hole growth: the most massive black holes likely grow in intense quasar phases which peak in the early universe, while less massive black holes have more extended, less intense (low Eddington-ratio) growth histories that peak at lower redshift [68; 15; 46]

This does not imply that star formation rate and black hole accretion rate simply track each other within each galaxy; not every galaxy with a high star formation rate is also a quasar, and vice versa. Rather, within individual galaxies there seems to be an interplay, a co-evolution which regulates the whole galaxy–black hole system to conform to the general trend. How this regulation works is at the heart of the question of how co-evolution works.

The other major piece of evidence often cited in favor of co-evolution is the $M_{\rm BH} - \sigma$ relation; since the gravitational sphere of influence of the black hole is tiny compared to the host galaxy, fine tuning of the growth of both is required to produce a tight relation, as is observed. However, recent work by Peng(2007; [43], refined by Jahnke & Maccio [19]) argues that a correlation between galaxy and black hole mass need not be the result of a causal relation at all. Rather, the nature

PoS(Bash11)010

of hierarchical assembly in a ΛCDM universe naturally results in a correlation after a sufficiently large number of mergers via the Central Limit Theorem. This does not mean that the $M_{\mathrm{BH}} - \sigma$ relation really has a non-causal origin, but rather that its interpretation is not straightforward.

3. Multiple Modes of Co-evolution

Recent observational advances in understanding the co-evolution of galaxies and black holes point to the existence of multiple modes. Thus, taking a 'macro' view of both the galaxy and the active galactic nucleus (AGN) host galaxy population is critical in any attempt to disentangle the large number of physical parameters such as mass, environment, morphology, and star formation rate. *Large samples and high-quality multi-wavelength data are thus essential if we are to map out the evolutionary pathways that lead to co-evolution and feedback.*

In order to understand co-evolution, we need to take such samples and assess two fundamental questions.

1. **At what stage in their lives do galaxies feed their black holes?**
   What are the physical properties of galaxies where accretion is favored? Are these galaxies transitioning from one evolutionary stage to another, or are they representatives of a general, stable phase? How many different, separate AGN host galaxy populations are there, *i.e.* how many pathways are there to black hole accretion?

2. **What effect does black hole growth have on the evolutionary trajectory of galaxies?**
   This question must be answered separately for each AGN host galaxy population: does the energy liberated by the accretion phase actually impact the host galaxy, or does it dissipate without consequences? How does the energy couple to the gas in the host galaxy, and how does this depend on accretion mode (radiative vs. kinetic feedback)?

It is important to address both questions as it is possible to imagine particular phases of galaxy evolution leading to accretion, but not feedback. In this case, the assumption that a high AGN fraction in this population is indicative of a high impact of AGN on the host galaxies is misleading.

3.1 The Local Universe

The advent of large samples from the Sloan Digital Sky Survey [70] has enabled large studies of AGN host galaxies. These studies showed that AGN host galaxies appear to be an 'intermediate' population: they are neither blue and actively star-forming, nor are they red and passively evolving; rather, they reside in the 'green valley' in between the two general galaxy populations. Their morphology also appeared to be in-between: large bulges with some disk component. These observations have led to the interpretation of AGN host galaxies as galaxies undergoing transformation from blue star-forming galaxies to red and dead ellipticals [21].

Recently, a more complex picture has emerged. The local AGN host galaxy population is in fact a composite of two distinct groups. The fraction of the local AGN host galaxy in major mergers is negligible [7], though the incidence of mergers in the *Swift* BAT sample is significantly higher [27]; this is most likely due to the very shallow flux limit of the BAT sample which biases it to high luminosity objects. The remainder is divided between early-type galaxies (∼10%) and late-type

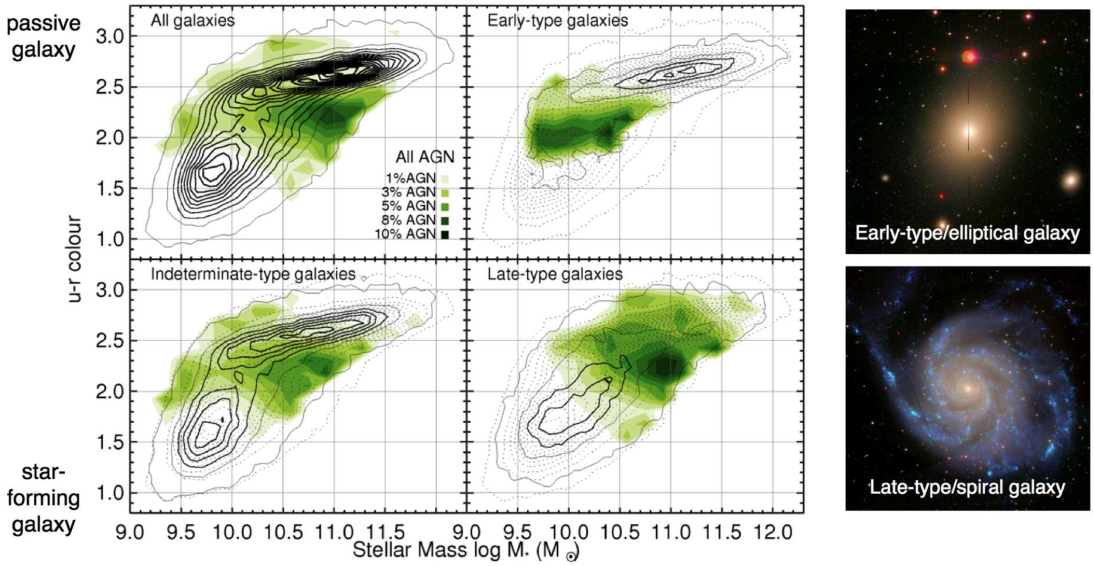

Figure 1: The distribution of the fraction of galaxies that host AGN on the color-mass diagram together with example images of an early-type (or elliptical) galaxy (top right) and a late-type (or spiral) galaxy (bottom right). The contours represent the normal galaxy population while the green shaded contours trace the fraction of galaxies with growing central black holes. The active fraction in a specific sub-population is a proxy for the duty cycle of AGN in that population; it reveals which galaxy populations have a high black hole growth duty cycle and illustrates the importance of morphology for understanding the role of black hole growth in galaxy evolution [51]. The morphological classifications were made by the citizen scientists taking part in the Galaxy Zoo project (`galaxyzoo.org`, Lintott et al. 28, 30)

galaxies ($\sim$ 90%). Both of these two populations are very specific subsets of their parent populations (early-type and late-type galaxies, respectively) indicating that there are two fundamentally different modes of black hole fueling and co-evolution in the local universe ([51] and Figure 1):

3.2 Early-type AGN Host Galaxies – Merger-driven Migration from Blue to Red

In the early-type galaxy population, black hole growth occurs in the least massive ($10^{9.5-10.5} M_\odot$) early-type galaxies with the bluest host galaxy colors amongst the early-type population. They reside in the 'green valley,' and their stellar populations show that they feature post-starburst objects migrating from the blue cloud to the red sequence at roughly fixed stellar mass, thus populating the low-mass end of the red sequence [48]. They *may* represent a 'downsized' version of the formation process undergone at high redshift by their more massive counterparts [61; 62]. Deep imaging of early-type galaxies along the evolutionary sequence migrating from blue to red indicate that this migration is initiated in at least half, and perhaps all cases, by a merger or interaction [52].

However, the concentration of AGN host galaxies in the green valley also challenges the traditional picture of the quenching of star formation by AGN feedback. Even assuming instantaneous quenching, stellar evolution dictates that the migration from the blue cloud to the green valley takes at least $\sim$ 100 Myr (roughly the lifetime of OB stars). Detailed stellar population age-dating by Schawinski et al. (2007) [48] shows that the typical post-starburst timing of high-Eddington Seyfert activity ranges from ~ 270 Myr to ~ 1 Gyr, *i.e.* long after the quenching event. Thus, the black hole growth in the green valley and the associated energy that is liberated cannot be responsible for the shutdown of star formation. An unbiased search for AGN host galaxies using hard X-rays yields no 'missing' powerful AGN in blue host galaxies [49].

This observation does not entirely negate AGN as the agent responsible for the shutdown of star formation, it merely shows that the radiatively efficient Seyfert phase in the green valley is not the accretion phase responsible for the quenching of star formation. It may simply be the 'mopping up' phase. At earlier times along the transition from the blue cloud to the red sequence, early-type galaxies do lose their molecular gas – the fuel for star formation – very rapidly [50]. This destruction of the molecular gas reservoir occurs before the high-Eddington Seyfert phase but coincides with weak AGN photoionization being present in the optical spectrum combined with still on-going star formation. Could this be the phase where a radiatively inefficient AGN is destroying the molecular gas reservoir?

Simple modeling of the depletion of molecular gas reservoirs following the Schmidt law for star formation [56] by Kaviraj et al. (2011) [22] shows that in the absence of an extra forcing mechanism, galaxies cannot rapidly quench their star formation since star formation is a self-regulated process. Every dynamical time, $t_{\rm dyn}$, they will convert a fraction of their available gas reservoir $M_{\rm gas}$ into stars with some efficiency ε (canonically ~ 0.02) resulting in a depletion timescale for gas-rich galaxies of many Gyrs—precisely what is observed for star-forming spirals. In order to rapidly quench star formation and enable the migration to the red sequence within ~ 1 Gyr, some process beyond star formation alone must destroy or make unavailable the present molecular gas reservoir; the best candidate for this process is (kinetic) AGN feedback.

3.3 Late-type AGN Host Galaxies – Secular Evolution and Stochastic Feeding

Most (up to 90%) of local AGN host galaxies are massive spirals. They show no evidence for post-starburst stellar populations [71] or morphological disturbances indicating a recent catastrophic interaction or change in star formation rate. In fact, the typical late-type AGN host galaxy has the physical parameters of the Milky Way [51; 36]: a massive spiral with a low specific star formation rate—hence the green valley host galaxy colors, in contrast to the early-types whose color is due to post-starburst stellar populations. Since there is no evidence for significant external forcing of the system, the most likely explanation for the accretion seen in these late-type host galaxies is stochastic feeding of the black hole via secular processes [26].

Since the typical local AGN host galaxy is similar to the Milky Way, the Galactic Center makes an excellent case study for what precisely leads to black hole feeding and feedback. While quiescent at the moment, observations show that the black hole in the Galactic Center was a low luminosity AGN as recently as 300 years ago as seen in hard X-ray light echos traveling across the molecular clouds surrounding the black hole [45; 40; 41]. The recently-discovered Fermi Bubble may also be a remnant of recent accretion [60].

3.4 The High Redshift Universe

The bulk of both black hole growth and star formation occurs at high redshift with the peak epoch for both occurring around $z \sim 2$. This peak epoch has been difficult to study due to the lack

PoS(Bash11)010

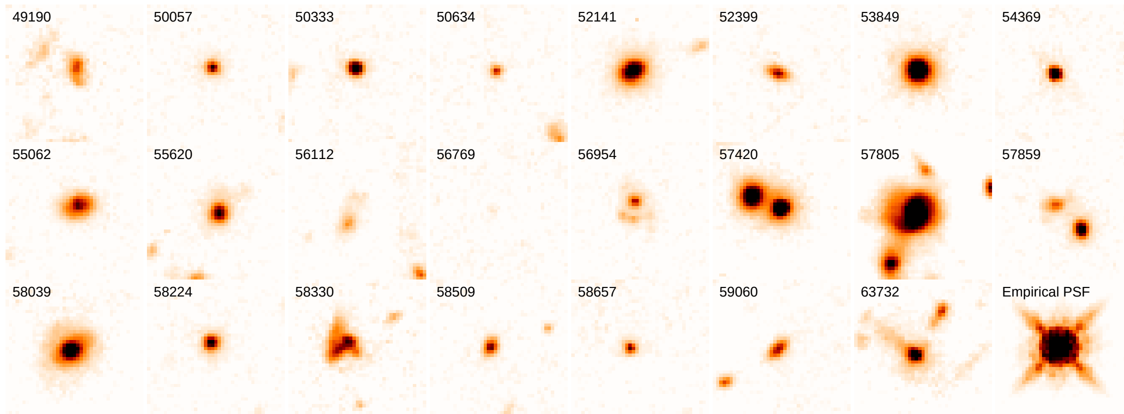

Figure 2: *Hubble Space Telescope* WFC3/IR images of typical z 2 moderate luminosity AGN host galaxies. These images are taken with the infrared channel of the Wide Field Camera 3 and show for the first time the rest-frame optical morphologies of $z \sim 2$ AGN. Analysis of the surface-brightness profiles of these galaxies show disk-like profiles in 80% of cases with the remainder composed of bulges and mergers. This means that a significant fraction of cosmic black hole growth in typical galaxies occurred in disk galaxies and are therefore likely driven by secular processes rather than major mergers as suggested by simulations by theorists [54].

of deep, high quality observations. Deep X-ray surveys over the last decade have captured black hole growth out to very high redshift and down to relatively low luminosities and have revealed a large population of moderate-luminosity AGN at $1 < z < 3$ where normal mass black holes grow [see reviews by 4; 67]. This growth is slow as the Eddington ratios are moderate [57].

Rest-frame optical spectroscopy from the ground is extremely challenging even with 8-10m telescopes [e.g. 64] while space-based infrared spectroscopy is only now becoming possible with the new *Hubble Space Telescope* Wide Field Camera 3 (WFC3) which has a slitless (grism) mode [e.g. 59; 55].

Recent imaging observations with WFC3/IR have revealed that the majority of the moderate luminosity AGN at $1 < z < 3$ feature disk light profiles rather than being massive bulges or major mergers (Schawinski et al. 54 confirmed by Kocevski et al. 24). This implies that the high redshift AGN host galaxy population is in fact very similar to that in the nearby universe: mostly disk galaxies, a few spheroids and virtually no major mergers. Thus, black hole growth at $z \sim 2$ is likely driven by stochastic fueling and secular processes. Observations from *Herschel* by [35] support this picture as the far-infrared derived specific star formation rates of X-ray selected AGN host galaxies up to $z \sim 3$ are indistinguishable from the underlying galaxy population.

Combining this observation with what we know from the local universe, we arrive at a picture where a significant fraction of cosmic black hole growth can be attributed to secular processes (Schawinski et al. 54 estimate $\sim 40\%$) and that major mergers as a driver for black hole growth may be restricted to only a small fraction of the black hole growth in normal mass galaxies. Only at the highest luminosities do highly disturbed morphologies indicative of major mergers begin to appear [e.g. 69; 72].

A large caveat on any conclusions drawn from X-ray selected sample is that even the deep-

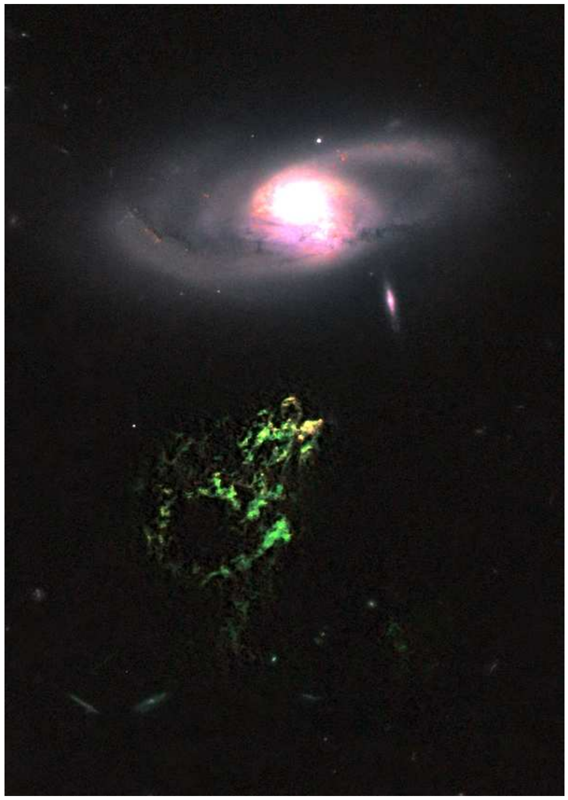

Figure 3: *Hubble Space Telescope* image of the galaxy IC 2497 (top) and Hanny's Voorwerp (green, [OIII] 5007). The Voorwerp is a light echo from a past quasar episode of the dormant black hole in IC 2497. The light travel time between the nucleus and the Voorwerp implies a time delay of less than 70,000 years, preserving a record of a powerful quasar phase in IC 2497 in the recent past (credit: NASA, ESA, W. Keel (University of Alabama), and the Galaxy Zoo Team)

est *Chandra* deep field surveys miss the most obscured black hole growth phases even when the underlying bolometric luminosity of the AGN is high. The X-ray emission from these AGN is so heavily absorbed that they are only betrayed by 'excess' mid-infrared emission from hot dust in the nucleus, which even large amounts of extinction cannot remove [e.g. 63; 6; 10; 64; 11; 65]. Expectations from simulations [e.g. 8; 17; 18] indicate that heavily obscured, high luminosity AGN (quasars) at high redshift should reside in galaxies undergoing major mergers, and that it is during this obscured phase preceding the classical unobscured quasar phase that the quasar begins to blow the gas, thus quenching the star formation in the host galaxy. Near future observation with *Hubble* may shed light on these poorly studied obscured AGN and whether they conform to the picture expected from simulations.

4. Accretion States and Transitions

The previous discussion of AGN host galaxy properties approaches the second question – the question of whether the energy liberated by black hole growth actually affects the host galaxy –

only indirectly by observing that most AGN host galaxies appear to be stable disk galaxies with, at least locally, no evidence for recent enhancement or quenching of star formation.

This raises the question of where we actually see AGN terminating, or at least modifying, star formation properties in their host galaxies. More or less the only unambiguous cases are the giant ionized outflows observed in powerful radio galaxies by [38; 39]. Even in the case of dramatic examples such as the powerful molecular gas outflows seen in Mrk 231 by Fischer et al.(2010) [12], a starburst-driven wind cannot be entirely ruled out.

The commonality of black hole accretion phenomenology and physics exhibited by X-ray binaries (XRBs) and AGN has been discussed extensively in the literature [e.g. 31; 34; 25] and is particularly interesting since some XRBs are known to put out large amounts of kinetic energy, directly impacting their environment [e.g. 13; 42]. If, as has been hypothesized, AGN can undergo rapid accretion state transitions similar to XRBs, could the radiatively efficient (quasar) phase be less important for feedback work? And could radiatively inefficient, kinetic outflows be how a large fraction of feedback work by black holes actually occurs? If so, then how do we find these radiatively inefficient—i.e. dim—AGN?

One case where this *might* be occurring is the nearby ($z = 0.05$) galaxy IC 2497, which features a light echo of a recent (>200,000 yr) powerful quasar outburst preserved on a giant external atomic hydrogen cloud [29; 20; 44, see Figure 3]. The nucleus of IC 2497, which hosted a $L_{\rm bol} \sim 10^{46-47}$ ergs^{-1} less than 200,000 years ago, is now at least four orders of magnitude dimmer [53]. The rapidity of this 'switch off' makes IC 2497 the best and most accessible place to test the hypothesis that quasars can undergo state transitions into a radiatively inefficient, kinetic mode.

There are now other examples of similar 10-100 kyr timescale variability in local AGN [23; 32; 33], giving further support to the XBR-AGN analogy and raising the prospect that radiatively inefficient accretion modes are an important missing piece in the feedback puzzle.

5. Open Questions & Prospects

The role of black holes and their capacity to liberate large amounts of energy during their growth phases remains one of the thorniest issues in extragalactic astrophysics. While we are approaching a fairly complete census of black hole growth and host galaxy properties in the local universe, the high redshift universe remains only partially explored as low-luminosity and heavily-obscured AGN remain elusive in even the deepest surveys. Recent observational advances point to an increasing importance of secular processes in feeding black hole growth and to multiple, distinct pathways to black hole feeding. Thus, the answer to question 1 is that there are a number of very different points along the evolutionary pathways of galaxies during which black hole growth occurs.

The evidence for feedback remains conflicting and may well be limited to very specific phases of galaxy evolution, such as spheroid formation. The possibility that feedback is kinetic in form driven by radiatively inefficient black hole growth remains attractive. Despite this it remains poorly explored in the galaxy regime. Thus, question 2 remains more complex, though answers may be forthcoming in the near future. In particular, direct observations of black hole feedback on molecular gas reservoirs using the Atacama Large Millimeter Array (ALMA) will likely be revealing.

PoS(Bash11)010

Present-day facilities such as *Chandra* and *Hubble*, combined with the next generation of near-infrared spectrographs on 8-10m telescopes, will continue to inform our picture of galaxy and black hole growth at high redshift as first glimpses of the earliest phases of both start to come into view [66], though fully understanding the black hole – galaxy connection all the way to the first objects in the universe may require the *James Webb Space Telescope*.

Acknoweldgements

I am grateful for the Bash '11 Symposium organizers at the University of Austin – Texas for inviting me and for organizing such a wonderful meeting and I thank Ezequiel Treister and Meg Urry for comments. I acknowledge support by NASA through an Einstein Postdoctoral Fellowship (PF9-00069), issued by the Chandra X-ray Observatory Center, which is operated by the Smithsonian Astrophysical Observatory for and on behalf of NASA under contract NAS8-03060.

References

[1] Benson, A. J., Bower, R. G., Frenk, C. S., et al. 2003, ApJ, 599, 38

[2] Bower, R. G., Lucey, J. R., & Ellis, R. S. 1992, MNRAS, 254, 601

[3] Bower, R. G., Benson, A. J., Malbon, R., et al. 2006, MNRAS, 370, 645

[4] Brandt, W. N., & Hasinger, G. 2005, ARA&A, 43, 827

[5] Croton, D. J., Springel, V., White, S. D. M., et al. 2006, MNRAS, 365, 11

[6] Daddi, E., Alexander, D. M., Dickinson, M., et al. 2007, ApJ, 670, 173

[7] Darg, D. W., Kaviraj, S., Lintott, C. J., et al. 2010, MNRAS, 401, 1552

[8] Di Matteo, T., Springel, V., & Hernquist, L. 2005, Nature, 433, 604

[9] Ferrarese, L., & Merritt, D. 2000, ApJ, 539, L9

[10] Fiore, F., Grazian, A., Santini, P., et al. 2008, ApJ, 672, 94

[11] Fiore, F., Puccetti, S., Brusa, M., et al. 2009, ApJ, 693, 447

[12] Fischer, J., Sturm, E., González-Alfonso, E., et al. 2010, A&A, 518, L41

[13] Gallo, E., Fender, R., Kaiser, C., et al. 2005, Nature, 436, 819

[14] Gebhardt, K., Bender, R., Bower, G., et al. 2000, ApJ, 539, L13

[15] Hasinger, G., Miyaji, T., & Schmidt, M. 2005, A&A, 441, 417

[16] Heckman, T. M., Kauffmann, G., Brinchmann, J., et al. 2004, ApJ, 613, 109

[17] Hopkins, P. F., Hernquist, L., Cox, T. J., et al. 2005, ApJ, 630, 705

[18] Hopkins, P. F., Hernquist, L., Martini, P., et al. 2005, ApJ, 625, L71

[19] Jahnke, K., & Macciò, A. V. 2011, ApJ, 734, 92

[20] Józsa, G. I. G., Garrett, M. A., Oosterloo, T. A., et al. 2009, A&A, 500, L33

[21] Kauffmann, G., Heckman, T. M., Tremonti, C., et al. 2003, MNRAS, 346, 1055

[22] Kaviraj, S., Schawinski, K., Silk, J., & Shabala, S. S. 2011, MNRAS, 415, 3798

[23] Keel, W. C., Chojnowski, S. D., Bennert, V. N., et al. 2011, MNRAS, 2099

[24] Kocevski, D. D., Faber, S. M., Mozena, M., et al. 2011, arXiv:1109.2588

[25] Körding, E. G., Jester, S., & Fender, R. 2006, MNRAS, 372, 1366

[26] Kormendy, J., & Kennicutt, R. C., Jr. 2004, ARA&A, 42, 603

[27] Koss, M., Mushotzky, R., Veilleux, S., et al. 2011, ApJ, 739, 57

[28] Lintott, C. J., Schawinski, K., Slosar, A., et al. 2008, MNRAS, 389, 1179

[29] Lintott, C. J., Schawinski, K., Keel, W., et al. 2009, MNRAS, 399, 129

[30] Lintott, C., Schawinski, K., Bamford, S., et al. 2011, MNRAS, 410, 166

[31] Maccarone, T. J., Gallo, E., & Fender, R. 2003, MNRAS, 345, L19

[32] Marecki, A., & Swoboda, B. 2011, A&A, 530, A60

[33] Marecki, A., & Swoboda, B. 2011, A&A, 525, A6

[34] McHardy, I. M., Koerding, E., Knigge, C., Uttley, P., & Fender, R. P. 2006, Nature, 444, 730

[35] Mullaney, J. R., Pannella, M., Daddi, E., et al. 2011, MNRAS, 1756

[36] Mutch, S. J., Croton, D. J., & Poole, G. B. 2011, ApJ, 736, 84

[37] Nelan, J. E., Smith, R. J., Hudson, M. J., et al. 2005, ApJ, 632, 137

[38] Nesvadba, N. P. H., Lehnert, M. D., Eisenhauer, F., et al. 2006, ApJ, 650, 693

[39] Nesvadba, N. P. H., Lehnert, M. D., De Breuck, C., Gilbert, A. M., & van Breugel, W. 2008, A&A, 491, 407

[40] Nobukawa, M., Tsuru, T. G., Takikawa, Y., et al. 2008, PASJ, 60, 191

[41] Nobukawa, M., Ryu, S. G., Tsuru, T. G., & Koyama, K. 2011, ApJ, 739, L52

[42] Pakull, M. W., Soria, R., & Motch, C. 2010, Nature, 466, 209

[43] Peng, C. Y. 2007, ApJ, 671, 1098

[44] Rampadarath, H., Garrett, M. A., Józsa, G. I. G., et al. 2010, A&A, 517, L8

[45] Revnivtsev, M. G., Churazov, E. M., Sazonov, S. Y., et al. 2004, A&A, 425, L49

[46] Richards, G. T., Strauss, M. A., Fan, X., et al. 2006, AJ, 131, 2766

[47] Schawinski, K., Khochfar, S., Kaviraj, S., et al. 2006, Nature, 442, 888

[48] Schawinski, K., Thomas, D., Sarzi, M., et al. 2007, MNRAS, 382, 1415

[49] Schawinski, K., Virani, S., Simmons, B., et al. 2009, ApJ, 692, L19

[50] Schawinski, K., Lintott, C. J., Thomas, D., et al. 2009, ApJ, 690, 1672

[51] Schawinski, K., Urry, C. M., Virani, S., et al. 2010, ApJ, 711, 284

[52] Schawinski, K., Dowlin, N., Thomas, D., Urry, C. M., & Edmondson, E. 2010, ApJ, 714, L108

[53] Schawinski, K., Evans, D. A., Virani, S., et al. 2010, ApJ, 724, L30

[54] Schawinski, K., Treister, E., Urry, C. M., et al. 2011, ApJ, 727, L31

[55] Schawinski, K., Urry, M., Treister, E., et al. 2011, ApJ, 743, L37

[56] Schmidt, M. 1959, ApJ, 129, 243

[57] Simmons, B. D., Van Duyne, J., Urry, C. M., et al. 2011, ApJ, 734, 121

[58] Silk, J., & Rees, M. J. 1998, A&A, 331, L1

[59] Straughn, A. N., Kuntschner, H., Kümmel, M., et al. 2011, AJ, 141, 14

[60] Su, M., Slatyer, T. R., & Finkbeiner, D. P. 2010, ApJ, 724, 1044

[61] Thomas, D., Maraston, C., Bender, R., & Mendes de Oliveira, C. 2005, ApJ, 621, 673

[62] Thomas, D., Maraston, C., Schawinski, K., Sarzi, M., & Silk, J. 2010, MNRAS, 404, 1775

[63] Treister, E., Urry, C. M., Chatzichristou, E., et al. 2004, ApJ, 616, 123

[64] Treister, E., Cardamone, C. N., Schawinski, K., et al. 2009, ApJ, 706, 535

[65] Treister, E., Urry, C. M., Schawinski, K., Cardamone, C. N., & Sanders, D. B. 2010, ApJ, 722, L238

[66] Treister, E., Schawinski, K., Volonteri, M., Natarajan, P., & Gawiser, E. 2011, Nature, 474, 356

[67] Treister, E., & Urry, C. M. 2011, arXiv:1112.0320

[68] Ueda, Y., Akiyama, M., Ohta, K., & Miyaji, T. 2003, ApJ, 598, 886

[69] Urrutia, T., Lacy, M., & Becker, R. H. 2008, ApJ, 674, 80

[70] York, D. G., Adelman, J., Anderson, J. E., Jr., et al. 2000, AJ, 120, 1579

[71] Wong, O. I., Schawinski, K., Kaviraj, S., et al. 2011, arXiv:1111.1785

[72] Zakamska, N. L., Strauss, M. A., Krolik, J. H., et al. 2006, AJ, 132, 1496

PROCEEDINGS OF SCIENCE

Spectroscopy and the Age of Giant Telescopes

Sarah Tuttle*
McDonald Observatory
2511 Speedway
Austin, TX 78712
E-mail: tuttle@astro.as.utexas.edu

Is your 4 meter telescope just not cutting it anymore? Embarrassed to mention the telescope time you had just the other week when talking about your newest data project? Don't worry, the age of the giant telescope is upon us. I will review the status of the three current ELT projects, as well as spectroscopic technologies focusing on multi-object spectroscopy. HETDEX (the Hobby Eberly Dark Energy Experiment) uses a new approach to large instruments, replicating a spectrograph channel 150 times to produce 33,600 individual spectra across a 22 arcminute field. The technology being built can be easily modified and ported to other telescopes to take quick advantage of the integral field approach. I will touch on the many experiments that await first light as these instruments come to fruition. Let's discuss why we are pouring massive resources into these telescopes and see what they can do for us.

Frank N. Bash Symposium New Horizons In Astronomy,
October 9-11, 2011
Austin Texas

*Speaker.

PoS(Bash11)011

1. Introduction

Telescopes with a primary aperture of 8m or more pepper the mountains of both hemispheres and give us eyes to observe back to the beginnings of the Universe. Bigger is sometimes better but as telescope building becomes an increasingly refined art it is important to also become wiser. Good use of this abundance of photons will allow us to answer a diverse set of questions ranging from the creation and evolution of galaxies, to understanding the primary physics that shapes star and planet formation.

Three giant telescopes loom on the horizon. The US is currently planning for the GMT (Giant Magellan Telescope) and the TMT (Thirty Meter Telescope) while the E-ELT (European Extremely Large Telescope) is an ESO-based project . Understanding what distinguishes each of these telescopes will help us to understand the decisions made in designing, selecting, and building the instrumentation needed to reach our science ambitions.

The technique of multi-object spectroscopy (MOS) (of which integral field spectroscopy is a subset) has been exploited to great effect in the last decade. The ability to achieve a three dimensional "image" of the object (in reality an x, y, λ data cube) allows us to better compare observations to models and to dissect the interactions that govern the physics that shape our universe. The first light instruments identified for all three ELTs implement a variety of MOS techniques, discussed throughout.

In this paper I will first review the science cases for the largest telescopes and some plans for early instrumentation to meet those needs. Section 3 reports on the progress of the three currently slated ELTs (Extremely Large Telescopes). Next, I will discuss the techniques most commonly used in multi object spectroscopy and their advantages. Section 5 will cover the costs of large telescopes and their operations. Finally, I discuss replication as one answer to the question "How do we build cost effective instruments for ELT class telescopes?"

2. Science Cases for 40m class Telescopes

The costs and risks associated with increasingly large ground-based telescopes are high. As you will see below (Section 6), decades of money, collected across large collaborations (and many countries) is necessary to consider building a telescope on this scale. Operating costs will be non-trivial, and a single night of data will come at a high price. What science drivers make this next step imperative? Figure 1 shows some of the advantage over 8m class telescopes, highlighting the sensitivity and resolution regimes for different observational cases.

2.1 Exo-Planets

The first exoplanet was discovered twenty years ago, orbiting a pulsar (PSR 1257+12) [1]. Through diverse detection methods, including microlensing [2, 3, 4], radial velocity [5, 6], timing [7], and direct imaging, that number slowly moved upwards. As of December 2011, 721 planets have been observed, the majority through radial velocity methods (662 planets in 538 systems). The recent work of the Kepler satellite (currently having detected 35 planets over the last 2 years, with over 2000 planet candidates) has accelerated the rate of discovery and has changed the parameters

PoS(Bash11)011

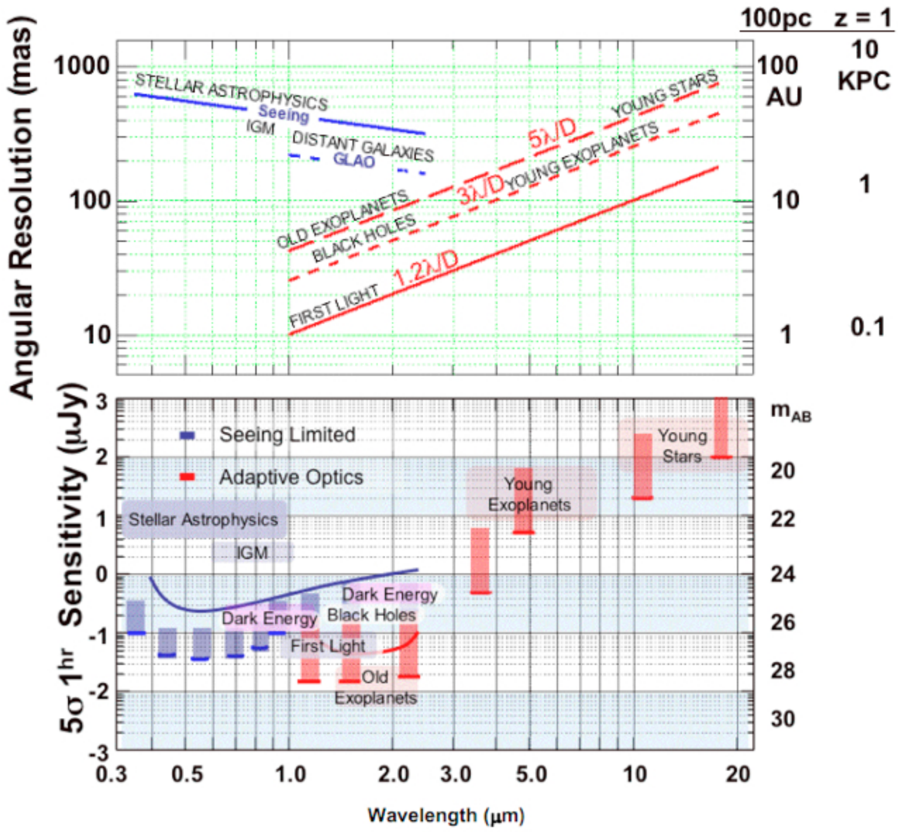

Figure 1: The projected sensitivity and angular resolution of the GMT as a function of wavelength. The bottom panel uses bars to show the improvements in sensitivity over current 8m telescopes. Blue cases are seeing limited while red are diffraction limited in both panels. $(http://www.gmto.org/Resources/GMT-ID-01404-GMT_{S}cience_{C}ase.pdf)$

of the "average" planet being detected, now discovering the lower mass Earth-like planets, as well as those in orbits most like the Earth as seen in figure 2 [8].

Radial velocity searches are possible from current telescopes, but require large amounts of time which limits meaningful statistical sampling especially when studying planets orbiting M and L dwarfs [9]. Moving to an ELT with adaptive optics makes even the detection of Terrestrial planets possible.

New instrumentation enabling high contrast imaging is crucial to push down to low mass ranges and smaller orbit systems (0.5-50 AU). Initial work can be done with the Infrared Imaging Spectrograph (IRIS), planned as a first light instrument for TMT. IRIS providing both a 16.4 arcminute field of view (diffraction limited, 4 mas sampling) as well as an IFU. This probes both bright planets in small orbits (10-15 AU in star forming regions) and bright "self-luminous" wide separation planets [10]. Plans also exist for the Planet Finding Imager (PFI), which exploits the large primary aperture and high-contrast adaptive optics [11]. E-ELT also has a Phase A instrument (EPICS) targeting exoplanets through direct imaging, spectroscopy and polarimetry [12, 13].

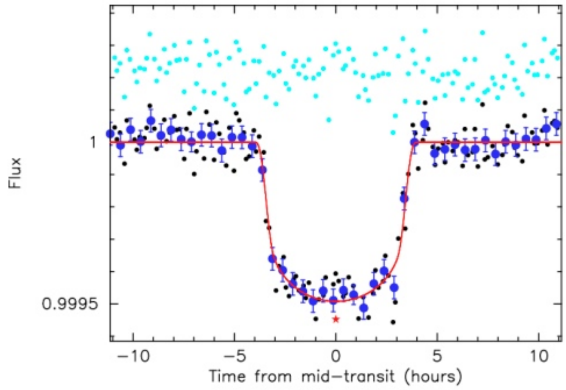

Parameter	Value
Effective temperature, T_{eff} (K)	5518 ± 44
Surface gravity, log g (cgs)	4.44 ± 0.06
Metallicity, [Fe/H]	-0.29 ± 0.06
Projected rotation $v \sin i$ (km s^{-1})	0.6 ± 1.0
Density, g cm^{-3}	1.458 ± 0.030
Mass, $M_{\odot}$	0.970 ± 0.060
Radius, $R_{\odot}$	0.979 ± 0.020
Luminosity, $L_{\odot}$	0.79 ± 0.04
Kepler Magnitude (mag)	11.664
Age (Gyr)	Not determined
Distance (pc)	190
Orbital period, P (days)	289.8623 +0.0016/-0.0020
Epoch, T0 (BJD-2454900)	66.6983 ± 0.0023
Scaled semi-major axis, a/R_*	186.4+1.1/-1.6
Scaled planet radius, R_p/R_*	0.0222 + 0.0012/-0.0011
Impact parameter, b (eccentric orbit)	0.768 + 0.132/-0.078
Orbital inclination, i (degree)	89.764 + 0.025/-0.042
Transit duration, Δ (hours)	7.415 + 0.067/-0.078
Radius, $R_{\oplus}$	2.38 ± 0.13
Mass, $M_{\oplus}$,(1σ, 2 σ, & 3σ upper limits)	36, 82, 124
Orbital semi-major axis, a (AU)	0.849 + 0.018/-0.017
Equilibrium temperature, T_{eq} (K)	262

NOTE. - Uncertainties are standard deviation or +1σ/-1σ unless otherwise noted.

Figure 2: Data from Kepler-22b, a transiting exoplanet with a period of 290 days. High resolution spectroscopy, analysis of the Kepler photometric, and HIRES data from Keck (taken over the course of a year) combine to demonstrate this is the first exoplanet found in the habitable zone. The left panel shows the folded light curve with model fit in red, and individual observations with black dots. (Reproduced by permission of the AAS and the author) [8]

2.2 Resolving Stellar Populations

Rich clusters contain the origins of many stars, but are difficult laboratories to study for star and planet formation. Observing these crowded stellar populations, especially the faint cluster members, is difficult. Being able to resolve cluster members means generating an increasingly deep and accurate initial mass function (IMF) [14, 15, 16]. Resolved positions of these stars then provides a distribution based on mass, with implications for formation scenarios - could collisions or mergers be involved in cluster formation?

Much of the work to explore the fundamental physics will be conducted using nearby protostars[17]. Being able to probe the central portions of collapsing protostellar systems will illuminate the processes that dictate how star systems (binary or multiple) and planetary systems form, as well as how outflows occur and influence protostars and their disks[18]. These questions ideally require very high resolution (R = 100,000) to probe low velocity absorption features, allowing measurement of temperature, density, and velocity.

2.3 Galaxy Assembly and Evolution

Astronomy is a field where we are generally unable to set our own experiments, but instead find the experiments running and observe them, the answers motivating the next set of questions. The evolution of galaxies has been an intriguing field since we first learned that galaxies were not individual island universes. Originally imagined within a black box, removed from the influence of the universe as a whole, we now know that the universe is an organism with galaxies retaining the imprint of the beginning [19], and that galaxies are shaped by interactions, both with other galaxies and with the IGM they have grown within.

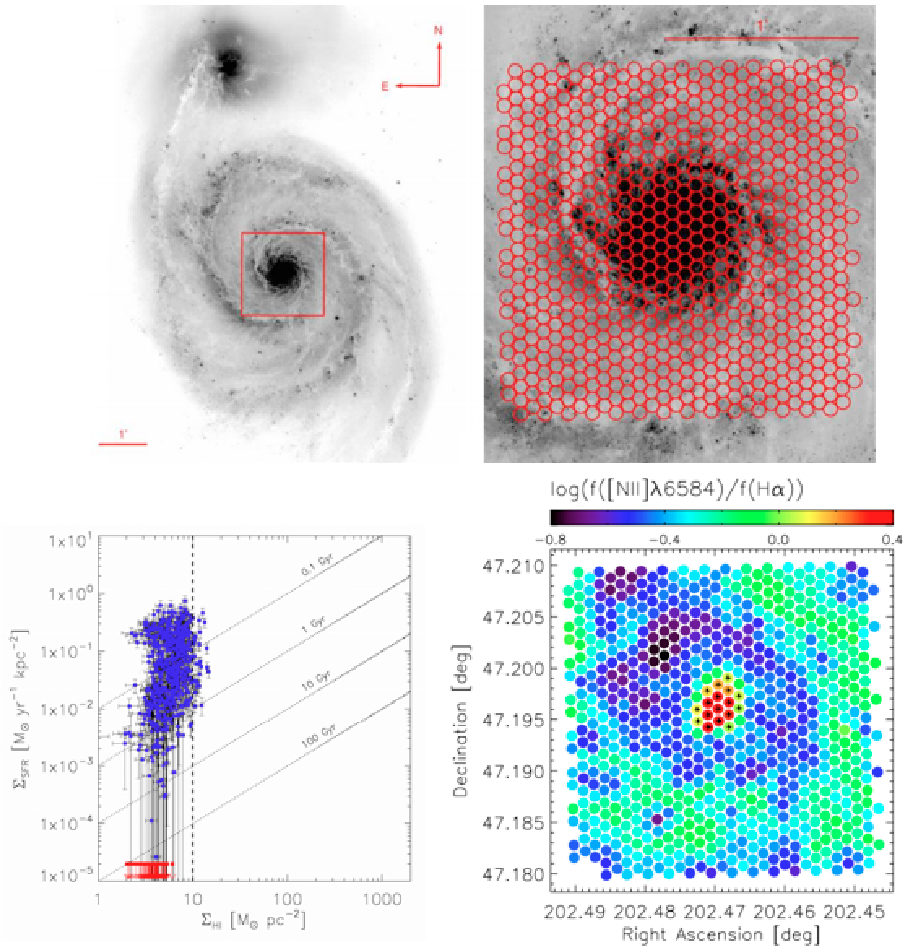

Figure 3: Four views of NGC 5194 from Blanc et al [21]. Clockwise from the upper left panel - The HST+ACS V-band image with the VIRUS-P field of view (1.7' x 1.7') boxed in red. The dithered fiber pattern is shown to the right, with each fiber 4.3" on the sky, or 170 pc at the distance of NGC 5194. The lower right panel shows [NII]λ6584/Hα emission line ratio with the black crosses indicating areas of AGN activity. The lower left panel shows atomic gas surface density versus SFR surface density. The data shown here consist only of the regions unaffected by AGN activity.

ELTs bring several advantages to bear on the question of how galaxies evolve. In particular, we do not yet know what physical processes are dominant generically across the growth of galaxies. Fundamental work in the field began with local and unresolved galaxies, leading to studies of star formation and dust as global properties [20]. Extensive work has now been done to resolve local star formation spatially (see figure 3) in the optical [21][22], directly measuring gas at radio and UV wavelengths [23], and evolution of galaxies out to z=2 [24]. Working with spatially resolved data identifies the root cause of the physical conditions in the galaxy as well as the possible external influences such as winds and filamentary streams.

At high redshift we are still limited to unresolved data. Integral field units on the upcoming ELTs will allow this exciting spatially resolved work to continue. IFUs matched to the appropriate physical scale can take tens of spectra over the area of high redshift galaxies, offering comparisons with current lower redshift work.

2.4 Cosmology

Understanding of the very high redshift universe (z > 7) will benefit greatly by an increase in primary size as well as the improved adaptive optics that will accompany the new largest telescopes. Extending many current works, including identification of quasars and other high redshift galaxies, star formation rates, and density and composition of the IGM will elucidate the early state of the Universe as well as its evolution.

The formation of single stars or clusters is not the only science case that benefits from resolving stellar populations. The nature of dark matter and its distribution throughout the universe is still poorly understood. Currently we can study the radial mass profiles of dwarf galaxies, a population whose mass is dominated by dark matter, and differentiate dark matter models [25]. Using an ELT will increase the sample size by a factor of ten and improve the velocity measurements down to 5 km/s accuracy.

Increased telescope size also opens a window into the faint baryonic matter that dominates the matter budget hidden away in the intergalactic medium (IGM)[26, 28]. The IGM is described as the "Cosmic Web" and traces the distribution of matter left behind as gravitational instabilities have collapsed [27]. This predominately hydrogen gas has been studied mostly in absorption using quasars as illuminators along the line of sight [29]. With a small number of sources, metallicities, distributions and even sizes of clumpy gas have been revealed[30]. The recent installation of the Cosmic Origins Spectrograph (COS) on HST has improved the resolution of absorption lines in the IGM as well as improved source statistics[31]. The increase in primary aperture on the ELTs also means galaxies can be used as well as quasars for background objects. Probing the distribution and make up of the gas along this increased number of lines of sight (with decreased bias) will reveal the larger filamentary structure. Outstanding questions in galaxy evolution rely on understanding the accretion and outflow of gas, and it will be crucial to understand the reserve of hydrogen that galaxies are born within.

2.5 The James Webb Space Telescope

It is important to briefly note that even the most advanced ground-based telescopes benefit from complementary space-based observations [32]. Ground-based telescopes have an advantage in primary aperture, mass restrictions, and accessibility. This translates to observing increasingly small and faint sources within reasonable exposure times. In space, telescopes such as JWST provide a much reduced background and access to much redder wavelengths, pushing observations beyond redshifts of 20. This combination probes the oft neglected extremes as opposed to the commonly studied brightest and most accessible objects.

3. On the Horizon - The Next Generation of Ground Based Telescopes

Here we review briefly the status of the three next generation ground-based telescopes being planned. Over the last decade, several more have been discussed but groups have naturally formed based on approach, geography, and primary science drivers. Some of the fundamental characteristics of the individual telescopes can be found in Table 1.

Table 1: ELT Parameter Comparison

Telescope	Collecting Area (m^2)	Throughput	FOV ($arcmin^2$)	Resolution Range	Scaled AΩ
GMT	387	0.8	145	1500-5000	1.00
TMT	705	0.7	40.5	500-5000	0.44
E-ELT	1190	0.6	25	300-2500	0.4

Table 2: GMT Phase A Instruments

Name	Type (R)	Bandpass (μm)
GMACS	MOS Spectrograph (2000)	0.38 - 1.0
GMTNIRS	Spectrograph (50000-10000)	1.15-5.3
NIRMOS	MOS Spectrograph (3000)	0.9-2.5
MIISE	Imaging Spectrograph (1500)	3.0-25
HRCAM	AO Imager	0.9-5.0
QSpec	Slit Spectrograph (30000)	0.3-1.0

3.1 Giant Magellan Telescope Status

The Giant Magellan Telescope (GMT) is being built by an international consortium including groups from Australia, Korea, and the United States. The telescope site has been chosen at Las Campanas, Chile in the southern hemisphere. Las Campanas is an excellent observing site, having several telescopes currently on location. This means the infrastructure to support the telescope is substantially developed. The telescope optical design includes a primary constructed of seven 8.4m mirrors. The first primary mirror is built and the second casting was begun in mid-January 2012. Phase A instrument studies took place and down selection has begun (see Table 2). GMT is expected to see first light in 2019.

3.2 TMT Status

The Thirty Meter Telescope (TMT) started off as a collaboration between the Association of Canadian Universities for Research in Astronomy(ACURA), California Institute of Technology, and the University of California. Now it has expanded to include groups from China, India, and Japan. TMT will be based in the Northern hemisphere on Mauna Kea, and is in many ways a descendent of the Keck observatories. The primary mirror is composed of 492 segments, with 82 unique shapes and optical prescriptions to be achieved. Each segment will be controlled by three actuators to give the final primary mirror shape.

TMT selected three early light instruments in 2006 which are moving ahead. IRIS [10], the Wide Field Optical Imager and Spectrometer (WFOS)[33], and the Infrared Multislit Spectrometer (IRMS) were chosen to be flexible in scope and allow early work on characterizing the telescope as other instruments were built. Two of the three (IRIS and IRMOS) contain IFUs, and design of the three show a balance between targeting breadth and depth of the objects observed. IRIS will come online first and be the only early light instrument to operate at the diffraction limit.

Table 3: TMT Early Instrumentation

Name	Type (R)	Bandpass (μm)
IRIS (Early)	Imager/Spectrograph	0.8-2.5
IRMS (Early)	Spectrograph (4600)	0.95-2.45
WFOS (Early)	Imager/Spectrograph (1000-5000)	0.31 - 1.0
IRMOS	Spectrograph (2000-100000)	0.8-2.5
MIRES	Echelle Spectrograph (5000-100000)	8.0-18.0
PFI	Imaging Spectrograph(< 100)	1-2.5
NIRES	Echelle Spectrograph (20000-100000)	1.0-5.0
HROS	Spectrograph (50000)	0.31-1.1
WIRC	Imager	0.8-5.0

Table 4: E-ELT Phase A Instruments

Name	Type (R)	Bandpass (μm)
CODEX	Spectrograph (135000)	0.37 - 0.72
EAGLE	Spectrograph (4000)	0.80 - 2.45
EPICS	Imager/Spectrograph/Polarimeter	0.6 - 1.65
HARMONI	IF Spectrograph (4000- 20000)	0.47 - 2.45
METIS	Imager/Spectrograph (Low and High)	2.9 - 14
MICADO	Imager/Slit Spectrograph (<3000)	0.8 - 2.5
OPTIMOS-DIORAMAS	Wide-Field Imager/Slit Spectrograph (Low)	0.37 - 1.6
OPTIMOS-EVE	Fiber MOS (5000-30000)	0.37 - 1.7
SIMPLE	Echelle Spectrograph (130000)	0.8 - 2.5

3.3 E-ELT Status

The European Extremely Large Telescope (E-ELT) is ESO's contribution to the current effort to the next generation of telescopes. The E-ELT will have a primary mirror 39.3m in diameter with a field of view of .1 of a square degree. The primary is built of just less than 798 1.4m segments. The mirror design is somewhat unusual, using a five-mirror design. Adaptive optics are integrated into the telescope design. A site has been selected at Cerro Armazones, Chile in the southern hemisphere. After passing a design review in December 2010, E-ELT construction is expected to begin in January 2012 [34]. It is expected to begin operation roughly a decade later. Phase A studies were completed and recommendations were made for two first light instruments: a single-field near-infrared wide-band integral field spectrograph and a diffraction-limited near-infrared imager. The next suite of instruments expected are a high resolution spectrograph, a multi-object spectrograph, and a mid-infrared imager/spectrometer. See Table 4 for details of the current instruments in development.

The end of 2011 brought approval of the next year's budget, moving the E-ELT towards final approval by member states in mid-2012. Component development is also set to begin this year in preparation for final approval. The final construction cost of the E-ELT is currently estimated to be 1 billion euro.

3.4 Adaptive Optics

Adaptive optics are crucial for many of the science goals discussed above [35] (see figure 1). Each telescope has a different approach to implementation, and some instruments will integrate their own AO systems [11]. Design work is under way and will likely evolve even as the telescopes come online[36].

3.5 OH Suppression

A brief mention, when discussing the next generation of ground-based telescopes, must go to the new technology of OH suppression. A glance at Tables 2, 3, and 4 show that exploiting available infrared wavelengths is ideal. However, the abundance of sky lines makes much work difficult. Even when individual lines are suppressed, scattered Lorentz wings pollute the continuum to a level that is difficult to remove. Several new techniques are underway to completely remove the photons from the skylines and prevent their entrance into an instrument to scatter and degrade efficiency[37, 38]. The ELTs will benefit greatly from technology which eliminates skylines and makes the infrared an even more fruitful band [39].

4. Multi-Object Spectroscopy : Techniques and Current Instruments

Multi-object spectroscopy (MOS) refers to any technique that captures multiple spectra simultaneously in an exposure. The ability to observe many objects simultaneously provides improved statistics without untenably long observing programs, and this is one reason why multi-object spectrographs have become common on large telescopes. Spatial and spectral information is measured with a MOS, and this three dimensional sampling puts the onus on the instrument designer to balance resolution and field of view across the available detector area[40]. One way to think about these trades can be seen in figure 4.

Multi-object spectrographs come in several flavors. At one end of the range we find plug plates and masks, such as the Sloan Digital Sky Survey (SDSS) [41] and DEIMOS (on Keck) [42]. Masks or plates must be generated for each field, and for plug plates human interference is required to route fibers every time a field changes. Increasingly, technology is used for flexibility and reliability. Robots or magnets move fibers (or small packed bundles) from target to target. HYDRA has been used at NOAO facilities for many years and through several upgrades. It uses robotic positions over a field of view of 60 arcminutes diameter and places 288 fibers that can be reconfigured in 20 to 25 minutes [43, 44]. The positioning accuracy is 0.3 arcseconds, and the minimum spacing between fibers is 37 arcseconds. Fields do not need to be specified weeks or months in advance to machine the plates, and it decreases the likelihood of incorrectly locating fibers. All of these methods are limited from any sort of integral field packing due to the external coverage of the fibers or bundles - objects are lost when they are too close to be covered by interfering fibers but spaced to far apart to fill a single element. This is usually resolved by ignoring one object, or if they are both of extreme interest (or the field is very crowded) by taking a second configuration on the same field.

Integral field units (IFUs) provide contiguous coverage of a field. Taking an image gives spectra of the entire field of view and there is no configuration or orientation to change. The fill factor or distribution of fibers across the field can vary, as shown in figure 5. Bundles might be close

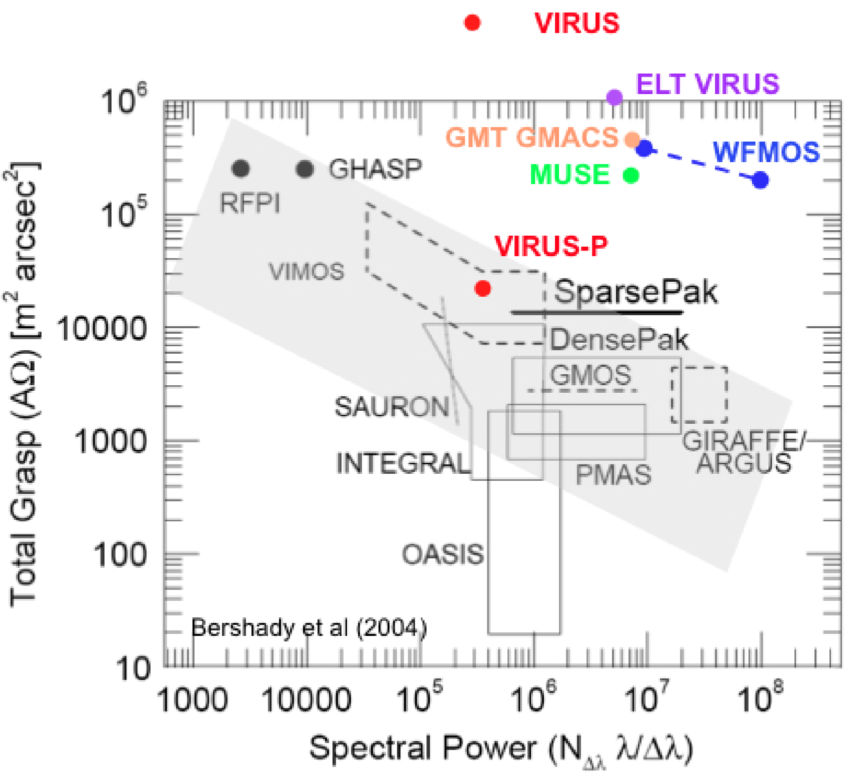

Figure 4: A modified figure from Bershady [40]. Spectral power versus total grasp of many of the current and planned MOS instruments shown.

packed to provide relatively complete coverage, such as with FIREBALL [45] or Densepak[46]. Fibers can also be distributed to target a more specific science result, such as with Sparsepak [47]. The fibers in Sparsepak were distributed to study local galaxies, splitting the fibers (and therefore detector coverage) between the dense center of the galaxy, the more diffuse halo, and providing an optimized number of fibers (7) along the edge of the field of view for sky coverage (see figure 5). Image slicers and fiber optics are often deployed to these ends, as well as lenslet arrays[48]. Micro-shutters are an interesting technological development as they introduce the idea of a configurable integral field - bright objects could be occulted, for example, and faint structures could be searched for with deep exposures[49].

The flexibility of these instruments has meant that a steady stream of exciting results have continued. The Sloan Digital Sky Survey is, even a decade after its first data release, being used to do compelling new research, contributing to large scale structure work in the local universe[50].

5. Large Telescopes and Their Costs

The community has looked ahead to 40m class telescopes for the last 15-20 years [51]. One of the most difficult things for astronomers to wrap their minds around is the cost of running large telescopes. Early work done to understand and project the cost of new telescopes made even the cost of a 5m class telescope appear prohibitive [52]. But successful large telescopes beat this

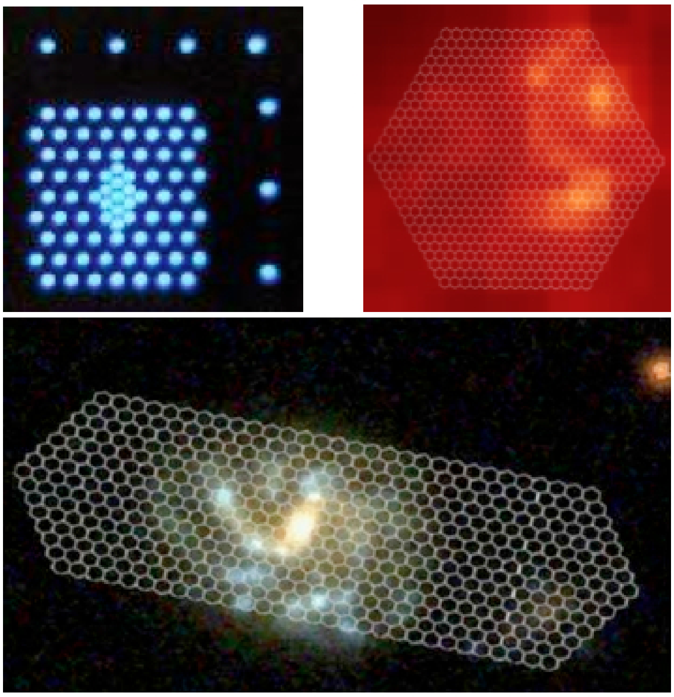

Figure 5: Three IFU configurations. The top right shows Sparsepak illuminated from the slit end [47]. The top left shows an overlay of the FIREBall bundle on a simulation of an IGM clump at z=1 [45]. The bottom image is a proposed IFU for TMT (J. Larkin)

prediction. Stepp et al [53] discuss that if one were to extrapolate from the Kitt Peak Mayall 4m to Keck I, the projected cost was 4 times more than the actual cost.

A conversation that has been taking place for the last several years centers on the need to shut down many smaller telescopes to move forward in support of next generation telescopes. Creating extended cost benefit analysis of these choices is difficult, as each subfield and scientist have different scientific interests and agendas, and most feel they can use almost any instrument to good effect. Given these conditions, how do you decide to cut 10 1m telescopes to support one 5m? How do you value infrastructure and experience? Many of these questions have been asked and answered, and I try to summarize here some of the relevant work.

van Belle et al [54] review the changes in cost as a direct effect of the primary aperture of the telescope, as well as development in the engineering approach. Evolution of telescope design over time has led to several eras of telescope cost. Most costs fold in not only the telescope itself but the support systems and buildings (but exclude instrumentation and operations). Earlier telescopes had monolithic mirrors that had no light weighting, large domes which were (eventually understood to be) ineffectual in suppressing seeing, and slow speeds, and were designed on traditional equatorial mounts. After 1980, technical changes improved the cost of increasing aperture size - in particular, the move to alt-az mounts, thin or segmented mirrors, and much faster optical systems (F/# < 1.8). The implication here is that if we build a giant telescope using similar techniques without a significant cost break in technological approach, we might expect to be hindered to the same costing, which places a thirty meter telescope at over $2 billion (as seen in figure 6). The rough

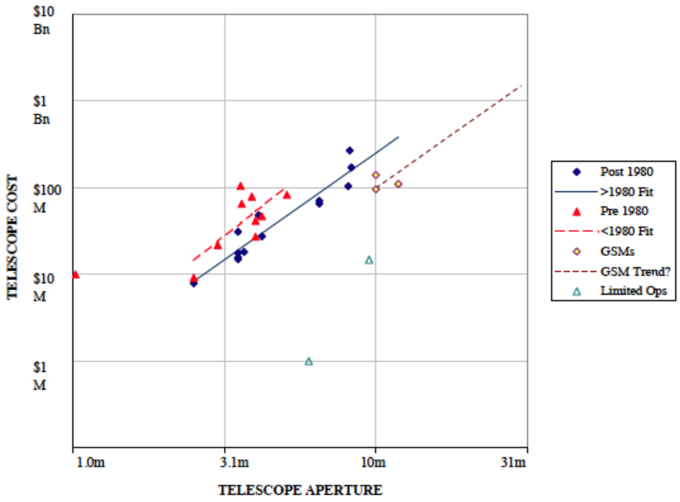

Figure 6: Telescope diameter versus telescope cost. Data found in [54]. The three lines show the trend with pre-1980 technology, post-1980, and a possible projected trend for the ELTs.

cost estimate for GMT is currently $700 million.

Construction costs are not, in the end, the dominant cost of telescopes. Over the course of a 30 year lifetime, an intermediate sized telescope (4-10m) will cost two to three times its construction costs [53]. This is estimating the operating costs at 3 to 6 percent of the construction cost of the facility, and doesn't include instrument development. For such large projects, cost savings must be found where available.

6. Replication as a Solution

One possible way to ameliorate the cost of large telescopes is to provide cost efficient instrumentation. Here I briefly describe the current status of the Hobby-Eberly Telescope Dark Energy Experiment (HETDEX) [55] and its replicated spectrograph VIRUS [56]. VIRUS takes advantage of small scale optics and replication of optical and mechanical components to provide spectroscopy of 33,600 fibers (1.5 arcseconds on the sky) spread across a 20 arcminute field. The baseline survey observes 60 square arcminutes, probing a volume of 9 Gpc to measure the baryonic acoustic oscillation by mapping Lyman α emitters from $2 < z < 4$. The spectrograph has a bandpass of 350-550nm with a R = 900. We predict roughly 750,000 Lyα emitters will be detected.

VIRUS is designed to minimize the size of individual optics while optimizing sky coverage The fibers are packed into 82 IFUs which then split again at the slit to feed 164 spectrograph channels. The cameras are a f/1.33 vacuum Schmidt design, with two channels enclosed in a single cryostat. Figure 7 shows some of the replicated spectrograph parts in progress as well as the lay out of the camera and the VIRUS "pair" (two channel assembly).

The two instrumental components necessary to the HETDEX project (the Wide Field Upgrade - WFU and VIRUS) are currently under construction and will be installed at the HET starting in the Summer of 2012. VIRUS will come online over the course of the fall with first light of the full complement of spectrographs scheduled for early 2013.

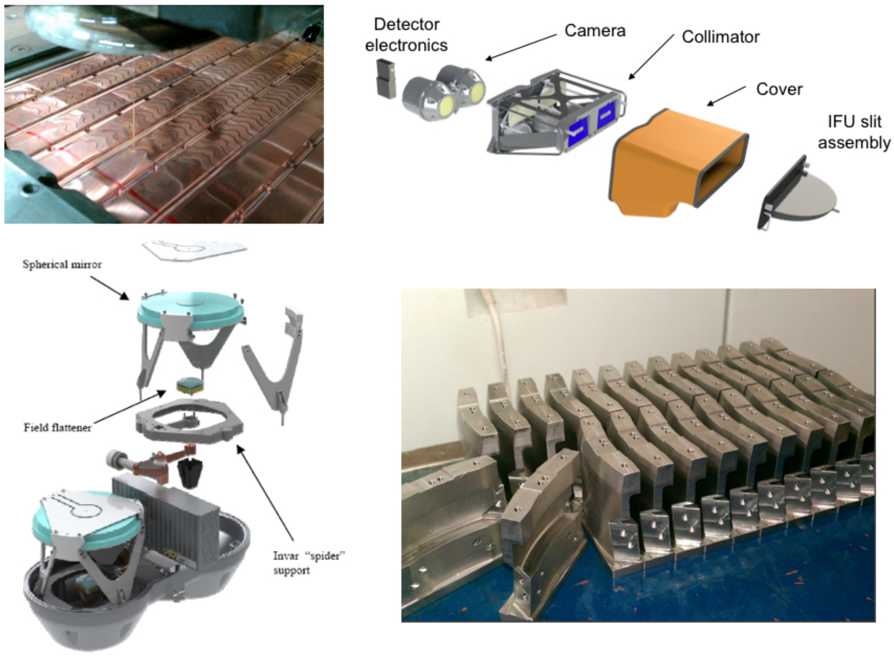

Figure 7: The VIRUS spectrographs. The top left and bottom right show partial batches of two production parts. The copper is part of the cold link and in the process of being cut out using wire electrical discharge machining (wire EDM). The Invar parts in the lower right are mirror mounts and adjusters - three are used in each channel, as can be seen in the exploded view on the lower left. Here you can see the two channels with the upper cryostat removed for easy viewing. The detector controller electronics box is shown in between the two channels. The upper right panel shows the full pair assembly as it will be mounted on HET.

Replication is an attractive possibility for an ELT instrument design. With large telescope instruments it is easy to fall back on designs that include large optics and complex mechanisms to manage the mass and beam size. When internal optics exceed the size of small (1m) telescopes, coatings and handling become prohibitively expensive and technically difficult. A replicated instrument reduces the size of the parts and introduces economies of scale to reduce the overall price of the instrument. A fiber optic IFU or MOS decouples the instrument from the telescope as well, eliminating possible mounting constraints. Instruments can be maintained and upgraded in a similar fashion to segmented mirrors, with a small number coming offline without a severe impact on the usefulness of the instrument.

VIRUS was built based on a prototype instrument (VIRUS-P, now known as the George Mitchell Spectrograph [57]). Although not identical, the prototype allowed proof of concept, lifetime testing of several components in-situ, as well as offered the opportunity to conduct a pilot survey to study the technique of Lyman α detection and mapping with optimization for the fiber IFU [58]. VIRUS-P is now one of the most highly subscribed instruments at McDonald Observatory.

7. Conclusion

The next decade will see first light of one, if not several, ELTs. The investment, in both time and money, is at a level never seen before especially when discussing ground-based instrumentation and competitive with our most expensive space-based missions. It behoves all of us to understand the benefits of these telescopes as they come to fruition.

In the past, the most effective way to control the cost of new telescope facilities is to use technological advances to break the relationship between primary mirror aperture and cost. The last 30 years have made much progress in this area, including light weighted and segmented mirrors. The next break very well might come from changes in approach to instrumentation, such as using replication to decrease the size of individual components and take advantage of economies of scale. Multi-object spectrographs, either through IFUs which achieve coverage over the entire field, or a more dispersed approach (such as single fibers, several small bundles, or slit masks), often offer the best compromise between field of view and detector coverage.

References

[1] Wolszczan, A., & Frail, D. A. 1992, Nature, 355, 145

[2] Udalski, A., Jaroszyński, M., Paczyński, B., et al. 2005, Astrophysical Journal, Letters, 628, L109

[3] Gould, A. 2009, The Variable Universe: A Celebration of Bohdan Paczynski, 403, 86

[4] Gould, A., Dong, S., Gaudi, B. S., et al. 2010, Astrophysical Journal, 720, 1073

[5] Struve, O. 1952, The Observatory, 72, 199

[6] Butler, R. P., Wright, J. T., Marcy, G. W., et al. 2006, Astrophysical Journal, 646, 505

[7] Beuermann, K., Hessman, F. V., Dreizler, S., et al. 2010, Astronomy and Astrophysics, 521, L60

[8] Borucki, W. J., Koch, D. G., Batalha, N., et al. 2012, Astrophysical Journal, 745, 120

[9] Riaud, P., & Schneider, J. 2007, Astronomy and Astrophysics, 469, 355

[10] Wright, S. A., Barton, E. J., Larkin, J. E., et al. 2010, Proceedings of the SPIE, 7735,

[11] Macintosh, B., Troy, M., Doyon, R., et al. 2006, Proceedings of the SPIE, 6272

[12] Kasper, M., Beuzit, J.-L., Verinaud, C., et al. 2010, Proceedings of the SPIE, 7735,

[13] Gratton, R., Kasper, M., Vérinaud, C., Bonavita, M., & Schmid, H. M. 2011, IAU Symposium, 276, 343

[14] Kim, H., Whitmore, B. C., Chandar, R., et al. 2011, Bulletin of the American Astronomical Society, 43, #246.17

[15] Greggio, L., Tosi, M., Clampin, M., et al. 1998, Astrophysical Journal, 504, 725

[16] Calamida, A., Comeron, F., & Zinnecker, H. 2011, arXiv:1109.6235

[17] Wolf-Chase, G., Smutko, M., Sherman, R., Harper, D. A., & Medford, M. 2012, Astrophysical Journal, 745, 116

[18] Wang, K., Zhang, Q., Wu, Y., Li, H.-b., & Zhang, H. 2012, Astrophysical Journal, Letters, 745, L30

[19] de Lapparent, V., Geller, M. J., & Huchra, J. P. 1986, Astrophysical Journal, Letters, 302, L1

[20] Kennicutt, R. C., Jr. 1998, Astrophysical Journal, 498, 541

[21] Blanc, G. A., Heiderman, A., Gebhardt, K., Evans, N. J., II, & Adams, J. 2009, Astrophysical Journal, 704, 842

[22] Blanc, G. A., Gebhardt, K., Heiderman, A., et al. 2010, New Horizons in Astronomy: Frank N. Bash Symposium 2009, 432, 180

[23] Bigiel, F., Leroy, A., Walter, F., et al. 2008, Astronomical Journal, 136, 2846

[24] Genzel, R., Burkert, A., Bouché, N., et al. 2008, Astrophysical Journal, 687, 59

[25] Strigari, L. E., Bullock, J. S., & Kaplinghat, M. 2007, Astrophysical Journal, Letters, 657, L1

[26] Fukugita, M., Hogan, C. J., & Peebles, P. J. E. 1998, Astrophysical Journal, 503, 518

[27] Cen, R., & Ostriker, J. P. 1999, Astrophysical Journal, 514, 1

[28] Shull, J. M., Smith, B. D., & Danforth, C. W. 2011, arXiv:1112.2706

[29] Danforth, C. W. 2009, American Institute of Physics Conference Series, 1135, 8

[30] Danforth, C. W., & Shull, J. M. 2008, Astrophysical Journal, 679, 194

[31] Green, J. C., Froning, C. S., Osterman, S., et al. 2012, Astrophysical Journal, 744, 60

[32] Kissler-Patig, M., & McCaughrean, M. 2010, The Messenger, 140, 57

[33] Pazder, J. S., Roberts, S., Abraham, R., et al. 2006, Proceedings of the SPIE, 6269,

[34] Gilmozzi, R., & Kissler-Patig, M. 2011, The Messenger, 143, 25

[35] Hubin, N., Ellerbroek, B. L., Arsenault, R., et al. 2006, The Scientific Requirements for Extremely Large Telescopes, 232, 60

[36] Hinz, P. M., Bouchez, A., Johns, M., et al. 2010, Proceedings of the SPIE, 7736,

[37] Bland-Hawthorn, J., Ellis, S., Haynes, R., & Horton, A. 2009, Anglo-Australian Observatory Epping Newsletter, 115, 15

[38] Bland-Hawthorn, J., Ellis, S. C., Leon-Saval, S. G., et al. 2011, arXiv:1112.1694

[39] Günster, S., Ristau, D., & Davies, R. 2011, Proceedings of the SPIE, 8168,

[40] Bershady, M. A. 2009, arXiv:0910.0167

[41] Owen, R. E., Siegmund, W. A., Limmongkol, S., & Hull, C. L. 1994, Proceedings of the SPIE, 2198, 11

[42] Faber, S. M., Phillips, A. C., Kibrick, R. I., et al. 2003, Proceedings of the SPIE, 4841, 1657

[43] Barden, S. C., Armandroff, T., Massey, P., et al. 1993, Fiber Optics in Astronomy II, 37,185

[44] Barden, S. C., & Armandroff, T. 1995, Proceedings of the SPIE, 2476, 56

[45] Tuttle, S. E., Schiminovich, D., Grange, R., et al. 2010, Proceedings of the SPIE, 7732,

[46] Barden, S. C., & Wade, R. A. 1988, Fiber Optics in Astronomy, 3, 113

[47] Bershady, M. A., Andersen, D. R., Harker, J., Ramsey, L. W., & Verheijen, M. A. W. 2004, Publication of the ASP, 116, 565

[48] Matuszewski, M., Chang, D., Crabill, R. M., et al. 2010, Proceedings of the SPIE, 7735,

[49] Fleming, B. T., McCandliss, S. R., Kaiser, M. E., et al. 2011, Proceedings of the SPIE, 8145,

[50] Reyes, R., Mandelbaum, R., Seljak, U., et al. 2010, Nature, 464, 256

[51] Carlberg, R. G. 2006, The Scientific Requirements for Extremely Large Telescopes, 232, 25

[52] Whitford, A. E. 1964, Astronomical Journal, 69, 675

[53] Stepp, L. M., Daggert, L. G., & Gillett, P. E. 2003, Proceedings of the SPIE, 4840, 309

[54] van Belle, G. T., Meinel, A. B., & Meinel, M. P. 2004, Proceedings of the SPIE, 5489, 563

[55] Hill, G. J., Gebhardt, K., Komatsu, E., et al. 2008, Panoramic Views of Galaxy Formation and Evolution, 399, 115

[56] Hill, G. J., Lee, H., Vattiat, B. L., et al. 2010, Proceedings of the SPIE, 7735,

[57] Hill, G. J., MacQueen, P. J., Smith, M. P., et al. 2008, Proceedings of the SPIE, 7014,

[58] Adams, J. J., Blanc, G. A., Hill, G. J., et al. 2011, Astrophysical Journal, Supplement, 192, 5

PROCEEDINGS OF SCIENCE

Recent Advances in Cosmological Hydrogen Reionization

Kristian Finlator[*] [†]
UC Santa Barbara
E-mail: finlator@physics.ucsb.edu

I discuss recent advances in the study of hydrogen reionization, focusing on progress that was achieved during the years 2010–2011. First, I discuss recent measurements of the progress of reionization. Next, I discuss recent observational constraints on the nature and abundance of the dominant ionizing sources. Finally, I discuss recent progress in modeling reionization. This review is written for an audience of astronomers who do not specialize in the high-redshift Universe.

PoS(Bash11)012

Frank N. Bash Symposium New Horizons In Astronomy,
October 9-11, 2011
Austin Texas

[*]Speaker.

[†]I am grateful to the University of Texas Department of Astronomy Board of Visitors for supporting the 2011 Frank N. Bash Symposium. I also thank NASA for support through Hubble Fellowship grant HF-51254.01 awarded by the Space Telescope Science Institute, which is operated by the Association of Universities for Research in Astronomy, Inc., for NASA, under contract NAS 5-26555.

1. Introduction

The Reionization Epoch consists broadly of the time interval between the moment when photons and matter decoupled, at a redshift z of 1088 [73], and the moment when enough ionizing sources had formed to ionize the hydrogen and helium in the intergalactic medium (IGM), or $z \sim 3$ [69]. This was the most active period in the Universe's history: Galaxies were forming stars up to ten times as rapidly as they are today even as they expelled comparable amounts of gas back into their environments. The supermassive black holes that are largely dormant today were each swallowing a dwarf galaxy's worth of gas over just a few billion years and glowing brightly enough to heat the IGM. Reionization converted the IGM into a plasma, suppressed the growth of dwarf galaxies, and altered the conditions under which subsequent generations of galaxies grew. Its pivotal position at the outset of the story of structure formation rendered it one of the central science goals in the 2010 Decadal Survey [1].

The Reionization Epoch is generally divided in two: During the hydrogen reionization epoch, hydrogen was ionized and helium was singly ionized. During the helium reionization epoch, helium was further ionized from He II to He III. Two considerations justify this division. First, most of the photons that brought about hydrogen reionization were not energetic enough to remove the second electron from a helium atom. At the same time, the cross section for hydrogen atoms to absorb photons that are energetic enough to ionize a He II atom is small. Hence the dominant photons were different. Second, hydrogen-ionizing photons were probably generated by massive stars in young galaxies while He II-ionizing photons were predominantly generated by quasars. Quasars did not grow abundant enough to participate in reionization until hydrogen reionization was largely complete [67]. Hence the sources were also different.

This review focuses on hydrogen reionization (from now on, "reionization"). I shall discuss insights that have been won during 2010–2011, with reference to earlier results whenever necessary for context. This field is routinely reviewed. For a more technical introduction on early structure formation, see the classic discussions by Barkana and Loeb [3, 45]. For overviews of the first galaxies and their role in reionization, see [14] and [11].

I divide my discussion into three parts. In Section 2, I discuss progress in measuring the history of reionization. When did reionization begin ? How long did it take? In Section 3, I discuss progress in identifying and understanding the ionizing sources that drove reionization. What were they? How many were there? Did the progress of reionization leave any observable signatures on their properties? In Section 4, I discuss progress in modeling reionization.

2. Measuring the Progress of Reionization

It is currently believed that reionization was driven by ionizing photons from dwarf galaxies. If true, then its history can be divided into three stages [29]. During the first stage, galaxies create enough ionizing photons to reionize their immediate surroundings, but the ionized regions remain small compared to the typical distance between galaxies. During the second stage, ionized regions begin overlapping with each other and the typical distance traveled by ionizing photons grows rapidly. During the final stage, the Universe is largely ionized and its residual opacity is dominated by slowly-shrinking “islands" of moderately overdense gas. In this Section, I discuss efforts to reconstruct when the Universe went through these stages.

2.1 Lyman-α absorption

The classic indication that reionization has already completed is the absence of a “Gunn-Peterson trough" from the spectra of high-redshift quasars. Intuitively, the cross-section for neutral hydrogen atoms to absorb photons that boost their electrons from the ground state (n=1) to the first excited state (n=2) is very large. Any photon that is in resonance with this transition (Lyα) while traversing a region with neutral hydrogen will probably be absorbed. [33] showed that, if the volume-averaged neutral hydrogen fraction x_{HI} is ~ 1, then the optical depth to scattering is $\sim 10^4$. Put differently, as UV photons redshift through resonance with Lyα, they will on average be scattered unless fewer than 1 in 10^4 hydrogen atoms is neutral. In the post-reionization Universe, this phenomenon creates a “forest" of absorption lines, where the amount of absorption at a rest-frame wavelength in the range 912-1216 Å traces the amount of neutral gas in the Universe at the moment when those photons redshifted through resonance with Lyα. In a reasonably neutral Universe, the forest converts into complete absorption, and is called the Gunn-Peterson trough.

The first reported Gunn-Peterson trough was identified in the spectrum of a quasar at $z = 6.28$ [5], leading to speculation that reionization may have ended around this redshift. In practice, however, the detection of a Gunn-Peterson trough only indicates that $x_{\mathrm{HI}} > 10^{-3}$ [18], which is still highly ionized. [19] followed up on this by applying several complementary analyses to 19 quasars, tracing the evolution of x_{HI} from $5 \rightarrow 6$. They found that x_{HI} evolves rapidly during this interval and inferred that the IGM is mostly neutral at $z \geq 6$. In detail, their analyses all assumed a spatially homogeneous ionizing background, which is clearly an approximation near the end of reionization. Relaxing this assumption leads to the more conservative limit $x_{\mathrm{HI}}(z=6.1) < 0.8$ [47].

A complementary constraint on x_{HI} comes from modeling the “proximity zones" of high-redshift quasars. A proximity zone is a region centered on a quasar that is more ionized than the ambient IGM owing to the quasar's extra ionizing photons. Its size, which can be measured and is typically a few Megaparsecs, is sensitive to (1) the quasar's ionizing luminosity; (2) the neutral hydrogen fraction before the quasar “turned on"; and (3) the amount of time that the quasar has been active. The quasar's ionizing luminosity can be constrained observationally, so if the duration of its active phase can be derived through other means then x_{HI} can be inferred using a straightforward Strömgren Sphere calculation [67].

Recently, [52] and [7] applied this approach to a newly-discovered quasar at $z = 7.085$ called ULAS J1120+0641. Its proximity zone is unusually small in comparison to other high-redshift quasars, and it is the smallest when its radius is scaled to the quasar's luminosity. This is consistent with the IGM being more neutral than at lower redshifts. Of course, it is also possible that the proximity zone is small because the quasar just “turned on". Fortunately, the UKIDSS will soon yield more quasars at similar redshifts, enabling independent measurements of x_{HI} [36].

It is also possible to infer x_{HI} from stronger Lyα absorbers. If a region's neutral hydrogen column density exceeds $10^{20.3}\mathrm{cm}^{-2}$ (and it will if the IGM is neutral), then Lyα absorption enters the damped portion of the curve of growth. In this case, the red damping wing's shape constrains x_{HI}. [75] used the absence of a damping wing in the afterglow spectrum of a gamma-ray burst to infer that $x_{\mathrm{HI}}(z = 6.3) < 0.17$. By contrast, [7] find evidence for this feature in the spectrum of

ULAS J1120+0641, and they infer from it that $x_{\rm HI}(z=7.085) > 0.1$. Of course, it is also possible that the surrounding IGM is highly ionized but a neutral parcel of gas (such as a satellite galaxy) happens to sit just in front of the quasar. This possibility again indicates the need for a larger sample of reionization-epoch quasars.

2.2 Redshifted hyperfine emission from neutral hydrogen

A hydrogen atom has slightly lower energy when the spins of its proton and electron are antiparallel than when they are parallel, and it can transition between these energy states by emitting or absorbing a photon of wavelength 21.1 cm. Early in the reionization epoch, when the IGM had been warmed by quasars and stars but not yet ionized, the entire Universe was glowing brightly in this transition. Many of those photons were never re-absorbed, leading to a background that should be visible today at a frequency of 1420.4 Mhz$/(1+z) \approx 140$ Mhz. In fact, it should be possible to image the sky at a range of frequencies around 140 Mhz and document the progress of reionization [76] either by directly imaging brighter neutral and fainter ionized regions or through statistical approaches. In practice, the observation is challenging because the expected flux is five orders of magnitude weaker than foreground sources. Nonetheless, many low frequency radio experiments are under development that will use novel calibration techniques to isolate this signal and map out the history of reionization [51].

Recently, [10] used the simpler approach of measuring the all-sky spectrum of redshifted 21cm emission. They inferred that, if reionization occured between $z=13$ and $z=6$, then its duration was longer than $\Delta z > 0.06$ with 95% confidence. Models generally predict that its duration was significantly longer than this, so it is not yet a strong constraint. Nonetheless, it is the first result from what promises to be a rich field over the coming decades.

2.3 The Cosmic Microwave Background

Another approach to constraining the timing of reionization involves measuring the impact that Thomson scattering by free electrons had on the anisotropies in the cosmic microwave background (CMB). This is quantified by $\tau_{\rm es}$, which can be thought of as the probability that a given CMB photon scattered at some redshift below roughly 30. Measurements by the WMAP satellite indicate that $\tau_{\rm es} = 0.088 \pm 0.015$ [44]. Of this, 0.050 originates from the portion of the photon's path between $z=7$ and $z=0$. The remaining 0.035 is an integral constraint on the history of reionization. It could indicate that reionization occurred over a short interval (but longer than $\Delta z = 0.06$!) around $z=10.6$, but it is equally consistent with some scenarios in which reionization began at $z=14$ and completed around $z=6$ (see Figure 4 of [85]).

Additional constraints come from much smaller-scale fluctuations in the CMB. The idea is that CMB photons can gain energy by inverse-Compton scattering off of energetic electrons. If the scattering electrons reside within a galaxy cluster, then they create "hot spots" in CMB maps; this is called the thermal Sunyaev-Zel'dovich (tSZ) effect. If the scattering electrons exhibit bulk motions, then it is called the kinetic Sunyaev-Zel'dovich (kSZ) effect. Some kSZ scattering occurs after reionization, but an additional contribution is expected from ionized patches at $z > 6$. The kSZ signature constrains the duration of reionization because the distribution of ionized and neutral patches that a line of sight passes through depends on how long reionization lasted. Since

2007, the South Pole Telescope (SPT) and the Atacama Cosmology Telescope (ACT) have been measuring small-scale fluctuations in the CMB that are sensitive to this effect. [85] recently combined measurements from the SPT and WMAP, finding with 95% confidence that reionization had a duration of less than $\Delta z = 7.9$ and ended before $z = 5.8$. Their inferences will improve with more data and a better understanding of dusty star-forming galaxies at lower redshifts.

2.4 Signatures of Reionization on Galaxies

Star-forming galaxies irradiate their interstellar media (ISMs) with ionizing photons from massive stars. Two thirds of the resulting hydrogen recombinations produce Lyα photons. Now, Lyα is the lowest-energy transition to the ground state of hydrogen. This means that a Lyα photon in a neutral region will be repeatedly absorbed and re-emitted, performing a random walk until it either escapes or is destroyed. The photon is “destroyed" if an absorbing atom decays through two-photon emission. It can also be destroyed through dust absorption or OIII Bowen fluorescence. If the IGM is fully ionized, then any photons that escape their galaxy’s ISM will no longer scatter. This is the case at $z < 6$, where many galaxies show strong Lyα emission lines [54]. If a galaxy emits Lyα photons into an IGM that is not fully ionized, however, then its Lyα photons will be scattered into a low surface-brightness halo. This has several measureable consequences.

The luminosity function of Lyα emitters should evolve. Galaxies that are selected to have bright Lyα emission lines are called Lyα emitters (LAEs). Models indicate that, at epochs during which the IGM is more than 50% ionized, the observed abundance of LAEs should drop precipitously owing to IGM scattering [26, 49]. Recently, three studies reported that the luminosity function (LF) of LAEs decreases from $z = 5.7$ to $z = 6.5$ [37, 57, 41]. This evolution could owe to a partially-neutral IGM at $z = 6.5$, but it could also owe to an overall decline in the abundance of galaxies. [41] therefore verified that the distribution of UV-continuum fluxes from their LAEs at $z = 5.7$ and $z = 6.5$ are similar. This conflicts with the view that the $z = 6.5$ sample is fainter in Lyα owing to lower star formation rates and suggests a partially-neutral IGM. If so, [41] inferred that x_{HI} increases from 0 to 0.3–0.4 from $z = 5.7 \rightarrow 6.5$. However, the amount by which the LAE LF evolves differs between the different studies, leading to uncertainty in the strength of the constraint on reionization. Larger samples will eventually settle this question.

The Lyα escape fraction should evolve. A complementary way to identify IGM attenuation on Lyα emission lines is to identify galaxies at a range of redshifts using a selection technique that does not involve Lyα, then explore the evolution in their Lyα properties. Samples that push into the reionization epoch should have suppressed Lyα emission for the same reasons as before. Galaxies that are identified via the Lyman-dropout technique can be used in this way [68].

Over the past two years, evidence has accumulated that the equivalent width of Lyα emission from such samples grows with increasing redshift to $z = 6$ and then drops to higher redshifts [57, 56, 60, 66, 74]. This evolution is often referred to as an evolving “escape fraction" of Lyα, but its physical interpretation remains controversial. [56] present evidence that the Lyα escape fraction drops for faint objects but not for bright ones and interpret this as a constraint on the topology of reionization, or the order in which regions of different densities reionized. This conflicts with the expectation that reionization will suppress the abundance of bright Lyα sources by the same factor as faint ones [26, 49]. Therefore, differential evolution in the Lyα escape fraction could also be a signature of differential evolution in galaxies’ ISMs. If, for example, the gas fraction evolves rapidly for low-mass galaxies, then they could simply destroy their Lyα photons more effectively at higher redshift. Settling this question will require improved constraints on bright and faint galaxies.

The clustering of LAEs should increase. Galaxies are not distributed uniformly in space, and the degree to which they cluster constrains the dominant growth processes. Conceptually, observers quantify clustering through the enhanced probability that a galaxy has a neighbor at a given distance over what would be expected if galaxies were distributed uniformly. If galaxies produced the photons that drove cosmological reionization, then their clustering influences the history of reionization. In particular, by the time that $x_{\rm HI}$ has dropped to $\sim 50\%$, the average ionized gas parcel sits within an ionized region that is of order 10 comoving Megaparsecs in radius and whose ionization is maintained by many hundreds of galaxies working together. A Lyα photon emitted within such a region redshifts out of resonance with Lyα after traveling ~ 1 Mpc [12]. By the time it reaches the neutral IGM, it will no longer be able to scatter. The implication is that LAEs ought to exhibit increased clustering as observations push into the reionization epoch because Lyα photons from galaxies in crowded neighborhoods will travel farther before reaching the neutral IGM. [57] searched for this signal and found that LAEs' clustering properties at $z = 6.6$ were indistinguishable from samples at lower redshifts, suggesting that the IGM was already more than 50% ionized by $z = 6.6$.

The mean shape of the Lyα line profile should evolve. As $x_{\rm HI}$ increases, the tendency for the IGM to scatter the Lyα line should evolve more strongly on the blue side of the line than on the red side. Consequently, the typical profile of the Lyα line could evolve in redshift. [57] compared the stacked line profiles of LAEs at $z = 5.7$ and $z = 6.6$, finding at most 1σ evidence for evolving line profiles. This is inconsistent with some models in which $x_{\rm HI}$ increases from 0 to > 0.5 during this redshift interval.

In summary, some of the expected signatures of reionization on the Lyα properties of galaxies have been detected while others have not. Unfortunately, the interpretation of these observations remains unclear. A major source of uncertainty involves the role that bulk gas motions could play in modulating Lyα line profiles. For example, gas outflows can endow Lyα photons with a net redshift, making it easier for them to avoid scattering off of the IGM once they emerge from the galaxy. [15] showed that this effect can allow more than half of all Lyα photons to avoid scattering even if $x_{\rm HI} = 0.6$. More generally, a consensus as to the physical interpretation for Lyα line profiles does not yet exist owing to degeneracies between the processes that could affect them. For this reason, observations of Lyα emission cannot by themselves constrain the history of reionization even though they yield a variety of useful and complementary clues.

3. Measuring the Sources of Reionization

Reionization clearly happened. Hence while some investigators reconstruct its timing, others ask which ionizing sources could have been responsible. The sources that can be constrained observationally are quasars and galaxies; I shall touch on more speculative sources in Section 4.

Quasars did not dominate reionization. In particular, by measuring their abundance, estimating their total ionizing luminosity, and comparing it to the IGM recombination rate, many studies have shown that quasars could not have contributed more than half of all ionizing photons at $z > 4$ [67, 28] and only 1–5% at $z = 6$ [79]. This leaves galaxies, which in turn raises two questions:

(1) How many galaxies were there as a function of luminosity and redshift? and (2) How many ionizing photons did they emit into the IGM?

Counting Galaxies By counting galaxies and making simple assumptions regarding their ionizing luminositites, it is possible to show that the observed galaxies could not have kept the Universe ionized at $z = 6$. What about fainter galaxies? The extrapolated abundance of faint galaxies is quantified by the slope of the power law that fits the LF's faint end. Galaxies may drive reionization as long as this slope, α, is steeper (more negative) than -1.6 [82, 62]. A number of groups have recently used extraordinarily deep images taken by the Wide Field Camera 3 (WFC3) on board the Hubble Space Telescope (HST) to constrain the abundance of Lyman dropout galaxies out to $z = 10$ [21, 8, 17, 31, 32, 48, 55]. A consensus is emerging that α is between -1.8 and -2 for $z \geq 6$. In a complementary study, [35] measured the faint-end slope of the LAE LF at $z = 5.7$, finding $\alpha = -1.7$. Both results are consistent with the view that faint galaxies drove reionization.

A complementary way to constrain the activity in galaxies involves counting gamma-ray bursts (GRBs). "Long" gamma-ray bursts are associated with core-collapse supernovae, hence their abundance tracks the total star formation rate density. This inference is subject to its own systematic uncertainties, but unlike galaxy-counting studies it does not require a correction for the contribution from faint galaxies. Recent work indicates that the GRB abundance implies enough star formation in galaxies to complete reionization by $z \approx 8$ [42, 80, 63].

Inferring Their Ionizing Luminosities How many ionizing photons did each galaxy emit into the IGM? This depends on the metallicity and age of its stars as well as the amount of dust in its ISM. Each of these properties also impacts the ultraviolet (UV) continuum ($\lambda \approx$912-3000 Å) of a galaxy's spectrum. Broadly, galaxies with young stars, low metallicities, and low amounts of dust have bluer UV continua and higher ionizing luminosities. Hence constraining the UV continua of reionization-epoch galaxies is a way to learn about their ionizing luminosities.

Recent studies have used WFC3 observations to show that fainter reionization-epoch galaxies are bluer [9, 22]. They interpret this trend as evidence that fainter galaxies have less dusty ISMs. If so, then dust was nearly absent from the faint galaxies that probably dominated reionization. The UV continuum luminosity is then a more direct tracer of the ionizing luminosity than at lower redshifts, where the UV continuum is invariably modulated by dust extinction. Moreover, a larger fraction of ionizing photons probably escape into the IGM. Both of these studies also find that the UV continuum slopes lie within the range expected for moderately metal-enriched stellar populations. In other words, observations do not yet provide evidence for the long-sought zero-metallicity stars, which are expected to show very blue UV continua [64].

What fraction of ionizing photons escape into the IGM and participate in reionization? Clearly, this question is impossible to answer directly because ionizing photons emitted by reionization-epoch galaxies were absorbed by the IGM. However, it is possible to constrain the ionizing escape fraction, f_{esc}, at lower redshifts. [71] and [53] recently used direct detections of ioinizing photons from galaxies at $z \sim 3$ to show that the ratio of escaping ionizing continuum flux F_{LyC} to 1500 Å flux F_{1500} increases both with increasing redshift and decreasing luminosity. This suggests that f_{esc} increases to high redshift and faint luminosity. Remarkably, their measurements also favor higher ratios of $F_{\mathrm{LyC}}/F_{1500}$ than is expected of standard stellar population sythesis models. Both findings enhance the role of faint galaxies in driving reionization.

4. Modeling Reionization

4.1 Sources of Reionization

Although it is widely believed that galaxies and quasars dominated reionization, they need not have acted alone. The theoretical search for plausible additional ionizing sources reads somewhat like a murder mystery in which the crime occurs in a crowded room. [40] recently argued that supernova remnants could have emitted up to 10% as many ionizing photons into the IGM as massive stars. The idea is that shocks produce a harder ionizing continuum than hot stars. Their more energetic photons experience a longer mean free path, hence their contribution to the photons that escape into the IGM could be significant.

Shocks from structure formation have also been forwarded [50, 16]. Here, the idea is that gas that accretes into relatively massive halos ($> 3\times10^{10}\mathrm{M}_\odot$ for [16] and $10^{11}-10^{12}\mathrm{M}_\odot$ for [50]) shocks as it accretes and virializes, converting gravitational potential energy into ionizing photons. [81] recently showed that, even if all baryons that fall into massive halos convert their gravitational potential energy into photons at the hydrogen ionization edge, they only produce 1 ionizing photon per three hydrogen atoms by $z = 6$. This is far less than the likely contribution from galaxies. Nonetheless, these inquiries suggest that shocks may have impacted the IGM's thermal history, the topology of hydrogen reionization, and played a role in He II reionization.

Star formation in the progenitors of globular clusters (GCs) has also been proposed [61]. This is especially plausible if the total mass that formed in the progenitors of present-day GCs was $\sim 10\times$ as large as their current stellar masses and if $f_{\mathrm{esc}} \sim 1$. This idea has recently gained momentum from new observations of the metal abundances of GCs and the identification of candidate second-generation stars in the Milky Way's stellar halo. By using these observations to constrain the stellar initial mass function of GCs as well as the mass function of GCs themselves, [65] have shown that the contribution of GCs to reionization could have been quite large. If true, then the progenitors of massive GCs could have had masses of $10^6\mathrm{M}_\odot$ and will be visible to JWST.

More exotic sources of ionizing photons such as decaying dark matter particles and evaporating primordial black have not received much attention in recent years. We refer the reader to Section 3.4.4 of Furlanetto et al. [27] and Section 1 of Choudhury & Ferrara [13] for an introduction to these alternatives.

4.2 The Ionizing Escape Fraction from Galaxies

The fraction of ionizing photons that escaped into the IGM, f_{esc}, is a crucial parameter that is regularly studied theoretically. [20] review both observational and theoretical inquiries into f_{esc}; interested readers may refer to their introduction for an overview. Broadly, analytical and numerical models predict values that span the full range from 0–1. In order to understand this apparent lack of consensus, [20] use a simple model of stars embedded in a disk to explore how the properties of a galaxy's ISM and its stellar population modulate f_{esc}. They show that galaxies that deposit a large fraction of their ISM into a small number of high-density clumps possess a large f_{esc}. They also show that more intensely star-forming galaxies possess higher f_{esc} partly because fewer baryons remain in the ISM and partly because the number of optically-thin sightlines through the ISM increases. They then attribute the wide range spanned by theoretical studies primarily to differences in the assumed gas masses and ISM topologies. The implication is that the predicted $f_{\rm esc}$ will remain uncertain until the ISMs of high-redshift galaxies are understood.

4.3 The IGM Recombination Rate

In Section 3, I discussed efforts to measure the rate at which new ionizing photons were emitted into the IGM. Closing the loop requires us to know how many photons were required to achieve reionization, which in turn depends on the IGM's mean recombination rate. At early times ($z \geq 20$), the Universe was relatively homogeneous and the recombination rate per volume in an ionized region was well-approximated by $\alpha\langle n_{\rm H}\rangle^2$, where α is the hydrogen recombination coefficient at a characteristic temperature such as 10^4K and $\langle n_{\rm H}\rangle$ is the mean hydrogen number density. By $z = 6$, however, the IGM was inhomogeneous. Correcting for this involves multiplying the above rate by the clumping factor C, which depends on the probability distribution function of baryon densities, the topology of reionization—that is, which regions are ionized and which ones remain neutral—and the temperature of the ionized gas. [58] used realistic density fields culled from three-dimensional numerical simulations to predict that C lies within the range 3–8 by $z = 6$. More recently, [70] used a different numerical model to predict that C =2–4 by $z = 6$. Neither of these works included a self-consistent treatment of cosmological reionization, hence they were forced to make assumptions regarding the densities and temperatures of ionized regions. Their simulations also subtended different cosmological volumes at different spatial resolutions, hence it is possible that the slightly lower value of [70] owes to differences in resolution and the assumed topology of reionization. Broadly, however, both works prefer values C that lie within the range of 3–10. This range is low enough to allow dwarf galaxies to drive reionization.

4.4 One-Dimensional Models

As we have seen, the history of reionization remains subject to many uncertainties such as the ionizing emissivity of stars and quasars, $f_{\rm esc}$, C, and the way in which these quantities evolve. A popular approach to understanding how these factors interact involves distilling reionization to a single equation that follows the growth of the ionized volume fraction with time. In this "photon-counting" exercise (for example, Equation 64 of [34]), the time rate of change of the neutral volume fraction is given by $-$(the ionizing emissivity per hydrogen atom from all sources) $+$(the recombination rate per hydrogen atom). The first term includes $f_{\rm esc}$ and the second includes C. [34] have shown that this formalism brings observations of the abundances of galaxies, quasars, IGM absorbers, and the optical depth to Thomson scattering (Section 2.3) into agreement with one another. Importantly, they assume a relatively low value $C = 3$ at $z = 6$, and they assume that the luminosity-weighted mean $f_{\rm esc}$ increases at earlier times such that it exceeds 50% for $z > 9.3$. These insights serve both as valuable inputs to complementary theoretical efforts and as predictions for future observational campaigns that will constrain $f_{\rm esc}$.

4.5 Three-dimensional Models

Theorists have been attempting to model reionization in three dimensions for over a decade. A central goal is to model cosmic structure formation starting from $z \geq 100$ with as few physical assumptions as possible while reproducing as many observables as possible. I will divide the factors that models must consider into “agents", “processes", and “parameters". Agents include density fluctuations, Lyman limit systems, galaxies, and quasars. Processes include gas flows, the absorption of ionizing photons by an inhomogeneous IGM, recombinations, spectral hardening, and Jeans smoothing (Section 4.5.1). Emerging parameterizations that quantify these processes include the star formation efficiency as a function of dark matter halo mass; $f_{\rm esc}$; the latent heat per IGM photoionization; and the IGM temperature, metallicity, ionization state, and recombination rate. To date, the chief observables have consisted of $\tau_{\rm es}$ (Section 2.3) and $x_{\rm HI}(z)$. In the near future, reionization models will begin confronting complementary observations of galaxies, the IGM metallicity, and the post-reionization Universe more generally.

The challenge of modeling these processes self-consistently is often summarized as follows: Properly sampling long-wavelength density fluctuations requires computational volumes to subtend at least $100h^{-1}$ Mpc [4]. Meanwhile, the lowest-mass dark matter halos that can form stars have a total mass of $\sim 10^8 M_\odot$; these must be resolved with > 100 resolution elements. This implies a spatial dynamic range of 3×10^5. State-of-the-art hydrodynamic simulations currently achieve one tenth of this range. Folding in a treatment for radiation transport increases the computational expense by an additional 1–2 orders of magnitude. This dynamic range can be achieved within individual regions in “zoom-in" simulations, but not throughout a representative cosmological volume. In the face of these demands, progress is made by omitting or treating approximately some subset of the relevant physical processes or scales. Here I shall review recent efforts to this end. For a more comprehensive overview of cosmological radiation transport, see the code comparison papers [38, 39] or the review article by Trac & Gnedin [78].

4.5.1 Dark Matter + Radiation Transport

Many studies use N-body (gravity-only) simulations to derive the cosmic density field, assume that gas follows matter, populate dark matter halos with ionizing sources following simple prescriptions, and then compute the inhomogeneous reionization history (see [78] for a summary of these works). The most recent of these calculations benefit from excellent spatial dynamic range, and they have simultaneously reproduced observations of $\tau_{\rm es}$ and $x_{\rm HI}$. The tradeoff is that they do not treat hydrodynamics and must therefore make assumptions regarding the scaling between ionizing luminosity and halo mass, the impact of photoionization heating on the IGM clumping factor, and the response of low-mass systems to photoionization heating. The latter processes are called “Jeans smoothing" and “Jeans suppression" and are simple to understand: When mildly overdense regions are photoheated, they expand until their self-gravity balances the local gas pressure (Jeans smoothing). Dark matter halos with total masses below $5\times 10^8 M_\odot$ cannot accrete gas in such regions [24], hence their star formation is quenched within a few dynamical times (Jeans suppression).

Another approach is to derive the cosmological density field from precomputed hydrodynamic simulations, which can account (though not self-consistently) for Jeans smoothing by assuming a precomputed ionizing background. Such studies have also confirmed that galaxies could have driven reionization despite the Jeans suppression of low-mass sources. Interestingly, they fail to reproduce the post-reionization $x_{\rm HI}$ and ionization rate. This could owe to resolution limitations [23] or to observational systematics [2].

In a pathbreaking work, [77] combined a high-resolution N-body calculation of the density field with a medium-resolution hydrodynamical calculation that directly models Jeans smoothing while omitting Jeans suppression. They found that, following reionization, the IGM temperature and density are inversely related. This is because overdense regions are reionized and photoheated first, and have therefore had the most time to cool by $z = 6$. Observational tests of predictions such as these will provide complementary constraints on the history of reionization.

4.5.2 Semi-analytical Models

Semi-analytical models (SAMs) [for example, 72] treat the formation of dark matter halos with relatively few approximations, then model how galaxies grow within those halos by using analytic prescriptions for baryonic processes such as gas infall, outflows, and star formation. By sidestepping the expense of discretizing the gas into parcels and integrating the gas equations, they sacrifice some realism in exchange for expanded flexibility. The governing physical parameters can, however, be tuned using observations and numerical simulations, improving their realism.

Benson et al. [6, and references therein] adapted a SAM to compute reionization self-consistently by modeling how ionizations and recombinations drive $x_{\rm HI}(z)$. Their approach accounts for Jeans suppression and includes a model for the clumping factor. It treats radiative processes such as self-shielding and shadowing only approximately and does not predict the topology of reionization. However, its ionizing emissivity can be tuned through observations of galaxy and quasar abundances in the post-reionization Universe, a major advantage. By varying parameters such as $f_{\rm esc}$ and the strength of star formation feedback, they showed that galaxies could give rise to a range of reionization histories including some that are consistent with observations.

State-of-the-art SAMs use a statistical approach to confront many complementary observations simultaneously, yielding joint constraints on processes that regulate galaxy evolution [for example, 46]. Augmenting these models with treatments for inhomogeneous reionization will render them a powerful complement to numerical simulations.

4.5.3 Semi-numerical Models

If reionization was driven by galaxies, then the ionizing photons experienced a short mean free path and, on large enough scales, reionization was a local process. Semi-numerical models build upon this idea: if the number of ionizing photons produced within a region exceeds the number of hydrogen atoms (corrected for recombinations), then the region is probably ionized. These ideas were introduced within the context of an analytical model for reionization [25], and have since been adapted successfully for three-dimensional volumes [for example, 83]. They reproduce the spatial distribution of neutral and ionized regions predicted by the more exact numerical methods on scales larger than $\sim 1h^{-1}$ Mpc [84]. Given that they are inexpensive computationally, they can be combined with a statistical formalism to invert observations of the IGM ionization state and constrain the history of reionization [for example, 85]. They cannot treat processes that occur on spatial scales below which the assumption of local ionization does not apply such as spectral filtering, shadowing, and self-shielding within overdense regions.

4.5.4 Cosmological Radiation-Hydrodynamic Simulations

Simulations that treat dark matter, gas, and the radiation field self-consistently are the most realistic and computationally-intensive approach to modeling reionization. Their principal advantage is that they accurately model small-scale processes such as Jeans smoothing and Jeans suppression.

The tradeoff is that their computational expense prevents them from modeling volumes that are larger than $(\sim 10h^{-1}\ \mathrm{Mpc})^3$, hence they do not capture long-wavelength density fluctuations.

Gnedin & Fan [30] compared predictions from cosmological radiation hydrodynamic simulations with observations of the reionization-epoch Lyα forest and τ_{es}. They showed that high-resolution simulations subtending 4 and $8h^{-1}$ Mpc volumes yield converged predictions of the Lyα forest during the redshift range $5 < z < 6.2$ if the ionizing efficiency is adjusted to reproduce observations at $z = 6 \pm 0.1$. The predicted $x_{\mathrm{HI}}(z > 6.1)$ and τ_{es} depend on the adopted mass resolution owing to star formation activity in systems whose mass lies near or below the resolution limit. The predicted IGM transmission grows less resolution-convergent in the reionization epoch because it is dominated by rare optically-thin regions. This work showed that simulations can reproduce the evolution of several observables of the reionization-epoch IGM. However, accounting for their sensitivity to resolution and volume limitations represents a formidable challenge.

In order to leverage the extensive observational constraints available from the post-reionization epoch, Finlator et al. [24] merged a well-studied galaxy evolution model with a radiation transport solver. They then used this framework to explore the impact of outflows and Jeans smoothing on star formation and reionization. They found that models combining strong outflows with an escape fraction of $f_{\mathrm{esc}} = 50\%$ simultaneously reproduces the observed galaxy abundance at z =6–8 while completing reionization by $z = 6$. They also studied how outflows and an ionizing background couple, finding that outflows promote star formation in dwarf galaxies by delaying reionization while suppressing it in more massive systems by coupling nonlinearly to the ionizing background (see also [59]). Their preferred model overproduced the ionizing background at $z < 6$ while underproducing τ_{es}. They interpreted this as evidence that f_{esc} must evolve (consistent with [34]).

The problem of how to use radiation hydrodynamic simulations to improve our understanding of reionization-epoch galaxies and the IGM is a theoretical frontier owing to its computational expense. Over the next decade, efforts will be directed at two complementary goals. First, models will be generalized in order to expand the range of observables against which they can be tested. For example, artificial lines of sight through simulations will be compared with quasar absorption spectra in order to measure the reionization-epoch IGM's metallicity and temperature. Likewise, testing models against measurements of galaxies' colors and luminosities will constrain the abundance and activity in the putative ionizing population. These studies can be undertaken using existing simulations and will test current assumptions. Relaxing those assumptions is the second goal, and doing so requires expanding the dynamic range. Here there are two ways forward. The "brute-force" approach involves chipping away at the limitations of monolithic simulations through improved algorithms and hardware. The other approach uses high-resolution, small-volume simulations to tune the assumptions that underlie cosmological simulations. For example, [43] used small-volume simulations to estimate C while other authors are using high-resolution simulations to model the star formation rates, metallicities, and f_{esc} from reionization-epoch dwarf galaxies [11]. This approach will remain important until dynamic range limitations are overcome.

5. Summary

Over the past decade, CMB and galaxy observations have given rise to a consensus that galaxies could have driven hydrogen reionization, which in turn ended at some point before $z = 6$. While little else is clear at the moment, a wide variety of studies are whittling away at the dominant questions. New observations of emission lines, the CMB, and redshifted 21 centimeter emission will soon measure the history of reionization. Ground- and space-based observations will locate and characterize the sources that caused it. On the theoretical side, “brute force" campaigns are expanding the dynamic range of numerical simulations. At the same time, approximate techniques are under development that will synthesize observational and theoretical insights into models that have broad applicability. All of this activity will render the coming decade a very active one, and there is every reason to believe that it will yield a much clearer picture of what went on during the second half of the first billion years.

References

[1] National Research Council. *New Worlds, New Horizons in Astronomy and Astrophysics.* Washington, DC: The National Academies Press, 2010.

[2] Aubert, D., & Teyssier, R., *Reionization Simulations Powered by Graphics Processing Units. I. On the Structure of the Ultraviolet Radiation Field*, 2010, ApJ, 724, 244

[3] Barkana, R., & Loeb, A., *In the beginning: the first sources of light and the reionization of the universe*, 2001, Phys. Rep., 349, 125

[4] Barkana, R., & Loeb, A., *Unusually Large Fluctuations in the Statistics of Galaxy Formation at High Redshift*, 2004, ApJ, 609, 474

[5] Becker, R. H., Fan, X., White, R. L., et al., *Evidence for Reionization at* $z \sim 6$*: Detection of a Gunn-Peterson Trough in a z=6.28 Quasar*, 2001, AJ, 122, 2850

[6] Benson, A. J., Sugiyama, N., Nusser, A., & Lacey, C. G., *The epoch of reionization*, 2006, MNRAS, 369, 1055

[7] Bolton, J. S., Haehnelt, M. G., Warren, S. J., et al., *How neutral is the intergalactic medium surrounding the redshift* $z = 7.085$ *quasar ULAS J1120+0641?*, 2011, MNRAS, 416, L70

[8] Bouwens, R. J., et al., *Lower-Luminosity Galaxies could reionize the Universe: Very Steep Faint-End Slopes to the UV Luminosity Functions at* $z \geq 5$–8 *from the HUDF09 WFC3/IR Observations*, 2011, arXiv:1105.2038

[9] Bouwens, R. J., Illingworth, G. D., Oesch, P. A., et al., *UV-continuum slopes at* $z \sim 4$–7 *from the HUDF09+ERS+CANDELS observations: Discovery of a well-defined UV-color magnitude relationship for* $z \geq 4$ *star-forming galaxies*, 2011, arXiv:1109.0994

[10] Bowman, J. D., & Rogers, A. E. E., *A lower limit of* $\Delta z > 0.06$ *for the duration of the reionization epoch*, 2010, Nature, 468, 796

[11] Bromm, V., & Yoshida, N., *The First Galaxies*, 2011, ARA&A, 49, 373

[12] Cen, R., & Haiman, Z., *Quasar Strömgren Spheres Before Cosmological Reionization*, 2000, ApJ, 542, L75

[13] Choudhury, T. R., & Ferrara, A., *Physics of Cosmic Reionization*, 2006, arXiv:astro-ph/0603149

[14] Ciardi, B., & Ferrara, A., *The First Cosmic Structures and Their Effects*, 2005, Space Science Reviews, 116, 625

[15] Dijkstra, M., Mesinger, A., & Wyithe, J. S. B., *The detectability of Ly*α *emission from galaxies during the epoch of reionization*, 2011, MNRAS, 414, 2139

[16] Dopita, M. A., Krauss, L. M., Sutherland, R. S., Kobayashi, C., & Lineweaver, C. H., *Reionizing the universe without stars*, 2011, Ap&SS, 335, 345

[17] Dunlop, J. S., McLure, R. J., Robertson, B. E., et al., *A critical analysis of the ultraviolet continuum slopes (β) of high-redshift galaxies: no evidence (yet) for extreme stellar populations at $z > 6$*, 2012, MNRAS, 420, 901

[18] Fan, X., Narayanan, V. K., Strauss, M. A., et al., *Evolution of the Ionizing Background and the Epoch of Reionization from the Spectra of $z \sim 6$ Quasars*, 2002, AJ, 123, 1247

[19] Fan, X., et al., *Constraining the Evolution of the Ionizing Background and the Epoch of Reionization with $z \sim 6$ Quasars. II. A Sample of 19 Quasars*, 2006, AJ, 132, 117

[20] Fernandez, E. R., & Shull, J. M., *The Effect of Galactic Properties on the Escape Fraction of Ionizing Photons*, 2011, ApJ, 731, 20

[21] Finkelstein, S. L., Papovich, C., Giavalisco, M., Reddy, N. A., Ferguson, H. C., Koekemoer, A. M., & Dickinson, M., *On the Stellar Populations and Evolution of Star-forming Galaxies at $6.3 < z \leq 8.6$*, 2010, ApJ, 719, 1250

[22] Finkelstein, S. L., Papovich, C., Salmon, B., et al., *CANDELS: The Evolution of Galaxy Rest-Frame Ultraviolet Colors from $z = 8$ to 4*, 2011, arXiv:1110.3785

[23] Finlator, K., Özel, F., & Davé, R., *A new moment method for continuum radiative transfer in cosmological reionization*, 2009, MNRAS, 393, 1090

[24] Finlator, K., Davé, R., Özel, F., *Galactic Outflows and Photoionization Heating in the Reionization Epoch*, 2011, ApJ, 743, 169

[25] Furlanetto, S. R., Zaldarriaga, M., & Hernquist, L., *The Growth of H II Regions During Reionization*, 2004, ApJ, 613, 1

[26] Furlanetto, S. R., Zaldarriaga, M., & Hernquist, L., *The effects of reionization on Lyα galaxy surveys*, 2006, MNRAS, 365, 1012

[27] Furlanetto, S. R., Oh, S. P., & Briggs, F. H., *Cosmology at low frequencies: The 21 cm transition and the high-redshift Universe*, 2006, Phys. Rep., 433, 181

[28] Glikman, E., Djorgovski, S. G., Stern, D., et al., *The Faint End of the Quasar Luminosity Function at $z \sim 4$: Implications for Ionization of the Intergalactic Medium and Cosmic Downsizing*, 2011, ApJ, 728, L26

[29] Gnedin, N. Y., *Cosmological Reionization by Stellar Sources*, 2000, ApJ, 535, 530

[30] Gnedin, N. Y., & Fan, X., *Cosmic Reionization Redux*, 2006, ApJ, 648, 1

[31] González, V., Labbé, I., Bouwens, R. J., Illingworth, G., Franx, M., & Kriek, M., *Evolution of Galaxy Stellar Mass Functions, Mass Densities, and Mass-to-light Ratios from $z \sim 7$ to $z \sim 4$*, 2011, ApJ, 735, L34

[32] Grazian, A., et al., *A critical analysis of the UV luminosity function at redshift ~ 7 from deep WFC3 data*, 2011, A&A, 532, A33

[33] Gunn, J. E., & Peterson, B. A., *On the Density of Neutral Hydrogen in Intergalactic Space.*, 1965, ApJ, 142, 1633

[34] Haardt, F., & Madau, P., *Radiative Transfer in a Clumpy Universe. IV. New Synthesis Models of the Cosmic UV/X-Ray Background*, 2012, ApJ, 746, 125

[35] Henry, A. L., Martin, C. L., Dressler, A., Sawicki, M., & McCarthy, P., *The Faint-end Slope of the Redshift 5.7 Lyα Luminosity Function*, 2012, ApJ, 744, 149

[36] Hewett, P. C., Warren, S. J., Leggett, S. K., & Hodgkin, S. T., *The UKIRT Infrared Deep Sky Survey ZYJHK photometric system: passbands and synthetic colours*, 2006, MNRAS, 367, 454

[37] Hu, E. M., Cowie, L. L., Barger, A. J., et al., *An Atlas of $z = 5.7$ and $z = 6.5$ Lyα Emitters*, 2010, ApJ, 725, 394

[38] Iliev, I. T., Ciardi, B., Alvarez, M. A., et al., *Cosmological radiative transfer codes comparison project - I. The static density field tests*, 2006, MNRAS, 371, 1057

[39] Iliev, I. T., Whalen, D., Mellema, G., et al., *Cosmological radiative transfer comparison project - II. The radiation-hydrodynamic tests*, 2009, MNRAS, 400, 1283

[40] Johnson, J. L., & Khochfar, S., *The Contribution of Supernovae to Cosmic Reionization*, 2011, ApJ, 743, 126

[41] Kashikawa, N., et al., *Completing the Census of Lyα Emitters at the Reionization Epoch*, 2011, ApJ, 734, 119

[42] Kistler, M. D., Yüksel, H., Beacom, J. F., Hopkins, A. M., & Wyithe, J. S. B., *The Star Formation Rate in the Reionization Era as Indicated by Gamma-Ray Bursts*, 2009, ApJ, 705, L104

[43] Kohler, K., Gnedin, N. Y., & Hamilton, A. J. S., *Large-Scale Simulations of Reionization*, 2007, ApJ, 657, 15

[44] Komatsu, E., et al., *Seven-year Wilkinson Microwave Anisotropy Probe (WMAP) Observations: Cosmological Interpretation*, 2011, ApJS, 192, 18

[45] Loeb, A., & Barkana, R., *The Reionization of the Universe by the First Stars and Quasars*, 2001, ARA&A, 39, 19

[46] Lu, Y., Mo, H. J., Weinberg, M. D., & Katz, N., *A Bayesian approach to the semi-analytic model of galaxy formation: methodology*, 2011, MNRAS, 416, 1949

[47] McGreer, I. D., Mesinger, A., & Fan, X., *The first (nearly) model-independent constraint on the neutral hydrogen fraction at $z \sim 6$*, 2011, MNRAS, 415, 3237

[48] McLure, R. J., Dunlop, J. S., de Ravel, L., et al., *A robust sample of galaxies at redshifts $6.0 < z < 8.7$: stellar populations, star formation rates and stellar masses*, 2011, MNRAS, 418, 2074

[49] McQuinn, M., Hernquist, L., Zaldarriaga, M., & Dutta, S., *Studying reionization with Lyα emitters*, 2007, MNRAS, 381, 75

[50] Miniati, F., Ferrara, A., White, S. D. M., & Bianchi, S., *Ultraviolet background radiation from cosmic structure formation*, 2004, MNRAS, 348, 964

[51] Morales, M. F., & Wyithe, J. S. B., *Reionization and Cosmology with 21-cm Fluctuations*, 2010, ARA&A, 48, 127

[52] Mortlock, D. J., Warren, S. J., Venemans, B. P., et al., *A luminous quasar at a redshift of $z = 7.085$*, 2011, Nature, 474, 616

[53] Nestor, D. B., Shapley, A. E., Steidel, C. C., & Siana, B., *Narrowband Imaging of Escaping Lyman-continuum Emission in the SSA22 Field*, 2011, ApJ, 736, 18

[54] Nilsson, K. K., & Meisenheimer, K., *Understanding Lyα emitters*, 2009, New A Rev., 53, 37

[55] Oesch, P. A., Bouwens, R. J., Illingworth, G. D., et al., *Expanded Search for $z \sim 10$ Galaxies from HUDF09, ERS, and CANDELS Data: Evidence for Accelerated Evolution at $z > 8$?*, 2012, ApJ, 745, 110

[56] Ono, Y., Ouchi, M., Mobasher, B., et al., *Spectroscopic Confirmation of Three z-dropout Galaxies at* $z = 6.844$–7.213*: Demographics of Ly*α *Emission in* $z \sim 7$ *Galaxies*, 2012, ApJ, 744, 83

[57] Ouchi, M., et al., *Statistics of 207 Ly*α *Emitters at a Redshift Near 7: Constraints on Reionization and Galaxy Formation Models*, 2010, ApJ, 723, 869

[58] Pawlik, A. H., Schaye, J., & van Scherpenzeel, E., *Keeping the Universe ionized: photoheating and the clumping factor of the high-redshift intergalactic medium*, 2009, MNRAS, 394, 1812

[59] Pawlik, A. H., & Schaye, J., *Photoheating and supernova feedback amplify each other's effect on the cosmic star formation rate*, 2009, MNRAS, 396, L46

[60] Pentericci, L., Fontana, A., Vanzella, E., et al., *Spectroscopic Confirmation of* $z \sim 7$ *Lyman Break Galaxies: Probing the Earliest Galaxies and the Epoch of Reionization*, 2011, ApJ, 743, 132

[61] Ricotti, M., *The Fate of the First Galaxies. I. Self-consistent Cosmological Simulations with Radiative Transfer*, 2002, MNRAS, 336, L33

[62] Robertson, B. E., Ellis, R. S., Dunlop, J. S., McLure, R. J., & Stark, D. P., *Early star-forming galaxies and the reionization of the Universe*, 2010, Nature, 468, 49

[63] Robertson, B. E., & Ellis, R. S., *Connecting the Gamma Ray Burst Rate and the Cosmic Star Formation History: Implications for Reionization and Galaxy Evolution*, 2012, ApJ, 744, 95

[64] Schaerer, D., *On the properties of massive Population III stars and metal-free stellar populations*, 2002, A&A, 382, 28

[65] Schaerer, D., & Charbonnel, C., *A new perspective on globular clusters, their initial mass function and their contribution to the stellar halo and the cosmic reionization*, 2011, MNRAS, 413, 2297

[66] Schenker, M. A., Stark, D. P., Ellis, R. S., et al., *Keck Spectroscopy of Faint* $3 < z < 8$ *Lyman Break Galaxies: Evidence for a Declining Fraction of Emission Line Sources in the Redshift Range* $6 < z < 8$, 2012, ApJ, 744, 179

[67] Shapiro, P. R., & Giroux, M. L., *Cosmological H II regions and the photoionization of the intergalactic medium*, 1987, ApJ, 321, L107

[68] Shapley, A. E., *Physical Properties of Galaxies from* $z = 2$–4, 2011, ARA&A, 49, 525

[69] Shull, J. M., France, K., Danforth, C. W., Smith, B., & Tumlinson, J., *HST/COS Observations of the Quasar HE 2347-4342: Probing the Epoch of He II Patchy Reionization at Redshifts* $z = 2.4$–2.9, 2010, ApJ, 722, 1312

[70] Shull, M., Harness, A., Trenti, M., & Smith, B., *Critical Star-Formation Rates for Reionization: Full Reionization occurs at* $z = 7$, 2011, arXiv:1108.3334

[71] Siana, B., Teplitz, H. I., Ferguson, H. C., et al., *A Deep Hubble Space Telescope Search for Escaping Lyman Continuum Flux at* $z \sim 1.3$*: Evidence for an Evolving Ionizing Emissivity*, 2010, ApJ, 723, 241

[72] Somerville, R. S., Primack, J. R., & Faber, S. M., *The nature of high-redshift galaxies*, 2001, MNRAS, 320, 504

[73] Spergel, D. N., Verde, L., Peiris, H. V., et al., *First-Year Wilkinson Microwave Anisotropy Probe (WMAP) Observations: Determination of Cosmological Parameters*, 2003, ApJS, 148, 175

[74] Stark, D. P., Ellis, R. S., & Ouchi, M., *Keck Spectroscopy of Faint* $3 > z > 7$ *Lyman Break Galaxies: A High Fraction of Line Emitters at Redshift Six* , 2011, ApJ, 728, L2

[75] Totani, T., Kawai, N., Kosugi, G., et al., *Implications for Cosmic Reionization from the Optical Afterglow Spectrum of the Gamma-Ray Burst 050904 at* $z = 6.3$, 2006, PASJ, 58, 485

[76] Tozzi, P., Madau, P., Meiksin, A., & Rees, M. J., *Radio Signatures of H I at High Redshift: Mapping the End of the "Dark Ages"*, 2000, ApJ, 528, 597

[77] Trac, H., Cen, R., & Loeb, A., *Imprint of Inhomogeneous Hydrogen Reionization on the Temperature Distribution of the Intergalactic Medium* , 2008, ApJ, 689, L81

[78] Trac, H., & Gnedin, N. Y., *Computer Simulations of Cosmic Reionization*, 2009, arXiv:0906.4348

[79] Willott, C. J., Delorme, P., Reylé, C., et al., *The Canada-France High-z Quasar Survey: Nine New Quasars and the Luminosity Function at Redshift 6*, 2010, AJ, 139, 906

[80] Wyithe, J. S. B., Hopkins, A. M., Kistler, M. D., Yüksel, H., & Beacom, J. F., *Determining the escape fraction of ionizing photons during reionization with the GRB-derived star formation rate*, 2010, MNRAS, 401, 2561

[81] Wyithe, J. S. B., Mould, J., & Loeb, A., *The Shocking Truth: The Small Contribution to Hydrogen Reionization from Gravitational Infall*, 2011, ApJ, 743, 173

[82] Yan, H., & Windhorst, R. A., *The Major Sources of the Cosmic Reionizing Background at* $z \approx 6$, 2004, ApJ, 600, L1

[83] Zahn, O., Zaldarriaga, M., Hernquist, L., & McQuinn, M., *The Influence of Nonuniform Reionization on the CMB*, 2005, ApJ, 630, 657

[84] Zahn, O., Mesinger, A., McQuinn, M., et al., *Comparison of reionization models: radiative transfer simulations and approximate, seminumeric models*, 2011, MNRAS, 414, 727

[85] Zahn, O., Reichardt, C. L., Shaw, L., et al., *Cosmic microwave background constraints on the duration and timing of reionization from the South Pole Telescope*, 2011, arXiv:1111.6386

PROCEEDINGS OF SCIENCE

First Light

John H. Wise[*†]

Center for Relativistic Astrophysics, Georgia Institute of Technology, 837 State Street, Atlanta, GA 30332, USA
E-mail: `jwise@physics.gatech.edu`

The first stars in the universe are thought to be massive, forming in dark matter halos with masses around 10^6 solar masses. Recent simulations suggest that these metal-free (Population III) stars may form in binary or multiple systems. Because of their high stellar masses and small host halos, their feedback ionizes the surrounding 3 kpc of intergalactic medium and drives the majority of the gas from the potential well. The next generation of stars then must form in this gas-poor environment, creating the first galaxies that produce the majority of ionizing radiation during cosmic reionization. I will review the latest developments in the field of Population III star formation and feedback and its impact on galaxy formation prior to reionization. In particular, I will focus on the numerical simulations that have demonstrated this sequence of events, ultimately leading to cosmic reionization.

Frank N. Bash Symposium New Horizons In Astronomy,
October 9-11, 2011
Austin, Texas

[*]Speaker.

[†]The speaker appreciated the hospitality and efforts by the symposium organizers and the invitation to speak at this venue. This review covers some of my own work, which could not have been accomplished without the help of my collaborators, Tom Abel, Marcelo A. Alvarez, Renyue Cen, Michael L. Norman, and Matthew J. Turk.

PoS(Bash11)013

1. Introduction

The universe was a very dark place in the first tens of millions of years before any luminous structure had formed. This epoch is sometimes referred to as the "Dark Ages", when dark matter (DM) collapsed into bound objects but hosted no stars whatsoever. These DM halos collected a primordial mix of primarily hydrogen and helium in their potential wells after they reached the cosmological Jeans mass $M_J \sim 5 \times 10^3 [(1+z)/10]^{3/2}$ [9]. The first DM halos to cool and collapse produced the first stars in the universe that, in turn, produced the first metals to spark the transition to galaxy formation. Before reviewing the current status of research on the first stars and galaxies, it is worthwhile to step back, pose three simple but informative questions, and review historical pieces of literature that addressed these questions.

The first question we can ask ourselves is: *Why do all observed stars contain metals?* [54] focused on the Milky Way (MW) stellar population and observed (i) that the oldest Population II stars were metal-poor, (ii) a high frequency of white dwarfs, and (iii) a red excess in elliptical galaxies. These points led them to the conclusion that the "original Population II contained a large number of relatively massive stars".

The next question that naturally follows is: *Without any metals, how does gas cool and condense to form stars?* Metal-enriched gas cools mainly through H_2 formation on dust grains and other fine-structure transitions in heavy elements. [40] recognized that H_2 can slowly form in the gas phase through the following reactions:

$$\begin{aligned} \mathrm{H} + \mathrm{e}^- &\rightarrow \mathrm{H}^- + \gamma \\ \mathrm{H}^- + \mathrm{H} &\rightarrow \mathrm{H}_2 + \mathrm{e}^- \end{aligned}$$

or less efficiently

$$\begin{aligned} \mathrm{H} + \mathrm{H}^+ &\rightarrow \mathrm{H}_2^+ + \gamma \\ \mathrm{H}_2^+ + \mathrm{H} &\rightarrow \mathrm{H}_2 + \mathrm{H}^+. \end{aligned}$$

[51] were the first to realize that H_2 formation in the gas-phase was important in star formation in the early universe. They used these reactions to determine that H_2 cooling dominates the collapse of a pre-galactic cloud at number densities $n > 10^4$ cm^{-3}. These high density regions can cool to $\sim$300 K and continue to collapse. [47] suggested that globular clusters were the first bound objects in the universe with masses $\sim 5 \times 10^5$ M$_\odot$. In their calculations, they first compute the properties of these objects from linear perturbation theory and then follow the initial contraction of the cloud, including H_2 cooling. They find that molecular hydrogen cooling is indeed efficient enough to drive a free-fall collapse, in which only a small fraction of the total gas mass forms stars due to the inside-out nature of the collapse.

The third pertinent question is: *When and where do the first stars form?* Applying the properties of cooling primordial gas to the cold dark matter model, [21] determined that the first objects to cool and collapse due to H_2 formation would be hosted in DM halos with masses $\sim 10^6$ M$_\odot$ at $z = 20 - 30$. A decade later, [58] used a detailed chemical model to follow the formation of H_2 in virialized objects, starting from recombination. They found that the redshift-dependent minimum DM halo mass to host H_2 cooling, rising from 5×10^3 M$_\odot$ at $z \sim 100$ to 10^6 M$_\odot$ at $z \sim 15$.

These early analytical works provided the theoretical basis for current and recent simulations that focus on the formation of the first stars and galaxies in the universe. Here I review the progress that the field has made in the past decade.

2. Population III star formation

Following a cosmological gaseous collapse over many orders of magnitude in length makes such a simulation technically difficult, but with improvements in algorithms and physical models, several groups have been able to make substantial progress. In the late 1990's and early 2000's, two independent groups used three-dimensional simulations to study Population III star formation. Using smoothed particle hydrodynamics (SPH) simulations of isolated and virialized dark matter halos with masses 2×10^6 $M_\odot$ at $z = 30$, one group found that the object cooled to 300 K through H_2 formation, using the chemical network of [30], and fragmented into a filamentary structure with a Jeans mass of 10^3 $M_\odot$ [13, 14]. In the second paper, they followed the collapse to higher gas densities of 10^8 cm^{-3} and studied the continued formation of dense clumps with the same 10^3 $M_\odot$ characteristic mass. The other group used cosmological adaptive mesh refinement (AMR) simulations to focus on the formation of a molecular cloud hosted by a 7×10^5 $M_\odot$ DM halo [1, 3, 4]. In each successive paper, the H_2 chemistry model [2, 8] was improved to include more processes, such as the three-body H_2 formation process, to follow the central collapse to gas densities up to 3×10^{13} cm^{-3}. Both groups came to the conclusion that further fragmentation was suppressed because of a lack of cooling below 300 K and that Population III stars were *very massive* in the range $30 - 300$ $M_\odot$.

These simulations only represented a limited sample of collapses and could not provide much insight to the Population III initial mass function (IMF). Twelve additional AMR simulations were conducted to look at any variations in primordial gas collapses [45]. They found that the collapses occurred in DM halos with masses in the range $1.5 - 7 \times 10^5$ $M_\odot$ with the scatter caused by differing halo formation histories. The mass accretion rate onto the central molecular cloud was higher at 10^{-4} $M_\odot$ yr^{-1} at $z \sim 30$, and it can increase by two orders of magnitude at $z \sim 20$ in some halos, agreeing with [4].

Following the collapse to densities higher than 10^{13} cm^{-3} required the inclusion of collisionally induced emission, chemical heating from H_2 formation, and gas opacity above 10^{18} cm^{-3}. [77] found with SPH simulations that the initial collapsing region did not fragment as it condensed to protostellar densities $n \sim 10^{21}$ cm^{-3}, forming a protostellar shock in the process. The inner 10 $M_\odot$ had an accretion rate varying between 0.01 and 0.1 $M_\odot$ yr^{-1}, possibly growing to 10 $M_\odot$ within 1000 yr.

In the past few years, multiple groups have been focusing on the subsequent growth of these protostars over several dynamical times, improving upon the earlier works that stopped at the first collapse. This has proved to be challenging because of the ever-decreasing Courant factors at higher densities. One workaround is the creation of "sink particles" that accrete nearby gravitationally-bound gas, allowing the simulation to progress past the first collapse; however, one loses all hydrodynamical information above some density threshold. In one out of five realizations in AMR calculations without sink particles, [65] found that the collapsing core fragmented at a density of 10^{11} cm^{-3} into two clumps that are separated by 800 AU with 100 $M_\odot$ of gas within a sphere with radius twice their separation. At the same time, [56] also found that disk instabilities causes fragmentation into a binary system with a 40 $M_\odot$ and 10 $M_\odot$. This was later confirmed by simulations of a collapse of an isolated Jeans-unstable primordial gas cloud that fragmented into many multiple systems with some very tightly bound to separations less than an AU [19]. Utilizing a new moving mesh code, [29] studied the collapse in five different primordial DM halos, and they evolved them for 1000 yr after the first protostar forms. By evolving these protostars further, they included the effects of protostellar radiative feedback in the infrared in the optically-thin limit. In all cases, the molecular cloud fragments into ~ 10 sink particles, some of which later merge to form more massive protostars. The mass function from these simulations is relatively flat, i.e. a top-heavy IMF.

After the protostar has reached $\sim 10\ M_\odot$, radiative feedback from ionizing radiation will begin to suppress further accretion. Only recently has this been incorporated into numerical simulations of Population III star formation. Starting from initial conditions extracted from a cosmological simulation [77], two-dimensional axi-symmetric radiation hydrodynamical simulations showed that an accretion disk forms around a new protostar with the ionizing radiation preferentially escaping through the polar regions [32]. The disk itself is slowly photo-evaporated, halting accretion after 70,000 yr. At this point, the final mass of the Population III star is 43 $M_\odot$. Without any radiative feedback, the protostar would have continued to grow to $\sim 100\ M_\odot$. In a cosmological setting, [57] found a binary system still forms in the presence of radiative feedback. Without feedback, the primary star grows to 28 $M_\odot$ over 5,000 yr. With feedback, the primary and secondary stars only grow to 19 and 10 $M_\odot$, respectively. An extrapolation of the mass accretion history shows that both stellar masses will asymptote to 30 $M_\odot$, creating an equal-mass binary. Once the stars have entered the main sequence, they will start to ionize and heat their cosmic neighborhood, which I will review next.

3. Population III radiative feedback

Some of the first calculations of the growth and overlap of cosmological H II regions originating from quasars concluded that they could not fully account for reionization. Other radiation sources must have contributed to the photon budget [55]. Later with $z > 4$ galaxy observations, it was clear that low-luminosity galaxies were the primary source of ionizing photons [e.g. 12, 23, 59]. However, Population III preceded galaxy formation, and they were the first sources of ionizing radiation, starting cosmic reionization. They are thought to have a top-heavy IMF, as discussed in the previous section, and zero-metallicity stellar models were constructed to estimate their luminosities, lifetimes, and spectra as a function of mass [15, 53, 64]. One key feature is mass-independent surface temperature of 10^5 K above 40 $M_\odot$, caused by a lack of opacity from metal lines. Thus, Population III are copious producers of ionizing photons with an average photon energy ~ 30 eV and also H_2 dissociating radiation, which is < 13.6 eV where the neutral universe is optically-thin. Because the formation of Population III stars is primarily dependent on H_2 formation, any H_2 dissociating radiation can suppress Population III star formation from large distances [22, 34, 38, 46, 69].

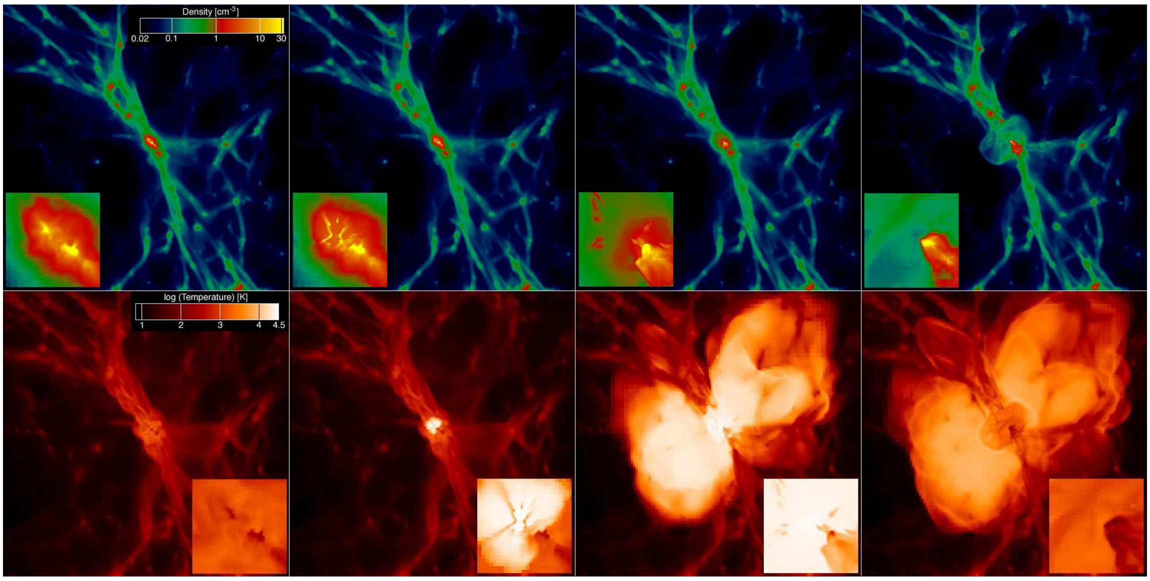

Figure 1: The formation of a H II region from a Population III star, shown with projections of gas density (top) and temperature (bottom) of a ~ 3 proper kpc region, centered on the first star at $z = 20$. From left to right, the depicted times correspond to 0, 1, 2.7, and 8 Myr after the star formed. The insets correspond to the same times, have the same color scale, and show the central 150 pc. From [6].

3.1 H II regions from Population III stars

Combining the main sequence properties of Population III stars and the endpoints of cosmological simulations, one-dimensional radiation hydrodynamics simulations followed the growth of an H II region from Population III stars with masses ranging from 25 to 500 $M_\odot$ [36, 66]. The ionization front drives a 30 km s^{-1} shock wave. Because the escape velocity of 10^6 $M_\odot$ halos is only ~ 3 km s^{-1}, approximately 90% of the gas is expelled from the DM halo, leaving behind a warm ($T \sim 3 \times 10^4$ K) and diffuse ($\rho \sim 0.1$ cm^{-3}) medium. At the end of the star's lifetime, a 100 $M_\odot$ star creates an H II region with a radius ~ 3 kpc.

Shortly afterward, it became feasible to include radiative transfer in cosmological simulations, either through moment methods or ray tracing. In three dimensions, it is possible to investigate the ionization of a clumpy and inhomogeneous medium and any ionization front instabilities [67] that might arise. [7] found that between 70% and 90% of the ionizing photons escaped into the IGM, using ionization front tracking and an approximate method to calculate the thermodynamic state behind the front. This calculation also showed that some nearby halos are not fully photo-evaporated, leaving behind a neutral core. Furthermore, nearby filamentary structure is slower to ionize, and the ionization front grows faster in the voids, creating a "butterfly" shape [5]. The first three-dimensional radiation hydrodynamics simulations uncovered multi-fold complexities that were not seen in previous simulations, such as cometary structures and elephant trunks seen in nearby star forming regions [6]. Figure 1 shows the growth of the H II region emanating from the host minihalo. The density structures in the nearby filaments were largely unaffected by the radiation because they are self-shielded. The 30 km s^{-1} shock wave collects 10^5 $M_\odot$ of gas into a shell over the lifetime of the star, which is Jeans stable and is dispersed after the star's death.

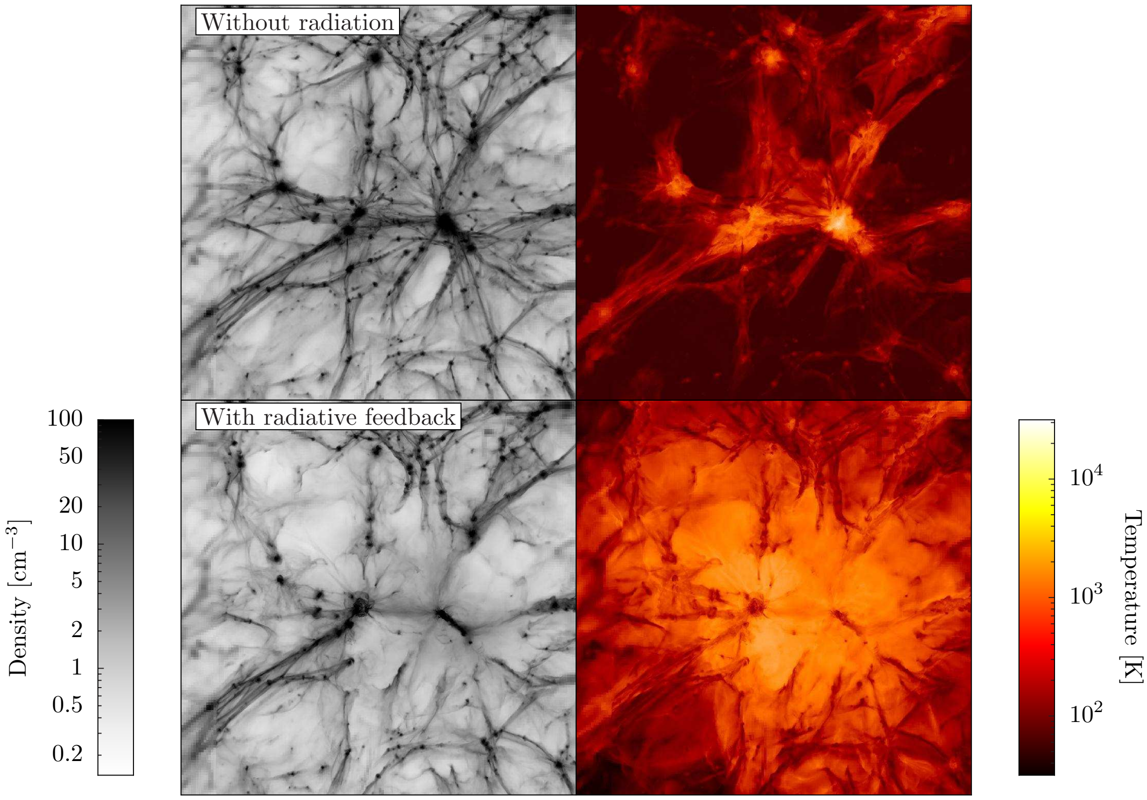

Figure 2: The effects of radiative feedback from the first stars, shown in projections of gas density (left) and temperature (right) in a field of view of 8.5 proper kpc in a region heated and ionized by tens of Population III stars at $z = 16$. Notice how most of the nearby substructures are photo-evaporated. From [70].

As the H II region grows up to 3 kpc in radius, nearby halos become engulfed in a sea of ionized gas. Because free electrons are the catalyst for H_2 formation, a boosted electron fraction promotes more efficient cooling; furthermore, HD cooling becomes relevant in the collapse of these halos in relic H II regions [41, 44, 75, 76]. Instead being limited to a 300 K temperature floor, this gas cools to ~ 50 K, resulting in a Jeans mass a factor of $\sim 5/2$ lower. Thus, it is expected that these Population III stars will have a lower characteristic mass in the approximate range of 5–60 $M_\odot$. After this discovery, it was felt that these two different population needed to be separated, where metal-free stars forming in an unaffected region are termed “Population III.1”, and metal-free stars forming in ionized gas were coined “Population III.2” [43].

3.2 Contribution to reionization

The H II regions from metal-free stars are much larger than present-day H II regions and can have a sizable impact on the reionization history. [70] found that Population III stars can ionize up to 25% of the local IGM in a biased region, surrounding a rare $3-\sigma$ overdensity. Because Population III stars are short lived (~ 3 Myr), the H II regions are fully ionized only for a short time and then quickly recombines over the next ~ 50 Myr. Within a local cosmological region, there are many relic H II regions but only a handful of active H II regions with $T > 10^4$ K. Once the

H II regions start to overlap, each star can ionize a larger volume as the neutral hydrogen column density decreases. At the end of the simulation, one in ten ionizing photons results in a sustained ionization in the intergalactic medium (IGM). In addition to ionizing the IGM, the photo-heating of the host halo and IGM delays further local star formation by smoothing out gas overdensities in nearby minihalos and IGM, which is depicted in Figure 2. Reducing the IGM clumpiness reduces the recombination rate, which is measured by the clumping factor $C = \langle\rho\rangle^2/\langle\rho^2\rangle$, by 50% [70].

This simulation only considered a small region (1 comoving Mpc^3) and cannot make predictions for global reionization history. To address cosmic reionization, simulations with sizes ~ 100 Mpc are necessary. Here the small-scale clumpiness cannot be resolved, and clumping factor plays a key role in subgrid models. In general, H II regions from Population III stars generate more small-scale power, and at late times, they are quickly overrun by nearby H II regions produced by larger galaxies [33]. In addition, Population III H II regions start reionization earlier and prolongs reionization [61].

4. Supernovae from Population III

Massive metal-free stars can end their lives in a unique type of supernova, a pair-instability SN [e.g. 10, 11, 31]. Non-rotating models find that this occurs in a mass range between 140 and 260 $\mathrm{M}_\odot$, where nearly all of the helium core with mass $M_{\rm He} \approx 13/24(M_\star - 20\,\mathrm{M}_\odot)$ is converted into metals in an explosion of $10^{51} - 10^{53}$ erg. The ejecta can be an order of magnitude greater than typical Type II SNe [73] and hypernovae [42]! The chemical abundance patterns are much different than those in typical explosions with the carbon, calcium, and magnesium yields independent of mass. These pair-instability SNe are one possible cause for carbon-enhanced damped Lyα absorbers [e.g. 20, 48].

These very energetic SNe can exceed the binding energy of halos with masses $M \lesssim 10^7\,\mathrm{M}_\odot$. [16] investigated two explosion energies, 10^{51} and 10^{53} erg, in a cosmological halo with $M \sim 10^6\,\mathrm{M}_\odot$, neglecting any radiative feedback. Nevertheless, they found that over 90% of the gas was expelled into the IGM, and metals propagate to distances of ~ 1 kpc after 3–5 Myr. They argued that pair-instability SNe could have resulted in a nearly uniform metallicity floor in the IGM of $\sim 10^{-4} Z_\odot$ at high redshifts. Subsequent works built upon this idea of a IGM metallicity floor with various techniques: (i) volume-averaged semi-analytic models [24, 52, 74], (ii) models using hierarchical merger trees [37, 50, 63], (iii) post-processing of cosmological simulations with blastwave models [35, 62], and (iv) direct numerical simulations with stellar feedback [39, 49, 60, 72].

Because blastwaves do not penetrate overdensities as efficiently as a rarefied medium, the voids will be preferentially enriched [18]. This raises the following questions. Will the first galaxies have a similar metallicity as the IGM? How much metal mixing occurs in the first galaxies as they accrete material? The complex interplay between radiative and supernova feedback, cosmological accretion, and hydrodynamics are best captured by numerical simulations. Two groups [27, 71] showed that the enrichment from pair-instability SNe resulted in a nearly uniform metallicity in a $10^8\,\mathrm{M}_\odot$ halo at $z \sim 10-15$. These types of halos can efficiently cool through atomic hydrogen cooling, and the halo will form a substantial amount of stars for the first time. Both groups find that the metals are well-mixed in the galaxy because of turbulence generated during virialization

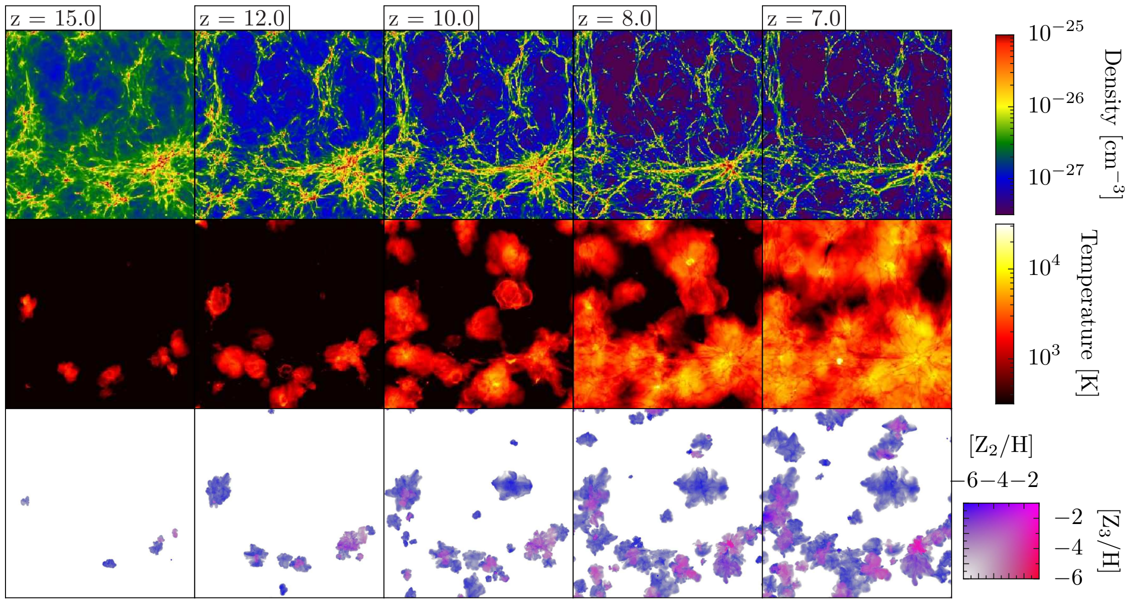

Figure 3: Evolution of the entire simulation volume ($L_{\rm box} = 1$ Mpc) at redshifts 15, 12, 10, 8, and 7 (left to right) that follows the formation of 38 dwarf galaxies and over 300 Population III stars. Pictured here are the density-weighted projections of density (top), temperature (middle), and metallicity (bottom). Note how the stellar radiative feedback from low-mass galaxies reionize the majority of the volume. The metallicity projections are a composite image of metals originating from Pop II (red) and III (blue) stars with magenta indicating a mixture of the two. From [72].

[28, 68] to a metallicity $Z/Z_\odot = 10^{-3} - 10^{-4}$. In these simulations, about 60% of the metals from SNe are reincorporated into the halo, whereas the remaining fraction stays in the IGM. In the end, Population III star formation is ultimately halted by the enrichment of the minihalos from nearby or previously hosted supernovae (SNe), marking the transition to galaxy formation.

5. High-redshift dwarf galaxies

The first galaxies are generally defined as halos that can undergo atomic line cooling, are metal-enriched, and can host sustained star formation [17]. Here I present some of the highlights of our latest numerical work on the formation of the first galaxies [72]. These radiation hydrodynamics AMR simulations tracked the formation and feedback of over 300 Population III stars and the buildup of 38 low-mass galaxies in a 1 comoving Mpc^3 volume until $z = 7$. The cosmic Population III star formation rate (SFR) is nearly constant at 3×10^{-5} M$_\odot$ yr^{-1} Mpc^{-3} from $z = 15$ to $z = 7$. The largest galaxy has a final total and stellar mass of 1.0×10^9 M$_\odot$ and 2.1×10^6 M$_\odot$, respectively. Galaxies above 10^8 M$_\odot$ generally have a mass-to-light ratio between 5 and 30, whereas the very low-mass galaxies have mass-to-light ratios between 100 and 3000 because of their inability to efficiently form stars.

The evolution of the density, temperature, and metallicity of the entire volume is shown in Figure 3. At $z = 7$, 76% of the volume is ionized, and 6.5% (1.9%) of the mass (volume) is enriched above 10^{-3} Z$_\odot$. We focused on the buildup of the largest galaxy and an isolated dwarf

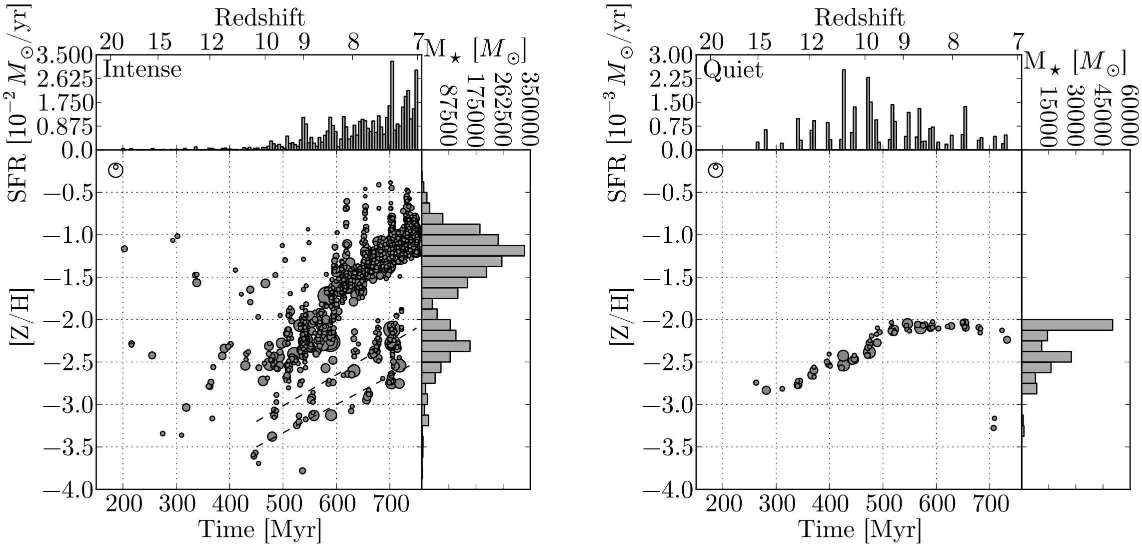

Figure 4: The scatter plots show the metal-enriched (Pop II) star formation history of a 10^9 M$_\odot$ (left) and a 10^8 M$_\odot$ (right) halos as a function of total metallicity, i.e. the sum of metal ejecta from both Pop II and Pop III SNe, at $z = 7$. Each circle represents a star cluster, whose area is proportional to its mass. The open circles in the upper right represent 10^3 and 10^4 M$_\odot$ star clusters. The upper histogram shows the SFR. The right histogram depicts the stellar metallicity distribution. The larger halo shows a large spread in metallicity at $z > 10$ because these stars formed in progenitor halos that were enriched by different SN explosions. At $z < 10$, the majority of stellar metallicities increase as the halo is self-enriched. The spikes in metallicity at t = 620, 650, and 700 Myr show induced star formation with enhanced metallicities in SN remnant shells. The dashed lines in the left panel guide the eye to two stellar populations that were formed in two satellite halos, merging at $z = 7.5$. The smaller halo evolves in relative isolation and steadily increases its metallicity to [Z/H] $\sim$ –2 until there is an equilibrium between *in-situ* star formation and metal-poor inflows from filaments. From [72].

galaxy with a total mass of 10^8 M$_\odot$. Figure 4 shows the metallicity of the star formation history and metallicity distribution functions in both halos. The mass resolution of this simulation captures the formation of all star-forming minihalos with $M > 10^5$ M$_\odot$.

The smaller galaxy experiences rapid mass accretion until $z \sim 12$ and afterward it evolves in relative isolation. It begins forming metal-enriched stars after a nearby pair-instability SN enriches a nearby halo to $\sim 10^3$ Z$_\odot$. This may be a peculiar case at high redshift, where a halo is enriched from a neighboring halo and does not form any Population III stars itself. It begins to form stars in a bursts at a rate of 5×10^{-4} M$_\odot$ yr^{-1} Mpc^{-3}, peaking at 2×10^{-3} M$_\odot$ yr^{-1} Mpc^{-3} at $z = 10$. The galaxy is self-enriched by these stars, gradually increasing from 10^{-3} Z$_\odot$ to 10^{-2} Z$_\odot$ by $z = 10$. Afterward there is an equilibrium between metal-rich outflows and metal-poor accretion from the filaments, illustrated by the plateau in stellar metallicities in Figure 4.

The larger galaxy forms in a biased region of 50 comoving kpc on a side with ~ 25 halos with $M \sim 10^6$ M$_\odot$ at $z = 10$. About half of these halos form Population III stars with a third producing pair-instability SNe, enriching the region to 10^{-3} Z$_\odot$, the metallicity floor that has been extensively studied in previous works. However, the metal-rich ejecta does not fully escape from the biased region, and most of it falls back into the galaxies or surrounding IGM, leaving the voids pristine.

PoS(Bash11)013

After $z = 10$, these ~ 25 halos hierarchically merge to form a 10^9 $M_\odot$ halo at $z = 7$ with two major mergers at $z = 10$ and $z = 7.9$. At late times, this galaxy grows mainly through mergers with halos above the filtering mass [25, 26, 70], i.e. gas-rich halos that are not photo-evaporated, and the gas fraction increases from 0.08 to 0.15 over the last 200 Myr of the simulation. The left panel of Figure 4 shows a large scatter in metallicity at early times, which is caused by inhomogeneous metal enrichment of its progenitors. Once it hosts sustained star formation after $z = 10$, the metallicity trends upwards as the stars enriches its host galaxy. In contrast with the smaller halo, the larger galaxy undergoes a few mergers with halos with an established stellar population. This creates a superposition of age-metallicity tracks in the star formation history.

This simulation of the early stages of galaxy formation only covered a handful of galaxies and did not explore the differing galaxy populations. However, it has given us a clear picture of the inner workings of these galaxies and the important physical processes involved in shaping the first galaxies and their connections to the first stars. We hope to improve on this work to survey a larger galaxy population and focus on larger galaxies that the *Hubble Space Telescope* has already observed and the *James Webb Space Telescope* will observe at $z > 6$.

6. Summary

I have provided a brief review of the formation of the first stars and their radiative, chemical, and mechanical feedback that affects subsequent structure and galaxy formation. Over the past decade, many groups have used numerical simulations to study these astrophysics events in the first billion years of the universe. Currently, the general consensus is that Population III stars are still very massive with a characteristic mass of tens $M_\odot$ with an unknown fraction in binaries. The prospect of Population III binaries is exciting, and their impact on the universe prior to reionization, such as pre-ionization from X-rays, will be addressed in future studies. To summarize, the radiation from Population III expels most of the gas from the host halos, creating gas-poor halos that cannot form stars for 10–50 Myr. The SNe from the first stars enriches the first galaxies to a nearly uniform $\sim 10^{-3}\,Z_\odot$, and ultimately leads to the demise of this unique population of stars. The gas depletion, IGM pre-heating, and chemical enrichment all have a lasting impact on the formation of the first galaxies. Hopefully we can utilize these imprints to disentangle Population III stellar properties from the most distant galaxies in the universe.

References

[1] T. Abel, P. Anninos, M. L. Norman, and Y. Zhang, *First Structure Formation. I. Primordial Star-forming Regions in Hierarchical Models*, *ApJ*, 508 (1998), pp. 518–529.

[2] T. Abel, P. Anninos, Y. Zhang, and M. L. Norman, *Modeling primordial gas in numerical cosmology*, *New Astronomy*, 2 (1997), pp. 181–207.

[3] T. Abel, G. L. Bryan, and M. L. Norman, *The Formation and Fragmentation of Primordial Molecular Clouds*, *ApJ*, 540 (2000), pp. 39–44.

[4] ——, *The Formation of the First Star in the Universe*, *Science*, 295 (2002), pp. 93–98.

[5] T. Abel, M. L. Norman, and P. Madau, *Photon-conserving Radiative Transfer around Point Sources in Multidimensional Numerical Cosmology*, *ApJ*, 523 (1999), pp. 66–71.

[6] T. Abel, J. H. Wise, and G. L. Bryan, *The H II Region of a Primordial Star*, *ApJL*, 659 (2007), pp. L87–L90.

[7] M. A. Alvarez, V. Bromm, and P. R. Shapiro, *The H II Region of the First Star*, *ApJ*, 639 (2006), pp. 621–632.

[8] P. Anninos, Y. Zhang, T. Abel, and M. L. Norman, *Cosmological hydrodynamics with multi-species chemistry and nonequilibrium ionization and cooling*, *New Astronomy*, 2 (1997), pp. 209–224.

[9] R. Barkana and A. Loeb, *In the beginning: the first sources of light and the reionization of the universe*, *Phys. Rep.*, 349 (2001), pp. 125–238.

[10] Z. Barkat, G. Rakavy, and N. Sack, *Dynamics of Supernova Explosion Resulting from Pair Formation*, *Physical Review Letters*, 18 (1967), pp. 379–381.

[11] J. R. Bond, W. D. Arnett, and B. J. Carr, *The evolution and fate of Very Massive Objects*, *ApJ*, 280 (1984), pp. 825–847.

[12] R. J. Bouwens, G. D. Illingworth, R. I. Thompson, J. P. Blakeslee, M. E. Dickinson, T. J. Broadhurst, D. J. Eisenstein, X. Fan, M. Franx, G. Meurer, and P. van Dokkum, *Star Formation at $z \sim 6$: The Hubble Ultra Deep Parallel Fields*, *ApJL*, 606 (2004), pp. L25–L28.

[13] V. Bromm, P. S. Coppi, and R. B. Larson, *Forming the First Stars in the Universe: The Fragmentation of Primordial Gas*, *ApJL*, 527 (1999), pp. L5–L8.

[14] ——, *The Formation of the First Stars. I. The Primordial Star-forming Cloud*, *ApJ*, 564 (2002), pp. 23–51.

[15] V. Bromm, R. P. Kudritzki, and A. Loeb, *Generic Spectrum and Ionization Efficiency of a Heavy Initial Mass Function for the First Stars*, *ApJ*, 552 (2001), pp. 464–472.

[16] V. Bromm and A. Loeb, *Formation of the First Supermassive Black Holes*, *ApJ*, 596 (2003), pp. 34–46.

[17] V. Bromm and N. Yoshida, *The First Galaxies*, *ARA&A*, 49 (2011), pp. 373–407.

[18] R. Cen and M. A. Riquelme, *Lower Metal Enrichment of Virialized Gas in Minihalos*, *ApJ*, 674 (2008), pp. 644–652.

[19] P. C. Clark, S. C. O. Glover, R. J. Smith, T. H. Greif, R. S. Klessen, and V. Bromm, *The Formation and Fragmentation of Disks Around Primordial Protostars*, *Science*, 331 (2011), pp. 1040–.

[20] R. Cooke, M. Pettini, C. C. Steidel, G. C. Rudie, and R. A. Jorgenson, *A carbon-enhanced metal-poor damped Lyα system: probing gas from Population III nucleosynthesis?*, *MNRAS*, 412 (2011), pp. 1047–1058.

[21] H. M. P. Couchman and M. J. Rees, *Pregalactic evolution in cosmologies with cold dark matter*, *MNRAS*, 221 (1986), pp. 53–62.

[22] A. Dekel and M. J. Rees, *Physical mechanisms for biased galaxy formation*, *Nature*, 326 (1987), pp. 455–462.

[23] X. Fan, C. L. Carilli, and B. Keating, *Observational Constraints on Cosmic Reionization*, *ARA&A*, 44 (2006), pp. 415–462.

[24] S. R. Furlanetto and A. Loeb, *Is Double Reionization Physically Plausible?*, *ApJ*, 634 (2005), pp. 1–13.

[25] N. Y. Gnedin, *Effect of Reionization on Structure Formation in the Universe*, *ApJ*, 542 (2000), pp. 535–541.

[26] N. Y. Gnedin and L. Hui, *Probing the Universe with the Lyalpha forest - I. Hydrodynamics of the low-density intergalactic medium*, *MNRAS*, 296 (1998), pp. 44–55.

[27] T. H. Greif, S. C. O. Glover, V. Bromm, and R. S. Klessen, *The First Galaxies: Chemical Enrichment, Mixing, and Star Formation*, *ApJ*, 716 (2010), pp. 510–520.

[28] T. H. Greif, J. L. Johnson, R. S. Klessen, and V. Bromm, *The first galaxies: assembly, cooling and the onset of turbulence*, *MNRAS*, 387 (2008), pp. 1021–1036.

[29] T. H. Greif, V. Springel, S. D. M. White, S. C. O. Glover, P. C. Clark, R. J. Smith, R. S. Klessen, and V. Bromm, *Simulations on a Moving Mesh: The Clustered Formation of Population III Protostars*, *ApJ*, 737 (2011), pp. 75–+.

[30] Z. Haiman, A. A. Thoul, and A. Loeb, *Cosmological Formation of Low-Mass Objects*, *ApJ*, 464 (1996), p. 523.

[31] A. Heger and S. E. Woosley, *The Nucleosynthetic Signature of Population III*, *ApJ*, 567 (2002), pp. 532–543.

[32] T. Hosokawa, K. Omukai, N. Yoshida, and H. W. Yorke, *Protostellar Feedback Halts the Growth of the First Stars in the Universe*, *Science*, 334 (2011), pp. 1250–.

[33] I. T. Iliev, G. Mellema, P. R. Shapiro, and U. Pen, *Self-regulated reionization*, *MNRAS*, 376 (2007), pp. 534–548.

[34] J. L. Johnson, T. H. Greif, and V. Bromm, *Local Radiative Feedback in the Formation of the First Protogalaxies*, *ApJ*, 665 (2007), pp. 85–95.

[35] T. Karlsson, J. L. Johnson, and V. Bromm, *Uncovering the Chemical Signature of the First Stars in the Universe*, *ApJ*, 679 (2008), pp. 6–16.

[36] T. Kitayama, N. Yoshida, H. Susa, and M. Umemura, *The Structure and Evolution of Early Cosmological H II Regions*, *ApJ*, 613 (2004), pp. 631–645.

[37] Y. Komiya, A. Habe, T. Suda, and M. Y. Fujimoto, *Formation History of Metal-poor Halo Stars with the Hierarchical Model and the Effect of Interstellar Matter Accretion on the Most Metal-poor Stars, ApJ*, 717 (2010), pp. 542–561.

[38] M. E. Machacek, G. L. Bryan, and T. Abel, *Simulations of Pregalactic Structure Formation with Radiative Feedback, ApJ*, 548 (2001), pp. 509–521.

[39] U. Maio, S. Khochfar, J. L. Johnson, and B. Ciardi, *The interplay between chemical and mechanical feedback from the first generation of stars, MNRAS*, 414 (2011), pp. 1145–1157.

[40] M. R. C. McDowell, *On the formation of H2 in H I regions*, The Observatory, 81 (1961), pp. 240–243.

[41] I. D. McGreer and G. L. Bryan, *The Impact of HD Cooling on the Formation of the First Stars, ApJ*, 685 (2008), pp. 8–20.

[42] K. Nomoto, N. Tominaga, H. Umeda, C. Kobayashi, and K. Maeda, *Nucleosynthesis yields of core-collapse supernovae and hypernovae, and galactic chemical evolution*, Nuclear Physics A, 777 (2006), pp. 424–458.

[43] M. L. Norman, *Population III Star Formation and IMF*, in First Stars III, B. W. O'Shea & A. Heger, ed., vol. 990 of American Institute of Physics Conference Series, Mar. 2008, pp. 3–15.

[44] B. W. O'Shea, T. Abel, D. Whalen, and M. L. Norman, *Forming a Primordial Star in a Relic H II Region, ApJL*, 628 (2005), pp. L5–L8.

[45] B. W. O'Shea and M. L. Norman, *Population III Star Formation in a LCDM Universe. I. The Effect of Formation Redshift and Environment on Protostellar Accretion Rate, ApJ*, 654 (2007), pp. 66–92.

[46] ——, *Population III Star Formation in a ΛCDM Universe. II. Effects of a Photodissociating Background, ApJ*, 673 (2008), pp. 14–33.

[47] P. J. E. Peebles and R. H. Dicke, *Origin of the Globular Star Clusters, ApJ*, 154 (1968), p. 891.

[48] B. E. Penprase, J. X. Prochaska, W. L. W. Sargent, I. Toro-Martinez, and D. J. Beeler, *Keck Echellette Spectrograph and Imager Observations of Metal-poor Damped Lyα Systems, ApJ*, 721 (2010), pp. 1–25.

[49] M. Ricotti, N. Y. Gnedin, and J. M. Shull, *The Fate of the First Galaxies. III. Properties of Primordial Dwarf Galaxies and Their Impact on the Intergalactic Medium, ApJ*, 685 (2008), pp. 21–39.

[50] S. Salvadori, R. Schneider, and A. Ferrara, *Cosmic stellar relics in the Galactic halo, MNRAS*, 381 (2007), pp. 647–662.

[51] W. C. Saslaw and D. Zipoy, *Molecular Hydrogen in Pre-galactic Gas Clouds, Nature*, 216 (1967), pp. 976–978.

[52] E. Scannapieco, R. Schneider, and A. Ferrara, *The Detectability of the First Stars and Their Cluster Enrichment Signatures*, *ApJ*, 589 (2003), pp. 35–52.

[53] D. Schaerer, *On the properties of massive Population III stars and metal-free stellar populations*, *A&A*, 382 (2002), pp. 28–42.

[54] M. Schwarzschild and L. Spitzer, *On the evolution of stars and chemical elements in the early phases of a galaxy*, *The Observatory*, 73 (1953), pp. 77–79.

[55] P. R. Shapiro, *Cosmological H II regions and the photoionization of the intergalactic medium*, PASP, 98 (1986), pp. 1014–1017.

[56] A. Stacy, T. H. Greif, and V. Bromm, *The first stars: formation of binaries and small multiple systems*, *MNRAS*, 403 (2010), pp. 45–60.

[57] ——, *The First Stars: Mass Growth Under Protostellar Feedback*, ArXiv e-prints (1109.3147), (2011).

[58] M. Tegmark, J. Silk, M. J. Rees, A. Blanchard, T. Abel, and F. Palla, *How Small Were the First Cosmological Objects?*, *ApJ*, 474 (1997), pp. 1–+.

[59] R. I. Thompson, D. Eisenstein, X. Fan, M. Rieke, and R. C. Kennicutt, *Evidence for a $z < 8$ Origin of the Source-subtracted Near-Infrared Background*, *ApJ*, 666 (2007), pp. 658–662.

[60] L. Tornatore, A. Ferrara, and R. Schneider, *Population III stars: hidden or disappeared?*, *MNRAS*, 382 (2007), pp. 945–950.

[61] H. Trac and R. Cen, *Radiative Transfer Simulations of Cosmic Reionization. I. Methodology and Initial Results*, *ApJ*, 671 (2007), pp. 1–13.

[62] M. Trenti, M. Stiavelli, and J. M. Shull, *Metal-free Gas Supply at the Edge of Reionization: Late-epoch Population III Star Formation*, *ApJ*, 700 (2009), pp. 1672–1679.

[63] J. Tumlinson, *Chemical Evolution in Hierarchical Models of Cosmic Structure. I. Constraints on the Early Stellar Initial Mass Function*, *ApJ*, 641 (2006), pp. 1–20.

[64] J. Tumlinson and J. M. Shull, *Zero-Metallicity Stars and the Effects of the First Stars on Reionization*, *ApJL*, 528 (2000), pp. L65–L68.

[65] M. J. Turk, T. Abel, and B. O'Shea, *The Formation of Population III Binaries from Cosmological Initial Conditions*, *Science*, 325 (2009), pp. 601–.

[66] D. Whalen, T. Abel, and M. L. Norman, *Radiation Hydrodynamic Evolution of Primordial H II Regions*, *ApJ*, 610 (2004), pp. 14–22.

[67] D. J. Whalen and M. L. Norman, *Radiation hydrodynamical instabilities in cosmological and galactic ionization fronts*, *AP&SS*, 336 (2011), pp. 169–174.

[68] J. H. Wise and T. Abel, *Resolving the Formation of Protogalaxies. I. Virialization*, *ApJ*, 665 (2007), pp. 899–910.

[69] ———, *Suppression of H_2 Cooling in the Ultraviolet Background*, *ApJ*, 671 (2007), pp. 1559–1567.

[70] ———, *How Very Massive Metal-Free Stars Start Cosmological Reionization*, *ApJ*, 684 (2008), pp. 1–17.

[71] ———, *Resolving the Formation of Protogalaxies. III. Feedback from the First Stars*, *ApJ*, 685 (2008), pp. 40–56.

[72] J. H. Wise, M. J. Turk, M. L. Norman, and T. Abel, *The Birth of a Galaxy: Primordial Metal Enrichment and Stellar Populations*, *ApJ*, 745 (2012), p. 50.

[73] S. E. Woosley and T. A. Weaver, *The Evolution and Explosion of Massive Stars. II. Explosive Hydrodynamics and Nucleosynthesis*, *ApJS*, 101 (1995), pp. 181–+.

[74] N. Yoshida, V. Bromm, and L. Hernquist, *The Era of Massive Population III Stars: Cosmological Implications and Self-Termination*, *ApJ*, 605 (2004), pp. 579–590.

[75] N. Yoshida, S. P. Oh, T. Kitayama, and L. Hernquist, *Early Cosmological H II/He III Regions and Their Impact on Second-Generation Star Formation*, *ApJ*, 663 (2007), pp. 687–707.

[76] N. Yoshida, K. Omukai, and L. Hernquist, *Formation of Massive Primordial Stars in a Reionized Gas*, *ApJL*, 667 (2007), pp. L117–L120.

[77] ———, *Protostar Formation in the Early Universe*, *Science*, 321 (2008), pp. 669–.

PROCEEDINGS OF SCIENCE

Dark Matter

Annika H. G. Peter[*†]
Department of Physics and Astronomy, University of California, Irvine, CA 92697-4575
E-mail: annika.peter@uci.edu

From astronomical observations, we know that dark matter exists, makes up 23% of the mass budget of the Universe, clusters strongly to form the load-bearing frame of structure for galaxy formation, and hardly interacts with ordinary matter except gravitationally. However, this information is not enough to identify the particle specie(s) that make up dark matter. As such, the problem of determining the identity of dark matter has largely shifted to the fields of astroparticle and particle physics. In this talk, I will review the current status of the search for the nature of dark matter. I will provide an introduction to possible particle candidates for dark matter and highlight recent experimental astroparticle- and particle-physics results that constrain the properties of those candidates. Given the absence of detections in those experiments, I will advocate a return of the problem of dark-matter identification to astronomy, and show what kinds of theoretical and observational work might be used to pin down the nature of dark matter once and for all. This talk is intended for a broad astronomy audience.

Frank N. Bash Symposium 2011: New Horizons in Astronomy
October 9-11, 2011
Austin, Texas, USA

[*] Speaker.

[†] I would like to thank the organizers and staff at UT Austin for inviting me to and running an excellent symposium. I would like to acknowledge my collaborators James Bullock, Manoj Kaplinghat, Jonathan Loranger, Leonidas Moustakas, Miguel Rocha, and Kris Sigurdson for conversations that were useful for crafting the talk, as well as providing some of the plots that were in the talk. I am supported by a Gary McCue Fellowship through the Center for Cosmology at UC Irvine and NASA Grant No. NNX09AD09G.

PoS(Bash11)014

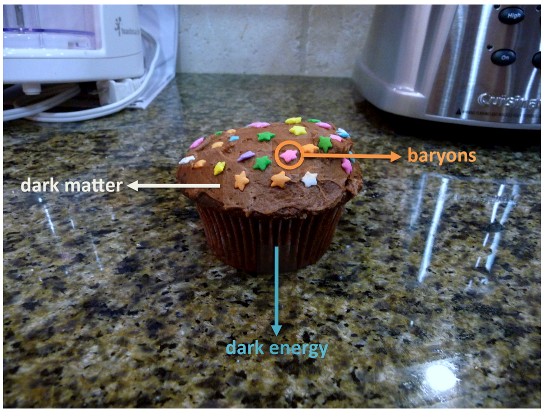

Figure 1: Contents of the Universe, as illustrated by a chocolate cupcake. Recipe available upon request.

1. Introduction

Dark matter is the dominant gravitationally attractive component in the Universe, but we do not know what it consists of. All the evidence for the existence of dark matter and constraints on its nature come from astronomy. This is what we know so far:

Abundance: We may infer the content of the Universe from observations of the cosmic microwave background and of large-scale structure [1, 2, 3]. The relative abundances of the major components of the Universe are illustrated by the chocolate cupcake in Fig. 1. Baryons lightly sprinkle the Universe, as they constitute only about 4% of the total mass-energy density. Dark energy makes up the bulk of the Universe at the present epoch, clocking in at $\sim$ 73%, just as the cake dominates the cupcake. Dark matter comprises $\sim$ 23% of the Universe. Just as the chocolate frosting glues the sprinkles together on the cupcake, dark matter binds baryons together to form galaxies, galaxy groups, and galaxy clusters.

A few things it cannot be: Dark matter cannot consist of baryons. There are two lines of evidence for this. First, if baryons made up all the dark matter, the cosmic microwave background and cosmic web of structure would look radically different. Second, the abundance of light elements created during big-bang nucleosynthesis depends strongly on the baryon density (more precisely, on the baryon-to-photon ratio) of the Universe (see [4] and references therein). Observed abundances of deuterium and ^{4}He give similar constraints on the baryon density in the Universe as those coming from cosmic microwave background observations. These lines of evidence imply that a once-popular class of baryonic dark-matter candidate, the Massive Compact Halo Object (MaCHO) class (e.g., brown dwarfs, stellar remnants), is cosmologically insignificant.

Dark matter cannot consist of light (sub-keV-mass) particles unless they were created via a phase transition in the early Universe (like QCD axions [5]). This is because light particles are relativistic at early times, and thus fly out of small-scale density perturbations. If particles were created thermally or via neutrino oscillations, the speed of the particles, and hence the distance they stream out of density perturbations, should be correlated with their mass. Thus, one may map the smallest distance scale on which one sees clumpy structure to set a lower limit on the dark-matter particle mass (low mass == high speed == large distance traveled == scale on which density perturbations are washed out). Current measurements of the Lyman-α forest, a probe of small-scale structures at $z \sim 3$, constrain the particle mass to be $m \gtrsim 2$ keV [6].

Electromagnetic neutrality: There are strong constraints on the electromagnetics of dark matter [7]. If dark matter had either a small charge or a small electric or magnetic dipole moment, it would couple to the photon-baryon fluid before recombination, thus altering the sub-degree-scale features of the cosmic microwave background as well as the matter power spectrum.

Self-interaction constraints: Dark matter is part of a new sector of physics. We may generically expect that dark-matter particles might interact with themselves or other new particles, mediated by new, dark gauge bosons. Even if the particles in the dark sector have no coupling to the Standard Model (i.e., the particles and forces we know of), such interactions will affect the structures of dark-matter halos, since dark-matter particles may transfer energy and angular momentum in the scatters [8]. For hard-sphere elastic scattering, the constraints are at the level of cross section per unit particle mass $\sigma/m \lesssim 1$ cm^2/g from observations of the structure of galaxy clusters [9].

Clumping on small scales: There is evidence for virialized structures of dark matter down to scales of $\sim 10^7 - 10^9 M_\odot$ halos. Vegetti et al. have used sophisticated modeling of perturbations to Einstein rings by subhalos in lens galaxies to estimate the masses of subhalos. They have identified several subhalos with masses $10^8 - 10^{10} M_\odot$ [10]. The Milky Way dwarf galaxies are both the most dark-matter-dominated structures known (see [11] and references therein). Within their half-light radii of $\sim 30 - 800$ pc, they contain $\sim 10^6 - 10^8 M_\odot$ of dark matter, with a mass-to-light ratio $\Upsilon_{1/2} \sim 10 - 4000 \Upsilon_\odot$. These galaxies are hosted by halos that were of order $10^9 - 10^{10} M_\odot$ before accretion onto the Milky Way.

In this admittedly biased walk through the state of the dark-matter identification landscape, I start in Sec. 2 by introducing popular dark-matter candidates. In Sec. 3, I describe dark-matter searches that rely on dark matter's non-gravitational interactions with the Standard Model. In Sec. 4, I describe how to further exploit astronomical observations to uncover dark-matter physics. In Sec. 5, I show how a synthesis of these approaches is needed to characterize dark matter.

2. The particle zoo

The only major non-particle candidate for dark matter is the primordial black hole, which would have collapsed directly from highly overdense regions of the early Universe, the existence of which requires funky physics [12]. At the risk of offending some of my colleagues, I claim that the only *really plausible* dark-matter candidates are new particles.

I sometimes joke, there must be at least one candidate per particle model builder. Nevertheless, there is a hierarchy among the particle candidates. The top tier of candidates are called "natural" dark-matter candidates. I call them the "buy one, get one free" candidates because we get these candidates "for free" from theories that solve other deep problems in physics. Here are the most popular "buy one, get one free" candidates or classes of candidate:

Weakly-interacting massive particles (WIMPs): This class of candidate, or at least its delightful moniker, was originally introduced by Steigman & Turner [13] (although some of the relevant ideas had been around for a while, e.g., [14]). The key features of this particle class are exactly as described: interactions around or near typical weak-force interactions (the fine-structure constant α near the weak-scale coupling $\sim 10^{-2}$), particle masses near the weak scale ($m \sim 100$ GeV in particle-physics units [15], similar to the mass of a silver atom).

Candidates in the WIMP class include the supersymmetric neutralino (the lowest-mass eigenstate of the supersymmetric partners of neutral Standard Model gauge bosons) and the Kaluza-Klein photon [17]. Both of these candidates emerge out of theories to introduce new physics at the electroweak breaking scale (the minimal supersymmetric standard model [MSSM] and universal extra dimensions [UED]), and possibly to explain why that scale is so much lower than the Planck scale. Other particles in these theories could be dark matter if they were the lightest of the new particles (and satisfied cosmological and collider constraints), which depends on where exactly we sit in the rather large theoretical parameter space, but the neutralino and Kaluza-Klein (UED) photon are typically the lightest stable new particles.

The WIMP candidate class has the additional feature that it may "naturally" make up all the dark matter, thus making it more "Black Friday sale" dark matter than the "buy one, get one free" candidate. This feature of WIMPs is called the "WIMP miracle". If WIMPs are in a thermal bath in the early Universe with other particles, having been born out of decays of the inflaton or something of the like, we can solve Boltzmann equations to find that WIMPs "freeze out" (i.e., stop being created/destroyed through annihilations with other particles) at a comoving density that is inversely proportional to the WIMP annihilation cross section σ_{ann}. Unless decays are important, this comoving number density is fixed for all future time. By dimensional analysis (recalling that mass is inversely proportional to the length scale in particle-physics units), the annihilation cross section should be $\sigma_{ann} \propto \alpha^2/m^2$. If you put this dimensional-analysis cross section into early-Universe Boltzmann equations, the comoving number density of WIMPs matches the number density inferred from cosmological observations [1, 2]. A miracle indeed!

Axions: Axions' "buy one, get one free" claim to fame is that they emerge out of a solution to the strong-CP problem in particle physics. In the quantum chromodynamics (QCD) Lagrangian, there exists a term which allows significant but as-yet unobserved CP violation in QCD and contributes to the electric dipole moment of the neutron. Upper limits on the neutron electric dipole moment suggest that the coefficient for this term should be $\lesssim 10^{-9}$, which smacks of fine tuning [18]. Now, there is in principle nothing wrong with a parameter having a small value—on the neutrino side, the active neutrinos are at least six orders of magnitude smaller in mass than the next-lightest Standard Model particle, the electron [19]. But, usually when a parameter that could be huge is nearly zero, it implies that some sort of protective symmetry is at work. The Peccei-Quinn solution to making this coefficient small is to turn that coefficient into a dynamical field, and add a global symmetry that, when broken, drives the offending term in the QCD Lagrangian to be precisely zero. The new field's fluctuations about the new vacuum of the broken theory are axions, the pseudo-Nambu-Goldstone bosons of the broken symmetry.

Axions are in some ways less natural than WIMPs because it is tricky to get their comoving number density to match the observed dark-matter density. There are a number of axion production mechanisms (all of which must be present to some extent), but the preferred way to produce dark-matter axions is through non-thermal coherent oscillations of the axion field near the QCD phase transition. In that case, axions are light ($\sim 10\mu$eV) and are born with no momentum. See Chapter 10 of Ref. [16] for a review of axion production mechanisms.

Gravitinos: While supersymmetric neutralinos are the dark-matter candidate of choice in

PoS(Bash11)014

some swaths of the MSSM, the gravitino, the supersymmetric partner of the graviton, may be dark matter in other swaths. Depending on exactly how supersymmetry is broken, the gravitino could be anywhere in the mass range of $\sim$eV to TeV, although masses $\lesssim$keV are disfavored because they wash out too much small-scale structure (see Sec. 4; [20]). In order for lighter gravitinos to be dark matter, one typically must introduce some non-standard cosmology lest the Universe be overclosed [21]. Heavy gravitinos are, in my opinion, more interesting. If the next-lightest supersymmetric particle (NLSP) is only barely more massive than the gravitino, that particle species may be thermally produced and then decay at a later time to gravitinos. Thus, even though gravitinos basically do not interact with the Standard Model (and thus would not typically be born as thermal relics), they can inherit the WIMP miracle from the NLSP. The gravitino in this scenario is a "superWIMP" [22]. Because these massive gravitinos are born out of decays at relatively high momentum, they can smear out primordial density perturbations on small scales. Gravitinos are not nearly as beloved as WIMPs as dark-matter candidates because of the difficulty of getting the abundance just right and because they are much harder to detect using conventional methods.

There are other dark-matter candidates that are plausible and solve some other problems in physics, although they do not provide quite the same bargain-hunting thrill of the previously discussed candidates. I will list only two classes of candidate.

Sterile neutrinos: Sterile neutrinos are neutrinos that do not interact electroweakly. Since mass eigenstates are not the same as the electroweak eigenstates (i.e., ν_e, ν_μ, ν_τ), sterile neutrinos may mix with electroweak, or active, neutrinos. Sterile neutrinos have been proposed in a number of contexts; they can be a mass-generating mechanism for the active neutrinos, they can simply be the right-handed counterparts to the active species, or explain certain neutrino-experiment anomalies [23]. As dark matter, sterile neutrinos may be created in the early Universe in a variety of ways. Depending on their creation mechanism, they can be constrained by their effects on smaller-scale structure in the Universe [6]. Because sterile neutrinos mix with active neutrinos, they have a small decay probability to an active neutrino and a photon [24]. The simplest model of sterile neutrino dark matter (Dodelson-Widrow neutrinos) are excluded by a combination of small-scale structure observations and non-detections of X-rays from galaxies [6, 24] (for an alternative view, see [25]).

Hidden-sector dark matter: There is no reason to expect that the dark sector consists of only one or a handful of boring particles; after all, the Standard Model has richly interesting physics. Extensions to the Standard Model open the door to other sectors of physics that may not have much contact with the Standard Model. For example, supersymmetry has to be a broken theory, and the MSSM (the simplest supersymmetric extension to the Standard Model) is not going to break itself; new fields are needed to break supersymmetry and communicate that to the Standard Model. Those fields may also communicate supersymmetry breaking to other sectors. Sectors that have little communication with the Standard Model are called "hidden" or "dark" sectors. A lot of interesting physics is allowed in the hidden sector, including the existence of "dark photons" [26].

At the far other end of the spectrum, there are dark-matter candidates that are considered "exotic" or "cooked up". These are typically highly specialized models designed to interpret so-called anomalies in cosmic-ray observations or particle-physics experiments as dark matter [27]. These candidates tend to have short lives but lead to interesting insights and new directions, especially in hidden-sector model building.

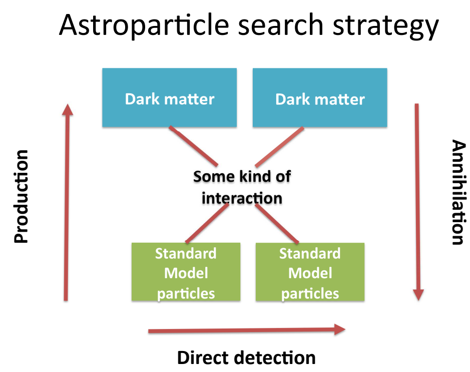

Figure 2: Sketch of the different types of astroparticle search strategies for dark-matter detection. The central figure is a toy Feynman diagram, and the search strategies depend on the direction in which one looks at the diagram. See text for details.

Good reviews on particle dark-matter candidates are given in Refs. [16, 20]. For an introduction to particle physics, I recommend Griffiths' book [28].

3. Astroparticle searches for dark matter

Astroparticle searches depend on the type and strength of the interaction between dark matter and the Standard Model. There are three main strategies for exploiting this interaction, as illustrated in Fig. 2. Going bottom-to-top in the diagram, we produce dark-matter particles through collisions with Standard-Model particles. This method is most commonly employed at large colliders (e.g., the Large Hadron Collider [LHC]) or using specialized experiments. Reading Fig. 2 sideways, we look for the effects on Standard-Model particles induced by their interactions with dark-matter particles. If we look at Fig. 2 top-to-bottom, we look for Standard-Model particles emerging from dark-matter annihilation or decays.

3.1 WIMP searches

Since WIMPs are the most popular class of dark-matter candidate (or at least the class which gets the most experiments), I will describe WIMP searches first and in the most detail.

3.1.1 Colliders

WIMPs will not directly be observed if they are created at colliders–given that they are neutral and weakly interacting, they are like gigantic neutrinos in terms of detection prospects. However, it is possible to infer their existence. The quarks and gluons in the protons smashed together at the LHC typically do not annihilate directly to WIMPs—since WIMPs belong to entire theories beyond the Standard Model, there are a panoply of other extra particles to which quarks and gluons may annihilate (e.g., colored particles like squarks and gluinos in the MSSM). Those other particles may eventually decay to WIMPs inside the detector, the signature of which is missing energy when one tries to reconstruct the chain of events. There has been a huge amount of effort to figure out which types of events (characterized by the number and types of jets, leptons, geometry, timing) are likely to lead to the best constraints on different WIMP models [29]. There is not yet experimental evidence of physics beyond the Standard Model [30]. Even if evidence for a WIMP is eventually found, we will not know if that particle is stable on timescales longer than a nanosecond.

3.1.2 Direct detection

Galactic WIMPs can ram into nuclei in the lab, depositing of order tens to hundreds of keV of kinetic energy to a single nucleus. This is of order 10^7 times less than the kinetic energy of a fruit fly, and the event rate is many orders of magnitude less than the ambient flux of cosmic rays, posing unique challenges to detection. Nevertheless, there are dozens of experiments planned or underway to look for WIMPs this way [31].

The DAMA/LIBRA, CRESST, and CoGeNT experiments claim (sometimes in mild terms) WIMP detections [32]. It would be fair to say that these claims are not widely believed, especially given the null detections of other experiments. Pretty much every experimentalist I have met has his or her own theory of the origin of the DAMA/LIBRA signal [33]. The DM-Ice collaboration is in the process of performing a DAMA-like experiment at the South Pole, ingeniously using the IceCube Neutrino Observatory as a cosmic-ray veto [34]. The best constraints from experiments that do not find significant events above background are XENON100, CDMS-II, and COUPP, and are cutting through swaths of WIMP model space [35]. Currently, experiments are making rapid gains in sensitivity because it is possible (through great effort!) to do nearly zero-background searches, but soon (in the next decade) experiments will hit the wall of irreducible astrophysical neutrino backgrounds [36]. *Neutrinos!*

3.1.3 Annihilation

The best places to look for WIMP annihilation are in dark-matter-dense objects, since the annihilation rate goes as the square of the density, and for which there are few other contaminating fore/backgrounds (or signals, depending on your point of view!). Such objects include galaxy clusters, Milky Way dwarf galaxies, the Milky Way halo, the diffuse gamma-ray background (both the average signal and anisotropies), possible nearby dark-matter subhalos, and the center of the Sun [27, 37, 38, 39]. WIMPs annihilate to a wide variety of Standard-Model particles, but some of those particles are easier to search for than others. There are some searches for WIMP annihilations to charged particles [27]. The two big problems with charged-particle searches are that even astrophysical emission mechanisms of charged particles are poorly understood and that charged particles have complicated diffusion histories, which are not nearly as well understood as it is sometimes made out to be. I personally won't touch most charged-particle probes of dark matter with a 30-foot pole, but some people have done interesting work in this field (in particular, work on locally-produced anti-matter hadrons is quite exciting [40]).

Gamma rays and neutrinos point directly back to their sources, and are thus easier to interpret than charged particles (with the exception of inverse-Compton gamma rays). Currently the most interesting constraints come from gamma-ray observations of the Milky Way halo and of the dwarf galaxies therein, and neutrino-telescope observations of the Sun [38, 39]. The Milky Way dwarf galaxies are the most dark-matter-dense objects known, have few baryons, and are nearby, thus

PoS(Bash11)014

making them the perfect targets for WIMP-annihilation searches [11]. The gamma-ray flux limits from the Fermi Gamma-ray Space Telescope indicates that we are starting to cut through interesting WIMP parameter space. The limits on gamma-ray annihilation in the Milky Way halo coming from Fermi and the ground-based H.E.S.S. telescope are only somewhat weaker and span a larger WIMP mass range than the current dwarf limits [38].

The Sun accumulates Galactic WIMPs when they scatter off solar nuclei to energies below the escape velocity of the Sun. If the capture and annihilation rates of WIMPs in the Sun are in equilibrium, the annihilation rate is exactly half the capture rate, making solar WIMP searches sensitive to the elastic-scattering cross section. Current constraints are competitive with direct-detection searches, even if there is still uncertainty in the capture-rate calculation [39].

3.2 Other

Dark-matter axions could be detected in laboratory experiments, exploiting the (quite weak) axions coupling to photons. While axion-production and indirect-detection experiments do not yet probe cosmologically significant axion parameter space [41], direct-detection searches will soon. The ADMX experiment will be upgrading to Phase 2 this year; an underappreciated fact about this experiment is that it should be able to rule in or out the most popular models of QCD axions as dark matter unless we are *incredibly* unlucky with the vacuum misalignment angle [42].

The APEX experiment is searching for a light hidden-sector gauge boson that mixes with photons, currently reporting null results (although these are early days for the experiment) [43].

4. The nature of dark matter through astronomical searches

However, if dark matter has only extremely weak couplings to the Standard Model, the astroparticle searches are dead on arrival. We will not necessarily be able to rule out candidates, merely rule out parts of their parameter space. Thus, it would be great if we had some way of characterizing dark-matter physics that did not depend on Standard-Model interactions. Fortunately, we have just such a thing! Astronomical observations of the effects of the gravity of dark matter on baryons! Recall that all we know about dark matter comes from exactly those “gravitational probes” of dark-matter physics (Sec. 1 and [44]).

4.1 Mapping dark-sector physics to observables

In order to use astronomical observations to constrain dark-matter physics, we need to find a mapping between the two. It is more useful to consider general dark-matter phenomenology than specific dark-matter models, at least at the present. One way to classify dark-matter phenomenology is by physics important at early or late times. This means of dark-matter classification is defined and explored in Ref. [44].

In the early Universe, the physics that matters most is the velocity distribution function of dark matter at its birth or freeze-out epoch. Dark matter that freezes out or is created non-relativistic is called cold dark matter (CDM). WIMPs and non-thermally-produced axions are CDM. Inflation lays down density fluctuations (more precisely: fluctuations in the gravitational potential) on an incredibly wide range of scales, and the non-relativistic nature of CDM means that these fluctuations are left largely intact except on tiny scales related to the free-streaming length. Hot dark matter (HDM) is dark matter that is born highly relativistic. Because of its high speed, HDM can escape from and thus wash out density perturbations on large scales in the early Universe. HDM is constrained to make up a tiny percentage of the mass-energy density of the Universe [19]. In between these two extremes is warm dark matter (WDM). Examples of WDM include gravitinos and sterile neutrinos. We should see evidence for the temperature of dark matter at all observable epochs in the Universe.

The other dimension to dark-matter classification is its late-time behavior. The dark-matter phenomenology that is important at late times is its stability to decays and self-interactions involving a hidden sector. Self-interactions are more important at late times than early times because the self-interaction rate scales as the square of the dark-matter density. There are simply more places in the Universe with high density at late times than early times. Late-time effects can be distinguished from early-time effects because of the arrow of time.

The stable CDM paradigm is *the top dog* among astrophysicists; nearly all structure-formation predictions are really stable CDM predictions (see [45] for reviews and references). From simulations, we know how CDM structure evolves (at least in the absence of baryons) and how dark-matter halos cluster. We find that dark-matter halos have cuspy density profiles, that halos are triaxial, and that the central density of halos depends on the mass of the halo. Dark-matter halos have subhalo mass functions that extend down beyond the smallest simulated scales.

Stable WDM looks like stable CDM on scales $\gtrsim 10$ Mpc, but deviates below those scales as the speediness of WDM particles in the early Universe creates a cutoff in the matter power spectrum [46]. At late times, the evolution of the matter power spectrum is more subtle as halos form. Large dark-matter halos are virtually indistinguishable from stable CDM halos except that they may be somewhat less concentrated, but smaller halos, which form out of density perturbations near the cutoff scale in the power spectrum, look fluffier and less cuspy than CDM halos. The subhalo mass function drops significantly on mass scales corresponding to that cutoff scale.

Unstable CDM deviates from stable CDM on large scales as well as small [47]. If unstable CDM decays to relativistic particles, it changes the background evolution of the Universe. Even if unstable CDM decays to non-relativistic particles, the particles stream out of dark-matter halos, causing the growth function of structure to acquire a scale dependence. On smaller scales, halos are less dense than stable CDM halos due to the injection of kinetic energy into the halos from the decays. The properties of subhalos have not been studied in great detail yet.

Stable self-interacting CDM has made a bit of a theoretical comeback of late as part of the hidden-sector paradigm [8, 26]. Self-interacting CDM looks like stable CDM on large scales through cosmic time. One finds deviations from CDM predictions only in the inner parts of dark-matter halos at late times. The inner parts of halos to become cored and rounder because of the exchange of energy and angular momentum among particles. It is hypothesized that there will be a deficit of subhalos in the central regions of halos, but this prediction remains poorly quantified.

4.2 Observations

Currently, observations of large-scale structure (scales $\gtrsim 10$ Mpc) across cosmic time are consistent with a stable, cold-dark-matter picture [1, 2, 6]. Since self-interactions and WDM only show deviations from stable CDM on small scales, this implies that the observations on large scales are *just as* consistent with the self-interacting CDM and WDM pictures as with the CDM paradigm. Large-scale structure observations indicate that the lifetime of the parent dark-matter particle must be $\gtrsim 3$ times the Hubble time for recoil speeds of the daughter dark-matter particle of $\gtrsim 100$ km s^{-1} [47]. Most of the constraints on decaying dark matter emerge from the Sloan Digital Sky Survey and X-ray cluster counts. Future large galaxy surveys, especially ones designed with dark-energy constraints in mind, will also constrain dark-matter models [47, 48]. Next-generation galaxy surveys will probe large redshifts, thus allowing for tomographic studies of the late-time physics of dark matter.

Observations of small-scale structure (i.e., on scales of individual dark-matter halos) have the potential to be quite constraining, although in practice such observations are often difficult to interpret. Observations of galaxy clusters and individual galaxies using strong lensing or galaxy-galaxy weak lensing indicate that dark-matter halos are indeed ellipsoidal, although a quantitative comparison with theoretical expectations is tricky [49]. There are hints from the smallest observed dark-matter halos (the halos of Milky Way dwarf galaxies) to the largest (galaxy clusters) that the density profiles are not well described by those found in stable CDM simulations without baryons [50]. It is not clear yet if those deviations are a result of baryonic or dark-matter physics.

The subhalo mass function and subhalo central densities ought to be interesting probes of dark-matter physics [51]. For (sub)halo masses smaller than $\sim 10^{10} M_{\odot}$, there are really only two ways to probe their mass function and central densities. First, next-generation deep galaxy surveys should reveal more dwarf companions of the Milky Way, which may be characterized using existing techniques [11, 48]. However, this method relies on the existence of a decent number of stars in small dark-matter subhalos. We do not really know how star formation proceeds in small halos. It is better to not have to depend on baryons to probe such small halos. Fortunately, we may look for subhalos using gravitational lensing. In strong lenses, subhalos in the lens can change the positions and magnifications of the images, and perturb the light travel times [10, 52]. I am part of the science team for the Observatory for Multi-Epoch Gravitational Lens Astrophysics (OMEGA) Explorer mission concept to monitor multiply-lensed active galactic nuclei for magnification and light arrival-time anomalies associated with subhalos in the lens galaxy [53]. This is a unique way of probing dark-matter physics, and highly complementary to other dark-matter searches. NASA should *definitely* fund us in the next Explorer-class mission call!

4.3 Caveats

Any interpretation of observations in the context of dark matter depends on a careful and accurate mapping of dark-matter physics to astronomical observables. A HUGE source of systematics for this mapping is our ignorance of the specific ways in which galaxy evolution alters dark-matter halos and measures of the matter power spectrum [54]. Most of the predictions discussed in this section were made using dark-matter-only simulations. However, we do not know the relative importance of various processes in galaxy evolution for dark-matter-halo evolution [55]. Even when a subset of the physics we think must be important for galaxy evolution is included in simulations, the effects on dark-matter halos is extremely sensitive to the implementation of the galaxy physics in the codes [54]. One thing that appears to be important both for getting the dark-matter-halo morphologies as well as galaxy properties right is to resolve giant-molecular-cloud-sized regions [55]. This is somewhat depressing because it is currently only possible to resolve such small scales for individual dwarf galaxies. On the other hand, it implies job security for computational physicists.

PoS(Bash11)014

5. Conclusion

Neither astroparticle nor astronomical searches for dark matter are going to characterize dark matter on their own. For example, say that in the next five years we find some sort of new, massive, neutral particle at the LHC, but do not see anything in direct-detection experiments or in neutrino telescopes or gamma-ray telescopes. Is this new particle stable, and can it be all the dark matter?

Astronomical observations can answer these questions, or at least provide some guidance. If the next generation of giant galaxy surveys sees some evidence of an anomalous scale-dependent growth of structure, it could hint that the dark matter is unstable but with a long lifetime. Thus the conventional WIMP model might be dead, but variants thereof may be alive. On the other hand, if the largest scales of the Universe evolve as they would for stable CDM but dark-matter halos continue to look somewhat cored, and if OMEGA finds a suppressed subhalo mass function in lens galaxies, then this might indicate a significant amount of self interaction in a hidden-sector model. Or it is possible that there is no deviation from stable CDM predictions, and we conclude that even if the particle found at the LHC is not all of the dark matter, dark matter must be pretty stable, fairly weakly interacting, and cold.

The next decade should be an exciting time for dark-matter identification efforts. However, I think it is important to be on guard for two essentially sociological phenomena in the dark-matter community, which I will illustrate with quotes from famous scientists. From Steven Weinberg, "It seems that scientists are often attracted to beautiful theories in the way that insects are attracted to flowers—not by logical deduction, but by something like a sense of smell." A (very) large segment of the community is thoroughly captivated by stable WIMP CDM. But just because WIMPs are beautiful dark-matter candidates does not mean that dark matter *must* consist of WIMPs, especially in light of null detections in every flavor of dark-matter detection method. While WIMPs are well-motivated dark-matter candidates, and in some sense our best bet, it sometimes worries me just how deeply entrenched they are in the canon of physics ideas, to the point where some data (e.g., the rotation curves of dwarf galaxies) are pooh-poohed if they do not match certain WIMP CDM calculations.

On the other hand, it is possible to fall too far on the other extreme. To illustrate this point, I present a few words of wisdom from Carl Sagan, "With insufficient data it is easy to go wrong." Every time an experimental or observational "anomoly" appears on arXiv, there is an immediate rush to create some new, highly specialized dark-matter model interpretation before the data have necessarily been vetted. There is then another rush to rule out models that, frankly, no one believed in the first place. I think this phenomenon is a sign both of the lack of "conventional" signals and a need for even deeper ties among different segments of the dark-matter community. We all hope that we will soon be in an era of abundant data. The key will be to see how all these different searches *really* fit together to present a unified picture of the nature of dark matter.

References

[1] B. Reid et al., *Cosmological constraints from the clustering of the Sloan Digital Sky Survey DR7 luminous red galaxies*, *MNRAS* **404** (2010) 60 [0907.1659]; W. Percival et al., *Baryon acoustic oscillations in the Sloan Digital Sky Survey Data Release 7 galaxy sample*, *MNRAS* **401** (2010) 2148 [0907.1660]; E. M. Huff et al., *Seeing in the dark II: Cosmic shear in the Sloan Digital Sky Survey*,

arXiv:1112.3143; J. L. Tinker et al., *Cosmological Constraints from Galaxy Clustering and the Mass-to-number Ratio of Galaxy Clusters*, *ApJ* **745** (2012) 16 [`1104.1635`].

[2] D. Larson et al., *Seven-Year Wilkinson Microwave Anisotropy Probe (WMAP) Observations: Power Spectra and WMAP-Derived Parameters*, *ApJS* **192** (2011) 16 [`1001.4635`]; J. Dunkley et al., *The Atacama Cosmology Telescope: Cosmological Parameters from the 2008 Power Spectrum*, *ApJ* **739** (2011) 52 [`1009.0866`].

[3] Wayne Hu maintains excellent tutorials on the physics of the cosmic microwave background and large-scale structure. The interested reader is enthusiastically recommended to check out http://background.uchicago.edu/index.html

[4] R. H. Cyburt, *Primordial nucleosynthesis for the new cosmology: Determining uncertainties and examining concordance*, *Phys. Rev. D* **70** (2004) 023505 [`astro-ph/0401091`]; G. Steigman, *Primordial Nucleosynthesis in the Precision Cosmology Era*, *Annu. Rev. Nucl. Part. Sci.* **57** (2007) 463 [`0712.1100`]; F. Iocco et al., *Primordial nucleosynthesis: From precision cosmology to fundamental physics*, *Phys. Rep.* **472** (2009) 1 [`0809.0631`]; B. Fields, *The Primordial Lithium Problem*, *Annu. Rev. Nucl. Part. Sci.* **61** (2011) 47.

[5] R. D. Peccei & H. R. Quinn, *Constraints imposed by CP conservation in the presence of pseudoparticles*, *Phys. Rev. D* **16** (1977) 1791; S. Weinberg, *A new light boson?*, *Phys. Rev. Lett.* **40** (1978) 223; F. Wilczek, *Problem of strong P and T invariance in the presence of instantons*, *Phys. Rev. Lett.* **40** (1978) 279.

[6] K. Abazajian, *Linear cosmological structure limits on warm dark matter*, *Phys. Rev. D* **73** (2006) 063513 [`astro-ph/0512631`]; M. Viel et al., *Can Sterile Neutrinos Be Ruled Out as Warm Dark Matter Candidates?*, *Phys. Rev. D* **97** (2006) 071301 [`astro-ph/0605706`]; A. Boyarsky et al., *Lyman-α constraints on warm and on warm-plus-cold dark matter models*, *JCAP* **005** (2009) 012 [`0812.0010`].

[7] K. Sigurdson et al., *Dark-matter electric and magnetic dipole moments*, *Phys. Rev. D* **70** (2004) 083501 [`astro-ph/0406355`]; S. D. McDermott, H.-B. Yu, & K. M. Zurek, *Turning off the lights: How dark is dark matter?*, *Phys. Rev. D* **83** (2011) 063509 [`1011.2907`].

[8] D. N. Spergel & P. J. Steinhardt, *Observational Evidence for Self-Interacting Cold Dark Matter*, *Phys. Rev. Lett.* **84** (2000) 3760 [`astro-ph/9909386`]; M. R. Buckley & P. J. Fox, *Dark matter self-interactions and light force carriers*, *Phys. Rev. D* **81** (2010) 083522 [`0911.3898`]; J. L. Feng, M. Kaplinghat, & H.-B. Yu, *Halo-Shape and Relic-Density Exclusions of Sommerfeld-Enhanced Dark Matter Explanations of Cosmic Ray Excesses*, *Phys. Rev. Lett.* **104** (2010) 151301 [`0911.0422`].

[9] N. Yoshida et al., *Weakly Self-interacting Dark Matter and the Structure of Dark Halos*, *ApJ* **544** (2000) L87 [`astro-ph/0006134`]; O. Y. Gnedin & J. P. Ostriker, *Limits on Collisional Dark Matter from Elliptical Galaxies in Clusters*, *ApJ* **561** (2001) 61 [`astro-ph/0010436`]; J. F. Hennawi & J. P. Ostriker, *Observational Constraints on the Self-interacting Dark Matter Scenario and the Growth of Supermassive Black Holes*, *ApJ* **572** (2002) 41 [`astro-ph/0108203`]; J. Miralda-Escudé, *A Test of the Collisional Dark Matter Hypothesis from Cluster Lensing*, *ApJ* **564** (2002) 60; S. W. Randall et al., *Constraints of the Self-Interaction Cross Section of Dark Matter from Numerical Simulations of the Merging Galaxy Cluster 1E 0657-56*, *ApJ* **679** (2008) 1173 [`0704.0261`].

[10] S. Vegetti et al., *Quantifying dwarf satellites through gravitational imaging: the case of SDSSJ120602.09+514229.5*, *MNRAS* **407** (2010) 225 [`1002.4708`]; S. Vegetti et al., *Detection of a dark substructure through gravitational imaging*, *MNRAS* **408** (2010) 1969 [`0910.0760`]; S. Vegetti

et al., *Gravitational detection of a low-mass dark satellite galaxy at cosmological distance*, *Nature* **481** (2012) 341 [1201.3643].

[11] L. E. Strigari et al., *A common mass scale for satellite galaxies of the Milky Way*, *Nature* **454** (2008) 1096 [0808.3772]; M. G. Walker et al., *A Universal Mass Profile for Dwarf Spheroidal Galaxies?*, *ApJ* **704** (2009) 1274 [0906.0341]; J. Wolf et al., *Accurate masses for dispersion-supported galaxies*, *MNRAS* **406** (2010) 1220 [0908.2995].

[12] B. J. Carr et al., *New cosmological constraints on primordial black holes*, *Phys. Rev. D* **81** (2010) 104019 [0912.5297].

[13] G. Steigman & M. S. Turner, *Cosmological constraints on the properties of weakly interacting massive particles*, *Nucl. Phys. B* **253** (1985) 375.

[14] B. W. Lee & S. Weinberg, *Cosmological lower bound on heavy-neutrino masses*, *Phys. Rev. Lett.* **39** (1977) 165; G. R. Blumenthal et al., *Galaxy formation by dissipationless particles heavier than neutrinos*, *Nature* **299** (1982) 37; A. L. Melott et al., *Cluster analysis of the nonlinear evolution of large-scale structure in an axion/gravitino/photino-dominated universe*, *Phys. Rev. Lett.* **51** (1983) 935.

[15] For readers unfamiliar to particle-physics units, you need to know the following: all physical quantities are related to energy. Thus, masses are given in units of rest-mass energy, lengths are described in terms of the energy a photon with the relevant length-scale as the wavelength, and units of time are related to the energy of a photon with a period of $2\pi/t$. For further information on unit conversion, see Appendix A of Ref. [16].

[16] E. W. Kolb & M. S. Turner, *The Early Universe*, Addison Wesley, New York 1990.

[17] K. Griest, *Cross sections, relic abundance, and detection rates for neutralino dark matter*, *Phys. Rev. D* **38** (1988) 2357; H.-C. Cheng, J. L. Feng, & K. T. Matchev, *Kaluza-Klein Dark Matter*, *Phys. Rev. Lett.* **89** (2002) 211301 [hep-ph/0207125]; G. Servant & T. M. P. Tait, *Is the lightest Kaluza-Klein particle a viable dark matter candidate?*, *Nucl. Phys. B.* **650** (2003) 391 [hep-ph/0206071].

[18] C. A. Baker et al., *Improved Experimental Limit on the Electric Dipole Moment of the Neutron*, *Phys. Rev. Lett.* **97** (2006) 13801 [hep-ex/0602020].

[19] K. Abazajian et al., *Nonlinear cosmological matter power spectrum with massive neutrinos: The halo model*, *Phys. Rev. D* **71** (2005) 043507 [astro-ph/0411552]; R. de Putter et al., arXiv:1201.1909.

[20] G. Jungman, M. Kamionkowski, & K. Griest, *Supersymmetric dark matter*, *Phys. Rep.* **267** (1996) 195 [hep-ph/9506380]; S. J. Asztalos et al., *Searches for Astrophysical and Cosmological Axions*, *Annu. Rev. Nucl. Part. Systems* **56** (2006) 293; D. Hooper & S. Profumo, *Dark matter and collider phenomenology of universal extra dimensions*, *Phys. Rep.* **453** (2007) 29 [hep-ph/0701197]; J. L. Feng, *Dark Matter Candidates from Particle Physics and Methods of Detection*, *ARA&A* **48** (2010) 495 [1003.0904].

[21] S. Weinberg, *Cosmological constraints on the scale of supersymmetry breaking*, *Phys. Rev. Lett.* **48** (1982) 1303; J. L. Feng, M. Kamionkowski, & S. K. Lee, *Light gravitinos at colliders and implications for cosmology*, *Phys. Rev. D* **82** (2010) 015012 [1004.4213].

[22] J. L. Feng, A. Rajaraman, & F. Takayama, *Superweakly Interacting Massive Particles*, *Phys. Rev. Lett.* **91** (2010) 011302 [hep-ph/0302215].

[23] S. Dodelson & L. M. Widrow, *Sterile neutrinos as dark matter*, *Phys. Rev. Lett.* **72** (1994) 17 [hep-ph/9303287]; X. Shi & G. M. Fuller, *New Dark Matter Candidate: Nonthermal Sterile Neutrinos*, *Phys. Rev. Lett.* **82** (1999) 2832 [astro-ph/9810076]; K. Petraki & A. Kusenko,

Dark-matter sterile neutrinos in models with a gauge singlet in the Higgs sector, *Phys. Rev. D* **77** (2008) 065014 [0711.4646]; A. Kusenko, *Sterile neutrinos: The dark side of the light fermions*, *Phys. Rep.* **481** (2009) 1 [0906.2968]; LSND, C. Athanassopoulos et al., *Results on* $\nu_\mu \to \nu_e$ *Neutrino Oscillations fron the LSND Experiment*, *Phys. Rev. Lett.* **81** (1998) 1774 [nucl-ex/9709006].

[24] K. Abazajian, G. M. Fuller, & W. H. Tucker, *Direct Detection of Warm Dark Matter in the X-Ray*, *ApJ* **562** (2001) 593 [astro-ph/0106002]; C. R. Watson, Z. Li, & N. K. Polley, *Constraining Sterile Neutrino Warm Dark Matter with Chandra Observations of the Andromeda Galaxy*, arXiv:1111.4217.

[25] K. Abazajian. Please contact Kev directly if you would like to hear more.

[26] M. Y. Khlopov, C. A. Stephan & D. Fargion, *Dark matter with invisible light from heavy double charged lepton of almost-commutative geometry?*, *Classical and Quantum Gravity* **23** (2006) 7305 [astro-ph/0511789]; D. Feldman, B. Kors & P. Nath, *Extra-weakly interacting dark matter*, *Phys. Rev. D* **75** (2007) 023503 [hep-ph/0610133]; J. L. Feng & J. Kumar, *Dark-Matter Particles without Weak-Scale Masses or Weak Interactions*, *Phys. Rev. Lett.* **101** (2008) 231301 [0803.4196]; L. Ackerman et al., *Dark matter and dark radiation*, *Phys. Rev. D* **79** (2009) 023519 [0810.5126]; J. L. Feng et al., *Hidden charged dark matter*, *JCAP* **07** (2009) 004 [0905.3039]; J. L. Feng, V. Rentala, & Z. Surujon, *WIMPless dark matter in anomaly-mediated supersymmetry breaking with hidden QED*, *Phys. Rev. D* **84** (2011) 095033 [1108.4689]; M. Pospelov, A. Ritz, & M. Voloshin, *Secluded WIMP dark matter*, *Phys. Lett. B* **662** (2008) 53 [0711.4866]; N. Arkani-Hamed et al., *A theory of dark matter*, *Phys. Rev. D* **79** (2009) 015014 [0810.0713]; D. E. Kaplan, M. A. Luty, & K. M. Zurek, *Asymmetric dark matter*, *Phys. Rev. D* **79** (2009) 115016 [0901.4117]; T. Cohen et al., *Asymmetric dark matter from a GeV hidden sector*, *Phys. Rev. D* **82** (2010) 056001 [1005.1655].

[27] O. Adriani et al., *An anomalous positron abundance in cosmic rays with energies 1.5-100 GeV*, *Nature* **458** (2009) 607 [0810.4995]; A. A. Abdo et al., *Measurement of the Cosmic Ray* $e^+ + e^-$ *Spectrum from 20 GeV to 1 TeV with the Fermi Large Area Telescope*, *Phys. Rev. Lett.* **102** (2009) 181101 [0905.0025].

[28] D. Griffiths, *Introduction to Elementary Particles*, Wiley, New York, 2008.

[29] J. L. Feng, J.-F. Grivaz, & J. Nachtman, *Searches for supersymmetry at high-energy colliders*, *Rev. Mod. Phys.* **82** (2010) 699 [0903.0046]; D. Alves et al., *Simplified Models for LHC New Physics Searches*, arXiv:1105.2838.

[30] S. Chatrchyan et al., *Search for supersymmetry in pp collisions at* $\sqrt{s} = 7$ *TeV in events with a single lepton, jets, and missing transverse momentum*, *JHEP* **08** (2011) 156 [1107.1870]; ATLAS Collaboration, *Search for supersymmetry in pp collisions at s=7 TeV in final states with missing transverse momentum and b-jets*, *Phys. Lett. B* **701** (2011) 398 [1103.4344].

[31] See the Dark Matter Working Group DUSEL White paper (2010) for a comprehensive list and review of direct-detection experiments, and references to those experiments: http://dmtools.brown.edu/DMWiki/index.php/File:DMWG_DUSEL_White_Paper_April_2010.pdf

[32] R. Bernabei et al., *New results from DAMA/LIBRA*, *Eur. Phys. J. C* **67** (2010) 39 [1002.1028]; C. E. Aalesth et al., *Results from a Search for Light-Mass Dark Matter with a p-Type Point Contact Detector*, *Phys. Rev. Lett.* **106** (2011) 131301 [1106.0650]; G. Angloher et al., *Results from 730 kg days of the CRESST-II Dark Matter Search*, arXiv:1109.0702.

[33] One popular theory for the origin of the DAMA/LIBRA signal is introduced in D. Nygren, *A testable conventional hypothesis for the DAMA-LIBRA annual modulation*, arXiv:1102.0815.

[34] J. Cherwinka et al., *A Search for the Dark Matter Annual Modulation in South Pole Ice*, arXiv:1106.1156.

[35] E. Behnke et al. *Improved Limits on Spin-Dependent WIMP-Proton Interactions from a Two Liter CF_3I Bubble Chamber*, *Phys. Rev. Lett.* **106** (2011) 021303 [1008.3518]; E. Aprile et al., *Dark Matter Results from 100 Live Days of XENON100 Data*, *Phys. Rev. Lett.* **107** (2011) 13102 [1104.2549]; Z. Ahmed, *Combined limits on WIMPs from the CDMS and EDELWEISS experiments*, *Phys. Rev. D* **84** (2011) 011102 [1105.3377].

[36] K. Scholberg, *Prospects for measuring coherent neutrino-nucleus elastic scattering at a stopped-pion neutrino source*, *Phys. Rev. D* **73** (2006) 033005 [hep-ex:0511042]; J. Monroe & P. Fisher, *Neutrino backgrounds to dark matter searches*, *Phys. Rev. D* **76** (2007) 033007 [0706.3019]; L. E. Strigari, *Neutrino coherent scattering rates at direct dark matter detectors*, *New J. Phys.* **11** (2009) 105011 [0903.3630].

[37] A. A. Abdo et al., *Constraints on cosmological dark matter annihilation from the Fermi-LAT isotropic diffuse gamma-ray measurement*, *JCAP* **04** (2010) 014 [1002.4415]; R. Abbasi et al., *Search for dark matter from the Galactic halo with the IceCube Neutrino Telescope*, *Phys. Rev. D* **84** (2011) 022004 [1101.3349]; A. Pinzke, C. Pfrommer, & L. Bergström, *Prospects of detecting gamma-ray emission from galaxy clusters: Cosmic rays and dark matter annihilations*, *Phys. Rev. D* **84** (2011) 123509 [1105.3240]; A. Cuoco et al., *Anisotropies in the diffuse gamma-ray background measured by Fermi LAT*, arXiv:1110.1047.

[38] K. N. Abazajian et al., *Conservative constraints on dark matter from the Fermi-LAT isotropic diffuse gamma-ray background spectrum*, *JCAP* **11** (2010) 041 [1002.3820]; A. Abramowski et al., *Search for a Dark Matter Annihilation Signal from the Galactic Center Halo with H.E.S.S.*, *Phys. Rev. Lett* **106** (2011) 161301 [1103.3266]; A. Geringer-Sameth & S. M. Koushiappas, *Exclusion of canonical WIMPs by the joint analysis of Milky Way dwarfs with Fermi*, *Phys. Rev. Lett.* **107** (2011) 241303 [1108.2914]; The Fermi LAT Collaboration, M. Kaplinghat, & G. D. Martinez, *Constraining Dark Matter Models from a Combined Analysis of Milky Way Satellites with the Fermi Large Area Telescope*, *Phys. Rev. Lett.* **107** (2011) 241302 (2011) [1100.3546]; R. C. Cotta et al., *Constraints on the pMSSM from LAT Observations of Dwarf Spheroidal Galaxies*, arXiv:1111.2604.

[39] A. Gould, *Weakly interacting massive particle distribution in and evaporation from the sun*, *ApJ* **321** (1987) 560; A. H. G. Peter, *Dark matter in the Solar System II. WIMP annihilation rates in the Sun*, *Phys. Rev. D* **79** (2009) 103532 [0902.1347]; T. Tanaka et al., *An Indirect Search for Weakly Interacting Massive Particles in the Sun Using 3109.6 Days of Upward-going Muons in Super-Kamiokande*, *ApJ* **742** (2011) 78 [1108.3384]; The IceCube Collaboration, *Multiyear search for dark matter annihilations in the Sun with the AMANDA-II and IceCube detectors*, *Phys. Rev. D* **85** (2012) 042002 [1112.1840]; S. Sivertsson & J. Edsjö, *WIMP diffusion in the solar system including solar WIMP-nucleon scattering*, arXiv:1201.1895.

[40] T. Aramaki et al., *Antideuterons as an indirect dark matter signatures: Si(Li) detector development and a GAPS balloon mission*, *Ad. Space Research* **46** (2010) 1349; O. Adriani et al., *PAMELA Results on the Cosmic-Ray Antiproton Flux from 60 MeV to 180 GeV in Kinetic Energy*, *Phys. Rev. Lett.* **105** (2010) 121101 [1007.0821].

[41] K. van Bibber et al., *Proposed experiment to produce and detect light pseudoscalars*, *Phys. Rev. Lett.* **59** (1987) 759; A. S. Chou et al., *Search for Axionlike Particles Using a Variable-Baseline Photon-Regeneration Technique*, *Phys. Rev. Lett.* **100** (2008) 080402 [0710.3783]; http://cast.web.cern.ch/CAST/

[42] P. Sikivie, *Experimental tests of the 'invisible' axion*, *Phys. Rev. Lett.* **51** (1983) 1415; http://www.phys.washington.edu/groups/admx/home.html

[43] S. Abrahamyan et al., *Search for a New Gauge Boson in Electron-Nucleus Fixed-Target Scattering by the APEX Experiment*, *Phys. Rev. Lett.* **107** (2011) 191804 [1108.2750].

[44] K. Sigurdson, M. Kaplinghat, & A. H. G. Peter, *Gravitational probes of dark-matter physics*, in prep.

[45] P. J. E. Peebles, *The large-scale structure of the universe*, Princeton University, Princeton, NJ, 1980; S. Dodelson, *Modern Cosmology*, Academic Press, Amsterdam, 2003; H. Mo, F. C. van den Bosch, & S. White, *Galaxy Formation and Evolution*, Cambridge University, Cambridge, UK, 2010.

[46] P. Colín, O. Valenzuela, & V. Avila-Reese, *On the Structure of Dark Matter Halos at the Damping Scale of the Power Spectrum with and without Relict Velocities*, *ApJ* **673** (2008) 203 [0709.4027]; F. Villaescusa-Navarro & N. Dalal, *Cores and cusps in warm dark matter halos*, *JCAP* **03** (2011) 024 [1010.3008]; M. Viel et al., *The Non-Linear Matter Power Spectrum in Warm Dark Matter Cosmologies*, *MNRAS* **421** (2012) 50 [1107.4094]; R. M. Dunstan et al., *The Halo Model of Large Scale Structure for Warm Dark Matter*, arXiv:1109.6291; R. E. Smith & K. Markovic, *Testing the warm dark matter paradigm with large-scale structures*, *Phys. Rev. D* **84** (2011) 063507 [1103.2134].

[47] A. H. G. Peter, *Mapping the allowed parameter space for decaying dark matter models*, *Phys. Rev. D* **81** (2010) 083511 [1001.3870]; A. H. G. Peter, C. E. Moody, & M. Kamionkowsi, *Dark-matter decays and self-gravitating halos*, *Phys. Rev. D* **81** (2010) 103501 [1003.0419]; M.-Y. Wang & A. R. Zentner, *Weak gravitational lensing as a method to constrain unstable dark matter*, *Phys. Rev. D* **82** (2010) 123507 [1011.2774]; M.-Y. Wang & A. R. Zentner, *Effects of Unstable Dark Matter on Large-Scale Structure and Constraints from Future Surveys*, *Phys. Rev. D* **85** (2012) 043514 [1201.2426].

[48] PanSTARRS: http://pan-starrs.ifa.hawaii.edu/public/; SkyMapper: http://msowww.anu.edu.au/skymapper/; Dark Energy Survey: http://www.darkenergysurvey.org/; LSST: http://www.lsst.org/lsst/; WFIRST: http://wfirst.gsfc.nasa.gov/; BOSS: http://cosmology.lbl.gov/BOSS/; Prime Focus Spectrograph: http://sumire.ipmu.jp/en/

[49] R. Mandelbaum et al., *Density profiles of galaxy groups and clusters from SDSS galaxy-galaxy weak lensing*, *MNRAS* **372** (2006) 758 [astro-ph/0605476]; R. Mandelbaum et al., *Ellipticity of dark matter haloes with galaxy-galaxy weak lensing*, *MNRAS* **370** (2006) 1008 [astro-ph/0507108]; D. J. Sand et al., *Separating Baryons and Dark Matter in Cluster Cores: A Full Two-dimensional Lensing and Dynamic Analysis of Abell 383 and MS 2137-23*, *ApJ* **674** (2008) 711 [0710.1069]; J. Richard et al., *LoCuSS: First Results from Strong-lensing Analysis of 20 Massive Galaxy Clusters at $z \sim 0.2$*, *MNRAS* **404** (2010) 325 [0911.3302].

[50] R. Kuzio de Naray, S. S. McGaugh, & W. J. G. de Blok, *Mass Models for Low Surface Brightness Galaxies with High-Resolution Optical Velocity Fields*, *ApJ* **676** (2008) 920 [0712.0860]; R. Mandelbaum, U. Seljak, & C. M. Hirata, *A halo mass—concentration relation from weak lensing*, *JCAP* **08** (2008) 006 [0805.2552]; M. Boylan-Kolchin, J. S. Bullock, & M. Kaplinghat, *Too big to fail? The puzzling darkness of massive Milky Way subhaloes*, *MNRAS* **415** (2011) L40 [1103.0007].

[51] A. H. G. Peter & A. J. Benson, *Dark-matter decays and Milky Way satellite galaxies*, *Phys. Rev. D* **82** (2010) 123521 [1009.1912]; E. Polisensky & M. Ricotti, *Constraints on the dark matter particle mass from the number of Milky Way satellites*, *Phys. Rev. D* **83** (2011) 043506 [1004.1459]; M. Lovell et al., *The Haloes of Bright Satellite Galaxies in a Warm Dark Matter Universe*, *MNRAS* **420** (2012) 2318 [1104.2929].

[52] N. Dalal & C. S. Kochanek, *Direct Detection of Cold Dark Matter Substructure*, *ApJ* **572** (2002) 25 [astro-ph/0111456]; C. R. Keeton & L. A. Moustakas, *A New Channel for Detecting Dark Matter Substructure in Galaxies: Gravitational Lens Time Delays*, *ApJ* **699** (2009) 1720 [0805.0309]; P. J. Marshall et al., *Dark Matter Structures in the Universe: Prospects for Optical Astronomy in the Next Decade*, Astro2010 Decadal Survey (2010) [0902.2963].

[53] L. Moustakas et al., *The Observatory for Multi-Epoch Gravitational Lens Astrophysics (OMEGA)*, *SPIE Conference Series* **7010** (2008) 41 [0806.1884].

[54] D. H. Rudd, A. R. Zentner, & A. V. Kravtsov, *Effects of Baryons and Dissipation on the Matter Power Spectrum*, *ApJ* **672** (2008) 19 [astro-ph/0703741]; S. Pedrosa, P. B. Tissera, & C. Scannapieco, *The joint evolution of baryons and dark matter halos*, *MNRAS* **402** (2009) 776 [0910.4380]; C. Scannapieco et al., *The Aquila Comparison Project: The Effects of Feedback and Numerical Methods on Simulations of Galaxy Formation*, arXiv:1112.0315.

[55] F. Governato et al., *Bulgeless dwarf galaxies and dark matter cores from supernova-driven outflows*, *Nature* **463** (2010) 203 [0911.2237]; P. F. Hopkins, E. Quataert, & N. Murray, *Self-regulated star formation in galaxies via momentum input from massive stars*, *MNRAS* **417** (2011) 950 [1101.4940]; M. Kuhlen et al., *Dwarf galaxy formation with H2-regulated star formation*, arXiv:1105.2376.

PROCEEDINGS OF SCIENCE

Evidence of Episodic Accretion in Spitzer IRS Spectra of Low-Luminosity Embedded Protostars

Hyo Jeong Kim[*],[a] **Neal J. Evans II**,[a] **Michael M. Dunham**[b], **and Jeong-Eun Lee**[c]

[a] *The University of Texas at Austin*
1 University Station, C1400, Austin, Texas, 78712-0259, USA
[b]*Department of Astronomy, Yale University New Haven, CT, USA*
[c]*Department of Astronomy and Space Science, Kyung Hee University*
Yongin-si, Gyeonggi-do 446-701, Korea
E-mail: `hyojeong@astro.as.utexas.edu`, `nje@astro.as.utexas.edu`, `michael.dunham@yale.edu`, `jeongeun.lee@khu.ac.kr`

We present *Spitzer* IRS, SH mode spectroscopy toward 21 young stellar objects (YSOs) with luminosity lower than 1 $L_\odot$ (4 with luminosity lower than 0.1 $L_\odot$). While the standard star formation model predicts protostars to have a luminosity higher than 1.6 $L_\odot$, *Spitzer* Legacy Project, From Molecular Cores to Planet Forming Disks (c2d) survey shows that 59 % of the 112 embedded protostars have luminosity lower than 1.6 $L_\odot$. One possible explanation is that mass accretion is not a constant process. If accretion is episodic, sources that currently are low luminosity may have had much higher accretion rates, and thus luminosities, in the past. In that case, imprints of the high luminosity stage in low luminosity YSOs would support the idea of episodic mass accretion. Evidence may be found in their 15.2 μm CO_2 ice features. Pure CO_2 ice can be formed only at elevated temperatures and thus higher luminosity. Current internal luminosities of YSOs with $L \leq 1\ L_\odot$ do not provide such conditions. We analyze 15.2 μm CO_2 ice bending mode absorption lines in comparison to laboratory data. Preliminary analysis indicates that the low luminosity YSOs may harbor pure CO_2 ice components. A detailed analysis is ongoing and the results are presented here.

Frank N. Bash Symposium New Horizons In Astronomy,
October 9-11, 2011
Austin Texas

[*]Speaker.

PoS(Bash11)019

1. Introduction

The *Spitzer Space Telescope* discovered a set of Very Low Luminosity Objects (VeLLOs; Young et al. 2004; Bourke et al. 2006; Dunham et al. 2006; Dunham et al. 2008), defined by di Francesco et al. (2007) to have luminosity lower than 0.1 $L_\odot$. The luminosity of accretion is given as $L_{acc} \propto M_\star \dot{M}$, where $M_\star$ is the mass of the star and $\dot{M}$ is the mass accretion rate. For accretion at the standard rate onto an object at the stellar/brown dwarf boundary, $L_{acc} \sim 1.6$ $L_\odot$ (Shu et al. 1987). The low luminosity must arise from a low mass accretion rate or a very low mass of the young stellar object. More generally, the range of luminosities of embedded Class 0/I sources is very large (Evans et al. 2009), and this range is not predicted by any model of steady accretion.

This wide range of luminosity is predicted by models of episodic accretion (Dunham et al. 2010). In this picture, accretion from the envelope is not transferred smoothly to the star, but instead builds up in the disk. When the embedded disk of a young stellar object becomes gravitationally unstable, the mass accretion to the central protostar increases (Vorobyov & Basu 2005). Once episodic accretion happens, the mass accretion rate gets higher, which results in high accretion luminosity.

Evidence can be found in molecular spectra in the gas and ice phase of low luminosity sources. Pontoppidan et al. (2008) analyzed the general shape of the 15.2 μm CO_2 ice bending mode spectrum toward 50 embedded young stars. The 15.2 μm CO_2 spectrum can be decomposed to the multiple components including a pure CO_2 ice component. Pure CO_2 ice can form by two processes. One is CO_2 segregation out of a CO_2-H_2O mixture. The other is a distillation process, in which CO evaporates from a CO_2-CO mixture, leaving pure CO_2 behind. The former process occurs at a high temperature (50 - 80 K) and the latter occurs at a lower temperature (20 - 30 K). Both pure CO_2 formation processes are irreversible (Hagen et al. 1983), since the bond between pure CO_2 ices is the most stable phase. Once the pure CO_2 ice has formed, it will not disappear unless evaporates. The past heating of the core can effect on the 15.2 μm CO_2 ice bending mode spectrum.

The total amount of CO_2 ice is another indicator. The episodic accretion scenario gives multiple long periods of low luminosity (Dunham et al. 2010) instead of the short period of low luminosity that the continuous accretion model predicts (Shu 1977; Young & Evans 2005). As a result, episodic accretion provides more time to form ice. The total amount of CO_2 ice can vary depending on the accretion scenario. With chemical modeling, the accretion scenario can affect the total amount of CO_2 ice, and can explain the observed total of CO_2 ice.

2. Observations

We observed a sample of 19 embedded YSOs with luminosities in the range between 0.08 - 0.69 $L_\odot$. We used Spitzer IRS, Short-High (SH) mode spectroscopy to study the 15.2 μm CO_2 ice feature. Currently existing envelopes around the selected sources in this study are not warm enough to form a pure CO_2 ice component either by distillation or segregation.

3. Results

We present one example in Fig. 1. IRAM04191-IRS (André et al. 1999; Dunham et al. 2006) is a VeLLO, which has current luminosity lower than 0.1 $L_\odot$. The current internal luminosity of a VeLLO with $L < 0.1\ L_\odot$ does not provide the conditions needed to produce pure CO_2 ice at a radius where a typical envelope begins. Significant amounts of pure CO_2 ice would signify a higher past luminosity. Using laboratory data, we find evidence for pure CO_2 ice toward 15 out of 19 young low luminosity sources. Eight sources show a significant double peak in the optical depth, which provides unambiguous evidence for pure CO_2 ice. The presence of the pure CO_2 ice component indicates higher dust temperature and hence higher luminosity in the past.

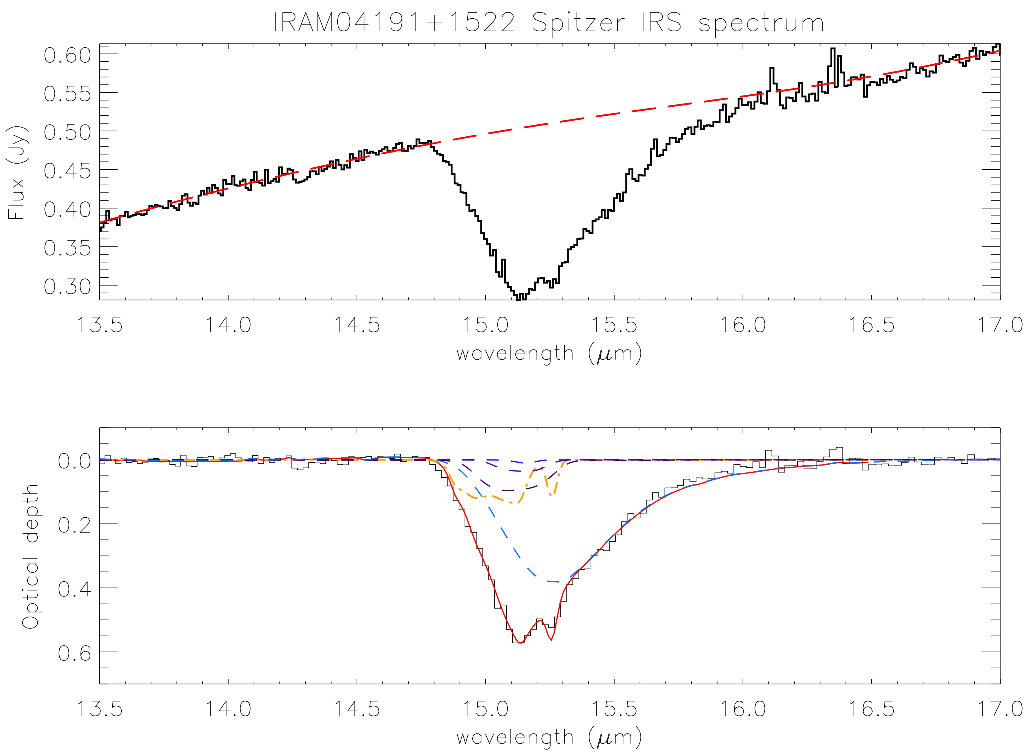

Figure 1: CO_2 ice component analysis of VeLLO, IRAM04191+1522, with laboratory data. The upper panel shows observed flux vs. wavelength. The lower panel shows the component analysis. The black solid line is the observed optical depth at 15.2 μm; the yellow line is the pure CO_2 ice component, the blue line is the water rich CO_2 ice component, and purple lines are the CO-CO_2 mixture ice components. The sum of all the components is plotted in red. The source has the pure CO_2 ice component, and shows a significant double peak.

In addition to the evidence for pure CO_2, the total amount of CO_2 ice, including that in mixed ices, can be explained by long periods of low luminosity between episodic accretion bursts, as predicted in an episodic accretion scenario. We use the evolutionary chemo-dynamical model by Lee et al. (2004) to test this idea. The model calculates the chemical evolution of a core from the prestellar core to the embedded protostellar core stage. At each time step, the model calculates the density profile, the dust temperature, the gas temperature, and the abundances self-consistently. We used two kinds of luminosity evolution models: continuous accretion model and episodic accretion. Also, we included an additional pathway to CO_2 ice from CO gas, and tested the chemical evolution model with and without the chemical network. Observed column densities show the best match with the range of episodic accretion with conversion of CO ice to CO_2 ice.

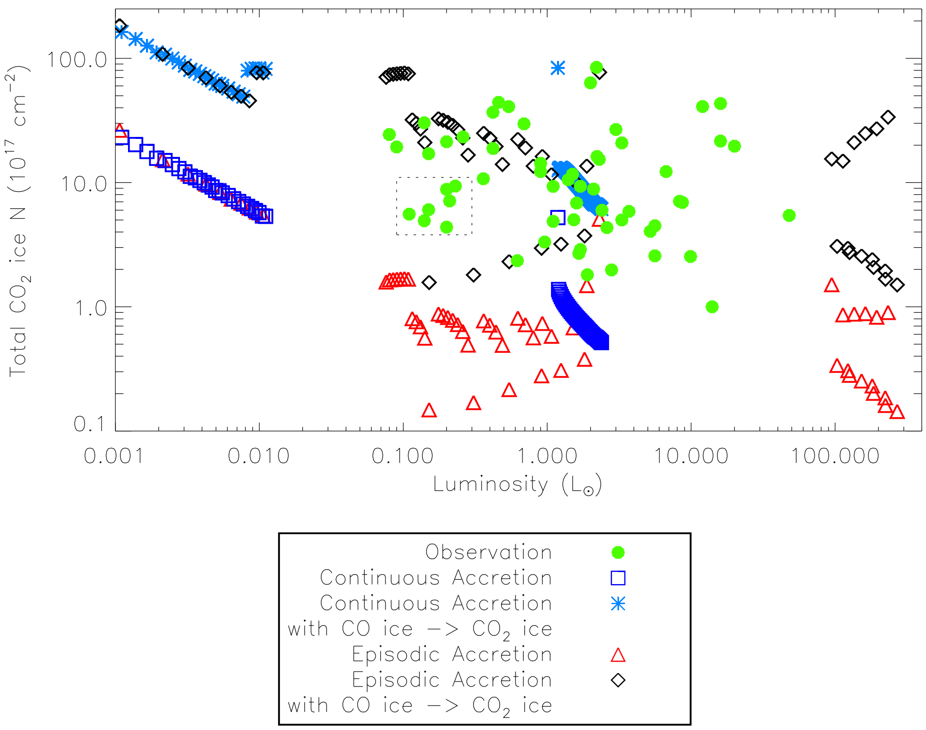

Figure 2: The column densities from observations and the chemical models are plotted versus luminosities. Green points are observations from the current study and the study of Pontoppidan et al. (2008). Together, the studies cover the luminosity range 0.1 $L_\odot$ to 100 $L_\odot$. Blue points are predictions from a continuous accretion model, red points are predictions from an episodic accretion model, and black points are from an episodic accretion model including 10% conversion of CO to CO_2 ice during each cycle. Observed column densities show best match with the range of episodic accretion with conversion of CO ice to CO_2 ice.

This material is based upon work supported by the National Aeronautics and Space Administration under RSA 137730 issued by the Jet Propulsion Laboratory. Jeong-Eun Lee was supported by Basic Science Research Program through the National Research Foundation of Korea(NRF) funded by the Ministry of Education, Science and Technology (No. 2011-0004781). Hyo Jeong Kim and Neal J Evans acknowledge support from NSF grant AST-0607793.

References

[1] André, P., Motte, F., & Bacmann, A. 1999, ApJ, 513, L57

[2] Bourke, T. L., Myers, P. C., Evans, II, N. J., et al. 2006, ApJ, 649, L37

[3] di Francesco, J., Evans, II, N. J., Caselli, P., et al. 2007, in Protostars and Planets V, ed. B. Reipurth, D. Jewitt, & K. Keil, 17–32

[4] Dunham, M. M., Evans, II, N. J., Bourke, T. L., et al. 2006, ApJ, 651, 945

[5] Dunham, M. M., Crapsi, A., Evans, II, N. J., et al. 2008, ApJS, 179, 249

[6] Dunham, M. M., Evans, N. J., Terebey, S., Dullemond, C. P., & Young, C. H. 2010, ApJ, 710, 470

[7] Evans, II, N. J., Allen, L. E., Blake, G. A., et al. 2003, PASP, 115, 965

[8] Evans, N. J., Dunham, M. M., Jørgensen, J. K., et al. 2009, ApJS, 181, 321

[9] Hagen, W., Tielens, A. G. G. M., & Greenberg, J. M. 1983, A&AS, 51, 389

[10] Lee, J.-E., Bergin, E. A., & Evans, II, N. J. 2004, ApJ, 617, 360

[11] Pontoppidan, K. M., Boogert, A. C. A., Fraser, H. J., et al. 2008, ApJ, 678, 1005

[12] Shu, F. H. 1977, ApJ, 214, 488

[13] Shu, F. H., Adams, F. C., & Lizano, S. 1987, ARA&A, 25, 23

[14] Vorobyov, E. I. & Basu, S. 2005, ApJ, 633, L137

[15] Young, C. H., Jørgensen, J. K., Shirley, Y. L., et al. 2004a, ApJS, 154, 396

[16] Young, C. H. & Evans, II, N. J. 2005, ApJ, 627, 293

PROCEEDINGS OF SCIENCE

Integral Field Spectroscopy of the center of the Draco Dwarf Spheroidal

John R. Jardel[∗,a] **Karl Gebhardt,**[a] **Maximilian Fabricius,**[b] **and Niv Drory**[c]
[a]*The University of Texas*
1 University Station C1400, Austin, TX 78712
[b]*Max-Planck Institut für extraterrestrische Physik*
Giessenbachstrasse, D-85741 Garching bei München, Germany
[c]*Instituto de Astronomía, Universidad Nacional Autónoma de México*
Avenida Universidad 3000, Ciudad Universitaria, C.P. 04510 México D.F., México
Email: `jardel@astro.as.utexas.edu`

We use the VIRUS-W Integral Field Spectrograph to simultaneously obtain radial velocities for 17 stars in the central $105'' \times 55''$ of the Draco dwarf spheroidal (dSph) galaxy. We apply a color-magnitude diagram filter to these stars which leaves 12 probable Draco members. From these 12 member stars we reconstruct a Line-of-Sight Velocity Distribution (LOSVD) and calculate a velocity dispersion of $\sigma = 16.1^{+0.8}_{-5.5}$ km s^{-1}. This LOSVD will allow us to dynamically model the center of the galaxy on smaller spatial scales where we hope to determine the slope of the dark matter density profile as well as investigate the possibility of an intermediate-mass black hole.

Frank N. Bash Symposium New Horizons In Astronomy,
October 9-11, 2011
Austin Texas

∗Speaker.

PoS(Bash11)021

1. Introduction

The centers of dwarf spheroidal galaxies (dSphs) are interesting tests for the cold dark matter (CDM) model of structure formation. Since they are some of the most dark matter dominated galaxies discovered, they are believed to be relatively unaffected by the gravity of the stellar component. This makes the determination of their dark matter density profiles more straightforward than in massive galaxies, and we can compare to CDM simulations more directly. Currently, observers are finding dark matter profiles with a flat central core (e.g. [1];[8]) while CDM simulations predict all galaxies should have a cuspy central profile ([7]).

Obviously it is important to have kinematics that sample the inner regions of these galaxies so that observations are able to differentiate between cored and cuspy dark halos. Since the Local Group dSphs are relatively nearby, we are able to resolve individual stars and target them for spectroscopy. Multi-fiber spectroscopy (MFS) would appear to be ideally suited to this task as it allows for the simultaneous targeting of many individual stars. Indeed [12] provide the best data set available by using this technique (over 5,000 stars in four dSphs). However, one of the limitations of MFS is that it is difficult to position multiple fibers closely together. Thus, the centers of these dSphs are frequently under-sampled.

Where MFS becomes difficult, spectroscopy with Integral Field Units (IFUs) can be useful. IFUs often have a closely-packed array of fibers, and this high density of fibers allows for simultaneous observation of many stars in a dense field. The drawback to IFUs, however, is that fiber positions are fixed.

We present here observations of the central region of Draco using integral field spectroscopy. Our data are the most centrally-located velocities available for Draco. We analyze these data and calculate the line-of-sight velocity distribution (LOSVD) of stars within the central 10 pc of Draco. We plan to use these data to further constrain the slope of the dark matter density profile through orbit-based dynamical models in a later paper.

2. Observations

We use the VIRUS-W IFU ([2]) on the 2.7m Harlan J. Smith Telescope at McDonald Observatory to target the center of the Draco dSph. This IFU packs 267 fibers into its $105'' \times 55''$ field of view with a 1/3 filling factor. Each fiber is $3\farcs2$ in diameter on the sky. We observed in the spectral range covering roughly 4900Å to 5500Å at a resolving power of $R = 6800$. This region allows radial velocities to be extracted from the Mg *b* stellar absorption feature.

Our observations were taken over the first half of five nights between 2011 August 1-5. Conditions were excellent for the first four nights with good transparency, and seeing was never worse than $2''$. We took the standard array of bias, twilight flat, and arc lamp calibration images. Since most of the fibers in the IFU are on empty sky, we did not need separate sky exposures. Our science exposures consist of 57 15-minute integrations, which we later combine. Total exposure time is roughly 14 hours.

Figure 1 shows the location of the IFU overlaid on a *Hubble Space Telescope (HST)* image from [9]. Note that typical seeing at McDonald Observatory is $2''$, much larger than the *HST*

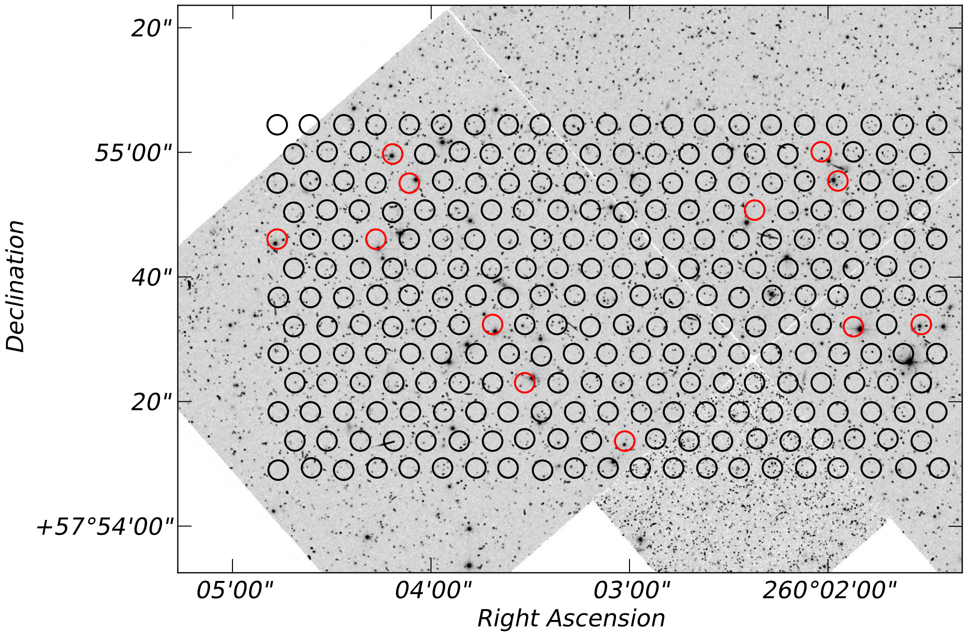

Figure 1: VIRUS-W IFU overlaid on top of an *HST* image from [9]. Red circles highlight fibers containing stars used in the analysis.

point-spread function. Red circles denote fibers with stars later used in the kinematic analysis. We obtained useful spectra of 17 stars with apparent magnitudes $V < 21$.

3. Analysis

To extract radial velocities we use the brightest star with known velocity in the field as our velocity standard. Using the IRAF task FXCOR we cross-correlate the other 16 spectra to this standard. Since this star's heliocentric velocity is known and it is in the same field of view, we do not need to further correct for heliocentric motion.

To determine membership, we place the 17 observed stars in a color-magnitude diagram (Figure 2). Stars that lie away from the red giant branch are discarded as non-members, as are stars with velocity offsets greater than 50 km s^{-1} from systemic velocity V_{sys}. We keep all 12 stars marked as red asterisks in Figure 2. Note that blind sigma-clipping of the velocities also results in these same 12 stars being classified as members.

We plan to study the mass profile of Draco with dynamical models (e.g.[4];[11];[5]). In order to use these 12 stars in future models we must first reconstruct the line-of-sight velocity distribution (LOSVD) of the center of the galaxy. The LOSVD is essentially a smoothed histogram of line-of-sight radial velocities for stars in a given region of the galaxy. We calculate this by using an adaptive kernel density estimate, adapted from [10] and explained in detail in [3]. We are able to estimate the 1-σ uncertainty in the LOSVD through bootstrap resamplings of the velocity data.

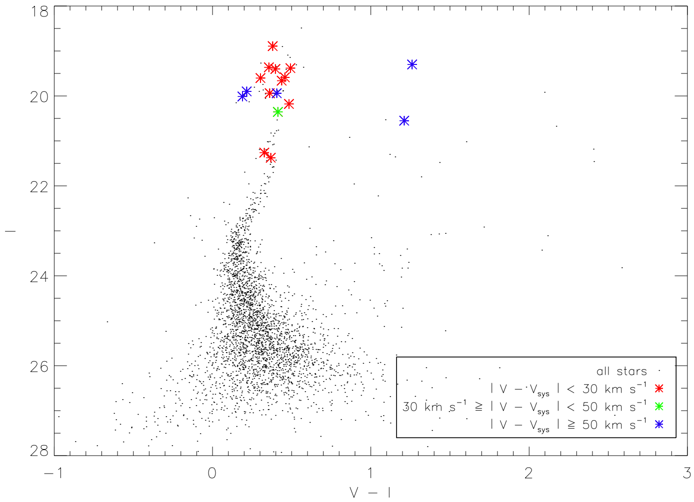

Figure 2: Color-magnitude diagram of Draco from *HST* photometry ([9]). Colored asterisks are stars we observe, coded according to their offset from Draco's systemic velocity V_{sys}.

4. Results

Figure 3 shows the LOSVD we calculate for the center of Draco. The stars in this LOSVD are orbiting at projected radii between 2 and 20 pc. We can fit Gauss-Hermite moments to the LOSVD and measure the mean velocity $V = 3.8^{+3.4}_{-7.3}$ km s^{-1} and velocity dispersion $\sigma = 16.1^{+0.8}_{-5.5}$ km s^{-1}. The higher order moments are consistent with zero. This LOSVD will be an important kinematic constraint in future models of the galaxy where we will investigate its dark matter content at small radii.

We conclude that integral field spectroscopy is indeed complementary to multi-fiber spectroscopy, and is particularly suited to studying the centers of dwarf galaxies where individual stars are resolved. We were able to extract kinematics for 17 stars with magnitudes $20 < V < 21$ in 14 hours of observing time on a 2.7-meter telescope. Obviously, larger telescopes with multi-object spectrographs are ideal, as slit masks are usually able to be positioned more easily. However, IFUs such as VIRUS-W can provide a low-cost alternative.

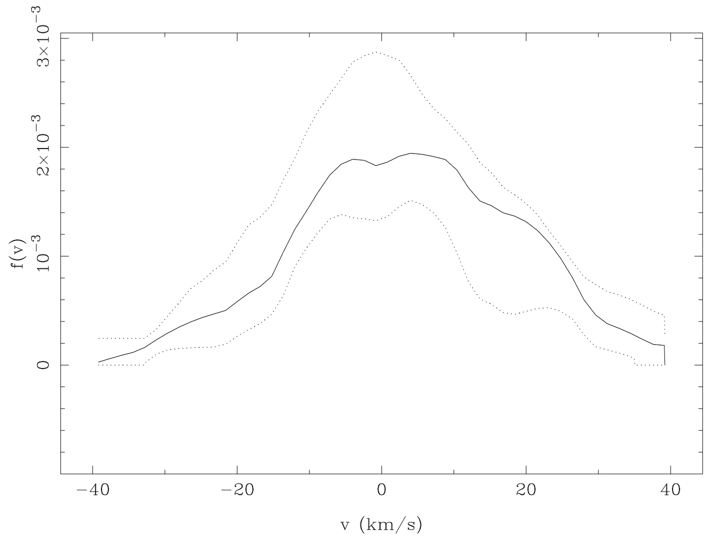

Figure 3: Line-of-sight Velocity Distribution of the 12 member stars we observe in the central region of Draco.

References

[1] Burkert, A., *The Structure of Dark Matter Halos in Dwarf Galaxies*, 1995, ApJL, 447, L25+

[2] Fabricius, M. H. et al., *VIRUS-W: an integral field unit spectrograph dedicated to the study of spiral galaxy bulges*, 2008, SPIE Proc., Vol. 7014

[3] Gebhardt, K., et al., *The Centers of Early-Type Galaxies With HST. III. Non-Parametric Recovery of Stellar Luminosity Distribution*, 1996, AJ, 112, 105

[4] Gebhardt, K., et al., *Axisymmetric Dynamical Models of the Central Regions of Galaxies*, 2003, ApJ, 583, 92

[5] Jardel, J., & Gebhardt, K., *The Dark Matter Density Profile of the Fornax Dwarf*, 2011, ApJ accpeted (ArXiv:1112.0319)

[6] Mateo, M. L., *Dwarf Galaxies of the Local Group*, 1998, ARA&A, 36, 435

[7] Navarro, J. F., Frenk, C. S., & White, S. D. M., *The Structure of Cold Dark Matter Halos*, 1996, ApJ, 462, 563

[8] Persic, M., Salucci, P., & Stel, F., The universal rotation curve of spiral galaxies - I. The dark matter connection, 1996, MNRAS, 281, 27

[9] Ségall, M., Ibata, R. A., Irwin, M. J., Martin, N. F., & Chapman, S. 2007, *Draco, a flawless dwarf galaxy*, MNRAS, 375, 831

[10] Silverman, B. W., *Density estimation for statistics and data analysis*, Chapman and Hall, London, 1986

[11] Siopis, C., et al., *A Stellar Dynamical Measurement of the Black Hole Mass in the Maser Galaxy NGC 4258*, 2009, ApJ, 693, 946

[12] Walker, M. G., Mateo, M., & Olszewski, E. W., *Stellar Velocities in the Carina, Fornax, Sculptor, and Sextans dSph Galaxies: Data From the Magellan/MMFS Survey*, 2009, AJ, 137, 3100

PROCEEDINGS OF SCIENCE

Photometry of the Stellar Tidal Stream in the Halo of Messier 63 *†

Taylor S. Chonis[‡,a], **David Martínez-Delgado**[b], **R. Jay Gabany**[c], **Steven R. Majewski**[d], **Gary J. Hill**[e], **Ignacio Trujillo**[f,g]

[a] *Department of Astronomy, The University of Texas at Austin*
[b] *Max-Planck Institut für Astronomie*
[c] *BlackBird Observatory*
[d] *Department of Astronomy, University of Virginia*
[e] *McDonald Observatory, University of Texas at Austin*
[f] *Instituto de Astrofísica de Canarias*
[g] *Departmento de Astrofísica, Universidad de La Laguna*
E-mail: tschonis@astro.as.utexas.edu, delgado@mpia-hd.mpg.de, rj2010@cosmotography.com, srm4n@virginia.edu, hill@astro.as.utexas.edu, itc@iac.es

We present surface photometry of a giant, low surface brightness stellar arc in the halo of the nearby spiral galaxy M63 (NGC 5055) that is consistent with being a part of a stellar stream resulting from the disruption of a dwarf satellite galaxy. Using the stream's "great-circle" morphology and its photometric properties, we estimate that the stream originates from the accretion of a $\sim 10^8\ M_\odot$ satellite in the last few Gyr. The $B-R$ color of the stream's stars is consistent with Local Group dwarfs and is also similar to the outer regions of M63's disk and stellar halo within our measurement uncertainties. Additionally, we identify several other low surface brightness features that may be related to the galaxy's complex spiral structure or may be tidal debris associated with the disruption of the galaxy's outer stellar disk as a result of the accretion event. Using our deep, panoramic optical view of M63 with additional existing multiwavelength data, we describe the possible effects of such an accretion event in the larger picture of the parent galaxy.

Frank N. Bash Symposium 2011: New Horizons in Astronomy
October 9-11, 2011
Austin, Texas, USA

*This contribution includes data taken at The McDonald Observatory of The University of Texas at Austin.
†Following its presentation at this symposium, this research was published unabridged [1].
‡Speaker.

PoS(Bash11)023

1. Introduction

In the ΛCDM paradigm, the merging of dark matter halos drives the evolution of galaxies. In the present epoch, minor mergers, which often alter stellar disks and help build stellar halos from the inside-out, are expected to be common. The signatures of these interactions (such as heated disks, warps, and stellar tidal debris) should be visible for several Gyr. Recent cosmological simulations predict that most large spiral galaxies should show signs of minor interactions if observed to sufficient depth (e.g., $\mu_V \sim 30$ mag arcsec^{-2}) [2, 3]. Several Local Volume spirals display signatures of recent minor mergers and show striking qualitative agreement with the cosmological models [4]. Here, we present deep follow-up surface photometry of the outer regions of M63, a galaxy that displays clear evidence of a recent minor merger [1]. We aim to determine the basic properties of what remains of the progenitor satellite galaxy and study the effects of the accretion event on the parent system. M63 is an isolated, flocculent SA(rs)bc spiral. It is 7.2 Mpc distant, has a stellar mass of $\sim 8 \times 10^{10}\ M_\odot$ at < 40 kpc, displays a pronounced HI warp, and hosts a Type 1 extended UV (XUV) disk [5, 6].

2. Observations

We obtained 6.5 (5.33) hrs of total exposure through B (R) filters with the McDonald Observatory 0.8 m telescope and PFC imager ($46.2' \times 42.6'$ FOV at $1.354''$ px^{-1}). A detailed description of the data analysis can be found in [1]. Standard data reduction methods were employed. We utilize a row-by-row and column-by-column background fitting routine with low-order polynomials to adaptively fit and subtract the background. "Tertiary" SDSS standards in the target field were used for photometric calibration. We correct for Galactic extinction, which is uniform over the FOV to < 0.01 mag. Through an extensive estimation of uncertainties, we find that random noise is insignificant for a typical measurement while the background subtraction is the limiting systematic uncertainty. A measurement of a diffuse feature with $\mu_R = 26.0$ has an uncertainty of ± 0.1 mag arcsec^{-2}. Figure 1*a* shows the final R-band image. Also shown are our final data products: an R-band surface brightness map (1*b*) and a $B-R$ color index map (1*c*) for features with $23 \lesssim \mu_R \lesssim 27$.

3. The Stellar Stream

The most striking low surface brightness feature we observe is the coherent arc structure that reaches $R \approx 29$ kpc (in projection) from the center of M63 (see Figure 1). The arc is reminiscent of a "great-circle" stellar tidal stream that would result from a tidally disrupted satellite galaxy [2]. An ellipse fit to the light distribution displays a 14.8° tilt with respect to the inner disk isophotes. The FWHM of the stream's light distribution, w, is 3.3 kpc (in projection). The stream has an average $\mu_R = 26.1 \pm 0.1$ and $B-R = 1.5 \pm 0.2$ within the FWHM, the latter of which is consistent with an average S0 galaxy [7] and redder Local Group dwarfs [8]. It is also consistent with the $B-R$ color of the outer disk of M63 at the $\mu_R = 23.5$ isophote within the 1σ measurement uncertainty. In Figure 2, it can be seen that existing multiwavelength data shows that there is little to no HI gas ($< 0.10\ M_\odot$ pc^{-2}) or UV flux associated with the stellar stream. Along with the red $B-R$ color measured in this work, these data suggest that the stream is composed of an old stellar population.

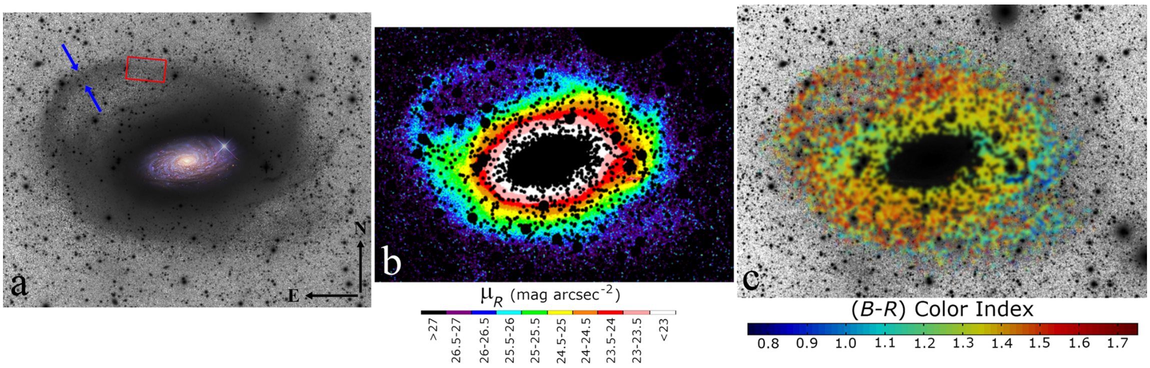

Figure 1: Optical data: **Panel *a*** - The final *R*-band image of M63. The directional arrows in the lower-right corner are $6'$ (12.6 kpc) long. The blue arrows indicate the location along the stream where w is measured. The red box indicates the location of a dim break in the stream that is ~ 1 mag arcsec^{-2} dimmer than the stream's average μ_R. A tri-color overlay of the M63 stellar disk is also shown [1]. **Panel *b*** - *R*-band surface brightness contour map derived from panel a for $23 \lesssim \mu_R \lesssim 27$. **Panel *c*** - $B-R$ color index map overlayed on the *R*-band image. Typical errors in $B-R$ are ± 0.2 mag for a feature with $\mu_R \approx 26$.

In addition to the coherent arc, we detect other low surface brightness features (see Figure 1). Some of these correspond to bright knots of UV flux associated with recent star formation in the XUV disk (see Figure 2*b*; all such features have $B-R < 1.1$). Several other faint features have red $B-R$ colors that are similar to the outer disk isophotes and stellar stream and appear asymmetric in an azimuthal manner about the inner stellar disk.

4. Discussion

• *Origin of the Faint Light Features* - We have presented data that make a strong case for the faint features around M63 being the result of an ongoing minor accretion event involving a satellite galaxy. The stream's morphology resembles the "great-circle" stellar streams in ΛCDM simulations [2, 3]. "Great-circle" streams that are still-bound result from recent accretion events (< 6 Gyr) where the progenitor is on an orbit with only mild eccentricity [2]. The stream's μ_R is among the brightest of those in the simulations [2], which suggests a very recent disruption of the progenitor satellite.

• *Fate of the Progenitor Dwarf* - Our data do not provide the current position or fate of a remaining bound core of the progenitor dwarf galaxy. It could be hidden behind or superposed on M63's stellar disk. While there are several faint features with redder $B-R$ colors that could be viable candidates, it is more likely that any remaining bound core is indiscernible in the stream since the core surface brightness decreases monotonically after the initial disruption.

• *Estimation of the Stream's Basic Dynamical Properties* - We estimate the current stream mass, m, and the time since the initial disruption, t, from the stream's morphological characteristics using the analytic framework of [9]. Assuming a near circular orbit and using R and w measured from our data along with $v_{circ}(R) \approx 180$ km s^{-1} [5], we find that $m \approx 3.5 \times 10^8\ M_\odot$. This is similar to several Local Group dSphs [8] and is consistent with the prominent satellites from $1 < z < 7$ that assemble stellar halos in the ΛCDM simulations [3]. The time since disruption depends linearly on Ψ, the stream's angular length; however, Ψ is not conclusive from our data. We thus use the

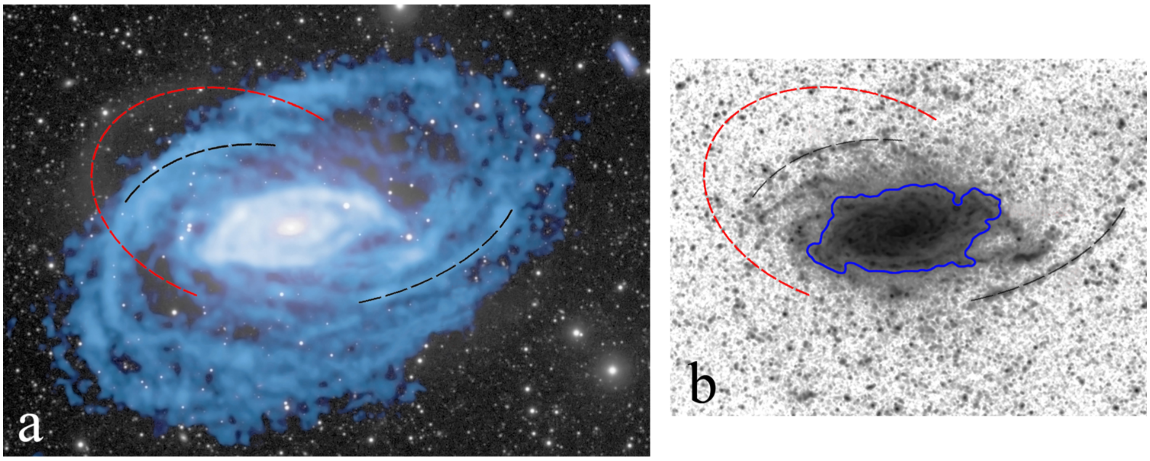

Figure 2: Multiwavelength data: **Panel *a*** - Comparison of the optical image (grayscale) with the distribution of HI gas (blue) at 67″ resolution [5]. The detection limit is 0.10 $M_\odot$ pc^{-2}. **Panel *b*** - Archival *GALEX* FUV+NUV image. The blue contour represents the $\mu_{FUV} = 27.25$ AB mag arcsec^{-2} isophote [6]. In both panels, the red dashed curve represents a segment of the stream ellipse fit. The black curve segments outline examples of features in the XUV disk that can be associated with HI spiral structure.

parameterization $\Psi = 2\pi\eta$ (where η is the number of wraps the stream makes around M63) so that $t \approx 1.8\eta$ Gyr. As an alternate estimation of m, we measure the stream's surface luminosity density Σ_R (in units of $L_{R\odot}$ pc^{-2}) and estimate a mass-to-light ratio, $\frac{m}{L_R}$, from the stream's $B-R$ color [10]. Using the results of the ellipse fit to the stream's light distribution, a sky projected area, A, is estimated (in units of pc^2). Using the η parameterization within A, we find that $m = \Sigma_R A(\frac{m}{L_R}) \approx (4 \pm 2)\eta \times 10^8$ $M_\odot$. Our data only clearly show a single coherent arc (i.e., $\eta \gtrsim 0.5$). The dim break in the otherwise coherent stellar stream (which may indicate the location of the ends of the leading and trailing tidal arms; see Figure 1*a*) as well as the color distribution about M63 (which is redder on the eastern half of the galaxy where possibly the stream is above M63's disk plane; see Figure 1*c*) possibly suggests only a single loop. If this situation is the case, $\eta \approx 1$, and the two estimations of m are subsequently in agreement. From our data, there is no evidence supporting additional stream wraps.

• *Effect on the Parent System* - The data hints at the inside-out formation of the stellar halo. The $B-R$ color similarity between the outer disk and the stream is consistent with recent ΛCDM simulations that show that a stellar halo after a typical minor merger can consist of a mixture of accreted stream stars *and* ejected disk stars [11]. This could homogenize the integrated color of the stars in the two structures. Several of the faint, redder, and azimuthally asymmetric features we detect could be stars ejected from the disk. These stars may eventually settle into a thick disk component. The accretion event could also be responsible for the large HI warp and the extended spiral structure in the HI disk [5] (see Figure 2*a*). The knots of star formation at large radii within these spiral arms that make up the XUV disk could also be caused by instabilities due to the ongoing accretion event [6] (see Figure 2*b*).

This research is a useful step in studying these elusive, yet important pieces of the galactic evolutionary and cosmological puzzles. Similar observations in statistically significant samples will provide an important test of the cosmological simulations that are based on the ΛCDM paradigm [4]. However, this work can only bring limited results, as sky projected stream morphologies and broad-band colors are not sufficient to fully constrain the dynamical and compositional properties of the stellar debris left over from the hierarchical evolutionary process. Future advancement in observational techniques and instrumentation will be needed to reasonably probe these extremely faint structures spectroscopically. This will better allow the use of stellar streams around external galaxies as probes of dark matter halos, as tools for studying the effect of minor mergers on galaxy evolution, and as a means of placing more stringent constraints on future cosmological simulations. Nevertheless, deep imaging of relatively isolated, Local Volume spiral galaxies has shown that their stellar halos still contain the relics from their hierarchical, inside-out formation. This presents a unique opportunity to be witnesses of one of the latest stages of galaxy evolution.

Acknowledgments

This work is partially supported by the Texas Norman Hackerman Advanced Research Program under grant 003658-0295-2007. We thank The McDonald Observatory and its staff for supporting the photometric observations. We acknowledge Ray Gralak for his contribution to the project, but whose data could not be included in this abbreviated proceeding.

References

[1] T.S. Chonis, D. Martínez-Delgado, R.J. Gabany, et al. *A Petal of the Sunflower: Photometry of the Stellar Tidal Stream in the Halo of Messier 63 (NGC 5055)*, 2011, *AJ*, 142, 166

[2] K.V. Johnston, J.S. Bullock, S. Sharma, et al. *Tracing Galaxy Formation with Stellar Halos. II. Relating Substructure in Phase and Abundance Space to Accretion Histories*, 2008, *ApJ*, 689, 936

[3] A.P. Cooper, S. Cole, C.S. Frenk, et al. *Galactic Stellar Haloes in the CDM Model*, 2010, *MNRAS*, 406, 744

[4] D. Martínez-Delgado, R.J. Gabany, K. Crawford, et al. *Stellar Tidal Streams in Spiral Galaxies of the Local Volume: A Pilot Survey with Modest Aperture Telescopes*, 2010, *AJ*, 140, 962

[5] G. Battaglia, F. Fraternali, T. Oosterloo, & R. Sancisi. *HI Study of the Warped Spiral Galaxy NGC 5055: a Disk/Dark Matter Halo Offset?*, 2006, *A&A*, 447, 49

[6] D.A. Thilker, L. Bianchi, G. Meurer, et al. *A Search for Extended Ultraviolet Disk (XUV-Disk) Galaxies in the Local Universe*, 2007, *ApJS*, 173, 538

[7] S. Barway, Y.D. Mayya, A.K. Kebhavi, & S.K. Pandey. *Multicolor Surface Photometry of Lenticular Galaxies. I. The Data*, 2005, *AJ*, 129, 630

[8] M. Mateo. *Dwarf Galaxies of the Local Group*, 1998, *ARA&A*, 36, 435

[9] K.V. Johnston, P.D. Sackett, & J.S. Bullock. *Interpreting Debris from Satellite Disruption in External Galaxies*, 2001, *ApJ*, 557, 137

[10] E.F. Bell & R.S. de Jong. *Stellar Mass-to-Light Ratios and the Tully-Fisher Relation*, 2001, *ApJ*, 550, 212

[11] C.W. Purcell, J.S. Bullock, & S. Kazantzidis. *Heated Disc Stars in the Stellar Halo*, 2010, *MNRAS*, 404, 1711

PROCEEDINGS OF SCIENCE

The Effects of Primordial Non-Gaussianity on Giant-Arc Statistics: A Scale-Dependent Example

Anson D'Aloisio[*a,b] **and Priyamvada Natarajan**[b,c]
[a]*Department of Astronomy & Texas Cosmology Center, University of Texas at Austin*
[b]*Department of Physics, Yale University*
[c]*Department of Astronomy, Yale University*

E-mail: anson@astro.as.utexas.edu, priyamvada.natarajan@yale.edu

In a recently published article, we quantified the impact of primordial non-Gaussianity on the probability of giant-arc formation. In that work, we focused on the local form of non-Gaussianity and found that it can have only a modest effect given the most recent constraints from Cosmic Microwave Background (CMB) measurements. Here, we present new calculations using a parameterization of scale-dependent non-Gaussianity in which the primordial bispectrum has the equilateral shape and the effective $f_{\rm NL}$ parameter depends on scale. We find that non-Gaussianity of this type can yield a larger effect on the giant-arc abundance compared to the local form due to both the scale dependence and the relatively weaker constraints on the equilateral shape from CMB measurements. In contrast to the maximum $\sim 40\%$ effect (within the latest CMB constraints) previously found for the local form, we find that the predicted giant-arc abundance for the scale-dependent equilateral form can differ by a factor of a few with respect to the Gaussian case.

Frank N. Bash Symposium New Horizons In Astronomy,
October 9-11, 2011
Austin Texas

[*]Speaker.

PoS(Bash11)025

The formation of giant arcs by strong gravitational lensing is reserved for the most massive collapsed structures whose statistical properties are sensitive to the expansion history and initial conditions of the Universe. Since the frequency of giant-arc formation depends on the abundance and characteristics of galaxy-clusters roughly half-way to the sources, it has long been recognized as a potentially rich source of information.

At the same time, the interplay between cosmological effects, cluster physics, and the source population makes their disentanglement non-trivial. The difficulties have been brought to light for over a decade following the initial claim of [1] that ΛCDM predicted approximately an order of magnitude fewer arcs than seen in observations. This claim stimulated a large amount of work towards understanding the most important characteristics of arc-producing clusters, how they may differ from the general cluster population, and the role of source characteristics in giant-arc production (see references in the introduction of [2]).

Despite such extensive efforts, the status of the giant-arc problem still remains unclear (see references in [2]). It is still possible that the cosmological model may have at least a partial role to play. Motivated by this fact, and the recent interest that structure formation with primordial non-Gaussianity (PNG) has received in the literature, we quantified the effects of PNG on the giant-arc abundance in [2]. Our work in [2] focused on a widely used parameterization of PNG - the local form (e.g. [3]) - in which the $f_{\rm NL}$ parameter is constant. Perhaps not surprisingly, we found that PNG of the local form can have only a modest effect within the most recent constraints from the Wilkinson Microwave Anisotrpy Probe (WMAP), which limit $-10 < f_{\rm NL} < 74$ at the 95% confidence level [4].

However, non-standard inflationary scenarios can lead to a scale-dependent $f_{\rm NL}$ which can have a larger impact on the scales relevant for galaxy cluster formation, while at the same time satisfying CMB and LSS constraints [5]. Here we extend our calculations in [2] to the parameterization proposed in [5], where the primordial bispectrum has the equilateral shape[6] and we make the replacement,

$$f_{\rm NL}^{\rm eq} \to f_{\rm NL}^{\rm eq}\left(\frac{k_1+k_2+k_3}{k_{\rm CMB}}\right)^{-2\kappa_{\rm NG}}. \tag{1}$$

From here on we refer to this parameterization as scale-dependent equilateral (SDE). In what follows, we will vary the exponent $\kappa_{\rm NG}$ in order to explore various scale-dependent examples, but we will assume a fixed pivot wavenumber $k_{\rm CMB} = 0.086h$ Mpc^{-1}, which approximately corresponds to the maximum multipole used in the WMAP year-seven analysis for constraining PNG [7]. The current WMAP 95% confidence limits for the equilateral shape are $-214 < f_{\rm NL}^{\rm eq} < 266$[4]. We will assume that these values also apply for the SDE case at the pivot scale, even though actual SDE constraints would likely be even weaker [5].

The probability for a background galaxy at redshift z_s to produce giant arcs is given by the optical depth [8],

$$\tau(z_s) = \int_0^{z_s} {\rm d}z \frac{{\rm d}V}{{\rm d}z} \int_{M_{\rm min}}^{\infty} {\rm d}M \, \frac{{\rm d}n}{{\rm d}M} \, \sigma_{\rm a}(M,z), \tag{2}$$

where $\sigma_{\rm a}$ is the giant-arc cross section[1], ${\rm d}V/{\rm d}z$ is the comoving volume element, ${\rm d}n/{\rm d}M$ is the halo mass function, and $M_{\rm min}$ is the minimum mass to produce giant arcs (see section 4.3 of [2] for a

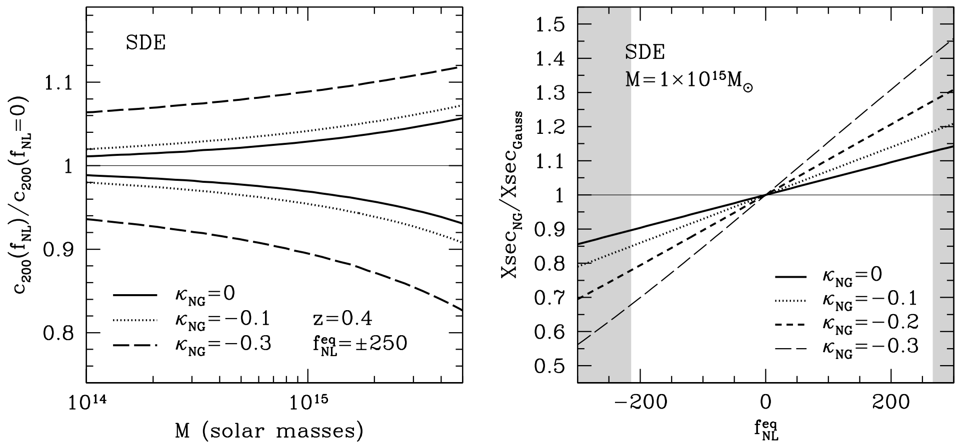

Figure 1: Left panel: the effect of SDE non-Gaussianity on mean halo concentrations. Right panel: resulting changes in giant-arc cross sections. We assume $z_l = 0.4$, $z_s = 1.82$, and $\varepsilon = 0.2$.

discussion).

As in [2], we focus on two potential ways that PNG can influence the giant arc frequency. First, PNG can affect the abundance of galaxy clusters, $\mathrm{d}n/\mathrm{d}M$, which would lead to a change in the number of supercritical lenses that are available in the appropriate redshift range. To take into account the effects of PNG on the cluster abundance, we use the mass function of [9], which is based on the form originally derived by [5] (also see [10]).

Secondly, PNG is expected to influence the central densities of halos through its effect on the timing of structure formation (see [2] and references therein). Consider two model universes: one with Gaussian initial conditions and the other with non-Gaussian initial conditions (with $f_{\mathrm{NL}} > 0$ for concreteness). In each universe, suppose we identified all halos with mass M at redshift z, and compared the two sets of halos. The set of halos in the universe where $f_{\mathrm{NL}} > 0$ would tend to have larger central densities compared to the Gaussian set. We turn to a simple heuristic argument to understand this effect. We may draw a rough correspondence between a halo with mass M and a point in the linearly extrapolated density field where the density fluctuation reaches a threshold for collapse, δ_c, when it is smoothed about that point on a scale corresponding to M. As the smoothing scale is decreased, the conditional probability that the density fluctuation makes upward excursions is larger for $f_{\mathrm{NL}} > 0$, relative to the Gaussian case, due to the enhanced tail of the conditional probability density function. Therefore, in the $f_{\mathrm{NL}} > 0$ case, one has to go to higher redshifts on average, relative to the Gaussian case, to reach the epoch at which the same fraction of the final mass was accumulated. Since the central density of a halo reflects the cosmic mean density at the epoch of its formation (e.g. [11]), we would therefore expect $f_{\mathrm{NL}} > 0$ to yield larger central densities on average, relative to the Gaussian case. A similar argument leads to the opposite conclusion for $f_{\mathrm{NL}} < 0$. In this case the formation epoch is delayed, and the central densities are lower.

[1]Note that we have utilized the approximation of [8] for σ_a. In this case, the cross section is in angular units. Note that the angular diameter distance to z_s does not appear in equation (2).

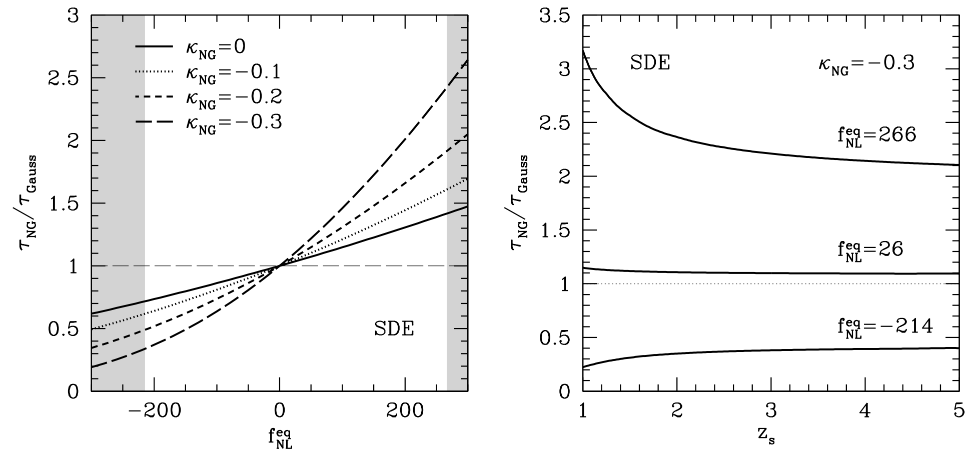

Figure 2: Relative changes in the giant-arc optical depth due to SDE non-Gaussianity. We assume $\varepsilon = 0.2$ and $\theta_{\rm min} = 10''$ (see [2] for a discussion of these parameters).

In [2] we used techniques introduced by [10] to quantify the above effects and the resulting changes in mean halo concentrations. Note that changes to central densities result in changes to the lensing cross sections, σ_a, and minimum mass threshold, $M_{\rm min}$, which appear in equation (2). Here, we extend our calculations to the SDE case. The left panel of Figure 1 shows the ratio of non-Gaussian to Gaussian mean halo concentrations as a function of mass. We use a fixed redshift $z = 0.4$, corresponding to the redshift of typical cluster lenses. The top and bottom set of curves correspond to $f_{\rm NL}^{\rm eq} = 250$ and $f_{\rm NL}^{\rm eq} = -250$ respectively. In the right panel of figure 1, we show the resulting changes to the giant-arc cross sections. The shading corresponds to $f_{\rm NL}^{\rm eq}$ values for the scale-independent equilateral shape excluded at the 95% level by the WMAP year seven analysis. We use a lens redshift of $z_l = 0.4$, $\varepsilon = 0.2$, which describes the ellipticity of the lensing potential (see section 4.2 of [2]), and a source redshift of $z_s = 1.82$, which is the median redshift observed in the Sloan Giant Arcs Survey [12].

The ratio of non-Gaussian to Gaussian giant-arc optical depths for $z_s = 1.82$ is shown in the left panel of Figure 2. The right panel of Figure 2 shows the ratio as a function of z_s. We note that the deviations from the Gaussian case in τ are due to the combined effects of modified central densities and halo abundance. For example, in the case with $f_{\rm NL}^{\rm eq} > 0$, central densities are enhanced *and* the abundance of large-mass halos is increased, which can boost the giant-arc optical depth substantially. Note that PNG of the SDE type can, within the latest CMB constraints, yield up to a factor of a few difference in the optical depth. Compare this to the maximum effect of a few tens of per cent found in [2] for the local form.

While our simple model allows us to quantify relative differences due to PNG, accurately predicting giant-arc abundances is well beyond the scope. However, we can use our model to get "back-of-the-envelope" estimates of what these changes imply in practice. For this task, we use a fixed dN_s/dz_s obtained from the observed galaxy redshift distribution in the Canada-France-Hawaii Telescope Legacy Survey [13], and the all-sky extrapolation of roughly 1000 arcs with length-to-width ratio ≥ 10 and R-band magnitudes < 21.5 [14, 1, 15]. If we assume that the theoretical prediction for the Gaussian model is of order ~ 1000 giant arcs, then the SDE non-Gaussian cases with $\kappa_{\rm NG} = -0.1$ and $f_{\rm NL}^{\rm eq} = 26(266)$ would predict 50(560) more giant arcs, whereas $f_{\rm NL}^{\rm eq} = -214$ would lead to 360 less. In the most extreme case considered here with $\kappa_{\rm NG} = -0.3$, $f_{\rm NL}^{\rm eq} = 26(266)$ would predict 100(1320) more giant arcs, while $f_{\rm NL}^{\rm eq} = -214$ would yield 640 less.

In summary, within the latest CMB constraints, PNG of the local type can alter the giant-arc abundance by a maximum of a few tens of percent [2]. In this work, we have shown that non-standard scenarios with other bispectrum shapes and scale-dependent $f_{\rm NL}$, such as the SDE model considered here, can modify the predicted giant-arc abundance by up to a factor of a few.

References

[1] M. Bartelmann, A. Huss, J. M. Colberg, A. Jenkins, and F. R. Pearce, *Arc statistics with realistic cluster potentials. IV. Clusters in different cosmologies*, 1998, A&A, 330, 1.

[2] A. D'Aloisio and P. Natarajan, *The effects of primordial non-Gaussianity on giant-arc statistics*, 2011, MNRAS, 415, 1913 (arXiv:1102.5097).

[3] E. Komatsu and D. N. Spergel, *Acoustic signatures in the primary microwave background bispectrum*, 2001, PRD, 63, 063002.

[4] E. Komatsu, K. M. Smith, J. Dunkley, C. L. Bennett, B. Gold, G. Hinshaw, N. Jarosik, D. Larson, and et al., *Seven-year Wilkinson Microwave Anisotropy Probe (WMAP) Observations: Cosmological Interpretation*, 2011, ApJS, 192, 18.

[5] M. Lo Verde, A. Miller, S. Shandera, and L. Verde, *Effects of scale-dependent non-Gaussianity on cosmological structures*, Journal of Cosmology and Astro-Particle Physics, 2008, 4, 14.

[6] P. Creminelli, A. Nicolis, L. Senatore, M. Tegmark, and M. Zaldarriaga, *Limits on non-Gaussianities from WMAP data*, 2006, JCAP, 5, 4.

[7] D. Crociani, L. Moscardini, M. Viel, and S. Matarrese, *The effects of primordial non-Gaussianity on the cosmological reionization*, MNRAS, 2009, 394, 133.

[8] M. Bartelmann, M. Meneghetti, F. Perrotta, C. Baccigalupi, and L. Moscardini, *Arc statistics in cosmological models with dark energy*, 2003, A&A, 409, 449.

[9] R. E. Smith, V. Desjacques, and L. Marian, *Nonlinear clustering in models with primordial non-Gaussianity: The halo model approach*, 2011, PRD, 83, 043526.

[10] M. Maggiore and A. Riotto, *The Halo Mass Function from Excursion Set Theory. III. Non-Gaussian Fluctuations*, 2010, ApJ, 717, 526.

[11] J. F. Navarro, C. S. Frenk, and S. D. M. White, *A Universal Density Profile from Hierarchical Clustering*, 2007, ApJ, 490, 493.

[12] M. B. Bayliss, M. D. Gladders, M. Oguri, J. F. Hennawi, K. Sharon, B. P. Koester, and H. Dahle, *The Redshift Distribution of Giant Arcs in the Sloan Giant Arcs Survey*, 2011, ApJ, 727, L26.

[13] L. Fu, E. Semboloni, H. Hoekstra, and et al., *Very weak lensing in the CFHTLS wide: cosmology from cosmic shear in the linear regime*, A&A, 2008, 479, 9.

[14] O. Le Fevre, F. Hammer, M. C. Angonin, I. M. Gioia, and G. A. Luppino, *Imaging of 16 distant EMSS clusters with Z greater than or equal to 0.2 and L(subx,44) greater than or equal to 4: New arcs and first consequences*, ApJ, 1994, 422, L5.

[15] N. Dalal, G. Holder, and J. F. Hennawi, *Statistics of Giant Arcs in Galaxy Clusters*, 2004, ApJ, 609, 50.

PoS(Bash11)025

PROCEEDINGS OF SCIENCE

The First Galaxies: Assembly with Black Hole Feedback

Myoungwon Jeon[*a], **Andreas H. Pawlik**[a], **Thomas H. Greif**[b], **Simon C. O. Glover**[c], **Volker Bromm**[a], **Miloš Milosavljević**[a], **and Ralf S. Klessen**[c]

[a]*Department of Astronomy and Texas Cosmology Center, University of Texas, Austin, TX 78712, USA*

[c]*Zentrum für Astronomie der Universität Heidelberg, Institut für Theoretische Astrophysik, Albert-Ueberle-Strasse 2, 69120 Heidelberg, Germany*

[b]*Max-Planck-Institut für Astrophysik, Karl-Schwarzschild-Strasse 1, 85740 Garching bei München, Germany*

E-mail: myjeon@astro.as.utexas.edu

We study how the first galaxies were assembled under feedback from the accretion onto a central black hole (BH) that is left behind by the first generation of metal-free stars through self-consistent, cosmological simulations. X-ray radiation from the accretion of gas onto BH remnants of Population III (Pop III) stars, or from high-mass X-ray binaries (HMXBs), again involving Pop III stars, influences the mode of second generation star formation. We track the evolution of the black hole accretion rate and the associated X-ray feedback starting with the death of the Pop III progenitor star inside a minihalo and following the subsequent evolution of the black hole as the minihalo grows to become an atomically cooling galaxy. We find that X-ray photoionization heating from a stellar-mass BH is able to quench further star formation in the host halo at all times before the halo enters the atomic cooling phase. X-ray radiation from a HMXB, assuming a luminosity close to the Eddington value, exerts an even stronger, and more diverse, feedback on star formation. It photoheats the gas inside the host halo, but also promotes the formation of molecular hydrogen and cooling of gas in the intergalactic medium and in nearby minihalos, leading to a net increase in the number of stars formed at early times. Our simulations further show that the radiative feedback from the first BHs may strongly suppress early BH growth, thus constraining models for the formation of supermassive BHs.

Frank N. Bash Symposium New Horizons In Astronomy,
October 9-11, 2011
Austin Texas

*Speaker.

 http://pos.sissa.it/

PoS(Bash11)026

1. Introduction

It has been a longstanding goal to understand the formation of the first galaxies subject to different accompanying feedback effects from the first stars, such as ionizing feedback from individual Pop III stars (e.g.,[1]; [2]), chemical feedback produced by a supernova (SN) explosion (e.g., [3]; [4]), and radiative feedback from accreting black holes (BHs) (e.g., [5]; [6]). The first stars are expected to form at a redshift $z \gtrsim 15$ inside dark matter minihalos with masses of $\sim 10^6 M_\odot$ (e.g., [7]; [8]). For progenitor masses within the range of $40\,M_\odot \lesssim M \lesssim 140\,M_\odot$ or $M \gtrsim 260\,M_\odot$, the Pop III star will become a massive BH via direct gravitational collapse. The ensuing merging of minihalos, provided they contain cold gas, and the smooth accretion of gas from the intergalactic medium (IGM) will feed the central BH. A fraction of the accreted mass-energy will then be released as radiative energy, resulting in a miniquasar (e.g., [9]; [10]), which will ionize the surrounding neutral medium and heat the pre-galactic gas.

We here briefly summarize our recent study ([11]), in which we investigated the feedback effects from such accreting stellar-mass BHs by focusing on the question: "How does a stellar black hole, a remnant of a Pop III star, influence the subsequent star formation and in turn the assembly process of the first galaxies?" Miniquasar feedback may also be expected to have important effects on BH growth. One outstanding question is how the supermassive black holes (SMBHs), observed by the *Sloan Digital Sky Survey* (SDSS) at $z \sim 6$ with masses of $\sim 10^9 M_\odot$ (e.g., [12]), were able to grow within such a short period of time after the Big Bang. A second goal of this study is to provide an improved understanding of whether a stellar BH can grow to become a SMBH in the presence of stellar and BH feedback.

2. Simulations

To survey the relevant parameter space, we have carried out three cosmological simulations. As a reference, simulation "BHN" includes stellar radiative feedback from Pop III stars, whereas the subsequent feedback due to BH accretion is not taken into account. The simulation "BHS" includes both the feedback from Pop III stars and from a single isolated BH. Finally, in simulation "BHB" we assume that the Pop III BH remnant has a stellar binary companion, giving rise to a HMXB.

For the simulations presented here, we use a customized version of the combined hydrodynamics and N-body code GADGET2 ([13]). We start running the simulations at $z \sim 30$, corresponding to the redshift just before the first Pop III star in the computational box is formed, and terminate them at $z \sim 10$, when the assembly of the first galaxy is expected to be complete. We propagate the ionization front around it to build up a primordial H II region, using a well-tested ray-tracing algorithm (for details see [14]). We follow Kuhlen & Madau (2005) ([5]) to model the propagation of high-energy photons emitted from the accretion onto a BH in which the accretion rate is estimated by the Bondi & Hoyle (1944) model (see [15]).

3. Results

In Figure 1, we show the evolution of the virial mass for the most massive halo, which will host the first galaxy at $z \sim 10$, as well as of the total and cold gas masses in the three simulations

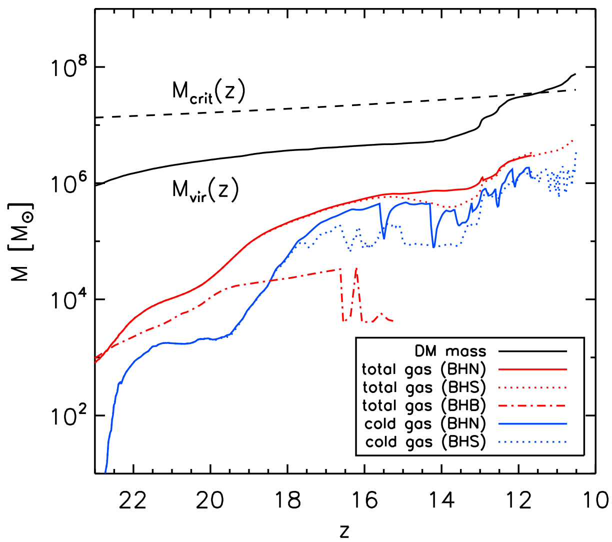

Figure 1: Assembly of the first galaxy. Shown is the redshift evolution of DM virial mass (*black solid line*) of the halo which will host the first galaxy at $z \sim 10$, as well as of the total gas mass (*red*) and the cold gas mass (*blue*) within the halo for simulations BHN (*solid lines*), BHS (*dotted lines*), and BHB (*dot-dashed line*). The black dashed line represents the critical mass required for the onset of atomic cooling in the halo at a given redshift. There is no cold gas within the halo in simulation BHB owing to the strong heating from the HMXB.

presented in this work. We find that at $z \gtrsim 18$, the halo is dominated by hot gas, exceeding the amount of cold gas by an order of magnitude. As time passes on, the cold gas mass increases, eventually accounting for $\gtrsim 80\%$ of the total gas mass in simulations BHN and BHS. This trend can be understood by the vulnerability of the halo gas to stellar radiative feedback. The corresponding evacuation of gas from the halo is very strong at high redshifts, $z \gtrsim 18$, because the halo potential wells were not yet deep enough to retain photo-heated gas.

While the total amount of gas is not sensitive to the BH feedback, the reduction in cold gas mass by a factor of ~ 5 indicates that the additional heating from this feedback, on top of the stellar feedback, has a significant impact on the gas in the center of the forming galaxy. As the halo grows further via smooth accretion and mergers with minihalos, however, at $z \sim 13$, both the total gas mass and mass of cold gas are no longer sensitive to the BH radiative feedback.

For simulation BHB, the heating from the HMXB is so strong that all gas particles have temperatures $T > 0.5\, T_{\rm vir}(z)$, over the entire range of simulated redshifts $z \gtrsim 15$, and the total gas mass is reduced by nearly an order of magnitude by photo-evaporation, as is evident from Figure 1 (see the dot-dashed lines). This implies that if an HMXB existed within a minihalo at high redshifts, it would take significantly longer for the halo to reassemble the lost gas, and to eventually evolve into a primordial galaxy.

Figure 2 shows the evolution of the accretion rate onto the BH, the density and temperature of the neighboring gas, as well as the BH mass for simulations BHN and BHS. The accretion rate

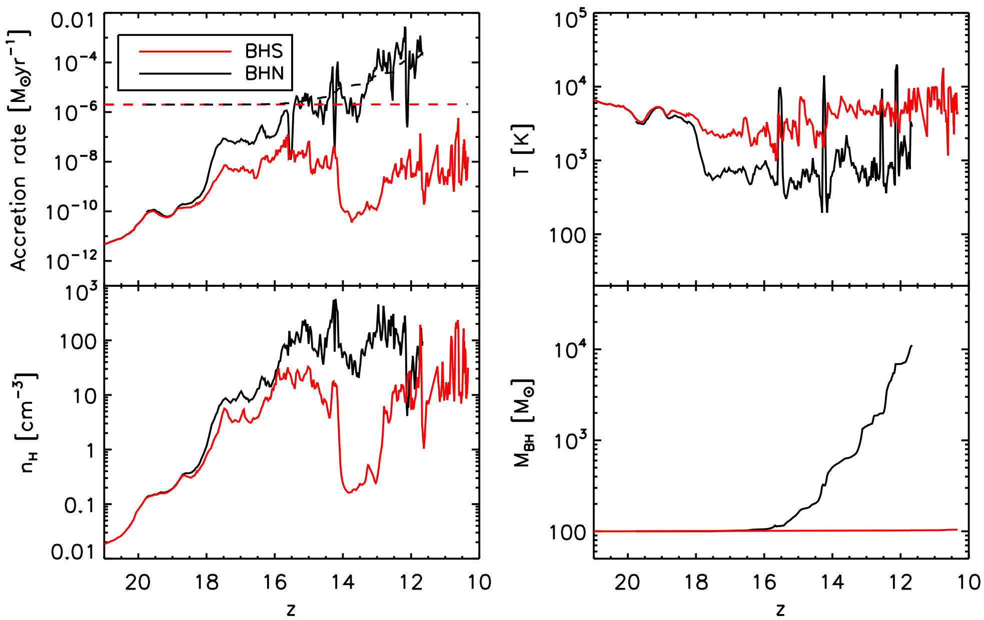

Figure 2: BH growth with and without feedback. Shown is the redshift evolution of the BH accretion rate, the density and the temperature of the gas in the immediate vicinity of the BH, as well as the resulting BH masses for simulations BHN (*black*) and BHS (*red*). In the top-left panel, we also indicate the corresponding Eddington-limited accretion rates for the two cases (*dashed lines*).

in the BHN simulation is already comparable to the Eddington value, depicted as dashed lines in Figure 2 (top-left panel), at $z \sim 15.5$, while it is still an order of magnitude lower in the BHS case. Occasionally, star formation takes place very close to the BH, e.g., ~ 1 kpc away at $z \sim 14$. The radiative feedback from this event acts to compound the heating effect from the BH accretion, thus rendering the removal of gas out of the shallow potential well more effective.

The combined stellar and BH radiative feedback results in an accretion rate that is on average 4 orders of magnitude below the Eddington value at $z = 14 - 13$. Even 300 Myr after BH formation, the mass of the BH has increased by only 1.5 % in the BHS simulation, whereas it has grown by two orders of magnitude in the BHN case. This indicates that the feedback from a stellar-mass BH is sufficiently strong to prevent significant growth, suggesting a very important constraint on SMBH formation scenarios. We infer that the radiative feedback from an accreting BH might be partly responsible for the low density of quasars at redshifts $z \sim 6$, by suppressing early BH growth.

4. Conclusions

We have studied how the assembly of a primordial galaxy is affected by the radiative feedback from an accreting, isolated stellar-mass BH and an HMXB, which are two possible end products of Pop III star formation. To accomplish this, we have carried out three cosmological simulations which self-consistently account for the radiation from individual Pop III stars, and from a central BH X-ray source.

We have shown that locally the feedback from an isolated, accreting BH is very efficient, leading to a strong suppression of the early growth of the seed BH. Without such feedback, the growth rate quickly reaches near-Eddington values. We suggest that the radiative feedback from accreting BHs plays a key role in suppressing early BH growth, thus constraining models for SMBH formation.

The feedback from an efficiently radiating HMXB is very strong locally, and moderately important globally. Locally, the effect on the surrounding primordial gas is to heat it to high temperatures of $\gtrsim 10^4$K, and to fully ionize it. The corresponding strong photo-evaporative outflow suppresses central gas densities, thus preventing any subsequent star formation within the emerging galaxy. Our results imply that once a halo of $\sim 10^6 M_\odot$ harbors an HMXB, the ensuing strong radiative feedback will delay the condensation of gas in the atomic cooling halo, possibly leading to a decrease in the number of first galaxies at a given epoch.

References

[1] Ricotti, M., Gnedin, N. Y., & Shull, J. M., *The Fate of the First Galaxies. II. Effects of Radiative Feedback*, 2002, ApJ, 575, 49

[2] Abel, T., Wise, J. H., & Bryan, G. L., *The H II Region of a Primordial Star*, 2007, ApJL, 659, L87

[3] Greif, T. H., Glover, S. C. O., Bromm, V., & Klessen, R. S., *The First Galaxies: Chemical Enrichment, Mixing, and Star Formation*, 2010, ApJ, 716, 510

[4] Wise, J. H., Turk, M. J., Norman, M. L., & Abel, T., *The Birth of a Galaxy: Primordial Metal Enrichment and Stellar Populations*, 2012, ApJ, 745, 50

[5] Kuhlen, M., & Madau, P., *The first miniquasar*, 2005, MNRAS, 363, 1069

[6] Alvarez, M. A., Wise, J. H., & Abel, T., *Accretion onto the First Stellar-Mass Black Holes*, 2009, ApJL, 701, 133

[7] Haiman, Z., Thoul, A. A., & Loeb, A., *Cosmological Formation of Low-Mass Objects*, 1996, ApJ, 464, 523

[8] Yoshida, N., Abel, T., Hernquist, L., & Sugiyama, N., *Simulations of Early Structure Formation: Primordial Gas Clouds*, 2003, ApJ, 592, 645

[9] Ricotti, M., & Ostriker, J. P., *X-ray pre-ionization powered by accretion on the first black holes - I. A model for the WMAP polarization measurement*, 2004, MNRAS, 352, 547

[10] Madau, P., Rees, M. J., Volonteri, M., Haardt, F., & Oh, S. P., *Early Reionization by Miniquasars*, 2004, ApJ, 604, 484

[11] Jeon, M., et al., *The First Galaxies: Assembly with Black Hole Feedback*, ApJ submitted (arXiv:1111.6305)

[12] Fan, X. et al., *A Survey of z > 5.7 Quasars in the Sloan Digital Sky Survey. IV. Discovery of Seven Additional Quasars*, 2006, AJ, 131, 1203

[13] Springel, V., *The cosmological simulation code GADGET-2*, 2005, A&A, 364, 1105

[14] Greif, T. H., Johnson, J. L., Klessen, R. S., & Bromm, V., *The first galaxies: assembly, cooling and the onset of turbulence*, 2009, MNRAS, 399, 639

[15] Bondi, H., & Hoyle, F., *On the mechanism of accretion by stars*, 1944, MNRAS, 104, 273

PROCEEDINGS OF SCIENCE

The Hunt for the First Supernovae: The Source Density and Observability of Pair-Instability Supernovae from the First Stars

Jacob A. Hummel*, **Andreas H. Pawlik, Miloš Milosavljević, and Volker Bromm**
Department of Astronomy and Texas Cosmology Center, The University of Texas at Austin
E-mail: jhummel@astro.as.utexas.edu

Some of the first stars are expected to have died as extremely energetic pair-instability supernovae (PISNe). With energies approaching 10^{53} ergs, these supernovae are expected to be within the detection limits of the upcoming *James Webb Space Telescope* (JWST), allowing us to constrain the properties of these objects for the first time. We estimate the source density of PISNe using a semi-analytic Press-Schechter based approach informed by cosmological simulations including feedback from star formation. We find that the main obstacle to detecting PISNe is their scarcity, not their brightness; exposures longer than a few times 10^4 s will do little to increase the number of PISNe found. Given this we suggest a mosaic style search strategy for detecting PISNe from the first stars. Even fairly high redshift PISNe are sufficiently bright to be found with moderately deep exposures. However, a large number of pointings will be required to ensure a detection due to their scarcity. For an observing program totalling 10^6 s, the probability of a detection is maximized by dividing the campaign into $\sim$150 individual fields with a $\sim$5000 s exposure in each.

Frank N. Bash Symposium New Horizons In Astronomy,
October 9-11, 2011
Austin Texas

*Speaker.

PoS(Bash11)027

1. Introduction

Following the launch of the upcoming *James Webb Space Telescope* (JWST) we will be able to probe the epoch of the first stars with unprecedented detail [1]. These so-called Population III (Pop III) stars formed in 10^5–$10^6\,M_\odot$ dark matter 'minihalos' at high redshifts and were predominantly very massive (e.g., [2, 3]). Recent work has revised this picture somewhat. Significant fragmentation likely occurred in the primordial gas clouds from which the first stars were born, lowering their characteristic masses from $100\,M_\odot$ to nearer $50\,M_\odot$, with a much broader initial mass function and significant rotation expected as well [4, 5, 6]. While the first stars themselves are unlikely to be visible [7], it is possible that some of the first stars died as pair-instability supernovae (PISNe). Non-rotating stars in the range 140–$260\,M_\odot$ are expected to die as PISNe, undergoing a pair-production instability following core oxygen burning to explode completely. These extremely energetic explosions—approaching a total energy of 10^{53} ergs—will be within the detection limits of the JWST [8, 9]. It has recently been found that the inclusion of rotation can significantly alter the initial mass required for a star to meet this fate, lowering the minimum mass required to encounter the pair-production instability to as little as $65\,M_\odot$ for the most rapidly rotating models [10]. While the basic properties of PISNe and the effect they have on their environment has been well studied, the source density of these events has yet to be well constrained. Our work complements previous investigations of the PISN rate (e.g., [9, 11, 12, 13, 14]) by including an extended discussion of the effects of feedback from star formation on the PISN rate, considering Lyman-Werner (LW) feedback and chemical feedback. We describe here our semi-analytic model for the PISN rate and assess the ability of the JWST to detect PISNe from the first stars. For further details see Hummel et al. [15], on which this work is based.

2. The PISN Rate

It is reasonable to assume that at most one PISN will occur per minihalo. PISNe are produced only by very massive stars. After the first star forms, photoionization quickly suppresses the density of the remaining gas, effectively halting star formation in the minihalo. The energy released by the first PISN disperses the gas in the halo, delaying star formation until the gas is able to recondense into more massive halos. While star formation resumes at this point, the gas in these systems will likely be enriched beyond the critical metallicity for Pop II star formation. As a result, the stars that form will no longer be large enough to reliably produce PISNe. Assuming the time required for the progenitor star to form, live and die is negligible, the formation rate of minihalos serves as a robust upper limit for the PISN rate. To quantify this, we assume exactly one PISN per minihalo [15], forming as soon as the halo exceeds the critical mass required for star formation. We then use the analytic Press-Schechter (PS) formalism for structure formation [16] to calculate the number density $n_{\rm PS}$ of critical mass minihalos at redshift z, estimating their formation rate $\dot{n}_+(z)$ using the expression derived by [17]. The resulting rate can be seen in Figure 1b.

Stellar feedback will suppress Pop III star formation in some minihalos and completely halt it in others, reducing the PISN rate. The feedback mechanisms responsible for this include the build-up of a background of H_2 dissociating LW photons and chemical feedback polluting the gas with metals, halting Pop III star formation. These feedback mechanisms can be represented by distinct efficiency factors $\eta(z)$, such that the true PISN rate, $\dot{n}_{\rm PISN}$, will be given by $\dot{n}_{\rm PISN}(z) = \eta_{\rm chem}(z)\,\eta_{\rm LW}(z)\,\dot{n}_{+}(z)$. To asses the impact of LW feedback we employ a set of two cosmological simulations. The first simulation we employ is similar to simulation *Z4* presented in [7]. This simulation follows the assembly of a galaxy in a halo reaching a mass of $\sim 10^9\,M_\odot$ at $z = 10$, including star formation but ignoring the associated feedback. The second simulation differs only in the inclusion of LW feedback. Determining the critical mass for star formation with and without LW feedback, the efficiency of LW feedback, $\eta_{\rm LW}$, can then be expressed as the ratio of the formation rate of minihalos at the critical mass with LW feedback to that without. The resulting efficiency factor $\eta_{\rm LW}$ is shown in Figure 1a, and the LW modulated PISN rate in Figure 1b. Once the critical mass reaches the atomic cooling threshold at $z \sim 12$, LW feedback is no longer efficient. The

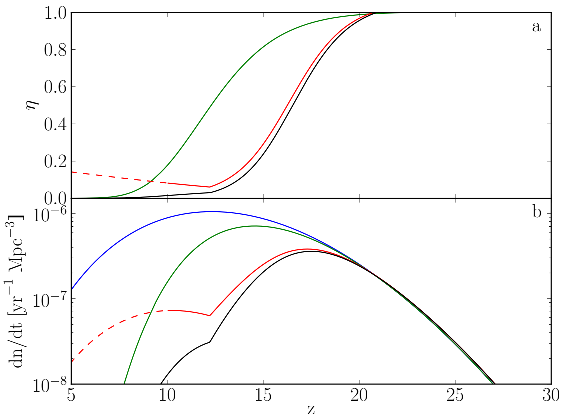

Figure 1: a) Evolution of the feedback efficiency factors η as a function of redshift. $\eta_{\rm chem}$ is shown in green and $\eta_{\rm LW}$ in red; $\eta_{\rm tot} \equiv \eta_{\rm chem}\eta_{\rm LW}$ is shown in black. The feature at $z \sim 12$ is due to the critical mass reaching the atomic cooling threshold. **b)** The PISN rate in the upper limit of no feedback (blue), with chemical feedback (green), LW feedback (red) and the final predicted PISN rate (black).

process of chemical enrichment is another crucial factor for determining the PISN rate. Gas that has been enriched beyond a critical metallicity of $Z_{\rm crit} \sim 10^{-4}\,Z_\odot$ will no longer form Pop III stars [18], and hence no PISNe. The effects of chemical feedback can thus be evaluated by computing the fraction of halos forming from pristine gas at a given redshift. In modeling $\eta_{\rm chem}$, we use the results of Furlanetto & Loeb [19]. Their semi-analytic treatment of SN winds yields a probability function $P_{\rm pristine}(z)$ that the gas in a newly formed halo is pristine. We identify this quantity as the fraction of newly collapsed halos polluted with metals, $\eta_{\rm chem}$. Given the recent detection of pristine gas at $z = 3$ by [20], we choose the weakest feedback scenario presented. The selected $\eta_{\rm chem}$ can be seen in Figure 1a, and the resulting PISN rate in Figure 1b.

3. JWST Observability

To determine the observability of PISNe at high redshifts we consider a representative case, that of the 250 $M_\odot$ PISN model presented in [21]. Given the large mass ejected, the ejecta will remain optically thick until late times, so we make the reasonable assumption that the PISN emits as a blackbody for the majority of its visible lifetime. The resulting lightcurves as they would appear at various redshifts are shown in the left panel of Figure 2. For further details see [15].

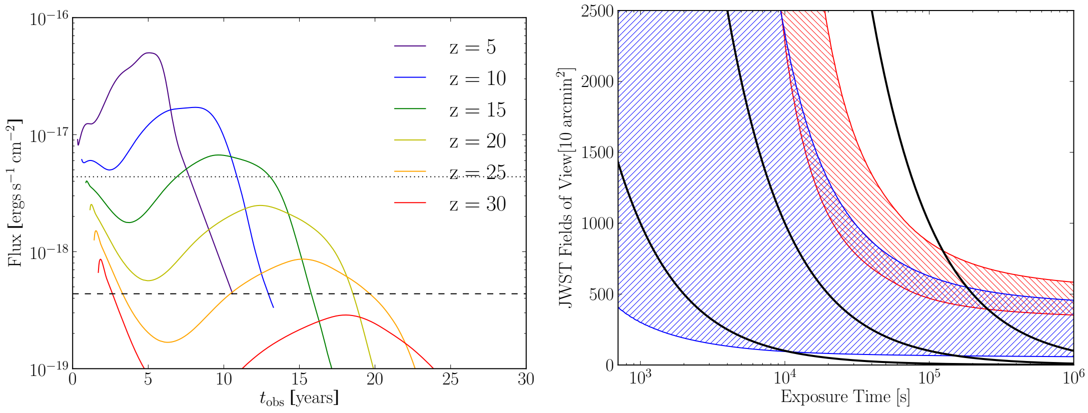

Figure 2: Left: Lightcurves for the PISN model as it would be observed by JWST's F444W NIRCam filter at $z = 5, 10, 15, 20, 25$ and 30. The flux limits for a 10^6 s (dashed line) and 10^4 s (dotted line) are shown for reference. **Right:** The observability of PISNe using the JWST's NIRcam F444W filter. Shown are the lower and upper limits for the number of JWST FoVs required to detect 10 sources as a function of exposure time. The blue range denotes the limits for PISNe from all redshifts, and the red for PISNe from $z > 15$. The lower limits of the ranges correspond to the no-feedback upper limit to the PISN rate and the upper limits to the rate derived with feedback. From bottom to top, the black lines represent the number of pointings possible in a total of 10^6 s, 10^7 s and 10^8 s.

4. Discussion and Conclusions

We conclude that the limiting factor in detecting PISNe will be the scarcity of sources rather than their faintness, in agreement with the results of [12]. PISNe should be readily detectable out to $z \sim 20$, but beyond a moderate exposure time of a few times 10^4 s their observability is controlled almost completely by the source density—approximately one PISN per 5 JWST fields of view (FoVs) above $z = 10$, and dropping off quickly beyond $z \sim 15$. This is clear from the right panel of Figure 2, where we have shown the number of JWST FoVs required to detect 10 PISNe (in blue) as a function of exposure time. Even for only high-redshift sources ($z > 15$, in red) the dependence on exposure time is minimal, being controlled by the lack of sources. While the detection of a PISN from a 'first' star at very high redshifts would be exciting and is in fact possible given the detection limits of the JWST, the scarcity of sources at these redshifts means that such a detection would be contingent on serendipity. The detection of a PISN at lower redshifts however appears to be within the realm of possibility. In this case, the strategy with the highest likelihood of detection will be a mosaic survey consisting of approximately 150 pointings to a depth of ~5000 s.

Acknowledgments

V.B. and M.M. acknowledge support from NSF grants AST-0708795 and AST-1009928 and NASA ATFP grant NNX09AJ33G. V.B. thanks the Max-Planck-Institut für Astrophysik for its hospitality during part of the work on this paper. The simulations were carried out at the Texas Advanced Computing Center (TACC).

References

[1] Gardner, J. P., et al., *The James Webb Space Telescope*, 2006, Space Sci. Rev. 123, 485

[2] Bromm, V., Coppi, P. S. & Larson, R. B. *Forming the first stars in the universe: The fragmentation of primordial gas*, 1999, ApJL 527, L5

[3] Abel, T., Bryan, G. L. & Norman, M. L. *The formation of the first star in the Universe*, 2002, Science 295, 93

[4] Stacy, A., Greif, T. H. & Bromm, V. *The first stars: formation of binaries and small multiple systems*, 2010, MNRAS 403, 45

[5] Clark, P. C. et al. *The formation and fragmentation of disks around primordial protostars*, 2011, Science 331, 1040

[6] Greif, T. H. et al. *Simulations on a Moving Mesh: the Clustered Formation of Population III Protostars*, 2011, ApJ 737, 75

[7] Pawlik, A. H., Milosavljević, M. & Bromm, V. *The First Galaxies: Assembly of Disks and Prospects for Direct Detection*, 2011, ApJ 731, 54

[8] Heger, A., Fryer, C. L., Woosley, S. E., Langer, N. & Hartmann, D. H. *How massive single stars end their life*, 2003, ApJ 591, 288

[9] Scannapieco, E., Madau, P., Woosley, S. E., Heger, A. & Ferrara, A. *The Detectability of Pair-Production Supernovae at* $z \lesssim 6$, 2005, ApJ 633, 1031

[10] Chatzopoulos, E. & Wheeler, J. C. *Effects of Rotation on the Minimum Mass of Primordial Progenitors of Pair Instability Supernovae*, 2012, ApJ, in press (arXiv:1201.1328v2)

[11] Mackey, J., Bromm, V. & Hernquist, L. *Three epochs of star formation in the high-redshift Universe*, 2003, ApJ 586, 1

[12] Weinmann, S. M. & Lilly, S. J. *The Number and Observability of Population III Supernovae at High Redshifts*, 2005, ApJ 624, 526

[13] Wise, J. H. & Abel, T. *The Number of Supernovae from Primordial Stars in the Universe*, 2005, ApJ 629, 615

[14] Trenti, M., Stiavelli, M. & Michael Shull, J. *Metal-Free Gas Supply at the Edge of Reionization: Late-Epoch Population III Star Formation*, 2009, ApJ 700, 1672

[15] Hummel, J., Pawlik, A., Milosavljevic, M. & Bromm, V. *The Source Density and Observability of Pair-Instability Supernovae from the First Stars*, 2011, ApJ, submitted (arXiv:1112.5207)

[16] Press, W. H. & Schechter, P. *Formation of Galaxies and Clusters of Galaxies by Self-Similar Gravitational Condensation*, 1974, ApJ 187, 425

[17] Sasaki, S. *Formation Rate of Bound Objects in the Hierarchical Clustering Model*, 1994, PASJ 46, 427

[18] Schneider, R., Ferrara, A., Natarajan, P. & Omukai, K. *First Stars, Very Massive Black Holes, and Metals*, 2002, ApJ 571, 30

[19] Furlanetto, S. R. & Loeb, A. *Is Double Reionization Physically Plausible?* 2005, ApJ 634, 1

[20] Fumagalli, M., O'Meara, J. M. & Prochaska, J. X. *Detection of Pristine Gas Two Billion Years After the Big Bang*, 2011, Science 334, 1245

[21] Kasen, D., Woosley, S. E. & Heger, A. *Pair Instability Supernovae: Light Curves, Spectra, and Shock Breakout*, 2011, ApJ 734, 102

PROCEEDINGS OF SCIENCE

The VIRUS-P Investigation of the eXtreme Environments of Starbursts (VIXENS): Survey and First Results

Amanda Heiderman[∗,1], **Neal J. Evans II**[1], **Karl Gebhardt**[1], **Guillermo Blanc**[2], **Timothy A. Davis**[3], **Casey Papovich**[4], **Daisuke Iono**[5] **and Min Yun**[6]

[1]*University of Texas at Austin Department of Astronomy 1 University Station, C1400 Austin, Texas 78712-0259*
[2]*Observatories of the Carnegie Institution 813 Santa Barbara Street Pasadena, California 91101*
[3]*ESO Karl-Schwarzschild-Strasse 2 D-85748 Garching bei München*
[4]*Texas A&M University Department of Physics and Astronomy College Station, TX 77843-4242*
[5]*Nobeyama Radio Observatory, NAOJ Minamimaki, Minamisaku, Nagano, 384-1305, Japan*
[6]*Department of Astronomy University of Massachusetts Graduate Research Tower B 619E 710 North Pleasant Street Amherst, MA 01003-9305*
E-mail: alh@astro.as.utexas.edu

The VIXENS project is an integral field unit (IFU) survey of 15 nearby infrared bright ($L_{IR} > 3 \times 10^{10} L_{\odot}$) starburst/interacting galaxies, chosen to cover a range of interaction stages (from early to late phase mergers), star formation rates, and gas surface densities. The main goal of VIXENS is to investigate the relation between the star formation rate (SFR) and gas surface densities on spatially resolved scales of 0.2-0.9 kpc by comparing various tracers of star formation and gas content. More specifically, we use the Hα from our IFU data, 24μm, and far-UV data to investigate star formation and archival CO and HI maps, as well as maps of dense gas as traced by HCN(1–0). VIXENS will provide 2D maps of ionized gas, SFRs, stellar and gas kinematics, and metallicities. This unique data set will enable us to test theoretical predictions at the high star formation rate and gas surface density regime of the Kennicutt-Schmidt relation.

Frank N. Bash Symposium 2011: New Horizons in Astronomy
October 9-11, 2011
Austin, Texas, USA

∗Speaker.

1. Introduction

A detailed understanding of the rate at which molecular gas is converted into stars is an essential prerequisite for models of galaxy formation and evolution. In fact, this rate, and the parameters that cause it to vary, are currently ill constrained, leading to large uncertainties in theoretical models of galaxy formation. This presents an observational need for a robust determination of the relation between star formation rate (SFR) and the amount of available dense molecular gas. Our focus is to explore the evolution of the rate at which molecular gas is converted into stars through detailed IFU spatially resolved observations of gas-rich nearby interacting galaxies.

Measuring the spatially resolved star formation efficiency in nearby starburst/ interacting galaxies has direct implication at high-z, where such galaxies play and increasing role in the total SFR density e.g., [13]. Recent work by [9] and [7] found a bi–modal relationship between the SFR and gas surface densities for high-z merging galaxies and normal disk galaxies (Figure 3). The high-z mergers [9] lie along the same relation as Galactic low- and high-mass star-forming regions [11], suggesting that the bulk of gas in merging systems traces star forming gas. While starburst and interacting galaxies are relatively rare in the low-z universe, they are the dominant mode of star formation in the distant universe. Understanding the physics of star formation in nearby interacting/starburst systems is therefore paramount and will provide key insight to the physical processes of star formation in high-z interacting galaxies.

Observations of many galaxies on global or disk-averaged scales have been fit to a power law of N = 1.4 [15]. Recently, this proposed SFR-gas relation has been studied on ∼kpc scales in nearby spiral galaxies where a deviation from the N = 1.4 Kennicutt power law is found e.g., [4, 17]. While some work has been done on the integrated emission SFR-gas relation in extreme star-forming environments [10], such as those in local (ultra)luminous infrared (IR) galaxies, ((U)LIRGs) [18], there has been little work done studying the spatially-resolved relation between the SFR and gas surface densities in extreme environments such as the triggered starbursts in interacting galaxies. The VIXENS observational program will provide the required constraints on theoretical models for galaxy evolution as well as a comparison sample for multiwavelength observational studies of high-z interacting galaxies.

2. The Survey

The VIRUS-P Investigation of the eXtreme Environments of Starbursts (VIXENS)[1] project is a large IFU survey of 15 nearby IR bright ($L_{IR} > 3 \times 10^{10} L_{\odot}$) interacting/starburst galaxies selected on carefully chosen criteria: (1) IRAS IR derived SFRs $\sim 5 - 280\ M_{\odot}\ \mathrm{yr}^{-1}$, and molecular hydrogen gas surface densities, $\Sigma_{\mathrm{H_2}} \sim 200 - 10^4\ M_{\odot}\ \mathrm{pc}^{-2}$ from ^{12}CO maps, (2) because star formation is crucially affected by the state of galaxy interactions [16], the sample is selected to include the full range of interaction stages with morphological signatures that range from early stage (close pairs) to late stage mergers (single system with multiple nuclei) and implied mass ratios $1/3 < M_1/M_2 \leq 1/1$ estimated from optical luminosity ratios. The latter requirement is justified because simulations suggest that the interaction stage significantly impacts the galaxies' evolution as seen in optical and HI imaging [3,14 and references therein], and (3) the availability of ancillary data sets, which include: archival *Spitzer* 24 μm, GALEX far-UV, and existing ^{12}CO(1–0) and HI maps. In

[1] http://www.as.utexas.edu/~alh/vixens.html

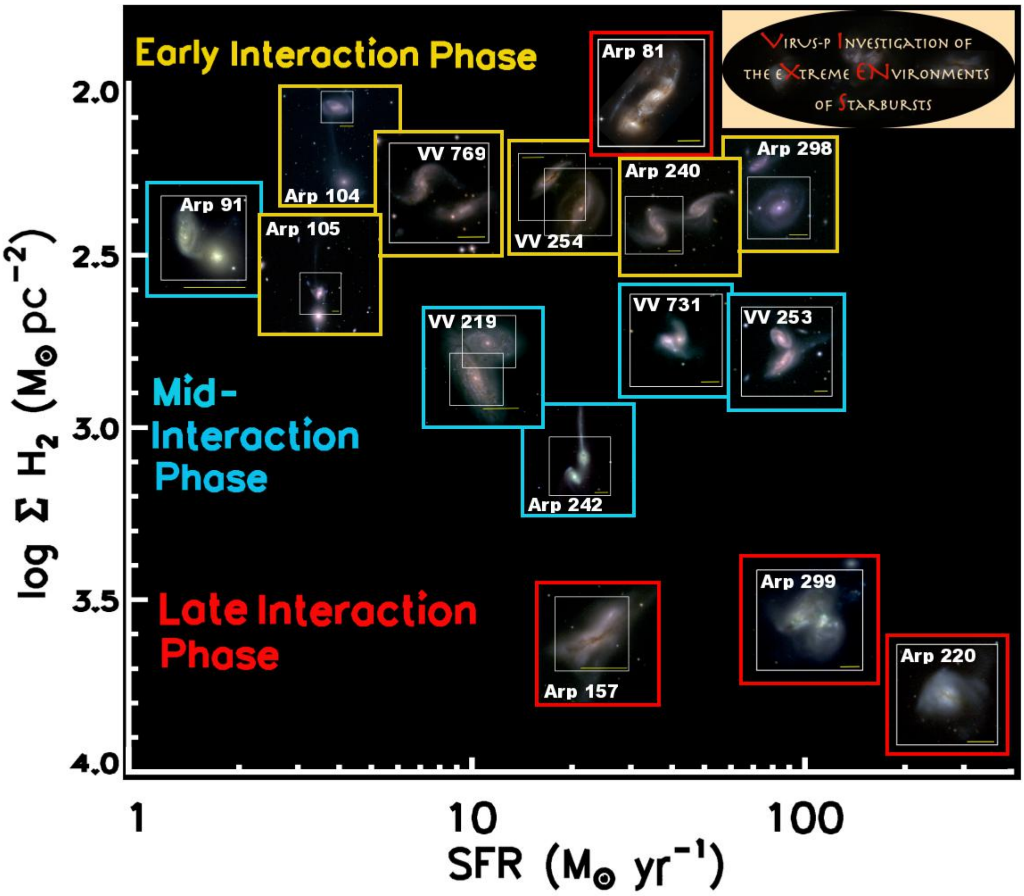

Figure 1: SDSS RGB (i,r,g) images of the VIXENS interacting galaxy sample. The white boxes show the VIRUS-P IFU field of view ($1.7' \times 1.7'$) and the yellow lines indicate a scale of 10 kpc. The range of total molecular hydrogen gas surface densities estimated from CO maps and SFRs from IRAS are shown.

addition to these archival data sets, we are also obtaining single-dish dense gas tracers (HCN(1–0), HCO^+(1–0), HNC(1–0)) from Nobeyama 45-m and IRAM 30-m telescopes for our whole sample, as well as HCN(1–0) maps for a subset of our sample from CARMA. Figure 1 shows SDSS RGB (i,r,g) images of the VIXENS sample with the exception of Arp 81, which instead shows an *HST* color image as this galaxy is not covered by the SDSS.

VIXENS uses the VIRUS-P spectrograph on the 2.7-m Harlan J. Smith telescope at McDonald Observatory. VIRUS-P has a field of view of $1.7' \times 1.7'$, and has 246 $4.3''$ optical fibers and a 1/3 filling factor for which three dithers provide contiguous coverage. One VIRUS-P pointing covers each system with the exception of VV 219 and VV 254 in which two pointings were necessary (Figure 1). The spectra cover each object in the wavelength range 4600 Å-6800 Å and have a spectral resolution of 5 Å FWHM ($\sigma_{\rm inst} \sim$120 km s^{-1}). The VIXENS IFU data will provide 2D maps of ionized gas, SFRs, stellar and gas kinematics, and metallicities.

VIRUS-P data reduction is done using VACCINE [2]. Spectral analysis, including measurement of gas and stellar kinematics as well as emission line fitting, is performed using PARADA, a modified version of the GANDALF software [19], which includes an implementation of the Penalized Pixel-Fitting method (pPXF) [6]. Figure 2 shows VIXENS data products linearly interpolated based on the discrete values at each fiber position, including integrated 4600 Å-6800 Å stellar flux, stellar velocity field, Hα flux, and Hα velocity field, for the late interaction phase galaxy merger Arp 299.

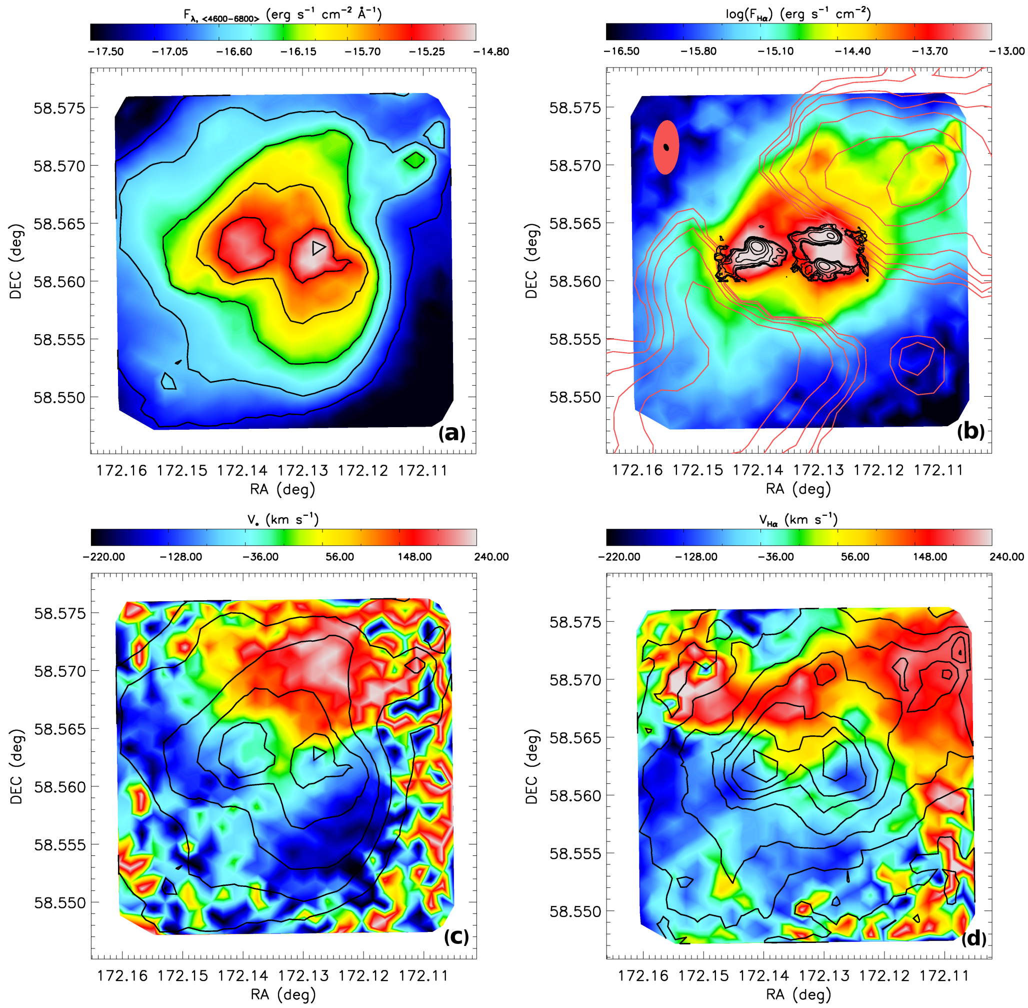

Figure 2: Late interaction phase galaxy merger Arp 299 VIRUS-P linearly interpolated IFU maps based on the discrete values at each fiber position of **(a)** 4600Å-6800Å integrated stellar flux, **(b)** Hα flux overlaid with CO(2-1) and HI integrated intensity map contours in intervals of 1–σ_{rms} and beam sizes from the CO(2-1) (black) and HI (red) maps, **(c)** stellar velocity field, and **(d)** Hα velocity field.

3. First Results: The Star Formation Rate and Gas Surface Density Relation in Galaxy Merger Arp 299

The main goal of VIXENS is to investigate the relation between star formation and gas content on spatially-resolved scales of 0.2-0.9 kpc in the extreme environments of IR bright interacting galaxy pairs and mergers. The VIXENS sample will allow us to study a wide range of SFRs and molecular gas surface densities (Figure 1). Figure 3 shows the first results from the VIXENS survey for late interaction phase galaxy merger Arp 299 [12]. We plot the spatially resolved SFR-gas surface density relation in Arp 299 on IFU fiber size scales of ~900 pc at our adopted distance of 44 Mpc. We use extinction-corrected Hα measurements from our IFU data to derive SFRs and a CO(2–1) gas map from [21] with a CO(2–1) to CO(1–0) ratio from [1] to derive H_2 surface densities. Two sets of points are shown, one using a Galactic CO–to–H_2 (X_{CO}) conversion factor [5] and the other using a starburst conversion factor [8]. Since Arp 299 has a high global IRAS IR SFR (94 $M_\odot$ yr^{-1}), this system is likely closer to starburst phase. It is unclear whether all the regions sampled by our IFU are starburst regions. However, since most of the fibers covered by the CO(2–1) gas map lie in the range of starburst galaxies [15], and SFRs based on Hα are likely lower limits, a starburst conversion factor may be more appropriate. Another caveat, however, is that X_{CO} likely varies as a function of interaction phase based on if the system is in starburst mode and therefore a bimodal X_{CO} is highly unlikely e.g., [20].

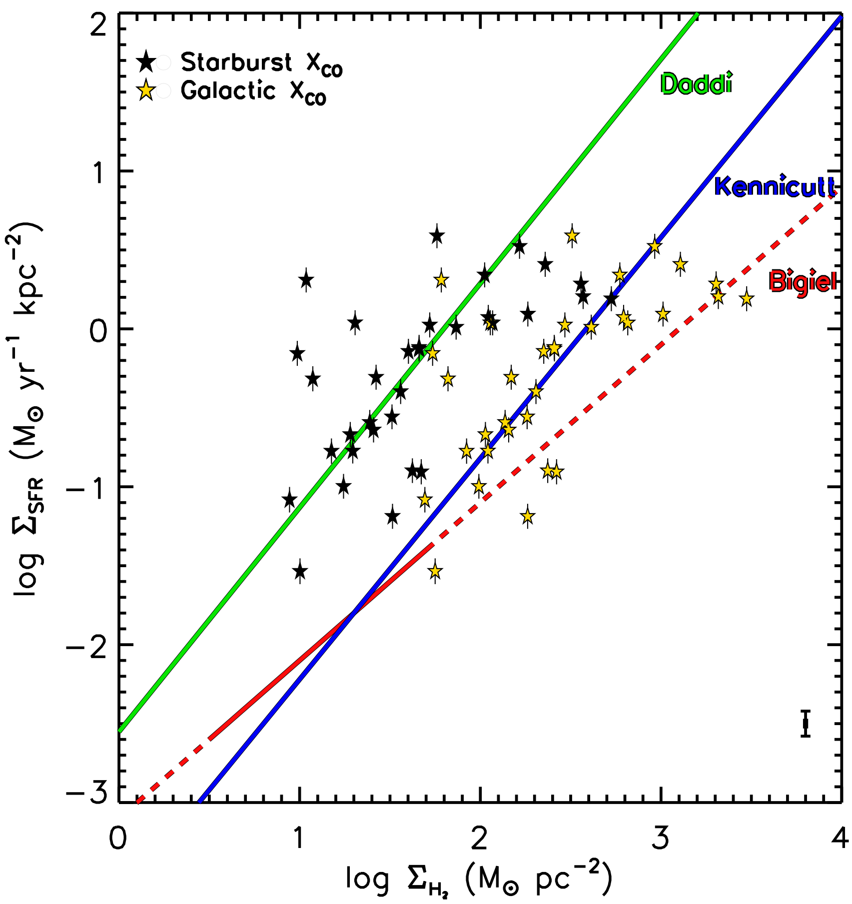

Figure 3: Spatially resolved SFR-H_2 surface density relation from measurements at each IFU fiber position with CO coverage (Figure 2) in late interaction phase galaxy merger Arp 299. Points are shown using a Galactic (yellow stars) and starburst (black stars) X_{CO} conversion factor. Lines indicate extragalactic relations on disk-averaged scales for spirals and starbursts (blue line) [15] and high-z mergers (green line) [7], as well as in 750 pc regions in spirals and dwarf galaxies (red line) [4].

Assuming a Galactic X_{CO} factor, spatially-resolved 900-pc regions in Arp 299 lie close to the Schmidt-Kennicutt relation (blue line), with slight deviations at the high gas surface density end (Figure 3). Since this late phase merger is likely closer to starburst phase, using a starburst X_{CO} factor would shift these points to the left, where they would lie in agreement with the relation (green line) found in high-z mergers [7,9]. If we assume that the X_{CO} starburst conversion factor [8] is correct for Arp 299, this implies there may be two regimes of star formation between normal disk galaxies and mergers at both low-z (this work) and at high-z [7,9]. However, this idea requires further testing on how the X_{CO} conversion factor varies on $\sim$kpc scales with interaction phase in interacting/starburst galaxies.

Acknowledgments

VIRUS-P construction was possible thanks to support from the Cynthia & George Mitchell Foundation. N.J.E. and A.H. were supported in part by NSF Grant AST-0607193.

References

[1] Aalto, S., Booth, R. S., Black, J. H., & Johansson, L. E. B., *Molecular gas in starburst galaxies: line intensities and physical conditions*,1995, *A&A*, 300, 369

[2] Adams, J. J. et al. , *The HETDEX Pilot Survey. I. Survey Design, Performance, and Catalog of Emission-line Galaxies*, 2011, *ApJS*,192, 5

[3] Barnes, J. E., & Hernquist, L. E., *Fueling starburst galaxies with gas-rich mergers*, 1991, *ApJ*, 370, 65

[4] Bigiel, F. et al. , *The Star Formation Law in Nearby Galaxies on Sub-Kpc Scales*, 2008, *AJ*, 136, 2846

[5] Bloemen. J. B. G. M. et al. , *The radial distribution of galactic gamma rays. III - The distribution of cosmic rays in the Galaxy and the CO-H2 calibration*, 1986, *A&A*,154, 25

[6] Cappellari, M., & Emsellem, E., *Parametric Recovery of Line-of-Sight Velocity Distributions from Absorption-Line Spectra of Galaxies via Penalized Likelihood*, 2004, *PASP*, 116, 138

[7] Daddi, E. et al. , *Different Star Formation Laws for Disks Versus Starbursts at Low and High Redshifts*, 2010, *ApJL*, 714, 118

[8] Downes, D., & Solomon, P. M., *Rotating Nuclear Rings and Extreme Starbursts in Ultraluminous Galaxies*,1998, *ApJ*, 507, 615

[9] Genzel, R. et al. , *A study of the gas-star formation relation over cosmic time*, 2010, *MNRAS*, 407, 2091

[10] Gao, Y., & Solomon, P. M., *The Star Formation Rate and Dense Molecular Gas in Galaxies*, 2004, *ApJ*, 606, 271

[11] Heiderman, A., Evans, II, N. J., Allen, L. E., Huard, T., & Heyer, M., *The Star Formation Rate and Gas Surface Density Relation in the Milky Way: Implications for Extragalactic Studies*, 2010, *ApJ*, 723, 1019

[12] Heiderman A. et al. , 2012, *ApJ*, in prep.

[13] Le Floc'h et al. , *Infrared Luminosity Functions from the Chandra Deep Field-South: The Spitzer View on the History of Dusty Star Formation at* $0 < z < 1$, 2005, *ApJ*, 632, 169

[14] Lotz, J. M., Jonsson, P., Cox, T. J., & Primack, J. R., *The effect of gas fraction on the morphology and time-scales of disc galaxy mergers*, 2010, *MNRAS*, 404, 590

[15] Kennicutt Jr. R. C., *Star Formation in Galaxies Along the Hubble Sequence*, 1998b, *ApJ*, 498, 541

[16] Nikolic, B., Cullen, H., & Alexander, P., *Star formation in close pairs selected from the Sloan Digital Sky Survey*, 2004, *MNRAS*, 355, 874

[17] Rahman, N. et al. , *CARMA Survey Toward Infrared-bright Nearby Galaxies (STING). II. Molecular Gas Star Formation Law and Depletion Time across the Blue Sequence*, 2012, *ApJ*, 745, 183

[18] Sanders, D. B. & Mirabel, I. F., *Luminous Infrared Galaxies*,1996, *ARAA*, 34, 749

[19] Sarzi M. et al. , *The SAURON project - V. Integral-field emission-line kinematics of 48 elliptical and lenticular galaxies*, 2006, *MNRAS*, 366, 1151

[20] Tacconi L. J. et al. , *Submillimeter Galaxies at* z *2: Evidence for Major Mergers and Constraints on Lifetimes, IMF, and CO-H2 Conversion Factor*, 2008, *ApJ*, 680, 246

[21] Wilson C. et al. , *Luminous Infrared Galaxies with the Submillimeter Array. I. Survey Overview and the Central Gas to Dust Ratio*, 2008, *ApJS*, 178, 189

PROCEEDINGS OF SCIENCE

Primordial Star Formation in the First Galaxies

Chalence Safranek-Shrader*, **Meghann Agarwal, Miloš Milosavljević, and Volker Bromm**
Department of Astronomy and Texas Cosmology Center, The University of Texas at Austin
E-mail: ctss@astro.as.utexas.edu

We present results of a high-resolution cosmological simulation which explores the process of primordial gas collapsing into a high-redshift atomic cooling halo, typically considered to be a 'first galaxy'. We consider a physically motivated scenario where a strong molecule destroying Lyman-Werner (LW) background prevents gaseous collapse, and thus star formation, in small mass halos. Only when molecular hydrogen can shield itself from LW radiation in a sufficiently massive halo will star formation be possible. We find that in a $1\,\mathrm{Mpc}^3$ (comoving) box with a LW background corresponding to $J_{21} = 100$ collapse first occurs in a $3\times10^7\,M_\odot$ dark matter halo at $z \simeq 12.1$. A distinct phase transition occurs in the center of the halo when molecular hydrogen (H_2) begins to self-shield, allowing baryons to cool, and to form a supersonically turbulent $\sim 10\,\mathrm{pc}$ core. We investigate the character of turbulence in this core, fragmentation properties, and impact on next generation star formation.

Frank N. Bash Symposium New Horizons In Astronomy,
October 9-11, 2011
Austin Texas

[1]University of Texas at Austin & Texas Cosmology Center
*Speaker.

PoS(Bash11)030

1. Introduction

The first metal-free stars (Pop. III) are theorized to form in $\sim 10^6\,\mathrm{M}_\odot$ dark matter minihalos at $z \sim 20-50$ (e.g., [1]). Determining their detailed initial mass function (IMF) is an ongoing challenge — estimates place their characteristic mass somewhere between ~ 10 and $\sim 100\ M_\odot$. The detectability of individual, high-redshift Pop. III stars is extremely low, even with the upcoming *James Webb Space Telescope*. However, clusters of Pop. III stars (which may form in larger mass halos if gas can remain metal-free) may be detectable [2]. Here, we present a cosmological simulation focused on the collapse of metal-free gas into the host of a typical first galaxy — an atomic cooling halo. We assume this halo forms in a region of space with a strong background LW radiation field capable of photodissociating H_2 and preventing gaseous collapse into low mass halos. Only when a halo becomes massive enough that H_2 can begin to self-shield will collapse, and thus star formation, be possible. We are primarily interested in this transition. When and where does this self-shielding transition take place? What environment does it produce? And what kind of subsequent star formation can we expect?

2. Methodology and Physical Details

We use the adaptive mesh refinement (AMR) code FLASH [3] to conduct our simulation. FLASH solves the Eulerian equations of hydrodynamics in comoving coordinates on an spatially adaptive grid. Baryons are represented by a hydrodynamic fluid while dark matter is modeled by collisionless, massive particles. The gravitational potential is computed by an iterative multigrid Poisson solver. We initialize our simulation at $z = 145$ in a $1\,\mathrm{Mpc}^3$ (comoving) box. Cosmological initial conditions were generated using current cosmological parameters. Our chemical model evolves the most thermally and chemically important species in metal-free gas — H, H^-, H^+, e^-, H_2, H_2^+, He, He^+, He^{++}, D, D^+, and HD. To trigger AMR refinement, we use two separate criteria based on local gas properties: one dependent on gas overdensity, and another enforcing that the Jeans length, $L_\mathrm{J} = \left(\pi c_s^2/G\rho_g\right)^{1/2}$, is adequately resolved by at least 12 grid cells. The most significant cooling mechanisms in metal-free first galaxies are Lyα emission from neutral hydrogen, molecular hydrogen cooling, and HD cooling. Lyα cooling is an extremely effective coolant above $\sim 10^4\,\mathrm{K}$ and can cool gas to $T \sim 8000\,\mathrm{K}$. Ro-vibrational emission from molecular hydrogen can potentially cool the gas further, although not below $\sim 200\,\mathrm{K}$. HD, if present, can cool gas further (limited by the CMB temperature floor), although an elevated electron fraction is likely required for it to form in significant quantities.

3. Pathway to a Metal Free Galaxy

For gas in our target halo to remain metal free, star formation in minihalos must be suppressed (e.g., [4], [5]). To this end, we impose a FUV flux of $J_{21} = 100$ across the entire box, such that $J_\nu = J_{21}\,10^{-21}\,\mathrm{erg\,s^{-1}\,cm^{-2}\,Hz^{-1}\,sr^{-1}}$ at the Lyman-limit. Above the Lyman-limit, $J_\nu = 0$. This UV flux strength will prevent gaseous collapse into minihalos (e.g., [6]) as it destroys molecular hydrogen, the key cooling agent for the first stars. From this radiation field, we only consider the photodissociation of H_2 and HD (not, for example, H^- destruction). We track the H_2 and HD column densities (N_{H_2} and N_{HD}) self-consistently to each point in the box assuming radiation is incident from the sides of the box. Given these column densities we can write the photo-dissociation rate of H_2 as $k_{H_2} = 1.38 \times 10^9 J_{LW} f^{H_2}_{shield}$, where J_{LW} is the mean radiation intensity at $h\nu = 12.87\,eV$ and $f^{H_2}_{shield}$ accounts for H_2 self-shielding, given by [7]

$$f^{H_2}_{shield} = \frac{0.965}{(1+x/b_5)^{1.1}} + \frac{0.035}{(1+x)^{0.5}} \times \exp[-8.5 \times 10^{-4}(1+x)^{0.5}] \tag{3.1}$$

where $x = N_{H_2}/5 \times 10^{14}\,cm^{-2}$, $b_5 = b/10^5\,cm\,s^{-1}$, and b is the velocity spread parameter of the gas. A similar approach is used for HD.

4. Results

With $J_{21} = 100$, H_2 is vigorously destroyed and gas density can only increase adiabatically. By $z \simeq 13$, a halo has grown massive enough that its virial temperature is on the order of $T \sim 10^4\,K$, the atomic cooling threshold, and its central region begins to collapse roughly isothermally at $T \simeq 8000\,K$. With increasing density, the H_2 formation and cooling rates increase. Additionally, the H_2 column rises, increasing the degree of LW self-shielding, and decreasing the H_2 destruction rate. These effects amplify each other and cause the H_2 abundance to increase in a runaway fashion. Specifically, this process occurs at a J_{21}-dependent critical density when $t_{cool,H_2} < t_{ff}$ (e.g., [8]) causing the gas to cool rapidly.

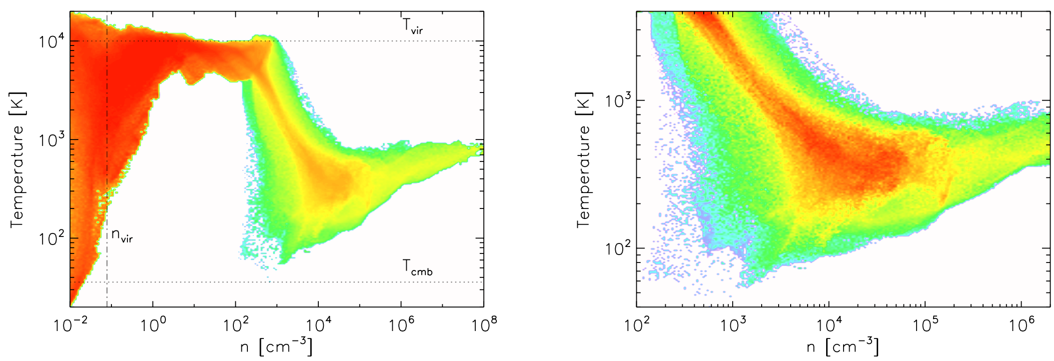

Figure 1: *Left*: Density-temperature phase plot of gas within $2R_{vir}$ of the target halo at $z \simeq 12.1$. We display the virial temperature of the halo, CMB temperature, and $n_{vir} = 18\pi^2\bar{n}$. *Right*: Same as the right figure, but different axes ranges, illustrating the 'loitering state' at $n \sim 2 \times 10^4\,cm^{-3}$ and $T \sim 400\,K$ and the further evolution along the standard metal-free molecular cooling track. Color coding corresponds to mass.

In Fig. 1 we show density-temperature phase plots at $z = 12.2$. Fig. 1(a), with a large dynamic range, illustrates gas being shock heated to $T \simeq 10^4\,K$ and the subsequent isothermal collapse occurring to a density of $n \sim 10^2\,cm^{-3}$. Fig. 1(b) highlights the state of the gas at intermediate densities. This behavior is similar in many respects to the canonical picture of metal-free gas collapse into a minihalo, as there is a fairly well defined 'loitering state' of gas at $n \sim 2 \times 10^4\,cm^{-3}$ and $T \sim 400\,K$, corresponding to the point where the energy levels of H_2 reach LTE and its cooling rate decreases. Further collapse occurs along the well-studied metal-free molecular cooling track. When the gas density reaches $n = 10^8\,cm^{-3}$, the self-shielding core (defined such that $f^{H_2}_{shield} <$

10^{-2}) has a mass of $\simeq 1.1\times10^4\,\mathrm{M}_\odot$, a diameter $\sim 10\,$pc, and mass- and volume-weighted RMS mach numbers ($\mathrm{Ma}\equiv c_s/v_{\rm tot}$) of 3.6 and 3.3, respectively. If this core produces one burst of star formation, the *maximum* star formation efficiency with respect to the total baryonic mass in the halo is $f_* = M_*/M_{bar} = 2\times10^{-3}$, likely much lower given we do not model any sort of stellar feedback. We introduce sink particles, using the method of [9], at a density of $n = 10^8\,\mathrm{cm}^{-3}$. For at least $2.5\times10^4\,$yrs after the formation of this sink no others are created, implying additional gaseous fragmentation and collapse (if any) in this timeframe occurred within the sink particle, an unresolved region. In Fig. 2(a), we plot the mass- and volume-weighted density PDFs for the self-shielding core. At low densities, the PDFs are well fit by log-normal distributions, suggesting supersonic turbulence, in the form of complex, interacting shocks, may be responsible for shaping the overall density distribution (e.g., [10]). The PDF power law tail at high densities is expected, arising from the gas gravitationally decoupling from the turbulent motion. Fig. 2(a) also displays standard deviation σ of the log-normal fits, which can be related to the mach number as $\sigma = \ln(1+b^2\mathrm{Ma}^2)^{1/2}$, where numerical experiments have found b to lie between 0.2 and 0.5. The log-normal fits then correspond to $\mathrm{Ma} = 1.71/b$ and $\mathrm{Ma} = 1.29/b$ for the mass- and volume-weighting, respectively, very much consistent with the measured mach numbers in the self-shielding core.

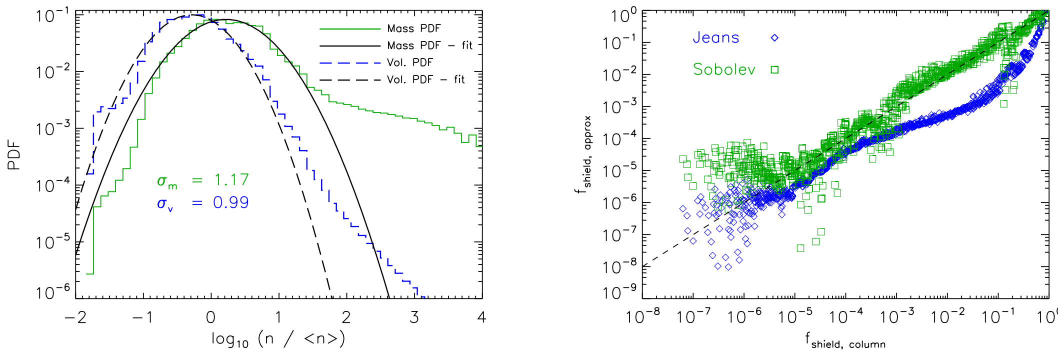

Figure 2: *Left*: Mass-weighted (*green histogram*) and volume-weighted (*blue dashed histogram*) density PDFs of self-shielding gas ($f_{\rm shield}^{\rm H_2} < 10^{-2}$) at $z \simeq 12.2$ plotted as a function of $\log_{10}(n/\bar{n})$. Black lines are log-normal fits to the PDFs — *solid*: mass-weighted PDF fit, *dashed*: volume-weighted PDF fit. In low density regimes, the PDFs are reasonably fit by log-normal distributions, which are known to describe turbulent flows. The disagreement at high densities is caused by the self-gravity of the gas. *Right*: Comparison of the H_2 self-shielding factor between our integrated column density approach ($f_{\rm shield,column}$), a Sobolev approach (green squares), and a Jeans length approach (blue diamonds). The black line represents a one-to-one mapping. As is clear, the Sobolev approximation is quite accurate for being a purely local approximation, except for a few places of stark disagreement, likely due to small velocity gradients. A combination of these two approaches would be useful for future work (e.g., [11]).

5. Discussion and Conclusion

Many details of this study were suppressed for space and will be presented in upcoming work. We do note several limitations and caveats, however. We neglect the photodissociation of H^-, which plays a key role in H_2 formation. Its impact, though, depends on the shape of the incident

PoS(Bash11)030

radiation spectrum and even if included would mainly shift the collapse redshift, unaffecting our results qualitatively. We also neglect the impact of large velocity gradients which, by doppler shifting of LW resonances, could cause our value of $N_{\rm H_2}$ to be overestimated compared with the actual column. Ref. [7], however, argue that radially coherent gas flow greatly reduces this effect's impact. A common approximation for $N_{\rm H_2}$ is given by $N_{\rm H_2} = n_{\rm H_2} L_{\rm char}$ where $L_{\rm char}$ is a characteristic length scale and $n_{\rm H_2}$ is the number density of molecular hydrogen. In Fig. 2(b), we compare our integrated approach for $f^{\rm H_2}_{\rm shield}$ to two common approximations for $L_{\rm char}$; (1) $L_{\rm char} = L_{\rm J}$ (Jeans length), and (2), a close analogue to the Sobolev length [11], $L_{\rm char} = v_{\rm th}/|\nabla \cdot \mathbf{v}|$, where $v_{\rm th} = (k_{\rm B}T/m_{\rm H})^{1/2}$. We note that both methods yield reasonable agreement, particularly the Sobolev length being fairly accurate over many decades in $f^{\rm H_2}_{\rm shield}$. Finally, a detailed examination of HD's role is warranted, especially given suggestions (e.g., [12]) that it may play a key role in shaping the thermodynamics inside the first galaxies. We note, however, that no significant HD cooling mode was seen in the simulation.

We have explored the process of metal free gas collapse into an atomic cooling halo, focusing on the turbulent and fragmentation properties of a central, self-shielding core. We find that while the gas density PDF appears to be partly shaped by supersonic turbulence, no concurrent fragmentation takes place, at least at densities below $n = 10^8\,{\rm cm}^{-3}$. Additional fragmentation may take place at higher densities. Indeed, other studies have shown that fragmentation does occur in metal-free gas at high densities, even in minihalos where turbulence is thought to play a minor role.

References

[1] V. Bromm & R. Larson, *The First Stars*, *ARA&A* **42**, 79-118

[2] E. Zackrisson et al., *The Spectral Evolution of the First Galaxies. I. JWST Detection Limits and Color Criter for Pop. III Galaxies*, *ApJ* **740**, 13

[3] B. Fryxell et al., *FLASH: An Adaptive Mesh Hydrodynamics Code for Modeling Astrophysical Thermonuclear Flashes*, *ApJS*, **131**, 273-334

[4] J. Johnson, T. Greif, & V. Bromm, *Occurrence of Metal-free Galaxies in the Early Universe*, *MNRAS* **388**, 26-38

[5] T. Greif, S. Glover, V. Bromm, & R. Klessen, *The First Galaxies: Chemical Enrichment, Mixing, and Star Formation*, *ApJ* **716**, 510-520

[6] B. O'Shea & M. Norman, *Pop. III Star Formation in a Lambda-CDM Universe. II. Effects of a Photodissociating Background*, *ApJ* **673**, 14-33

[7] J. Wolcott-Green, Z. Haiman, & G. Bryan, *Photodissociation of H2 in Protogalaxies: Modelling Self-Shielding in Three-Dimensional Simulations*, *MNRAS* **418**, 838-852

[8] K. Omukai, *Primordial Star Formation under Far-Ultraviolet Radiation*, *ApJ* **546**, 635

[9] C. Federrath, R. Banerjee, P. Clark, & R. Klessen, *Modeling Collapse and Accretion in Turbulent Gas Clouds: Implementation and Comparison of Sink Particles in AMR and SPH*, *ApJ* **713**, 269-290

[10] A. Kritsuk, M. Norman, P. Padoan, & R. Wagner, *The Statistics of Supersonic Isothermal Turbulence*, *ApJ* **665**, 416-431

[11] P. Clark et al., *Gravitational Fragmentation in Turbulent Primordial Gas and the Initial Mass Function of Pop. III Stars*, *ApJ* **727**, 110

[12] J. Johnson & V. Bromm, *The Cooling of Shock-Compressed Primordial Gas*, *MNRAS* **366**, 247-256

PROCEEDINGS OF SCIENCE

Revisiting the Post-reionization Kinetic Sunyaev-Zel'dovich Effect on the Cosmic Microwave Background Fluctuations

H. Park*, **E. Komatsu**, **P. R. Shapiro**
Univrsity of Texas at Austin, U.S.A.
E-mail: hcosmosb@astro.as.utexas.edu, komatsu@astro.as.utexas.edu, shapiro@astro.as.utexas.edu

In order to study the reionization contribution to the kinetic Sunyaev-Zel'dovich effect, we need to subtract the post-reionization contribution to the observed total signal. In this poster, we show post-reionization calculation of the kinetic Sunyaev-Zel'dovich (kSZ) effect required to acquire the reionization contribution for our subsequent study. In the poster, we present the 3rd order perturbation theory (3PT) as an effective approximation for calculating the post-reionization kSZ effect. We find that, at $l = 3000 \sim 7000$, about 60% of the contribution comes from large scale ($k < 1.5h/Mpc$) structure at high redshifts ($z > 1$) where the 3PT is valid. Future work should model the reionization contribution so that the observed data from currently ongoing surveys can be used to constrain the reionization history.

Frank N. Bash Symposium New Horizons In Astronomy,
October 9-11, 2011
Austin Texas

*Speaker.

PoS(Bash11)031

1. Introduction

New experiments are underway to measure the temperature fluctuations of the cosmic microwave background (CMB) on small angular scales caused by the Compton scattering of CMB photons by free electrons in the intergalactic medium, the Sunyaev-Zel'dovich (SZ) effect. Inside galaxy clusters, low-energy CMB photons were up-scattered by hot intergalactic electrons because of their microscopic thermal velocities (thermal SZ, tSZ). Outside clusters, free electrons with bulk motions that departed from pure Hubble flow also scattered CMB photons (kinetic SZ, kSZ), first during the epoch of reionization (EOR), when light from the first galaxies created giant patches of ionized gas, and later, after these patches had grown and merged to create a fully-ionized universe. The tSZ signal is strongest, but can be separated from the others by its unique frequency dependence, with a null at ~ 220 GHz. The post-reionization kSZ signals can be modeled with full ionization assumption. After subtracting the post-reionization kSZ signals to the total signal, we are left with the EOR contribution that contains information about the history of the first stars and galaxy formation that led to reionization.

In the poster, we revisit the post-reionization kSZ calculation and show the 3PT as an effective approximation for the calculation. We assume that the gas follows the total matter distribution at the scale of interest.

2. Formalism of the Post-reionization kSZ Effect

The change of the CMB temperature due to the kSZ effect is given by integration of the Doppler shift of the scattered photons along the line of sight ($\hat{\gamma}$)

$$\frac{\Delta T}{T}(\hat{\gamma}) = \int dl e^{-\tau} \bar{n}_e \sigma_T \hat{\gamma} \cdot X \mathbf{v}(1+\delta), \tag{2.1}$$

where n_e, σ_T and dl are number density of electrons, Thomson scattering cross-section and differential element of the physical distance, that are multiplied togerther to give the fraction of scattered photons as the light proceeds by dl. $e^{-\tau}$ with $\tau \equiv \int_0^l dl \sigma_T n_e$ expresses the attenuation of the signal due to the optical depth from oberserver to the medium where the signal is generated. Throughout the poster, we express the velocity in units of the speed of light. Therefore, by $\mathbf{v}$, we actually mean $\mathbf{v}/c$. X denotes the mean ionized fraction of the universe. The resulting CMB power spectrum from the kSZ effect is

$$C_l = \bar{n}_{e,0}^2 \sigma_T^2 \int \frac{dx}{x^2}(1+z)^4 e^{-2\tau} P_{Xq\cdot\hat{\gamma}}(\frac{l}{x}, z), \tag{2.2}$$

where $\mathbf{q} \equiv \mathbf{v}(1+\delta)$, $\bar{n}_{e,0} \equiv \bar{n}_e/(1+z)^3$ and x is the comoving distance from the observer to the medium. Hence, the key part in the estimation of the kSZ effect is to model the power spcetrum of the ionized line of sight momentum field, $P_{Xq\cdot\hat{\gamma}}(k,z)$.

For the post-reionization contribution of the kSZ effect, we can assume a fully ionized universe, i.e., $X = 1$, and only have to model the density and velocity field. If we assume the density and velocity field to be completely linear, $P_{Xq\cdot\hat{\gamma}} = P_{q\cdot\hat{\gamma}}$ reduces to a second order expression as following [1, 2].

$$P_{q\cdot\hat{\gamma}}(k,z) = \frac{\dot{a}^2 f^2}{2} \int \frac{d^3k'}{(2\pi)^3} P_{\delta\delta}(|\mathbf{k}-\mathbf{k}'|, z) P_{\delta\delta}(k', z) \frac{k(k-2k'\mu')(1-\mu'^2)}{k'^2(k^2+k'-2kk'\mu')} \tag{2.3}$$

In non-linear regime, [3] derived a non-linear expression assuming that the velocity field does not have vorticity and therefore the Fourier compononent of velocity is still parallel to the direction of the mode ($\mathbf{v} \propto \hat{\mathbf{k}}$). This is a good approxmiation since the gravity would not generate the vorticity in the velocity field unless we look at an extemely non-linear regime that would not be important for the kSZ effect. Under those assumptions, the power spectrum of the momentum field is given as following.

$$P_{q\cdot\hat{\gamma}}(k,z) = \frac{1}{2}\int \frac{d^3k'}{(2\pi)^3}(1-\mu'^2)(P_{\delta\delta}(|\mathbf{k}-\mathbf{k}'|)P_{vv}(k') - \frac{k'}{|\mathbf{k}-\mathbf{k}'|}P_{\delta v}(|\mathbf{k}-\mathbf{k}'|)P_{\delta v}(k')) \tag{2.4}$$

3. Modeling the Post-reionization kSZ Effect

In principle, when we evaluate Eq.2.4 with precise power spectra ($P_{\delta\delta}, P_{vv}, P_{\delta v}$), we obtain the line of sight momentum field and compute the kSZ signal from post-reionization regime precisely. In reality, computing the power spectra down to small enough scales requires large-scale and high-resolution simulations, and is too expensive to be done for different cosmological parameters. Therefore, one has to use an approximate way to compute the line-of-sight momentum power spectrum quickly.

[4] substituted a non-linear density power spectrum from the halo fitting model of [5] to the linear expression of the momentum power spectrum (Eq. 2.3) after justifying it by comparing it with their simulation. In this report, we use power spectra from the 3rd order perturbation theory with the non-linear expression (Eq. 2.4).

3.1 The 3rd Order Perturabtion Theory

Keeping the next-to-leading order terms in the cosmological equations for density and velocity of the medium enables us to extend the analytic solution to the non-linear regime [8]. The 3rd order perturabtion theory power spectrum is known to agree at 10% level at $z > 1.5$ and $k < 1$(h/Mpc) [6]. We investigate the validity of the 3PT in terms of calculating the kSZ signal. In this study, we adobt the WMAP7 cosmology parameters given by $\Omega_\Lambda = 0.728$, $\Omega_m = 0.272$, $\Omega_b = 0.0455$, $h = 0.704$, $\sigma_8 = 0.81$, $n_s = 0.967$ and $z_{ov} = 6$ [7].

4. Result

We first investigate the validity of the 3PT by comparing the C_l calculated from our formalism and another one by [4] (See figure 1). Our result shows a reasonable agreement with that of [4] within 10% between $l = 3000$ and $l = 10000$, which is being probed by current experiments. We also compare the contribution from where the 3PT is valid and where the 3PT is not valid by looking into the integrand (See Figure 2). We tabulated the relative ratio of the contribution from where the 3PT is valid to the total integral at different l's (See Table 1). We find that a significant contribution comes from the regime where the 3PT is valid.

5. Discussion and Future Work

In this report, we showed that the 3PT is useful for calculating the non-linear post-reionization kSZ effect in the range of the multipoles in which the kSZ signal is expected to be measured. About

PoS(Bash11)031

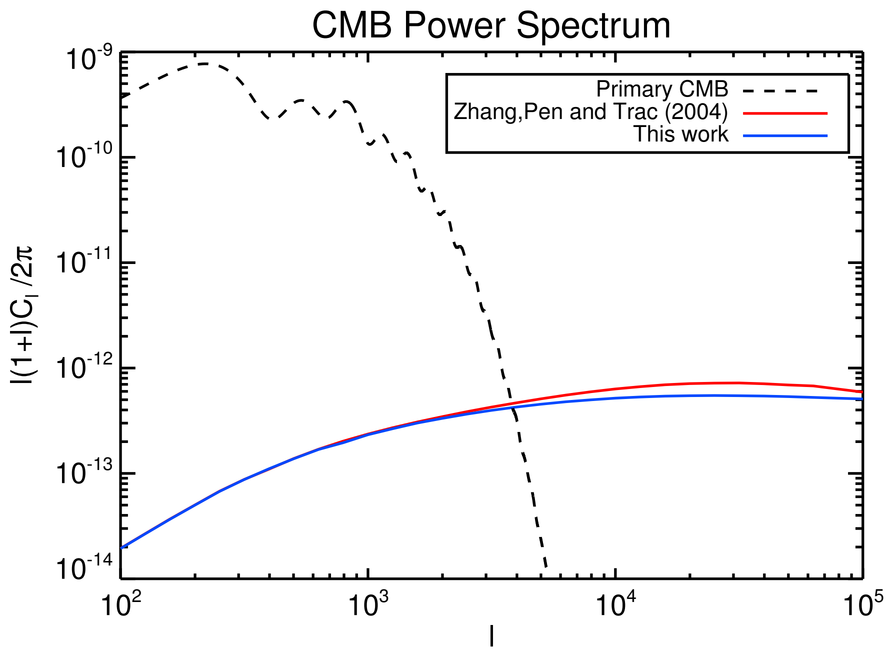

Figure 1: The power spectrum of the CMB and the kSZ effect. The dotted line shows the power in the limit of the linear theory. The blue solid line is the kSZ signal calculated from our 3PT formalism and the red line is calculated from the formalism of [4]. The primary CMB (dashed black line) is also plotted for comparison.

Table 1: The ratio of $z > 1$ contribution of C_l to the total value

Multipole moment (l)	$z > 1$ contribution
100	29%
300	54%
1000	61%
3000	60%
5000	60%
10000	61%

60% of the total signal is contributed by the wave number range where the 3PT is accurate enough. We obtain a power spectrum similar to that obtained with the method used by [4].

Our ultimate goal for the subsequent study is to model the full kSZ effect significantly contributed by the reionization epoch. We will study the reionization kSZ effect using our reionization simulation and construct a template that can be used to compare with current experiments like the South Pole Telescope and the Acatama Cosmology Telescope. We will focus on simulating the "patchy" signal that is thought to be the dominant factor of the reionization contribution by post-processing our n-body simulation data with radiative transfer.

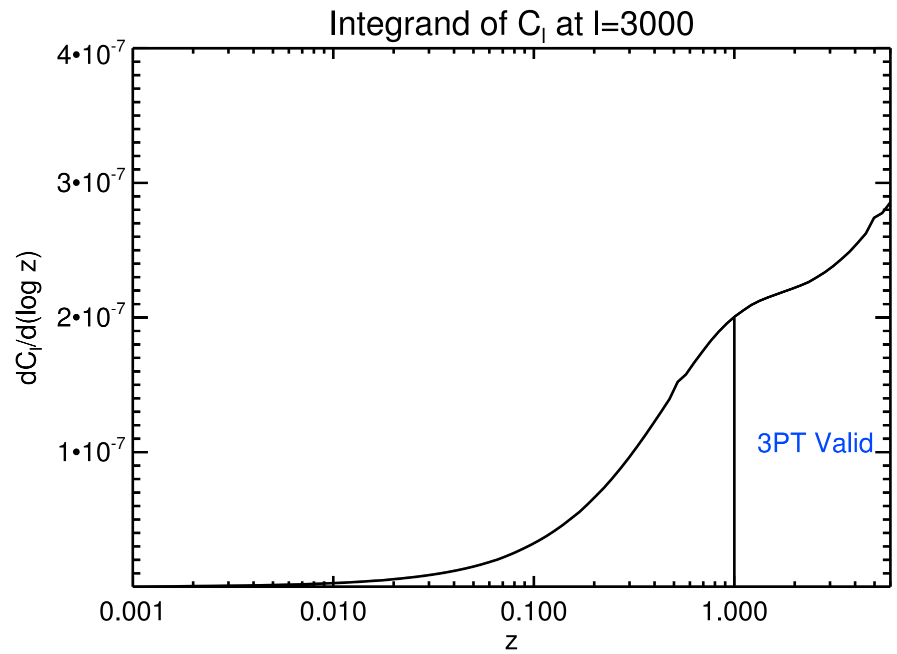

Figure 2: Integrand of C_l at $l = 3000$. The label is chosen so that the area under the curve gives the total integrated value of C_l. The right side of the vertical line marks where the 3PT is valid.

References

[1] Ostriker, J. P., Vishniac, E. T., *Generation of microwave background fluctuations from nonlinear perturbations at the ERA of galaxy formation Universe*, 1986, ApJ, 306L, 51O

[2] Vishniac, E. T., *Reionization and small-scale fluctuations in the microwave background*, 1987, ApJ, 322, 597V

[3] Vishniac, E. T., *Nonlinear Kinetic Sunyaev-Zeldovich Effect*, 1987, Physical Review Letters, vol. 88, Issue 21, id. 211301

[4] Zhang, P, Pen, U. L. Trac, H., *Precision era of the kinetic Sunyaev-Zel'dovich effect: simulations, analytical models and observations and the power to constrain reionization*, 2004, MNRAS, 347, 1224Z

[5] Smith, R. E., Peacock, J. A., Jenkins, A., White, S. D. M., Frenk, C. S., Pearce, F. R., Thomas, P. A., Efstathiou, G., Couchman, H. M. P., *Stable clustering, the halo model and non-linear cosmological power spectra*, 2003, MNRAS, 341, 1311S

[6] Jeong, D., Komatsu, E. , *Perturbation Theory Reloaded: Analytical Calculation of Nonlinearity in Baryonic Oscillations in the Real-Space Matter Power Spectrum*, 2006, ApJ, 651, 619J

[7] Komatsu, E., Smith, K. M., Dunkley, J., Bennett, C. L., Gold, B., Hinshaw, G., Jarosik, N., Larson, D., Nolta, M. R., Page, L., Spergel, D. N., Halpern, M., Hill, R. S., Kogut, A., Limon, M., Meyer, S. S., Odegard, N., Tucker, G. S., Weiland, J. L., Wollack, E., Wright, E. L. , *Seven-year Wilkinson Microwave Anisotropy Probe (WMAP) Observations: Cosmological Interpretation*, 2011, ApJS, 192, 18K

[8] Vishniac, E. T. , *Why weakly non-linear effects are small in a zero-pressure cosmology*, 1983, MNRAS, 203, 345V